Abstract

Control of Spatiotemporal Dynamics of Complex Lasers and Applications

Kyungduk Kim

2022

Complex lasers possess numerous spatial degrees of freedom and display diverse and rich behaviors. They open the possibility of laser-on-demand, i.e., providing the desired lasing performance. One example is the broad-area semiconductor laser with many transverse lasing modes, whose nonlinear interactions with gain material may induce lasing instabilities. In this dissertation, we control the spatiotemporal dynamics of multimode quantum-well semiconductor lasers by tailoring the geometry of the laser cavity. Furthermore, we demonstrate novel applications of the multimode lasers in speckle-free imaging and parallel random number generation.

First, we investigate the impact of asymmetric cavity geometries—from integrable to chaotic—on the spatiotemporal instabilities in broad-area edge-emitting semiconductor lasers. We aim to understand how the spatial structure of the lasing modes affects the nonlinear light-matter interactions and the mode competition for gain. This, in turn, allows understanding the role of classical ray dynamics, which dictates the wavefunction of the passive cavity resonances. We experimentally show that the cavity shape profoundly affects the laser fluctuation power and the spatiotemporal scales of the instabilities. It will eventually enable us to engineer the lasing dynamics by designing the cavity shape based on ray dynamical principles. Moreover, our method of manipulating nonlinear dynamics will have an impact on controlling not only semiconductor lasers but also other complex systems with spatiotemporal instabilities.

Secondly, we design, fabricate, and characterize novel semiconductor lasers as illumination sources for high-speed speckle-free imaging. To obtain directional emission, we fo-

cus on the stable cavity configuration. By optimizing the cavity shape, we experimentally demonstrate hundreds of transverse lasing modes in a single microcavity, with a decoherence time as short as a few nanoseconds. Furthermore, we show that a small perturbation from the planar cavity—a bifurcation point of classical ray dynamics—can dramatically modify the lasing behavior. Even with slightly curved end facets, our near-planar cavity laser features significantly reduced lasing instabilities. The unique combination of high power, low spatial coherence, short decoherence time, and directional emission will make our laser an excellent light source for speckle-free full-field imaging and parallel display.

Next, we invent a new physical random number generator based on our many-mode semiconductor laser. By tailoring the cavity geometry, we eliminate the long-range correlations in the emission intensity and process the complex interference pattern of numerous lasing modes in space and time for parallel random bit generation. We demonstrate the ultrafast generation of hundreds of independent random bit streams in parallel from a single chip-scale laser. We accelerate the total bit generation rate to 250 Terabits per second, which exceeds the state-of-the-art physical random bit generators with offline post-processing by two orders of magnitude. Our scalable, robust, and energy-efficient approach will pave the way for secure communications and high-performance computing.

Finally, we investigate the many-mode vertical-cavity surface-emitting lasers (VCSEL). A numerical method is developed to calculate the resonances in three-dimensional large-area VCSELs with intrinsic material birefringence with asymmetric cavity geometry. By tailoring the cavity cross-section shape, we enhance the number of transverse lasing modes by narrowing the distribution of quality factors or reducing the mode competition for gain. In addition to the complex spatiotemporal dynamics, the many-mode VCSELs feature ultrafast polarization dynamics, which can be controlled via cavity geometry.

Control of Spatiotemporal Dynamics of Complex Lasers and Applications

A Dissertation
Presented to the Faculty of the Graduate School
of
Yale University
in Candidacy for the Degree of
Doctor of Philosophy

By
Kyungduk Kim

Dissertation Director: Professor Hui Cao

December 2022

Acknowledgments

I would not have been able to complete this long journey without the dedicated support of my mentors, colleagues, and family.

First and foremost, I would like to sincerely express my gratitude to my thesis advisor Professor Hui Cao. Her advice and patience carried me through all the stages of my Ph.D. study. I feel extremely fortunate to have had an opportunity to study under her guidance.

I would also like to thank Professor Douglas Stone and Professor Jung Han for serving on my thesis committee and giving insightful comments on my research. I also thank Professor Takahisa Harayama for agreeing to be my external dissertation reader.

This endeavor would not have been possible without Dr. Stefan Bittner, who has been a wonderful mentor. I am indebted to him for his immense support throughout my research.

I have been lucky to work with fantastic researchers. I am grateful to have collaborated with Professor Qi Jie Wang, Dr. Yongquan Zeng, and Yuhao Jin, who have fabricated high-quality semiconductor devices. I also would like to acknowledge Professor Ortwin Hess and Dr. Stefano Guazzotti for numerical simulations and enlightening discussions.

I feel very humbled and blessed to work with the spectacular members of Becton. I had a pleasure working with and learned a lot from Dr. Hasan Yılmaz, Dr. Yaniv Eliezer, Dr. Chun-Wei Chen, Dr. Chia Wei Hsu, Dr. Olivier Spitz, Dr. Wen Xiong, Dr. Nicholas Bender, Dr. Shai Gertler, SeungYun Han, Liam Shaughnessy, and Rohin MacIntosh. I also would like to acknowledge the administrative support of Maria Rao, Alexander Bozzi, Giselle Maillet, and Jessica Tefft. Lastly, I want to thank the funding sources of my research: Yale University, the Air Force Office of Scientific Research (AFOSR), the Office of Naval Research (ONR), and the National Science Foundation (NSF).

Finally, I would like to give my special thanks to my family in Korea for their continuous unconditional appreciation and encouragement. It sustained me this far, and thank you for always being so supportive every step of my way.

Contents

List of Figures

List of Tables

Chapter 1

Introduction

The goal of this dissertation is to control the spatiotemporal dynamics of complex lasers. The main objective is to study how cavity ray dynamics impact nonlinear lasing dynamics by exploring various cavity geometries [1–5]. The next goal is to utilize the huge spatial degrees of freedom in complex lasers for diverse applications, such as a speckle-free light source [1, 2] and parallel random number generation [3].

1.1 Complex lasers

Conventional lasers feature coherent, directional, and high-power emissions. Most lasers consist of a cavity with two mirrors facing each other and a gain material between the mirrors. When the light amplification exceeds the cavity loss, lasing oscillation occurs in a cavity. Typically, the laser cavity is designed to support lasing of a single transverse mode. The simplest way is to keep the lateral dimension of a laser cavity small. With a reduced transverse dimension of the laser cavity, the diffraction loss of high-order transverse modes increases, and thus they are less likely to lase. The resultant single-mode operation and high spatial coherence enable a sharp focusing and propagation with a small divergence of laser beams. Such a high-brightness beam led to many applications of lasers in the industry, communications, medicine, and other research areas.

In contrast, complex lasers have extended cavity size or complicated structures, possessing a huge spatial degree of freedom in the laser cavity. Random lasers [6–8], degenerate-cavity lasers [9–11], and multimode fiber lasers [12, 13] are such examples supporting many distinct spatial modes. The numerous lasing modes interact nonlinearly with the gain material and compete with each other for gain. As a result, complex lasers exhibit rich physics, enabling many possible lasing states and diverse dynamics. There are many opportunities of using complex lasers for various applications. For instance, many spatially distinct lasing modes significantly reduce the spatial coherence, which can effectively suppress the coherent artifacts in many imaging systems [14, 15]. Moreover, as the laser emission is mapped into a high-dimensional phase space with a complicated landscape, the complex lasers can be useful for reservoir computing [16] and physical simulators [17].

1.2 Broad-area semiconductor lasers

Broad-area edge-emitting semiconductor laser is an example of a complex laser with numerous spatial degrees of freedom. Typically they have a stripe geometry, with an extended cavity width on the order of 100 micrometers and a longitudinal cavity length of a few millimeters. It operates with multiple transverse and longitudinal lasing modes, accommodating a high power reaching a Watt-level from a single emitter. With advantages of compactness, easiness of fabrication, and high quantum efficiency, broad-area lasers have been widely used for high-power applications such as material processing, medical applications, large-scale display, pump sources for solid-state and fiber lasers, and space communications.

One of the significant issues—yet an interesting physical phenomenon—of broad-area

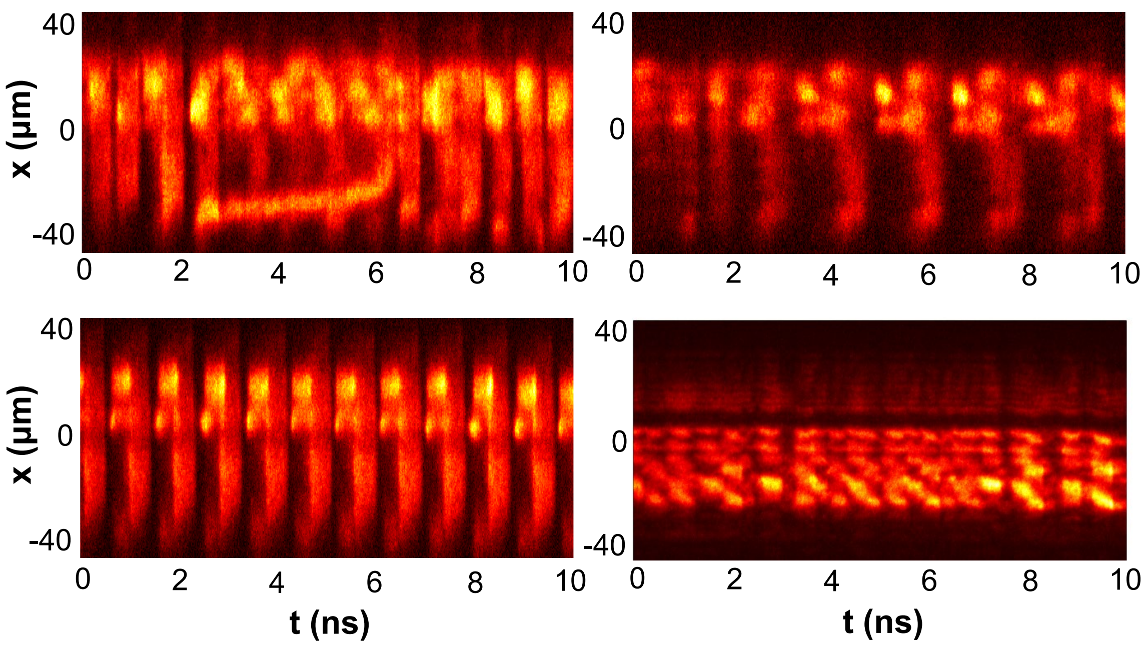

Figure 1.1: **Spatio-temporal lasing instabilities of broad-area edge-emitting semiconductor lasers.** Examples of the near-field spatiotemporal intensity distributions measured by a streak camera [4]. It features a variety of dynamics, ranging from regular to chaotic pulsations. The emission profile is disrupted into multiple filaments with a typical width of several micrometers, oscillating in time with the period of sub-nanoseconds. Moreover, the filaments are not fixed in space but migrate laterally.

lasers is the spatiotemporal lasing instability [18]. The instability is rooted in the strong nonlinear light-matter interaction between the multiple lasing modes and semiconductor gain material [19–26]. As shown in Fig. 1.1, The emission intensity often entails filamentation and irregular pulsation, which significantly degrade the spatial and temporal beam quality. As the nonlinearities become more substantial with increasing intensity, these instabilities greatly limit many applications that demand ever-increasing power requirements.

The filaments result from several effects, including spatial hole burning, carrier diffusion, and most importantly, carrier-induced index changes [22, 23]. In the active medium of the laser, the region of increased local intensity depletes the gain. For semiconductor gain medium with amplitude-phase couplings, such as GaAs quantum well, it can raise the refractive index locally and form a lens. The resulting lensing effect causes self-focusing and creates filaments. As a result, the spatial profile of a beam is no longer a clean Gaussian-shaped beam but breaks into irregular filaments, with a typical lateral size of several microns (Fig. 1.1).

These filaments vary in time and space, leading to complex spatiotemporal dynamics and instabilities. As the filaments with high local intensity can further deplete the gain, they soon diminish. The pump then replenishes the gain, and the filaments revive. This process repeats and leads to modulational instabilities, causing the pulsation of emission intensities. Moreover, the filaments can migrate laterally to other locations with higher gain. The typical time scale of this dynamics is on the order of sub-nanoseconds, which is determined by the intrinsic carrier dynamics of the semiconductor gain material. A typical radio-frequency (RF) spectrum of the broad-area semiconductor lasers features a strong oscillation power at a few GHz.

Several approaches have been proposed to stabilize the broad-area edge-emitting semiconductor lasers [18]. Most efforts aim to minimize the number of lasing modes by injection locking or optical feedback [27, 28]. However, realizing single-mode lasing in a large cavity and fine-tuning external operational parameters is highly challenging. In addition, these approaches are effective up to a certain power level, beyond which multiple modes lase and instabilities return [4].

An interesting question is whether we can control the lasing instabilities of these broad-area semiconductor lasers while keeping multimode operation. Maintaining a large gain volume is necessary to accommodate high-power and many lasing modes. Here the shape of the resonator is one of the degrees of freedom we can control. The spatial structure of cavity resonances might impact the mode competition and nonlinear light-matter interaction in an active medium. In turn, the lasing dynamics would be affected by tuning the geometry of the laser cavity.

1.3 Ray dynamics in optical cavities

The resonator shape is the essential parameter that determines the lasing behaviors. The traditional cavity design utilizes ray tracing, tracking the propagation of optical rays inside the cavity. For two-dimensional microlasers, there have been extensive studies of the cavity ray dynamics [29–34]. A resonator is often modeled as a photon billiard, in which a single point-like particle moves freely and reflects at the boundaries. Depending on the cavity geometry, the system can exhibit various ray dynamics.

The billiards can exhibit regular, chaotic, or mixed ray dynamics. A circular cavity is one example of cavities showing regular ray dynamics. Figure 1.2(a) shows its typical ray trajectory that propagates along the cavity boundary. When the initial direction of the ray slightly changes, the trajectories slowly diverge in time. For such an integrable system with regular ray dynamics, the divergence grows at most linearly in time.

In contrast, for chaotic billiards, the deviation grows exponentially in time. One can achieve this by simply making a straight cut on a circular cavity [Fig. 1.2(b)] [35, 36]. In the D-shaped cavity, a slight difference in initial directions induces a significant divergence after only a few reflections, and the propagation directions completely change. In a closed cavity with elastic reflections, the ray will eventually travel to every region inside the cavity. These striking differences between the circular and D-shape cavities demonstrate the impact of cavity shape on the ray dynamics.

Due to the ray-wave correspondence, the ray dynamics dictate the wavefunction of the cavity resonances. For the circular cavity, the ray trajectory going along the cavity boundary corresponds to the whispering gallery mode [Fig. 1.2(c)]. The mode has well-defined radial and azimuthal mode numbers. For an open circular resonator like semiconductor microdisk lasers, the optical ray is confined by total internal reflection; hence, these whispering-gallery modes have extremely high quality-factors, which led to numerous ap-

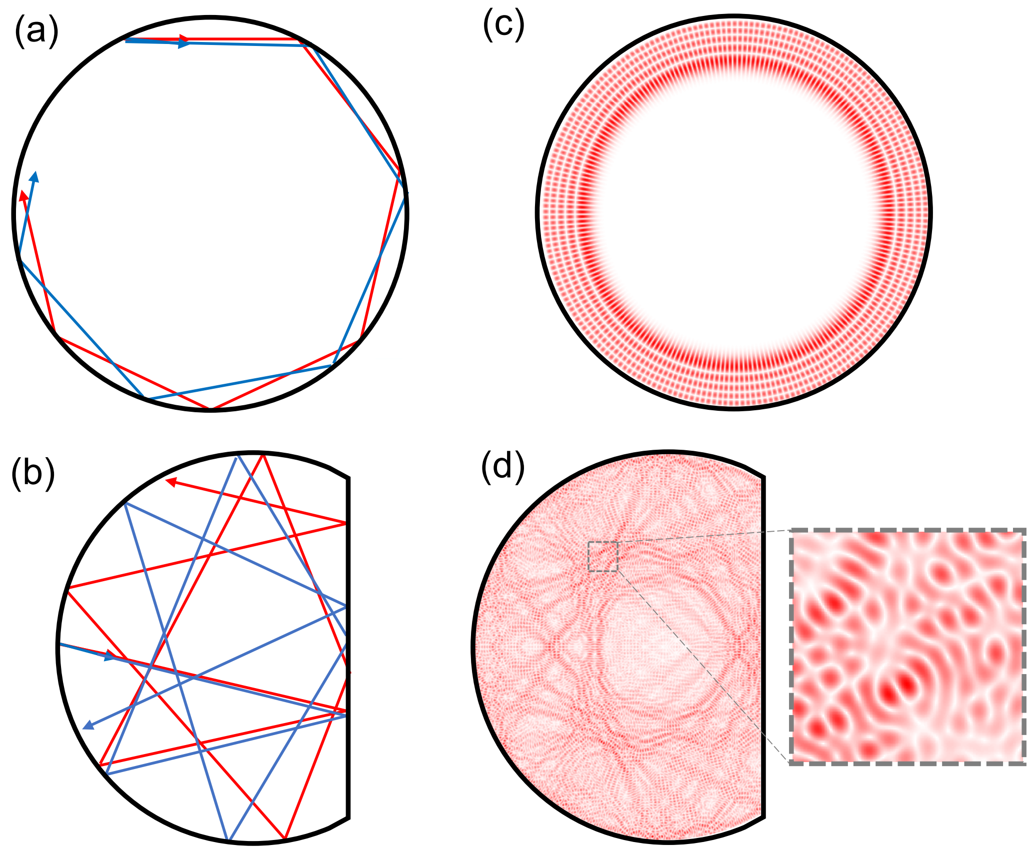

Figure 1.2: **Cavity ray dynamics and ray-wave correspondence.** Optical trajectories in (a) a circular and (b) a D-shaped cavity. Two trajectories with different colors have slightly different initial directions of propagation. For the integrable system (a), the deviation between two trajectories grows linearly, while for the chaotic system (b), it grows exponentially. (c) An exemplary whispering-gallery mode of a circular cavity. It has well-defined radial and azimuthal mode numbers. (d) For a D-shaped cavity, a passive mode has the spatial mode profile spread throughout the cavity. The wavefunction has a fine-grained speckle-like structure.

plications in modern photonics [37].

On the other hand, the chaotic ray trajectory of the D-shaped cavity leads to the passive mode that fills the entire resonator [Fig. 1.2(d)]. This chaotic resonance does not possess well-defined mode numbers. Moreover, as the ray propagates in all possible directions, in the wave perspective, the interference of many wave components leads to a speckle-like fine-grained structure inside the cavity. Therefore, the chaotic ray dynamics result in a complex spatial structure of passive modes.

Many studies have focused on the effect of the cavity geometry on the static properties of the laser emission [32–34], e.g., the optical spectra or spatial emission profiles. In contrast, a few studies focus on its dynamics [38–41]. An interesting question would be the effect of wave-chaotic cavities on the chaotic lasing dynamics of the broad-area semiconductor lasers. One would expect that adding the complexity of the chaotic ray dynamics would make the lasing dynamics even more unstable. Surprisingly, the D-shaped cavities could effectively suppress the spatiotemporal instabilities of the semiconductor lasers [4]. The stabilized lasing dynamics were attributed to the fine-grained spatial profile of lasing modes in wave-chaotic cavities, disrupting the formation of self-focusing instabilities. It demonstrates the importance of cavity geometry, which can change the spatial structure of passive modes and consequently alter the nonlinear light-matter interactions in a gain medium.

Even though the chaotic ray dynamics could help suppress the lasing instabilities, the chaotic optical propagation poses an issue of emission directionality, i.e., the emission does not have a preferential emission direction. Hence, the collection efficiency is significantly degraded. The cavity geometry can be optimized to improve the directionality of the laser emission [31, 42–46]. Here one might ask whether the chaotic ray dynamics are essential to suppress the spatiotemporal instabilities or whether the lasing dynamics could be controlled in other cavities with integrable or even mixed ray dynamics, which may improve the emission directionality. Understanding the role of classical ray dynamics on the lasing dynamics will eventually allow us to engineer the lasing dynamics by designing the cavity shape based on the ray dynamical principles.

1.4 Dissertation outline

In this dissertation, we present a method for controlling broad-area semiconductor lasers by tailoring the geometry of the laser cavity. Moreover, from a practical point of view, this dissertation proposes applications that harness massive spatial degrees of freedom of the many-mode semiconductor lasers.

Chapter 2 of this dissertation investigates the spatiotemporal dynamics of broad-area edge-emitting lasers with various asymmetric laser cavities. We explore diverse cavity geometries featuring integrable to chaotic ray dynamics. The cavity ray dynamics affect the spatial structure of cavity resonances, which profoundly impact the nonlinear light-matter interactions in semiconductor gain material. In particular, we find the spatial localization and the local characteristic length of cavity resonances primarily affect the lasing instabilities. This chapter concludes that suppression of lasing instabilities is not generic for wave-chaotic cavities but could be attained with integrable systems with judiciously designed cavity shapes.

Chapter 3 presents the control of the number of lasing modes in a stable cavity configuration with two end mirrors–one of the most well-known and simple integrable systems, yet a few studies exist, particularly for multimode semiconductor lasers [47–50]. In terms of emission directionality, the stable laser geometry outperforms wave-chaotic cavities. The number of modes could be maximized by curving both end mirrors and optimizing their curvatures in a near-concentric regime. Experimentally we enhance the number of lasing modes by two orders of magnitude and attain hundreds of spatial modes lasing simultaneously from a single laser diode. Such a laser, featuring a low spatial coherence combined with high output power, can be used as an ideal illumination source for speckle-free full-field imaging.

Chapter 4 discusses how sensitively the cavity shape can impact the lasing behavior.

The Fabry-Perot geometry with planar facets is located at a bifurcation point of unstable and stable ray dynamics. At such a cavity geometry, the ray dynamics, hence the spatial structure of resonances, can be changed dramatically by a slight change in the resonator shape. The near-planar cavities feature a drastically increased number of transverse lasing modes and a significantly more stable output than planar cavities. Compared to the near-concentric cavity in Chapter 3, the divergence angle of laser emission of the near-planar cavity is considerably narrowed, which will improve the collection efficiency of the laser output and facilitate its applications.

Chapter 5 presents a new application of the stable-cavity broad-area laser in Chapter 3 for ultrafast parallel random bit generation. Lasing of high-order transverse modes suppresses the filaments and eliminates spatiotemporal correlations in the emission intensity. As a result, the cavity geometry drastically accelerates the time scale of intensity fluctuation from sub-nanoseconds to a few picoseconds. The emission of this many-mode laser features ultrafast spatiotemporal interference of many transverse and longitudinal modes, which creates a complex intensity pattern in space and time. Moreover, spontaneous emission noise constantly feeds stochastic noise into the emission pattern, guaranteeing unpredictability and non-reproducibility. By employing spatial multiplexing of the emission intensity, our proof-of-principle demonstration shows the massively parallel generation of random bit streams at hundreds of spatial channels, accelerating the total bit generation rate to two orders-of-magnitude faster than state-of-the-art.

Lastly, in Chapter 6, our methodology of controlling edge-emitting lasers by cavity shape is extended to a vertical-cavity surface-emitting laser (VCSEL). Compared to edge-emitting lasers, VCSELs have greatly improved emission directionality thanks to their vertical cavity structure. A numerical framework to calculate the passive resonances in a broad-area VCSEL structure is developed. The numerical results show that specially-designed cavity geometries can enhance the number of lasing modes in VCSELs. Moreover, lasing of many spatial modes leads to complex and ultrafast spatiotemporal polarization dynamics. This many-mode large-area VCSEL with improved directionality would facilitate speckle-free imaging and parallel random number generation.

Chapter 2

Controlling lasing dynamics by asymmetric cavity geometry

2.1 Introduction

[1]Optical microresonators and microlasers have attracted a lot of interest as testbeds for studying the properties of open integrable or wave-chaotic systems and in view of applications [31, 33, 34]. A particular interest was the development of so-called asymmetric microlasers that exhibit low lasing thresholds but more directional emission than conventional circular microdisk lasers as on-chip light sources. So far, almost all studies of asymmetric dielectric microresonators and microlasers have concentrated on their static properties like spectra, quality factors and far-field intensity distributions, with the objective of understanding the relation between passive cavity modes and classical ray dynamics, the so-called principle of *ray-wave correspondence*. In contrast, the lasing dynamics of asymmetric microlasers has barely been investigated with only a few numeric studies [38, 39] and experiments [40, 41]. Hence we have so far no general understanding of the relations between the cavity shape and the classical ray dynamics on the one hand and the

[1]The chapter material is primarily taken from Kyungduk Kim*, Stefan Bittner*, Yongquan Zeng, Yuhao Jin, Qi Jie Wang, Hui Cao, "Spatio-temporal dynamics of asymmetric microcavity semiconductor lasers", *in preparation*. *These authors contributed equally.

lasing dynamics on the other hand. In chapter 2, we show that the nonlinear dynamics of asymmetric semiconductor microlasers is very rich and depends on the cavity shape.

Nonlinear lasing dynamics has been studied for a long time [18, 51, 52], and the field of laser chaos has attracted increasing interest for fundamental investigations and applications alike. In particular semiconductor lasers can be applied as ultra-fast random number generators, in secure telecommunication, for microwave photonics, optical computing and sensing [53, 54]. Hence the development of highly-stable semiconductor lasers as well as of lasers featuring broad-band chaos have become very active fields of research. Chaotic dynamics is typically induced via optical injection or delayed feedback [18, 54, 55]. However, also free-running semiconductor lasers can feature instabilities [56] and chaos [57] induced by multimode interaction. While almost all studies of semiconductor laser dynamics consider conventional Fabry-Perot (FP) cavities, our study of free-running edge-emitting lasers with various asymmetric cavity shapes demonstrates the great and so far untapped potential of using the cavity geometry to tailor the dynamics of semiconductor lasers. The resonator shape thus provides a huge but mostly unexplored parameter space for designing microlasers with specific dynamical properties.

Edge-emitting semiconductor lasers with cavities spatially extended in two dimensions can develop complex spatio-temporal dynamics [19, 21, 23–26, 58]. In particular the so-called filamentation in broad-area FP-type lasers is a well-known problem [19, 25], which can be explained as a modulational instability caused by a self-focusing effect [21, 23, 24]: a stronger optical field in one region of the cavity locally depletes the gain, and the reduction in carrier density increases the refractive index. The resulting lensing effect further increases the optical field in this region and thus creates a filament. However, the filaments are intrinsically unstable since gain depletion will eventually destroy them and lead to the creation of new filaments in regions with undepleted gain, which leads to complex, pulsating spatio-temporal emission patterns [19, 25].

In Ref. [4], filamentation and other spatio-temporal instabilities are strongly suppressed in asymmetric microlasers with a D-shaped cavity, which features chaotic ray dynamics. This was explained by the fine-grained structure of the lasing modes due to the chaotic ray dynamics: intensity variations on very small length scales appear to be too insignificant to create a lensing effect, thus preventing the formation of filaments. This raises the question whether such a mechanism is generic for wave-chaotic cavities, but also could be attained in integrable systems. Interesting questions would be which fundamental physical mechanisms influence the strength of spatio-temporal instabilities, and how these mechanisms are related to the cavity geometry and the classical ray dynamics.

We try to answer these questions by experimentally investigating the spatio-temporal dynamics of edge-emitting semiconductor microlasers with AlGaAs / GaAs quantum wells and five different resonator shapes. The different cavity geometries and their ray dynamics manifest in the structure of the passive cavity modes which we study in detail to correlate it with the strength of lasing instabilities. We surmise that the spatial structure of the modes strongly impacts the interaction with the active medium, and thus the cavity geometry directly affects the spatio-temporal dynamics.

The five different resonator shapes we study are the D-cavity, stadium, Limaçon, ellipse and square geometries, and they exhibit different types of ray dynamics. Our experimental results show that the cavity shape indeed strongly affects the occurrence and strength of lasing instabilities. In particular the degree of spatial localization and the fine structure size of the intensity distributions play a significant role. While resonators with spatially extended and fine-grained modes (D-cavity, stadium and square) feature quite stable lasing dynamics, resonators like the Limaçon and ellipse with whispering gallery modes that are spatially localized and exhibit a larger structure size display strong instabilities. Moreover, we observe that also the length and time scales of spatio-temporal instabilities are affected by the cavity shape.

2.2 Resonators, ray dynamics, and passive cavity modes

2.2.1 Device structure and fabrication

We fabricate edge-emitting GaAs/AlGaAs quantum well semiconductor microlasers based on a commercial epiwafer (Q-Photonics QEWLD-808). The lateral boundaries and thus the different cavity shapes are defined via UV-lithography and dry etching. The etch goes completely through the guiding layer and partially into the bottom cladding to provide good lateral light confinement due to a high refractive index contrast at the sidewalls. The sidewalls are very vertical and exhibit small, but non-negligible surface roughness (see Ref. [59]). After the etching, the top metal contacts for electrical pumping are deposited, which are withdrawn by a few micrometer from the cavity edges (see Section 3.4 for details of the fabrication process).

Figure 2.1 shows exemplary scanning electron microscope images of the five different cavity shapes. All cavities have an approximately equal area of about $2.53 \times 10^4 \mu\mathrm{m}^2$ to ensure equal pump current density and resonance density. The guiding layer supports a single vertical excitation, and thus the optical field propagates in the plane of the resonators with a phase velocity c/n_{eff}, where c is the speed of light in vacuum and $n_{\mathrm{eff}} = 3.37$ the effective refractive index. The laser emission has transverse electric (TE) polarization, that is, the electric field is parallel to the plane of the resonators.

2.2.2 Ray and wave simulations

Figure 2.2 shows typical ray trajectories and passive cavity modes with high quality (Q) factors for the five cavity shapes. The classical trajectories were calculated with a simple ray tracing algorithm. The power of the rays is reduced according to the Fresnel reflection

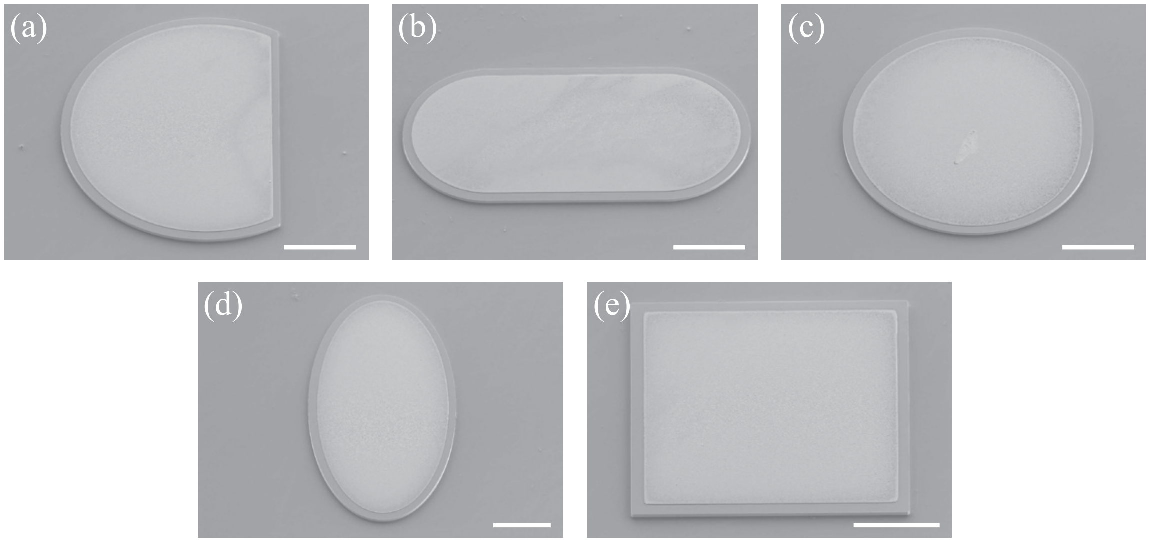

Figure 2.1: **Semiconductor lasers with different cavity shapes.** Perspective scanning electron microscope images of edge-emitting microlasers in the shape of (a) D-cavity, (b) stadium, (c) Limaçon, (d) ellipse and (e) square. The scale bars are 50 μm long.

coefficients at each reflection to account for the leakiness of the dielectric cavities[2].

We model the laser cavities as two-dimensional (2d) dielectric resonators, that is, the passive cavity modes are solutions of the 2d scalar Helmholtz equation

$$\{\Delta + n^2(\vec{r})k^2\}\Psi(\vec{r}) = 0\,, \tag{2.1}$$

with outgoing-wave boundary conditions [32, 34], where $\vec{r} = (x, y)^T$ are the coordinates in the plane of the cavity, $n(\vec{r})$ is the refractive index structure of the cavity ($n = n_{\text{eff}}$ inside and $n = 1$ outside of the cavity), and the wave function Ψ corresponds to the z-component of the magnetic field, H_z, for TE-polarized modes. The solutions are computed numerically using the COMSOL eigenfrequency solver module, where the outgoing-wave boundary conditions are implemented via perfectly matched layers at the boundaries of the computational domain. The real part of the resonance wave numbers k corresponds to the resonance frequency and the imaginary part to the life time, hence the quality factors

[2]The decay of the ray trajectories is not indicated in Fig. 2.2 for the sake of simplicity.

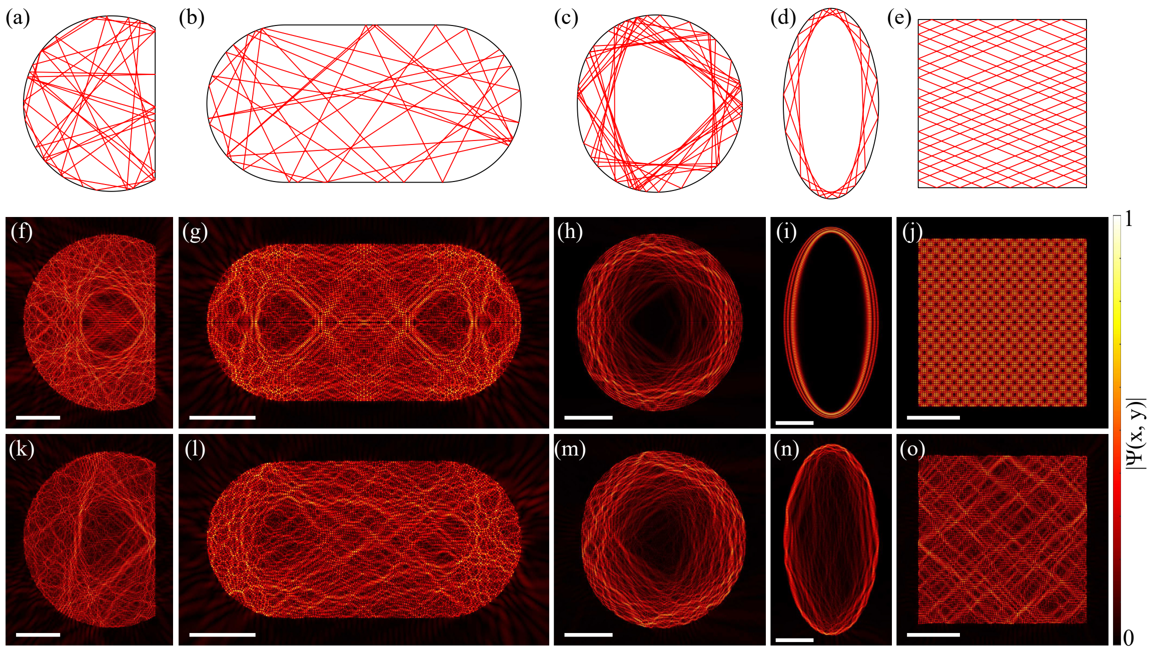

Figure 2.2: **Ray dynamics and wave functions for the five cavity shapes.** (a)–(e) Typical ray trajectories. (f)–(j) Wave functions of high-Q modes in a smooth and (k)–(o) a rough cavity. The scale bars are 5 μm long. The resonance wavelengths and quality factors of the resonances are (f) $\lambda = 799.33$ nm and $Q = 1597$, (g) $\lambda = 797.39$ nm and $Q = 2987$, (h) $\lambda = 797.37$ nm and $Q = 30,332$, (i) $\lambda = 800.88$ nm and $Q = 290.8 \times 10^9$, (j) $\lambda = 797.92$ nm and $Q = 10.8 \times 10^6$, (k) $\lambda = 799.5$ nm and $Q = 1814$, (l) $\lambda = 798.37$ nm and $Q = 2075$, (m) $\lambda = 800.95$ nm and $Q = 9514$, (n) $\lambda = 800.38$ nm and $Q = 8454$, and (o) $\lambda = 798.42$ nm and $Q = 18,580$.

are given by $Q = -\mathrm{Re}(k)/[2\mathrm{Im}(k)]$.

The wave simulations were performed for cavities with ten times smaller linear dimension (area of about 253 $\mu\mathrm{m}^2$) due to computational constraints. Since both the simulated and the fabricated cavities are well within the semiclassical regime $kR \gg 1$, where R is a typical linear dimension (e.g., the radius of the D-cavity), the simulation results can nonetheless be considered representative for the actual cavities. Calculations were performed both for cavities with smooth [Figs. 2.2(f)–(j)] and rough boundaries [Figs. 2.2(k)–(o)] to study the impact of the residual surface roughness on the quality factors and wave function structure.

Surface roughness

Since surface roughness is inevitable in real-world microresontors, we also calculate the passive cavity modes of resonators with surface roughness and compare the results to smooth cavities in order to understand the impact of roughness. The surface roughness model we use is very similar to the one in Refs. [4, 60]. The boundaries are perturbed by adding a superposition of high-order harmonics with random phase and amplitude. The cavity geometries of interest have a combination of curved and straight boundaries, and we adapt the roughness model to these two cases.

For Limaçon and ellipse resonators, the entire boundary is curved and the local radius of the cavity $r(\varphi)$ is defined in polar coordinates by a single closed form. In these cases as well as for the curved boundary parts of the D-cavity and stadium, a perturbation

$$\Delta R(\varphi) = \sum_{m=m_1}^{m_2} a_m \cos(m\varphi + \theta_m) \tag{2.2}$$

is added to the local radius $r(\varphi)$. The amplitudes a_m and phases θ_m are random variables with uniform distributions in the range of $a_m \in [-10, 10]$ nm and $\theta_m \in [0, 2\pi]$, respectively, where a_m determines the length scale of perturbations perpendicular to the boundary, which is in the low nanometer range. The range of the harmonics is from $m_1 = 5$ to $m_2 = 42$. The harmonics with the longest period m_1 is determined by R/ξ, where $R = 10$ μm is the typical radius of a cavity and $\xi = 2$ μm is the maximal length scale parallel to the boundary of the surface roughness in experimental cavities. The harmonics with the shortest period m_2 is determined by nR/λ, where $\lambda/n = 0.8/3.37$ μm is the in-medium wavelength of the optical field.

For the straight boundaries of D-cavity, stadium and square resonators, the perturbation

$$\Delta R(s) = \sum_{m=m_1}^{m_2} a_m \cos\left[m\left(2\pi\frac{s}{s_0}\right) + \theta_m\right] \tag{2.3}$$

is added in the direction perpendicular to the boundary, where s is the coordinate along the straight boundary and s_0 is the entire length of the cavity boundary. The amplitudes a_m and phases θ_m are random variables with the same distributions as for the curved boundaries.

2.2.3 Ray-wave correspondence

One of the cornerstones of wave-dynamical chaos is the principle of ray-wave correspondence, that is, the classical ray dynamics manifests in the properties of the spectrum: the structure of the wave functions and the quality factors. The two types of ray dynamics discussed in the following are integrable and chaotic dynamics. For chaotic dynamics, the ray trajectories exhibit an exponential sensitivity to their initial conditions and explore the entire phase space over time, that is, their dynamics is ergodic. Examples are the D-cavity and the stadium billiards [Figs. 2.2(a) and (b)]. For integrable dynamics, the trajectories exhibit a linear sensitivity to their initial conditions and are confined to invariant surfaces of lower dimension, that is, they cannot explore the complete phase space. Examples are the ellipse and the square billiard [Figs. 2.2(d) and (e)].

The semiclassical eigenfunction hypothesis [61, 62] states that the wave functions of a resonator reflect the underlying classical dynamics: for integrable ray dynamics, each wave function is based on a particular invariant surface in phase space, whereas for chaotic dynamics, wave functions are based on the entire chaotic part of phase space. Consequently, the wave functions of a closed resonator with completely chaotic ray dynamics are on average homogeneously distributed over the whole cavity since the ray dynamics is ergodic. The correspondence of a wave function with different parts of the phase space can be visualized using so-called Husimi distributions [63, 64]. For open systems like the dielectric resonators considered here, however, the wave functions are based only on certain parts of the chaotic phase space depending on the resonance lifetime [65–67], and they can hence exhibit a spatially inhomogeneous profile [5] like the examples shown in Figs. 2.2(f) and(g).

The quality factors of the resonant modes are also connected to the classical ray dynamics. In particular, the ellipse features so-called whispering gallery modes (WGMs) based on trajectories completely confined by total internal reflection (TIR)[3] that have ultra-high Q-factors [Fig. 2.2(i)]. For chaotic ray dynamics, in contrast, the quality factors are often much lower since almost all ray trajectories eventually reach a part of phase space where they escape refractively. In the following we discuss the ray-wave correspondence for the five cavity geometries in more detail.

The D-cavity is a circle of which a section has been cut off, where the distance from the circle center to the cut is $R/2$ with $R = 100\ \mu$m the radius[4]. The stadium consists of a square with side length $a = 119\ \mu$m between two semicircles of radius $a/2$. Both the D-cavity and stadium have completely chaotic ray dynamics [35, 36] with the exception of trajectories with measure zero in phase space which are of no importance in the following. Consequently, their classical trajectories cover the whole billiard [Figs. 2.2(a) and (b)] and the high-Q resonances are spatially extended [Figs. 2.2(f) and (g)], though they feature circular regions of reduced intensity due to the leakiness [5]. Their quality factors are lower than those of the other cavities since the chaotic ray dynamics leads to significant refractive losses [5, 68]. The wave functions exhibit an irregular, fine-grained and speckle-like structure. Surface roughness slightly reduces the Q-factors and makes the wave functions a bit more spatially homogeneous [Figs. 2.2(k) and (l)], but does not

[3]The critical angle for total internal reflection is $\chi_{\mathrm{crit}} \simeq 17.3^\circ$ in our case.

[4]The dimensions indicated in the following are those of the fabricated cavities. The simulated cavities have ten times smaller linear dimensions.

fundamentally change their structure. Various aspects of stadium microlasers including the mode competition [59, 69] have been studied. We have previously investigated the near-field intensity distributions and resonance lifetimes of D-cavity and stadium microlasers [5] as well as the spatio-temporal dynamics of the D-cavity [4], which serves as motivation for the present study.

The boundary of the Limaçon cavity [70] is defined in polar coordinates by

$$r(\varphi) = R_0(1 + \epsilon \cos\varphi) \tag{2.4}$$

where φ is the azimuthal angle, $R_0 = 86\ \mu$m the mean radius and $\epsilon = 0.42$ the deformation parameter. In contrast to the D-cavity and stadium, its ray dynamics is predominantly, but not completely chaotic: since it is a convex cavity, there remain invariant surfaces with whispering-gallery type trajectories very close to its boundary [71, 72], and there is a small stable island with integrable ray dynamics around the horizontal diameter orbit [70, 72] as well as further tiny stable islands around other stable periodic orbits [73]. So while technically a mixed system, we will consider it a chaotic billiard in the following since the integrable regions of phase space are very small and the relevant resonances are based on the chaotic part.

The dielectric Limaçon resonator with $\epsilon = 0.42$ is of great practical interest because it combines resonances with very high Q-factors and directional far-field emission [72]. This is due to the existence of trajectories [Fig. 2.2(c)] which remain confined by TIR for a long time before reaching the leaky region of phase space, which is attributed to the existence of partial barriers in phase space [74, 75]. Hence the high-Q resonances are WGMs [Fig. 2.2(h)], but with a more disordered structure and lower Q-factors compared to the integrable ellipse [Fig. 2.2(i)] since the modes of the Limaçon are based on chaotic trajectories. The resonances come in near-degenerate pairs with odd and even mirror symmetry.

Surface roughness reduces the Q-factors and decreases the degree of spatial localization a bit [Fig. 2.2(m)], but does not fundamentally change the structure of the high-Q resonances.

Our ellipse cavities with aspect ratio $b/a = 2$ have a minor (major) diameter of $a = 127$ μm ($b = 254$ μm). Like the circle, the ellipse has completely integrable ray dynamics [76] and features WGMs spatially localized near the boundary with ultra-high Q-factors which are based on trajectories confined by TIR [Fig. 2.2(d)]. Since the ray dynamics is integrable, the WGMs have a very regular structure [Fig. 2.2(i)] and can be labeled with azimuthal and radial quantum numbers [77]. These WGMs appear in near-degenerate doublets [78]. The ellipse resonators are strongly affected by surface roughness: the Q-factors are significantly reduced, and the modes lose their regular structure and are significantly less localized [Fig. 2.2(n)]. While the mode competition in ellipse microlasers has been studied [59, 69], the spatio-temporal dynamics has not been investigated so far.

The square microlasers have a side length of 159 μm. The square has completely integrable ray dynamics like the ellipse, however, the structure of ray trajectories and resonant modes is quite different. Since the moduli of the wave vector components, $|k_x|$ and $|k_y|$, are conserved quantities [Fig. 2.2(e)], there exist trajectories confined by TIR at all reflections which give rise to modes with very high Q-factors [79]. The wave functions exhibit a very regular structure like for the ellipse [Fig. 2.2(j)], however, they cover the whole cavity homogeneously in correspondence with the underlying ray trajectories and in contrast to the highly localized WGMs of the ellipse. The integrable ray dynamics allows to develop simple semiclassical models for the spectrum and wave functions of the square which explain the very regular structure [80–82]. Surface roughness significantly decreases the quality factors and renders the structure of the wave functions more irregular [Fig. 2.2(o)], but the modes retain fairly high Q-factors and spatial homogeneity.

The five geometries introduced above have been carefully chosen to elucidate how the resonator geometry and the resulting structure of the wave functions affects the spatio-temporal dynamics of semiconductor microlasers. In particular we vary the type of classical dynamics (integrable vs chaotic), which affects the fine structure of the modes, and the degree of spatial localization (spatially extended modes vs localized WGMs), since we presume that these are key properties affecting the lasing dynamics. The effect of surface roughness is another important aspect for practical applications.

There are several interesting comparisons to be made that will reveal the role of different properties. Both D-cavity and stadium have chaotic ray dynamics combined with spatially extended modes, though the stadium has somewhat lower lasing thresholds [5]. Comparing these two cavities will reveal if the very stable dynamics observed for the D-cavity [4] is a general feature of such resonator geometries. The Limaçon cavity also has chaotic ray dynamics, but its modes are localized WGMs. Comparing the Limaçon to D-cavity and stadium will reveal the role of spatial localization for wave-chaotic resonators and if stable dynamics can be combined with directional emission. The square exhibits spatially extended modes like the D-cavity and stadium, but the wave function fine structure is more regular since the square has integrable ray dynamics. Ellipse and Limaçon also contrast integrable with chaotic ray dynamics, however, they both feature localized WGMs in contrast to the other resonators. Finally the ellipse and square can be compared as two cases with integrable ray dynamics, but very different degree of spatial localization and different fine structure. Hence the comparisons outlined above should yield precise insights into the relation of the spatio-temporal dynamics with the resonator geometry, the degree of spatial localization and the classical ray dynamics.

2.2.4 Lasing thresholds and number of lasing modes

An important aspect of microcavity lasers is the mode competition and the resulting number of lasing modes since not only it determines the spatial coherence of the laser and but also the interaction of several lasing modes can lead to instabilities. While we do not have a simulation tool capable of simulating the dynamics of our asymmetric microlasers, which is computationally extremely expensive [4], the Steady-state Ab-initio Lasing Theory (SALT) [83–86] has proven very useful to estimate the number of lasing modes of such lasers even though it is strictly speaking not applicable when the laser does not reach a steady-state. As our microcavities have relatively high quality factors, we employ the single pole approximation to SALT (SPA-SALT) that uses the passive cavity modes as the elements [60, 87, 88]. We perform simulations for three different realizations of rough cavities since the smooth Limaçon, ellipse and square cavities feature unrealistically high Q-factors that would skew the results. Figure 2.3(a) shows the computed lasing thresholds for the five cavity shapes, which are inversely proportional to the quality factors $Q_{\max}$ of the most long-lived modes. Limaçon, ellipse and square have the lowest thresholds, whereas D-cavity and stadium have significantly higher thresholds. This demonstrates how strongly the cavity shape can affect the lasing threshold.

The onset of further lasing modes is determined by a combination of their Q-factors compared to the first lasing mode, which clamps the gain, and the spatial overlap of their intensity distributions. The number of modes N_Q with $Q \geq 0.8 \cdot Q_{\max}$ is shown in Fig. 2.3(b). N_Q is relatively high for the D-cavity and stadium since they feature a lot of modes with similar Q-factors, though there are significant variations for different roughness realizations. For the Limaçon, ellipse and square, in contrast, N_Q is only in the range of 1 to 4 since these cavities often feature an exceptionally high $Q_{\max}$.

The actual number of lasing modes, however, also depends on spatial gain-competition

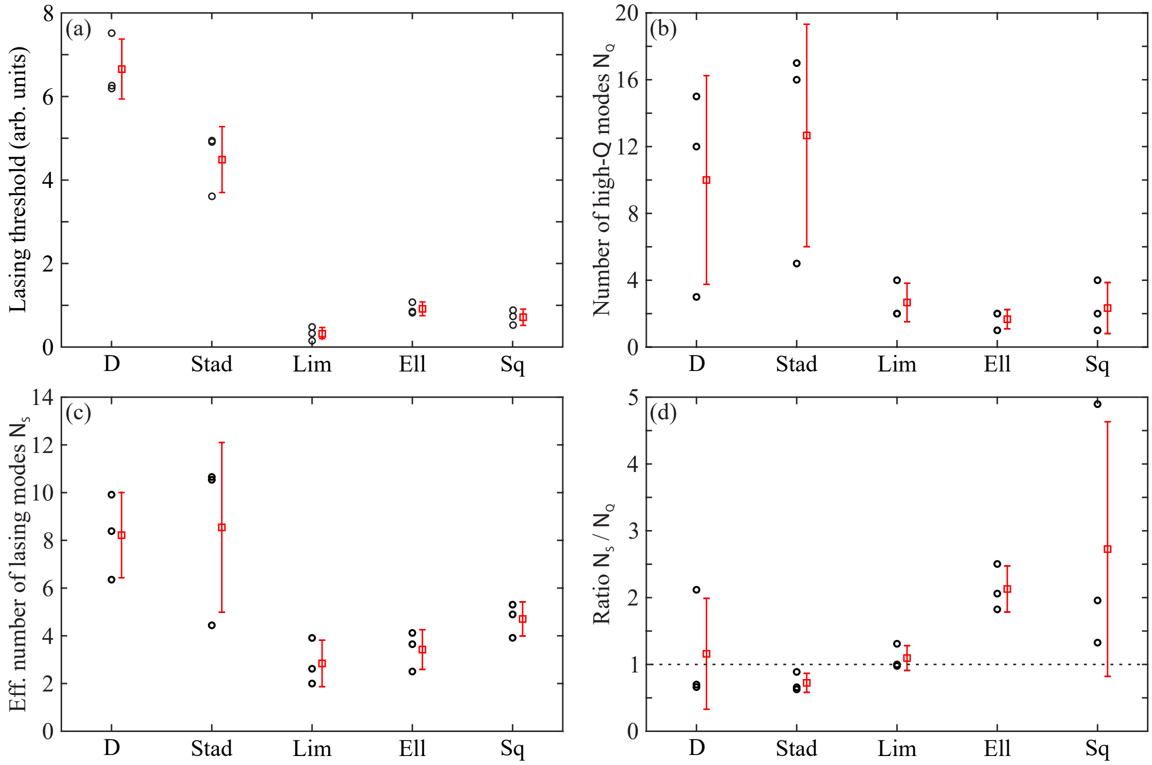

Figure 2.3: **Simulated lasing behavior for rough cavities as function of the cavity shape.** (a) Lasing thresholds according to SPA-SALT simulations. (b) Number of high-Q passive cavity modes N_Q with $Q > 0.8Q_{\max}$. (c) Effective number of lasing modes N_S at ten times the lasing threshold calculated by SPA-SALT simulations. (d) Ratio N_S/N_Q of lasing modes according to SPA-SALT simulations and high-Q modes. The dotted line indicates a ratio of 1. The black circles indicate the data for three different realizations of surface roughness, and the red squares and error bars indicate the corresponding mean and standard deviation.

effects, which are taken into account by the SPA-SALT simulations. We performed SPA-SALT simulations at 10 times the threshold even though we pump less strongly in experiments. The aim is to obtain a large and thus statistically more significant number of lasing modes since the simulated cavities are much smaller than the actual ones. The simulations yield the power P_μ of the μ-th lasing mode. Since the power of different lasing modes can vary significantly, we define an effective number of lasing modes as

$$N_S = \left[\sum_\mu P_\mu\right]^2 / \left[\sum_\mu P_\mu^2\right] , \tag{2.5}$$

which is shown in Fig. 2.3(c). For some cavity shapes we see again significant variations with surface roughness, however, we observe the same qualitative dependency on the cavity shape as for N_Q in Fig. 2.3(b). In particular, the Limaçon and ellipse cavities have the fewest lasing modes since their localized WGMs have a stronger spatial overlap. The square cavity with its spatially extended modes does not have many more lasing modes either, which we attribute to the low number N_Q of modes with Q-factors comparable to the first lasing mode.

A more detailed comparison of N_Q and N_S is presented in Fig. 2.3(d) where the ratio N_S/N_Q is plotted. For the D-cavity, stadium and Limaçon resonators, the ratio is close to 1, which demonstrates that the estimate N_Q is fairly accurate. However, we observe that for the D-cavity and stadium the ratio is a bit smaller than 1 in most cases, which highlights that the gain competition is non-negligible. For the ellipse and in particular the square, the ratio is significantly larger than 1 for most roughness realizations, which demonstrates that spatial hole burning can allow even modes with significantly lower Q-factor than the first lasing mode to start lasing eventually. Apparently N_Q underestimates the number of lasing modes for resonators that can feature modes with exceptionally high Q-factors like the ellipse and square.

In conclusion, the cavity shape as well as the surface roughness play an important role in determining the lasing thresholds and the number of lasing modes since the shape has a profound impact on the quality factors and spatial localization of the resonant modes. It should be emphasized that for all cavity shapes we predict multi-mode lasing, and the interaction of multiple lasing modes is an important ingredient in the development of lasing instabilities [18, 89].

2.3 Experimental results

2.3.1 Measurement setup

We perform experiments with five different microlasers for each cavity shape. The microlasers are contacted with a Tungsten needle and pumped electrically by a diode driver (DEI Scientific PCX-7401). We use short current pulses of $2\ \mu$s length and a very low duty cycle to reduce heating. The pump currents are as high as 500 mA (corresponding to about 1980 A/cm^2), and most of the data presented in the following is for 500 mA. The spectra are measured with an imaging spectrometer (Acton SP300i) equipped with an intensified CCD camera (ICCD, Andor iStar DH312T-18U-73) which also allows time-resolved measurements. The output facets of the microlasers are imaged onto a streak camera (Hamamatsu C5680) with a fast single-sweep unit (M5676) using a microscope objective ($20\times$, NA$=0.4$) and a tube lens to investigate the spatio-temporal dynamics of the microlasers.

2.3.2 Time-integrated measurements

Figure 2.4(a) shows the LI-curves obtained from the integrated lasing spectra of typical Limaçon and square microlasers, which show a clear threshold at about 80 mA. The thresholds for the different resonator geometries, averaged over five different microlasers each, are presented in Fig. 2.4(b). The fluctuations of the threshold amongst cavities of the same shape is very small, indicating the generally good reproducibility and consistency of the measurements. The lasing thresholds depend significantly on the geometry: the Limaçon, ellipse and square cavities have the lowest thresholds, followed by the stadia,

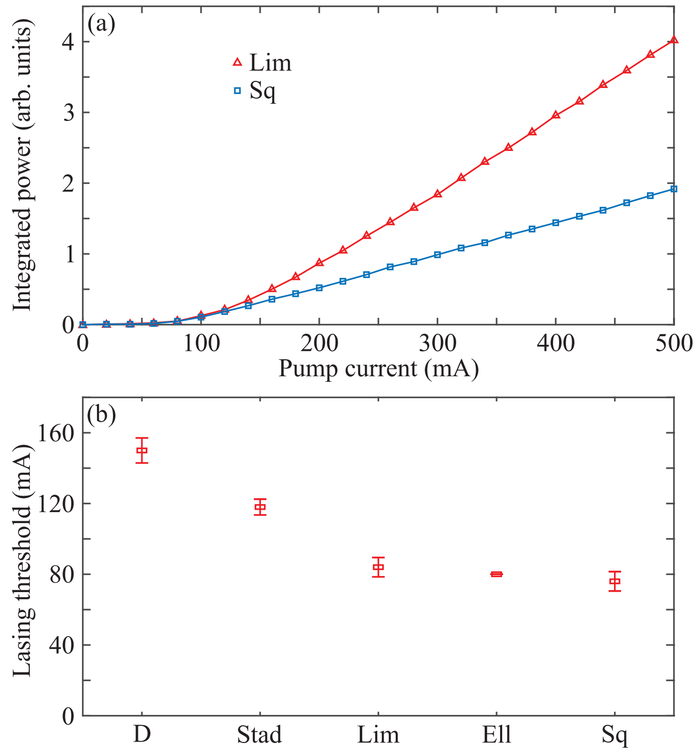

Figure 2.4: **Characterization of lasing behaviors.** (a) LI-curves for a Limaçon (red triangles) and a square microlaser (blue squares). (b) Experimental lasing thresholds for different cavity shapes. The mean and standard deviation for five different cavities per resonator shape are indicated.

and the D-cavities have the highest thresholds. This agrees well with the lasing thresholds [Fig. 2.3(a)] even though no quantitative agreement is found.

The measured lasing spectra for a Limaçon and a square microlaser are shown in Fig. 2.5. Lasing spectra for D-cavity, stadium and ellipse microlasers are presented in Ref. [59]. All microlasers show clear multi-mode lasing as predicted by the SPA-SALT simulations (Fig. 2.3). The spectra of cavities with the same shape are qualitatively consistent for all measured cavities.

The time-integrated near-field (NF) emission intensity distributions measured with the streak camera are presented in Fig. 2.6 (blue solid lines). The intensity distributions are shown on the scale of the cavities indicated to the left of the intensity distributions, and the

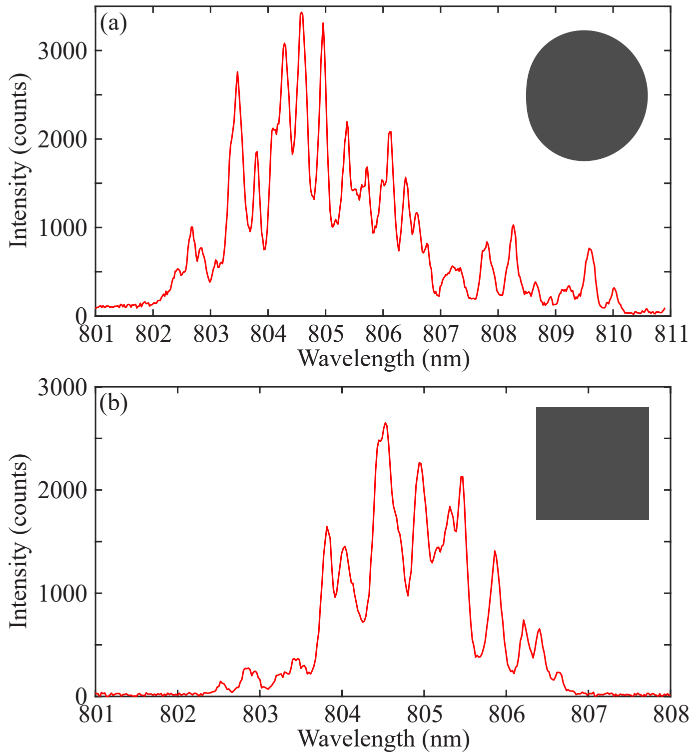

Figure 2.5: **Multimode lasing of the microcavities.** Measured lasing spectra at $500\ \mu$m pump current integrated over a single pump pulse for (a) a Limaçon and (b) a square microlaser.

image planes in relation to the cavities are indicated by the black dashed lines. Since the microlasers are multimode, the intensity distributions are an average over several lasing modes. The measured NF images are compared to passive cavity simulations of smooth cavities, and the average intensity distributions of the 10 highest-Q modes are superimposed in Fig. 2.6 (red dashed lines). The finite numerical aperture (NA $= 0.4$) of the imaging setup is taken into account in the calculations [4]. The simulation data was rescaled by a factor of 10 to match the measured images, which is why the emission lobes of the simulated data partially appear broader than the measured lobes. The agreement between measured and simulated NF intensity distributions is overall very good.

Even though only the light leaking out from the cavities is observed, the NF images allow a better understanding of the structure of the lasing modes since they reveal the

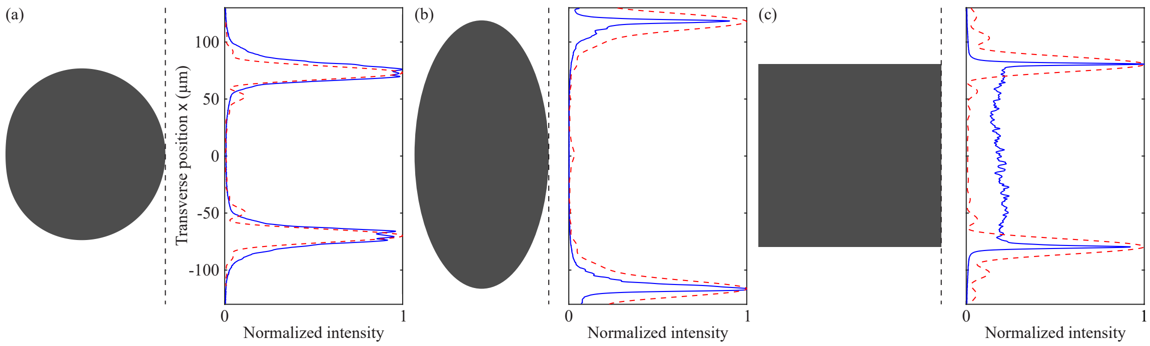

Figure 2.6: **Measured spatial intensity distribution of the laser emission.** Near-field emission intensity distributions of (a) Limaçon, (b) ellipse and (c) square microlasers. The measured near-field images (blue solid lines) for 500 mA are compared to passive mode simulations (red dashed lines) for smooth cavities (average over the 10 highest-Q modes). The cavities are indicated on the same scale as the transverse position x. The image planes are indicated by the vertical dashed black lines.

emission mechanisms. The emission from the high-Q modes of wave-chaotic microlasers follows an ensemble of particularly long-lived light rays that diffuse through the chaotic phase space till they finally escape refractively and can be predicted by ray tracing simulations [34, 67, 68]. This is discussed in detail for D-cavity and stadium microlasers in Ref. [5], including the comparison of NF images with wave and ray simulations which shows very good agreement. The same emission mechanism applies to Limaçon cavities [72], which is confirmed experimentally by the good agreement of the measured and simulated NF intensity distributions in Fig. 2.6(a).

Since the WGMs of the ellipse are confined by TIR, light is emitted via tunneling at the points of highest curvature with a grazing angle. This results in the narrow emission lobes originating from the upper and lower vertices of the ellipse [Fig. 2.6(b)], and their observation confirms that our ellipse microlasers exhibit WGMs as predicted by simulations. Since the ray trajectories supporting the modes of the square are confined by TIR, evanescent waves traveling along the sidewalls are emitted from the corners [90, 91], yielding the narrow emission lobes parallel to the sidewalls that we observe [Fig. 2.6(c)].

The measured NF images of the square additionally exhibit a broad background between the corners that we attribute to the residual surface roughness.

2.3.3 Time-resolved measurements

The time-integrated measurements demonstrate that the thresholds, spectra and intensity distributions of the microlasers are consistent with the theoretical expectations discussed in Section 2.3.2, and the next step is to investigate their dynamical behavior, which is the main objective of this article.

Figure 2.7 shows the spectrochronogram of a square microlaser which is measured with a tomographic technique: the ICCD connected to the spectrometer is gated on during a 50 ns long interval to measure spectra with high temporal resolution, and the delay t_d of the gate interval with respect to the start of the pump pulse is successively increased from one pulse to the next (cf. Ref. [4]). The spectrum changes continuously over the course of the pulse with a timescale of the order of 100 ns, which is much longer than the intrinsic time scales of the nonlinear laser dynamics discussed below. However, the laser remains multimode at any point in time, though the instantaneous number of lasing peaks is smaller than that in the time-integrated spectra in Fig. 2.5. Similar spectrochronograms are obtained for other the other microlaser geometries (cf. Ref. [4]).

The redshift of the individual resonances as well as the center of mass of the spectrum shows that the evolution of the spectrum is driven by Joule heating [4]. Consequently, the properties of the gain medium and the resulting lasing state are varied over the course of the pulse. This enables us to investigate an ensemble of different possible dynamical states by measuring streak images at different times during the pulse, where the individual streak images are shorter than the time scale of the heating-induced drift of the lasing spectrum.

We measured the evolution of the spatio-temporal lasing dynamics during a current pulse with single-sweep streak images of 10 ns length (temporal resolution about 30 ps),

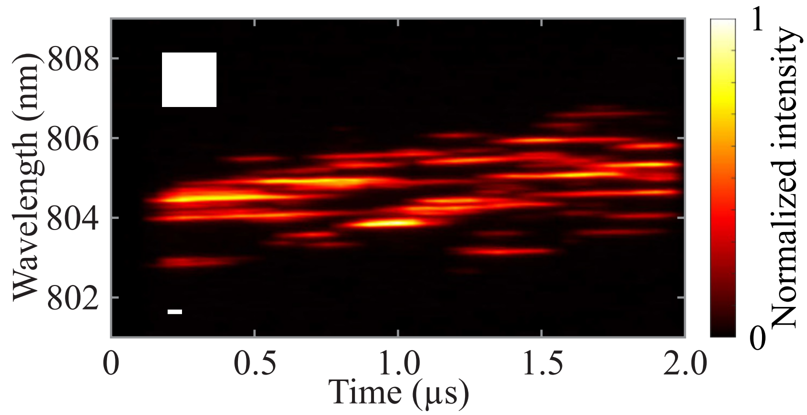

Figure 2.7: **Time-resolved multimode lasing spectrum.** Measured spectrochronogram of a square microlaser for 500 mA pump current. The time axis indicates the delay t_d of the gate interval to the start of the pump pulse. The white scale bar indicates the time resolution of 50 ns.

where the delay t_d between the streak image and the begin of the pulse was varied like for the measurement of the spectrochronograms [4]. For each microlaser, 161 consecutive streak images covering a total time of 1.61 μs were measured, omitting only the transient dynamics at the start and end of the pulses. Examples of these streak images are shown in Fig. 2.8. The spatial intensity distributions are consistent with the time-integrated NF images in Fig. 2.6 and Ref. [5].

For all five cavity shapes we find streak images exhibiting no significant temporal variations of the emission (top row of Fig. 2.8) as well as examples with strong fluctuations (bottom row). We observe many different examples of spatio-temporal dynamics that feature diverse time scales in the nanosecond to picosecond range and a wide variety of different spatio-temporal structures. The temporal fluctuations at different lateral positions x can be in phase or have a phase offset, while some points do not show fluctuations at all [cf. Figs. 2.8(b, d, f, h, j)]. In the following we present a comprehensive analysis of the amplitude, frequency scales and frequency of occurrence of spatio-temporal instabilities in order to understand (i) which cavity geometries suppress or promote spatio-temporal

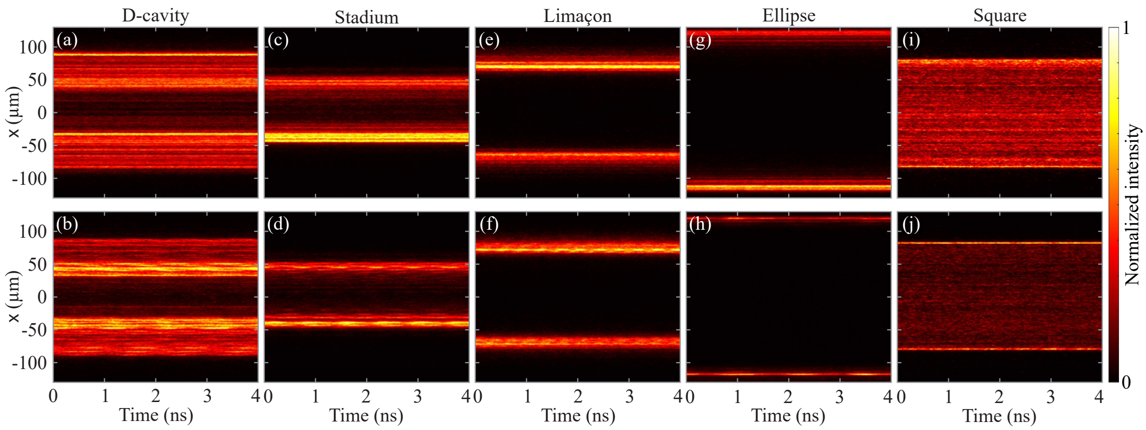

Figure 2.8: **Exemplary spatio-temporal intensity dynamics of asymmetric microlasers.** Measured streak images for microlasers with (a, b) D-cavity, (c, d) stadium, (e, f) Limaçon, (g, h) ellipse and (i, j) square geometry at 500 mA pump current. Only the first 4 ns of the 10 ns long streak images are shown for clarity. The transverse position x corresponds to the image planes indicated in Fig. 2.6.

instabilities and (ii) how the geometry affects the temporal and spatial characteristics of the instabilities.

2.3.4 Radio-frequency (RF) spectra

Our first approach to quantify the lasing instabilities is the analysis of the RF-spectra, which are obtained from the measured streak images as described in the following. Each streak image $I(x,t)$ is normalized such that $\langle I(x,t)\rangle_{x,t} = 1$ to enable a quantitative comparison of the fluctuation strength of different measurements. We first calculate the spatially-resolved Fourier transform (FT) of the streak image,

$$\tilde{I}(x,f) = \int dt\, I(x,t) \exp(-2\pi i f t)\,, \tag{2.6}$$

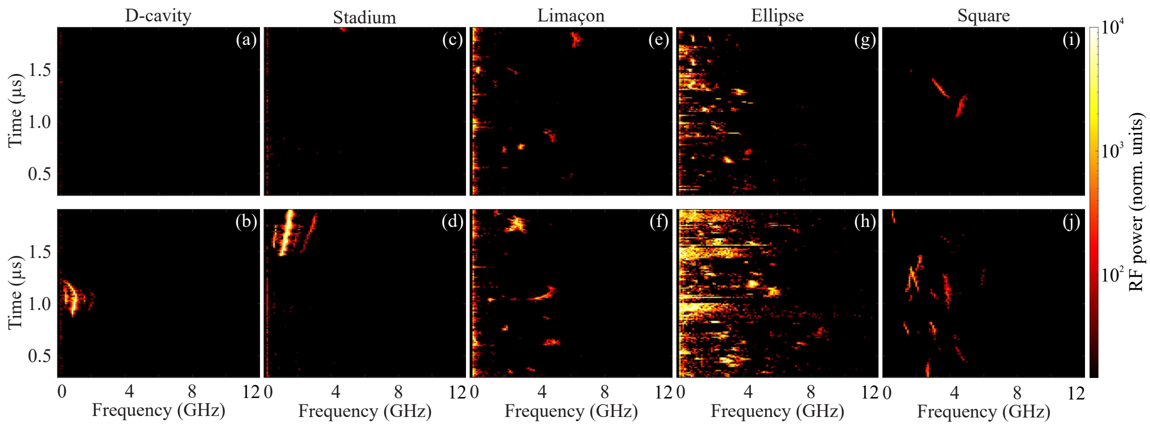

Figure 2.9: **Time-resolved RF spectra of asymmetric microcavities.** Refined RF-spectra $\hat{S}(f)$ obtained from the measured streak images as function of the time t_d during the pulse. Two examples for each cavity shape are presented: (a, b) D-cavity, (c, d) stadium, (e, f) Limaçon, (g, h) ellipse and (i, j) square. Please note the logarithmic scale for the RF-power.

where f is the RF-frequency, which is in the range up to 12 GHz in our case. Then we spatially average to obtain the RF power spectrum

$$S(f) = \langle |\tilde{I}(x,f)|^2 \rangle_x \tag{2.7}$$

of the streak image. All RF-spectra feature a generic, broad-band signal due to multi-mode interference that decays exponentially with f, and spatio-temporal instabilities create peaks at specific frequencies on top of it. In order to highlight the frequency contributions from the instabilities and facilitate the further analysis, the broad-band generic signal is subtracted to obtain refined RF-spectra $\hat{S}(f)$ featuring only the frequency components due to lasing instabilities. Additionally the DC component is removed. In the following only the refined RF-spectra $\hat{S}(f)$ are considered.

The refined RF-spectra $\hat{S}(f, t_d)$ for 10 different microlasers are presented in Fig. 2.9 as function of the time t_d during the pulse when the streak image is measured. Only the range $t_d = 0.3$–1.9 μs is considered to exclude transients. It should be noted that we restrict ourselves to the frequency range up to 12 GHz which is limited by the temporal resolution of the streak images. This frequency range appears to contain most of the fluctuations, but we know from measurements with better time resolution that also frequency components beyond 12 GHz can appear. Analogous to Fig. 2.8, the top row shows particularly stable and the bottom row unstable examples for each cavity shape. Individual microlasers can exhibit both periods of stability as well as periods with strong fluctuations during a single pulse. The RF-spectra evolve continuously as function of time since the microlasers slowly change their lasing state due to heating (cf. the spectrochronogram in Fig. 2.7).

The ten examples in Fig. 2.9 already allow to observe some trends as function of the cavity shape. The cases of D-cavity and stadium are quite similar: instabilities are very rare and even an entire pulse can pass without significant instabilities [Fig. 2.9(a, c)]. However, when instabilities appear, they can be quite strong, but exhibit only very few frequency components plus their harmonics [Fig. 2.9(b, d)]. Limaçon and ellipse microlasers show instabilities very often, where those of the ellipse are significantly stronger compared to the Limaçon. Interestingly, the Limaçon and ellipse microlasers exhibit a higher abundance of frequency components below 1 GHz compared to the other cavity shapes. Furthermore, the RF-spectra of the ellipse microlasers feature a higher number of frequency components than for other cavity geometries. The square microlasers are an intermediate case: they display instabilities a bit more often than D-cavities and stadia, but less frequently than Limaçon and ellipse cavities. In addition, their instabilities appear to be somewhat weaker and involve only few frequency components.

For a more quantitative evaluation of the RF-spectra we consider two quantities characterizing different aspects in the following. First, we look at the integrated RF-power,

$$S_{\mathrm{tot}} = \sum_{f,t_d} \hat{S}(f, t_d)\,. \tag{2.8}$$

Second, we calculate the frequency of occurrence of instabilities via the participation ratio

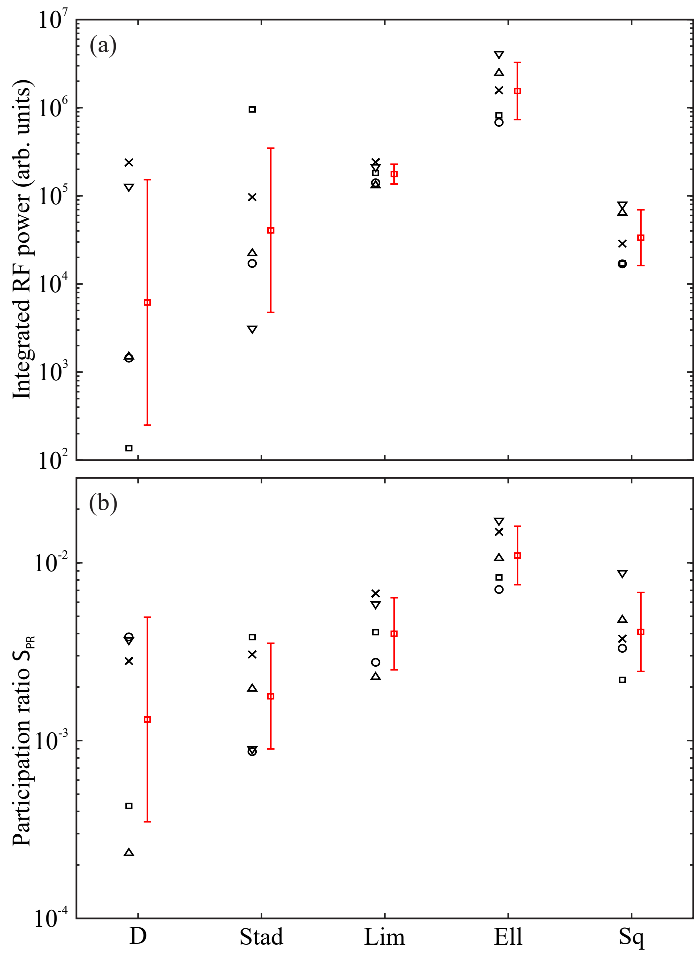

Figure 2.10: **Comparison of instabilities in different asymmetric microlasers.** (a) Total RF-power of instabilities S_{tot} and (b) frequency of occurrence S_{PR} of instabilities as function of cavity shape. The black symbols are the data points for five different cavities, and their mean and standard deviation is indicated in red.

of the RF-spectra,

$$S_{PR} = \frac{\langle \hat{S}(f, t_d) \rangle^2_{f,t_d}}{\langle \hat{S}^2(f, t_d) \rangle_{f,t_d}} \,. \tag{2.9}$$

These two quantities were extracted from measurements with five different microlasers per geometry and are plotted in Fig. 2.10. The results confirm the observations in the previous paragraph: the D-cavity microlasers have the overall weakest and rarest instabilities, followed by the stadium, which confirms the results in Ref. [4]. Limaçon and ellipse microlasers have much stronger and more frequent instabilities than D-cavities and stadia, and the ellipse is clearly the most unstable case. The square cavities, in contrast are about as stable as D-cavities and stadia, though instabilities appear a bit more frequently for the square.

In conclusion, our experimental results demonstrate a very strong influence of the cavity geometry on the formation of spatio-temporal instabilities. Both the overall RF-power and the frequency of occurrence of instabilities varies by several orders of magnitude as a function of the resonator shape. However, we find that the type of classical ray dynamics is not the relevant criterion whether instabilities are strong or weak. D-cavity, stadium and Limaçon all feature chaotic ray dynamics, but have very different strengths of instabilities. Interestingly, the stadium microlasers are a bit less stable than the D-cavities even though their ray dynamics and the structure of their wave function is very similar. The ellipse cavities with integrable ray dynamics exhibits by far the strongest instabilities, but the square microlasers are quite stable, similar to D-cavities and stadia. So both microlasers with chaotic and integrable ray dynamics can exhibit strong instabilities or suppress them. It is interesting to note that the resonators featuring WGMs, Limaçon and ellipse, have by far the strongest and most frequent instabilities. This leads us to suspect that the spatial localization and/or the particular fine structure of WGMs are responsible for destabilizing the lasing dynamics. We continue by analyzing the spatial and temporal scales of the lasing dynamics which also exhibit a significant dependency on the cavity geometry.

2.3.5 Temporal and spatial scales of lasing dynamics

The complex spatio-temporal dynamics of semiconductor lasers can exhibit various temporal and spatial scales due to different dynamical processes, and experimental data inevitably includes noise as well. A useful mathematical tool to analyze and separate these effects is the singular value decomposition (SVD), also called Karhunen-Loeve decomposition, which has been previously applied to broad-area FP lasers [20, 92]. We apply the

SVD to analyze the emission fluctuations of the microlasers as explained in the following.

The SVD is calculated separately for each measured streak image $I(x,t)$. We subtract the time-average from the streak image normalized by $\langle I(x,t)\rangle_{x,t} = 1$ to obtain the normalized emission fluctuations

$$\delta I(x,t) = I(x,t) - \langle I(x,t)\rangle_t \tag{2.10}$$

and then calculate the SVD which allows to express δI in the form

$$\delta I(x,t) = \sum_{\alpha} s_\alpha u_\alpha(x) v_\alpha(t) \tag{2.11}$$

where the s_α are the singular values (SVs), $u_\alpha(x)$ and $v_\alpha(t)$ are the normalized spatial and temporal singular vectors, and α is the index. By convention we order the SVs in descending order, i.e., s_1 is the biggest SV, and only the first 300 SVs are used in the following since the following ones only represent noise. We call each term in Eq. (2.11) a singular component (SC), and the product $u_\alpha(x)v_\alpha(t)$ is its spatio-temporal matrix which displays the fluctuation pattern of the SC.

It is important not to confound individual SCs with specific lasing modes or dynamical structures like a filament. By construction the SVD allows to approximate a streak image with a minimal number of spatio-temporal matrices that are separable in space and time. But often the fluctuation patterns caused by a filament or spatio-temporal speckle are themselves not separable and hence require a number of singular components to be well reproduced. In spite of these shortcomings the SVD is very useful since it allows to determine how much fluctuation power is exhibited in different spatial and temporal scales and furthermore allows to remove measurement noise [2].

The spatial (temporal) scale of a singular component is determined from the autocor-

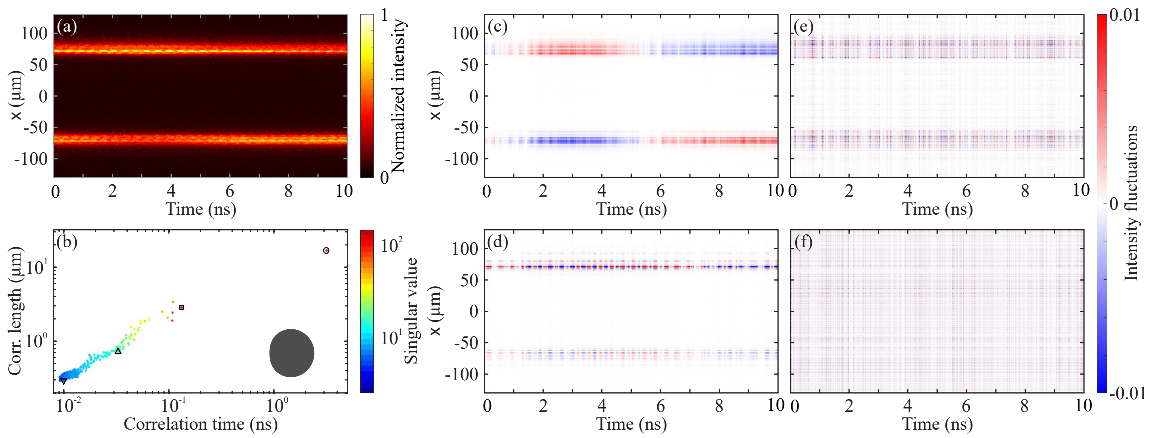

Figure 2.11: **Singular value decomposition for a single streak image of a Limaçon microlaser.** (a) Streak image at $t_d = 1780$ ns. (b) Scatter plot of singular values as function of the correlation times and lengths. The singular components presented in panels (c)–(f) are indicated by the black circle, square, upwards triangle and downwards triangle, respectively. (c) Spatio-temporal matrix for singular component $\alpha = 1$, (d) $\alpha = 2$, (e) $\alpha = 45$ and (f) $\alpha = 300$.

relation function of the spatial (temporal) singular vector,

$$\begin{aligned} C_\alpha(\Delta x) &= \langle u_\alpha(x) u_\alpha(x+\Delta x)\rangle_x \,, \\ C_\alpha(\Delta t) &= \langle v_\alpha(t) v_\alpha(t+\Delta t)\rangle_t \,. \end{aligned} \tag{2.12}$$

We define the correlation length l_α (correlation time t_α) of a SC as the full-width at half maximum (FWHM) of the spatial (temporal) autocorrelation function.

Figure 2.11 exemplifies the SVD for a single streak image of a Limaçon microlaser exhibiting strong instabilities. The scatter plot of the singular values as function of the correlation time and length in Fig. 2.11(b) shows a strong correlation between the SV and the correlation time (and length), i.e., the stronger SCs generally feature longer time scales. The spatio-temporal matrices of the two strongest SCs are shown in Figs. 2.11(c) and (d). The first SC $\alpha = 1$ in Fig. 2.11(c) reveals an antiphase oscillation with $t_1 = 3.1$ ns and $l_1 = 16.8$ μm that is hidden below fluctuations on shorter time scales in the original streak image [Fig. 2.11(a)]. The second SC $\alpha = 2$ in Fig. 2.11(d) represents these faster fluctuations which are in-phase and feature a much shorter time scale of $t_2 = 0.13$ ns and a correlation length of only $l_2 = 2.8$ μm. It should be noted that antiphase oscillations on a nanosecond time scale are a dynamical feature only observed for the Limaçon microlasers. The strongest SCs typically correspond to the lasing instabilities that we are interested in and allow to separate these from other processes on shorter timescales.

The SC $\alpha = 45$ in Fig. 2.11(e) has an even shorter correlation time of $t_{45} = 32.8$ ps and a correlation length of $l_{45} = 0.72$ μm. These are close to the temporal resolution of the streak camera (about 30 ps) and the spatial resolution of the optical setup (about 0.8 μm). The SCs with intermediate singular value in this region mainly represent the spatio-temporal speckle that is inevitably created by multimode interference [2, 3]. Therefore the spatial profile of the SC has the same shape as the near-field intensity distribution of the Limaçon microlaser [Fig. 2.6(a)]. It should be noted that the multimode interference creates fluctuations on even shorter time scales, determined by the total width of the optical spectrum, which we can however not resolve with the streak camera [3]. The weakest SC ($\alpha = 300$) in Fig. 2.11(f) has a correlation time of $t_{300} = 9.96$ ps and a correlation length of $l_{300} = 0.29$ μm. The spatio-temporal matrix shows no particular pattern and is extended over the whole streak image. The SCs in this region represent the camera noise, and the correlation time and length are of the order of a single pixel.

These examples demonstrate how the SVD allows a better understanding of the strength, spatial and temporal scales of instabilities. Additionally the SVD often enables a rough separation between the lasing instabilities, fluctuations created by spatio-temporal speckle and measurement noise thanks to their different time scales. However, some SCs are of course in transition regions between these three cases, and lasing instabilities cannot always be clearly distinguished from spatio-temporal speckle.

Figure 2.12 presents the ensemble of SVs of all 161 streak images for ten different microlasers. These are the same microlasers as in Fig. 2.8, where the top row shows relatively

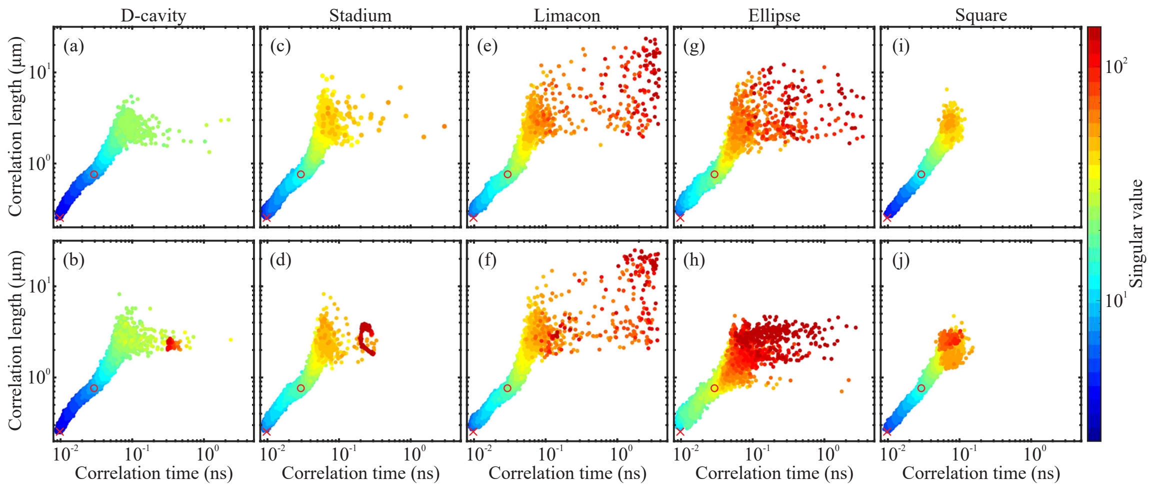

Figure 2.12: **Various sptio-temporal intensity fluctuation scales of different microlasers.** Scatter plots of the singular values as function of the correlation times and lengths for (a, b) D-cavity, (c, d) stadium, (e, f) Limaçon, (g, h) ellipse and (i, j) square microlasers. The singular values of all 161 streak images are shown for each microlaser. The data presented here is for the same microlasers as in Fig. 2.8. Please note the logarithmic scales for time, length and singular values. The red circles indicate the temporal and spatial resolution of the measurement setup, and the red crosses indicate the time and spatial scale of a single streak camera pixel.

stable and the bottom row the most unstable microlasers for each shape, respectively. All scatter plots show a stem of low SVs in the range of 0.01–0.1 ns. As explained above, these SCs are attributed to spatio-temporal speckle and noise since their correlation lengths and times are in the range from the camera pixel scale (indicated by red crosses) to somewhat beyond the measurement resolution (indicated by red circles).

The cavity-specific lasing instabilities manifest in the high SVs in the region $\gtrsim 0.1$ ns, and we can now analyze how their temporal and spatial scales depend on the cavity shape. The D-cavity and stadium microlasers shown in Fig. 2.12(b) and (d) exhibit instabilities with length scales of a few micron and time scales of a few 100 ps. In contrast, the D-cavity and stadium microlasers in Figs. 2.12(a) and (c) exhibit practically no singular components in this region since their dynamics is almost completely stable. The ellipse and Limaçon microlasers shown in Figs. 2.12(e)–(h) feature an almost continuous ensemble of strong SCs in the range[5] of 0.1–5 ns with correlation lengths of about 2–20 μm. The whispering gallery resonators thus exhibit instabilities with a wider range of spatial and temporal scales than the other cavity geometries. The Limaçon and ellipse microlasers in Figs. 2.12(e) and (g) display fewer and weaker, but nonetheless significant, SCs in this region compared to those in Figs. 2.12(e) and (g), that is, their dynamics is less unstable. However, we find that all Limaçon and ellipse microlasers have significant lasing instabilities [cf. Fig. 2.10]. The square microlaser presented in Fig. 2.12(j) exhibits strong SCs with correlation times around 0.1 ns and correlation lengths around 2 μm, that is, the scales of the instabilities are quite close to that of the spatio-temporal speckle which makes a clear distinction difficult. The square microlaser in Fig. 2.12(i) displays quite stable dynamics, and thus there are only a few moderately strong SCs in this region, which makes the distinction from spatio-temporal speckle even harder.

Next we quantify how the power of intensity fluctuations is distributed among different temporal scales. We define different correlation time intervals $[t_j, t_{j+1}]$ on a logarithmic scale and then calculate the total power of fluctuations in each interval as [2],

$$P_{\text{fluc}}^{(j)} = \sum_{t_\alpha \in [t_j, t_{j+1}]} s_\alpha^2 \, . \tag{2.13}$$

The resulting distributions are furthermore averaged over all five microlasers for each shape and presented in Fig. 2.13. The results confirm the discussion of Fig. 2.12 in the previous paragraphs. All cavity shapes exhibit significant fluctuations with correlation times below 0.1 ns due to spatio-temporal speckle and noise. For D-cavity and stadium microlasers [Figs. 2.13(a) and (b)], almost the entire additional fluctuation power is on time scales below 1 ns. For the square microlasers, the time scales are even shorter, mostly $\lesssim 0.1$ ns. The Limaçon and ellipse microlasers [Figs. 2.13(c) and (d)], in con-

[5] Since the streak images are 10 ns long, correlation times above 5 ns cannot be detected.

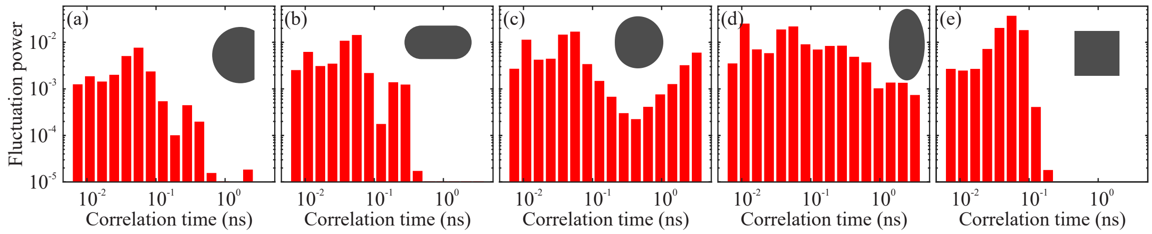

Figure 2.13: **Distributions of temporal fluctuation scales of lasing dynamics.** Integrated fluctuation power determined from SVD as function of the correlation time for (a) D-cavity, (b) stadium, (c)Limaçon, (d) ellipse and (e) square microlasers. The average over five cavities per shape and 161 streak images per microlaser is shown. Please note the logarithmic time and power scale.

trast, also exhibit a lot of fluctuation power in instabilities with longer time scales up to a few nanoseconds. Interestingly, the distribution for the Limaçon microlasers [Fig. 2.13(c)] shows a dip between 0.1 and 1 ns. This could mean that the Limaçon cavities exhibit two different types of instabilities with different time scales [cf. Figs. 2.11(c) and (d)]. We furthermore suspect that the fluctuations on nanosecond scales are related to the existence of near-degenerate doublets of modes, a feature that is found for Limaçon and ellipse resonators, but not the other shapes. However, we cannot confirm this hypothesis since we do not know the actual mode splitting frequencies of our microlaser cavities.

In summary, our analysis of the spatio-temporal measurements shows that the cavity shape strongly affects not only the strength, but also the typical time and length scales of the spatio-temporal instabilities. The measurement data for different cavities of the same shape is overall very consistent, which confirms that the different dynamical properties we observe are indeed related to the resonator geometry. In the following section we try to obtain a better understanding of the relation between cavity shape and lasing dynamics by analyzing the simulated passive cavity modes in greater detail since we believe that the spatial structure of the lasing modes plays a key role in the nonlinear light-matter interaction that causes instabilities [4]. Gaining a good understanding of this relation may ultimately enable us to tailor the laser dynamics based on ray-dynamical principles since the relations between classical dynamics and mode structure are fairly well understood for dielectric resonators [33, 34, 67].

2.4 Analysis of passive cavity modes

Evidently the spatio-temporal instabilities we observe are caused by multimode interaction. However, all of the microlasers investigated here operate in a multimode regime, but nonetheless display very different levels of instability. As the resonator geometry plays a very significant role, we infer that the spatial structure of the lasing modes strongly influences the interaction of optical field and active medium, and we set out to elucidate how different aspects of the mode structure are related to the formation or suppression of instabilities. Since the spatial structure of the lasing modes agrees well with our passive cavity mode simulations as shown in Fig. 2.6 and Ref. [5], we conclude that effects like carrier-induced index changes do not qualitatively affect the mode structure and we can thus base our analysis on the passive cavity mode simulations with surface roughness.

We concentrate on two aspects of the mode structure, the degree of spatial localization and the fine structure size of the intensity distributions, for the following reasons. In general, the appearance of modulational instabilities in nonlinear media (which cause, for example, filamentation in Fabry-Perot type broad-area lasers) is related to the energy density and the transverse wavelength of the perturbation [23, 93]. First, whispering gallery resonators like the Limaçon and ellipse exhibit spatially localized modes which significantly increase nonlinear interactions [94]. In addition, the spatial localization plays an important role for self and cross saturation effects in the gain competition [59, 69]. This can potentially explain the rather strong instabilities of the Limaçon ellipse microlasers. Second, perturbations of the optical field with a sufficiently small transverse wavelength do not grow exponentially, hence causing no instabilities [23, 93]. This is consistent with the low fluctuation power we observe for D-cavity, stadium and square microlasers which all feature fine-grained intensity distributions. In the following we investigate the degree of spatial localization as well as the structure size for the different cavity geometries more quantitatively, discuss how they are related to the classical ray dynamics, and correlate the results with the strength of instabilities observed in experiments.

2.4.1 Spatial localization

As a measure for the degree of spatial localization, we calculate the average modal area of the lasing modes of cavities with surface roughness, where the lasing modes are calculated at 10 times the lasing threshold using SPA-SALT (cf. Section 2.2.4). The modal area A_μ of a single wave function Ψ_μ with intensity distribution $I_\mu(\vec{r}) = |\Psi_\mu(\vec{r})|^2$ is given by its participation ratio

$$A_\mu = \frac{[\int dA\, I_\mu(\vec{r})]^2}{\int dA\, [I_\mu(\vec{r})]^2}\,, \tag{2.14}$$

where the integrals are over the interior of the resonator. Then we calculate the weighted average over the lasing modes,

$$\langle A \rangle = \frac{\sum_\mu P_\mu A_\mu}{\sum_\mu P_\mu}\,, \tag{2.15}$$

where P_μ is the power of mode μ at 10 times the threshold, to obtain the average modal area. The results as a function of the cavity shape and for three different roughness realizations each are presented in Fig. 2.14. For comparison, the modal area of a homogeneous speckle pattern, which is equal to one half the resonator area, is indicated by the black dashed line.

The average modal area varies significantly with the resonator geometry. We observe a clear qualitative correspondence of the modal area and the strength of lasing instabilities in Fig. 2.10: the D-cavity, stadium and square resonators have high modal areas close to the

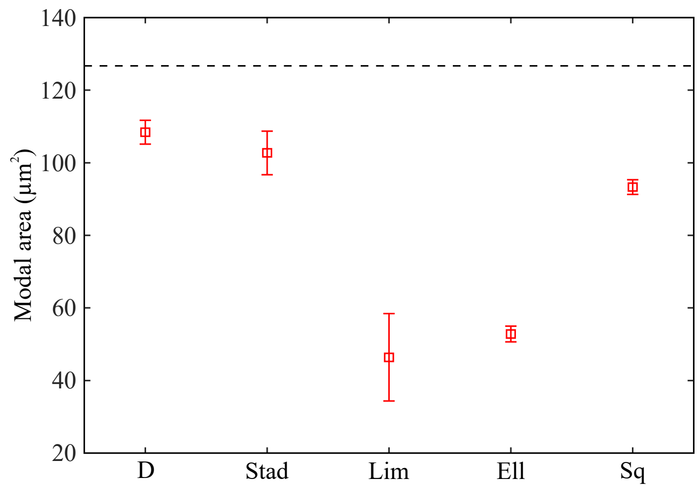

Figure 2.14: **Effective area of lasing modes.** Average modal areas $\langle A \rangle$ of lasing modes for (a) D-cavity, (b) stadium, (c) Limaçon, (d) ellipse and (e) square microlasers. The mean and standard deviation of the average modal area [Eq. (2.15)] for three roughness realizations is indicated. The dashed black line indicates one half of the cavity area.

maximum indicated by the black dashed line, and their dynamics is quite stable. On the other hand, the Limaçon and ellipse cavities feature much lower modal areas, which goes along with very unstable spatio-temporal dynamics. These results indicate that the degree of spatial localization plays indeed an important role in the dynamics, where highly localized lasing modes appear to favor the formation of instabilities. However, we do not find a clear quantitative correlation: for example, the Limaçon and ellipse cavities have roughly the same modal area, but the integrated RF-power for the ellipse microlasers [Fig. 2.10(a)] is approximately one order of magnitude higher than for the Limaçon microlasers. Evidently other factors apart from the modal area influence the lasing dynamics as well, and we hence investigate the fine structure size of the lasing modes in the following.

2.4.2 Structure size of intensity distributions

Due to the principle of ray-wave correspondence, the resonator shape has a significant influence on the structure of the wave functions. Figure 2.15(a) shows typical examples of wave functions of rough cavities. While we already discussed the general structure (e.g., degree of spatial localization, existence of whispering gallery modes) in the context of the classical ray dynamics, we now investigate the fine structure in greater detail.

Figure 2.15(b) shows magnified parts of the wave functions which show significant differences in the fine structure for the different resonator shapes. D-cavity and stadium wave functions [Figs. 2.15(b_1) and (b_2)] show seemingly random and isotropic patterns with intensity variations on the scale of the in-medium wavelength. The fine structure for the square [Figs. 2.15(b_5)] is quite similar, but somewhat more regular with a pattern oriented along the diagonals. For the Limaçon and ellipse [Figs. 2.15(b_3) and (b_4)], in contrast, the fine structure is anisotropic, that is, the patches of high intensity around local maxima are significantly elongated in one direction. This effect is particularly pronounced for the ellipse. Interestingly, the short axes of these patches are roughly parallel to the cavity boundary, and thus parallel to the whispering-gallery type trajectories following the boundary [cf. Figs. 2.2(c) and (d)] on which the high-Q modes are based. Thus it looks like the wave functions of Limaçon and ellipse resonators have a large "transverse wavelength" in much the same way that a lens or objective with low numerical aperture yields a broad spot (compared to the wavelength) when used to focus a light beam because rays with large angles with respect to the optical axis are lacking. In contrast, the ray trajectories for D-cavity, stadium and square are far less directional [Figs. 2.2(a), (b) and (e)], i.e., there is no dominant propagation direction in any given point, and hence the patches are smaller and more isotropic.

To quantify the typical extent of the patches of high intensity, that is, the fine structure size, we calculate the spatial autocorrelation (AC) function around a point $\vec{r}_0 = (x_0, y_0)$,

$$C_{sp}(\Delta\vec{r}) = \int_{x_0-\delta x}^{x_0+\delta x} dx \int_{y_0-\delta y}^{y_0+\delta y} dy \, I(\vec{r}) I(\vec{r} + \Delta\vec{r}) \, , \tag{2.16}$$

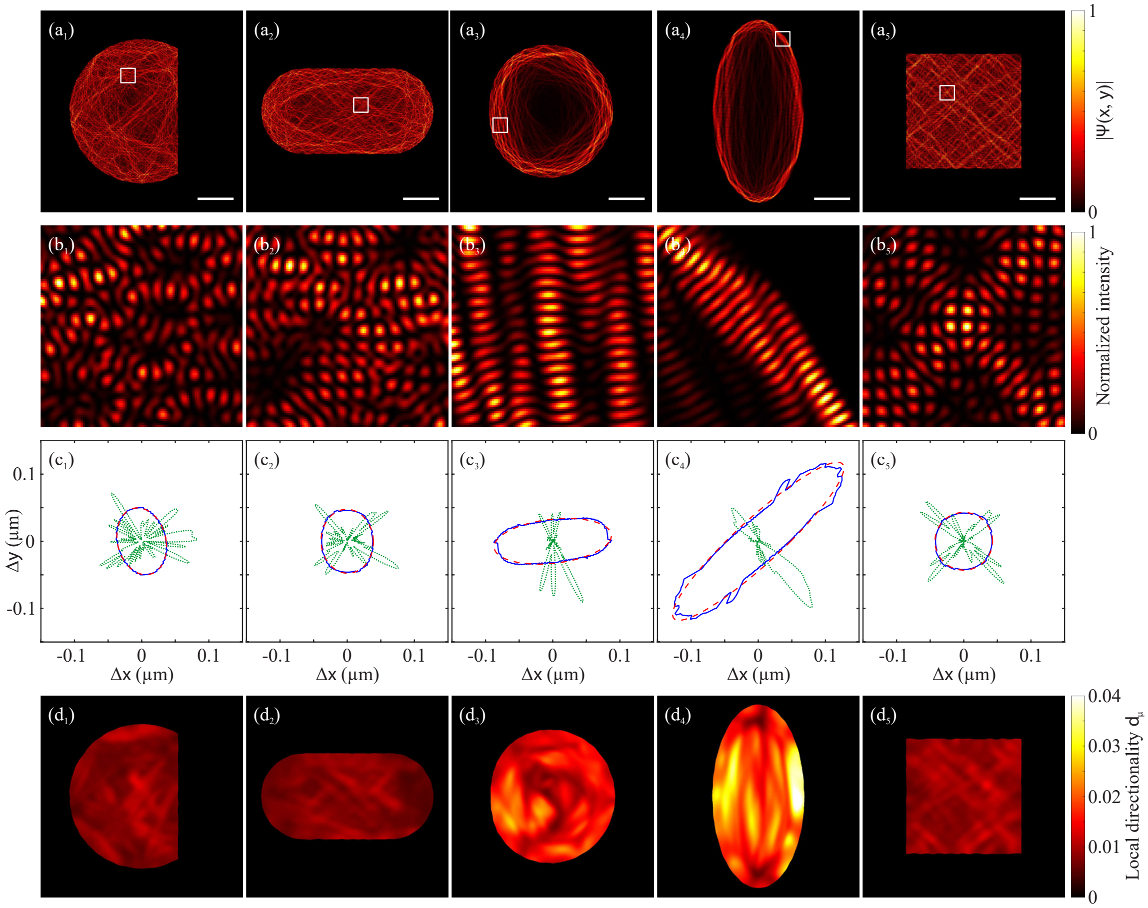

Figure 2.15: **Structure size and local directionality of wave functions.** (a) Typical high-Q wave functions of cavities with surface roughness. (b) Magnification of a 2×2 μm large part of the intensity distributions. The magnified parts are indicated by the white boxes in panel (a). (c) Half-maximum contour line of the spatial autocorrelation function (blue solid lines) of the magnified parts in panel (b), ellipse fit to the contour line (red dashed lines) and polar plot of the wavelet amplitude $|w_\mu(\vec{r}_0, \theta)|$ (directionality diagram) in the central point $\vec{r}_0$ of the magnified part (green dotted lines). (d) Map of local directionality $d_\mu(\vec{r})$ for the wave functions in panel (a).

where $I(\vec{r}) = |\Psi(\vec{r})|^2$ is the intensity distribution of the mode, $\Delta\vec{r} = (\Delta x, \Delta y)^T$, $\delta x = \delta y = 1$ μm (i.e., the integral is over a 2×2 μm large region), and the AC function is normalized to $C_{sp}(\vec{0}) = 1$. The central maximum of the AC function can have a more circular or elongated shape depending on whether the intensity distribution is more isotropic or anisotropic. Its shape, size and orientation are a good measure of the local fine structure of the intensity distribution.

We determine its size as follows: we extract the half-maximum contour line where $C_{\text{sp}} = 1/2$ around $\Delta\vec{r} = (0,0)^T$ [blue solid lines in Fig. 2.15(c)] and fit an ellipse to it [red dashed lines in Fig. 2.15(c)]. We define the local structure size s_{loc} in point $\vec{r}_0$ as the major diameter of the fitted ellipse, which can be regarded as a generalization of the spatial structure size. The structure size s_μ of mode μ is then obtained by the intensity-weighted average of the local structure size in the interior of the resonator,

$$s_\mu = \frac{\int dA\, I_\mu(\vec{r}) s_{\text{loc}}(\vec{r})}{\int dA\, I_\mu(\vec{r})}\,. \tag{2.17}$$

Finally we calculate the weighted average for the lasing modes with power P_μ obtained from SPA-SALT simulations at 10 times the threshold to obtain the average structure size

$$\langle s \rangle = \frac{\sum_\mu P_\mu s_\mu}{\sum_\mu P_\mu} \tag{2.18}$$

of a resonator.

The average structure size for the different cavity shapes is presented in Fig. 2.16(a). Whereas the D-cavity, stadium and square cavities all exhibit a small structure size of about 0.1 μm, that of the Limaçon and ellipse cavities is more than two times larger due to the anisotropic fine structure of their WGMs [see Figs. 2.15(b_3) and (b_4)]. Before we discuss the relation between the structure size and the lasing dynamics, we investigate the local directionality of the wave functions in order to better understand the dependency of

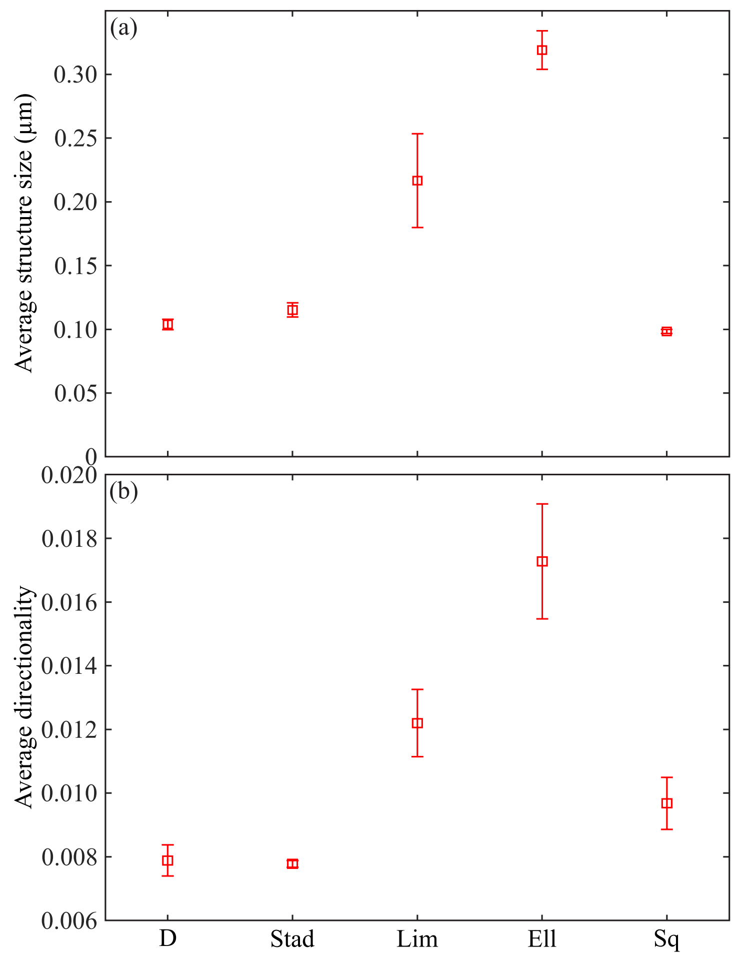

Figure 2.16: **Spatial structure sizes of lasing modes.** (a) Average structure size $\langle s \rangle$ and (b) average directionality $\langle D \rangle$ of lasing modes as a function of cavity shape. The red symbols and error bars indicate the mean and standard deviation for three different roughness realizations.

the structure size on the cavity shape and the directionality of wave propagation.

The wave functions of wave-chaotic resonators can be considered as a superposition of many plane wave components [61], which corresponds to the ray trajectories in a chaotic billiard propagating in all possible directions. This is revealed by calculating the spatial Fourier transform of the wave functions. We are particularly interested in the wave propagation directions in small regions of the resonator because it is the local directionality that determines the structure size of the intensity distributions. The ray trajectories in Fig. 2.2

demonstrate that the classical dynamics can be more (e.g., for Limaçon and ellipse) or less directional (e.g., for D-cavity and stadium) on a local level depending on the cavity shape. However, the spatial FT does not yield any spatially-resolved information.

Instead, we use the wavelet transform of the wave functions Ψ_μ which can be considered a local Fourier transform [95]. The wavelet transform is defined as

$$w_\mu(\vec{r}, \theta) = \int d\vec{r}\,' \, \Psi^*(\vec{r}\,')\hat{\Psi}(\vec{r}\,' - \vec{r}, \theta)\,, \tag{2.19}$$

where $\hat{\Psi}$ is the Morlet wavelet,

$$\hat{\Psi}(\vec{r}, \theta) = \exp(-ik_M x_R - x_R^2/(2\sigma^2) - y_R^2/\sigma^2)\,. \tag{2.20}$$

The rotated coordinate frame (x_R, y_R) is given by

$$\begin{aligned} x_R &= x\cos\theta + y\sin\theta \\ y_R &= -x\sin\theta + y\cos\theta \end{aligned} \tag{2.21}$$

where θ is the azimuthal angle with respect to the x-axis and $k_M = 2\pi n/\lambda$ is the in-medium wavenumber of the mode Ψ_μ. The width σ of the Morlet wavelet we use is $\sigma = 1.18$ μm, and thus $|w_\mu(\vec{r}, \theta)|$ yields the amplitude of waves propagating in direction θ in a small region with approximate diameter 2σ around $\vec{r}$.

We start by looking at the wavelet amplitude $|w_\mu|$ as function of θ in a single point, which we call directionality diagram in the following. Examples for the center points of the magnified parts in Fig. 2.15(b) are shown as dotted green lines in Fig. 2.15(c). The directionality diagrams for D-cavity and stadium [Figs. 2.15(c$_1$) and (c$_2$)] show many different propagation directions with a large range of angles. Consequently, the half-contour lines of the spatial AC function (blue solid lines) are almost circular and the local stucture size small. For the Limaçon and ellipse resonators [Figs. 2.15(c_3) and (c_4)], the directionality diagram features strong components in the directions approximately parallel to the cavity boundary, which is in good correspondence to the classical whispering-gallery trajectories [Figs. 2.2(c) and (d)]. These directions are roughly perpendicular to the long axis of the half-contour lines, which confirms that the long diameters of the contour lines can be considered as a measure of the transverse wavelength. It should be noted that the directionality diagram for the ellipse is more concentrated than for the Limaçon cavity, and correspondingly the major ellipse diameter for the ellipse is larger as well. This is probably due to the integrable ray dynamics of the ellipse which limits the possible propagation directions of rays more than for the chaotic ray dynamics of the Limaçon. The directionality diagram of the square [Fig. 2.15(c_5)] is dominated by four double-peaked lobes along the diagonals which correspond to the 8 plane wave components of which the wave functions of dielectric square resonator consist [80, 81]. So while the wave propagation is more directional than for D-cavity and stadium, the half-contour line is nonetheless circular since the propagation directions are distributed equally, resulting in a small structure size.

Next we quantify the directionality of wave propagation more globally. First, we define the local directionality d_μ of mode μ in point $\vec{r}$ as the inverse participation ratio of the directionality diagram,

$$d_\mu(\vec{r}) = \frac{\sum_i |w_\mu(\vec{r}, \theta_i)|^4}{\{\sum_i |w_\mu(\vec{r}, \theta_i)|^2\}^2}\,, \tag{2.22}$$

where the summation goes over 360 directions θ_i in the range of $0°$ to $360°$. Maps of the local directionality for the wave functions in Fig. 2.15(a) are presented in Fig. 2.15(d). The highest local directionalities are found for the Limaçon and ellipse resonators [Figs. 2.15(d_3) and (d_4)], whereas the local directionality is on average lower and more homogeneous for the D-cavity, stadium and square resonators [Figs. 2.15(d_1), (d_2) and (d_5)] as expected from their ray dynamics. Second, we calculate the directionality D_μ of mode μ as the average of the local directionality d_μ weighted by its intensity distribution $I_\mu(\vec{r})$,

$$D_\mu = \frac{\int dA\, I_\mu(\vec{r}) d_\mu(\vec{r})}{\int dA\, I_\mu(\vec{r})} \,. \tag{2.23}$$

Finally we calculate the average directionality $\langle D \rangle$ of a cavity as the power-weighted average over the lasing modes

$$\langle D \rangle = \frac{\sum_\mu P_\mu D_\mu}{\sum_\mu P_\mu} \tag{2.24}$$

with P_μ the lasing mode power at 10 times the lasing threshold calculated via SPA-SALT.

The results for the average directionality of the different cavity shapes are shown in Fig. 2.16(b), which are strongly correlated with the average structure size in Fig. 2.16(a). The Limaçon and ellipse cavities have clearly the highest directionality as expected from their ray dynamics, which explains their significantly higher structure size compared to the other three cavities. This confirms our understanding of how classical ray dynamics, the local directionality of wave propagation and the local structure size of wave functions are related, which will serve as a guide to tailoring the local structure size of the lasing modes via the cavity shape.

Let us finally compare the structure size and directionality of lasing modes of different cavity shapes with the strength of lasing instabilities summarized in Fig. 2.10. A large structure size caused by high directionality is clearly correlated with strong lasing instabilities. In particular it should be noted that the ellipse has an even larger structure size than the Limaçon which can explain why the RF-power of instabilities is significantly higher for the ellipse. The D-cavity and stadium have almost equally small structure size, which goes along with the low overall strength of their instabilities. Though D-cavity and stadium are very similar in almost all respects, the structure size of the stadium is a bit larger compared to the D-cavity, and the stadium exhibits a bit stronger instabilities as well. The square also has low structure size and weak instabilities, but a detailed comparison shows that while the structure size of the square is equal to that of the D-cavity, its instabilities are somewhat stronger. In conclusion, the structure size seems to be a very good predictor for the strength of lasing instabilities, but we do not observe a precise and quantitative correlation between these two properties.

We find that both the degree of spatial localization and the structure size are correlated with the strength of lasing instabilities at least on a qualitative level. This confirms our conjectures about the relations between wave function structure and formation of instabilities formulated at the beginning of this section. However, we cannot conclude which aspect is more or less important, or make more quantitative predictions about the lasing dynamics. This will require to look beyond the passive cavity modes and perform comprehensive simulations with a detailed model of semiconductor laser dynamics for asymmetric cavities. Still our results and analyses yield important insights into the relation between ray dynamics, passive cavity modes, and lasing dynamics.

2.5 Discussion and conclusion

In this chapter, we perform a comprehensive experimental study of the spatio-temporal dynamics of asymmetric cavity semiconductor microlasers. Five different cavity shapes featuring different types of ray dynamics and spatial structures of the lasing modes are investigated, and the experimental observations are complemented by a detailed analysis of the passive cavity modes. The cavity shape has a significant impact on the strength and frequency of occurrence of instabilities even in the presence of a small amount of surface roughness. We find that two properties appear to determine the strength of lasing instabilities: the degree of spatial localization and the fine structure size of the intensity distributions, where spatially extended modes with fine-grained structure lead to more stable lasing dynamics while localized modes with larger structure size such as WGMs cause more unstable dynamics. The structure size of the modes is related to the local directionality of the ray dynamics, an aspect that has not been studied so far. Understanding the relations between the structure of modes and classical ray dynamics will consequently enable us to engineer the lasing dynamics via the cavity shape. However, it should be emphasized again that not the type of classical dynamics (integrable or chaotic) is important, but how the ray dynamics manifests in the structure of the modes. Furthermore we observe that the spatial and temporal scales of the lasing dynamics also depend on the resonator geometry, though the reasons for this are not yet completely understood.

In conclusion, we establish the resonator geometry as an additional, powerful design parameter to control the degree of stability as well as the time and length scales of the spatio-temporal dynamics of semiconductor lasers. The advantage of modifying the cavity shape to change the laser dynamics compared to conventional methods like optical injection and time-delayed feedback is that it enables compact devices that can be readily integrated on chip. Potential applications are the development of broad-area lasers with stable dynamics for high-power applications as well as compact lasers featuring broadband chaos for chaos-based applications.

Chapter 3

Electrically-pumped semiconductor lasers with low spatial coherence

3.1 Introduction

[1]As discussed in Chapter 2, tailoring the cavity shape impacts the behavior of multimode semiconductor lasers. However, the asymmetric cavity geometries we have explored, particularly wave-chaotic cavities like a D-shaped cavity, lack a preferential direction of laser emission. Here a question arises: is it possible to attain the lasing of many spatial modes while maintaining a narrow output beam divergence? In Chapter 3, we optimize the cavity geometry for the maximal number of spatial lasing modes with directional emission of laser output. Instead of chaotic ray dynamics with no preferential direction of ray trajectories, we explore the cavities with integrable ray dynamics and focus on the stable cavity configuration. In contrast to many previous works to achieve single-mode lasing from conventional semiconductor lasers, we aim to enhance the number of transverse lasing modes, reducing the spatial coherence of the laser emission. Such a highly multi-transverse-mode

[1]The chapter material is primarily taken from reference [1]: Reproduced from Kyungduk Kim, Stefan Bittner, Yongquan Zeng, Seng Fatt Liew, Qijie Wang, Hui Cao, "Electrically pumped semiconductor laser with low spatial coherence and directional emission", *Appl. Phys. Lett.*, vol. 115, 071101 (2019), with the permission of AIP Publishing.

laser with low spatial coherence will facilitate applications of reducing coherent artifacts in imaging.

The high spatial coherence of conventional lasers can introduce coherent artifacts due to uncontrolled diffraction, reflection and optical aberration. A common example is the speckle formed by the interference of coherent waves with random phase differences [96, 97]. Speckle noise is detrimental to full-field imaging applications such as displays [98], microscopy, optical coherence tomography, and holography [91]. It also poses as a problem for laser-based applications like material processing, photolithography, and optical trapping of particles.

Various approaches to mitigate speckle artifacts have been developed. A traditional method is to average over many independent speckle patterns generated by a moving diffuser [99, 100], colloidal solution [101], or fast scanning micromirrors [102]. However, the generation of a series of uncorrelated speckle patterns is time-consuming and limited by the mechanical speed. A more efficient approach is to design a multimode laser that generates spatially incoherent emission, thus directly suppressing speckle formation [14]. Low spatial coherence necessitates lasing in numerous distinct spatial modes with independent oscillation phases. For example, a degenerate cavity [10, 103, 104] allows a large number of transverse modes to lase, but the setup is bulky and hard to align. Complex lasers with compact size such as random lasers [105–108] have low spatial coherence and high photon degeneracy, but are mostly on optically pumped. For speckle-free imaging applications, wave-chaotic semiconductor microlasers [109] have the advantages of electrical pumping and high internal quantum efficiency. However, disordered or wave-chaotic cavity lasers typically have no preferential emission direction, and the poor collection efficiency greatly reduces their external quantum efficiency. Our goal is creating an electrically pumped multimode semiconductor microlaser without disordered or wave-chaotic cavity to combine low spatial coherence and directional emission.

Moreover, the speed of speckle suppression is crucial for imaging applications. For instance, time-resolved optical imaging to observe fast dynamics requires speckle-free image acquisition with a short integration time, so the oscillation phases of different spatial lasing modes must completely decorrelate during the integration time to attain decoherence. The finite linewidth $\Delta\nu$ of individual lasing modes leads to their decoherence on a time scale of $1/\Delta\nu$. The frequency difference between different lasing modes can lead to even faster decoherence. For example, the emission from many random lasing modes with distinct frequencies exhibits low spatial coherence already within ten nanoseconds [110]. The decoherence time was measured for a solid-state degenerate cavity laser [111]. The intensity contrast of laser speckle is reduced by the dephasing between different longitudinal mode groups in tens of nanoseconds, but complete decoherence requires a few microseconds due to the small frequency spacing between transverse modes. We aim to further shorten the decoherence time by utilizing the larger mode spacings in a semiconductor microlaser.

3.2 On-chip stable cavity laser

Here we design an electrically-pumped chip-scale semiconductor laser with spatially incoherent and directional emission. The emission from conventional broad-area semiconductor lasers with flat end mirrors exhibits a good directionality. However, lasing occurs only in a few transverse modes since the high-order transverse modes have large divergence angles and hence experience severe losses [112, 113]. To lower the spatial coherence, we need to increase the number of transverse lasing modes. With curved end mirrors, the losses of high-order transverse modes can be reduced. We consider two-dimensional (2D) symmetric cavities with two circular concave mirrors with radius of curvature R_c as shown in Fig. 3.1(a). The mirrors are separated by the cavity length L. The geometry

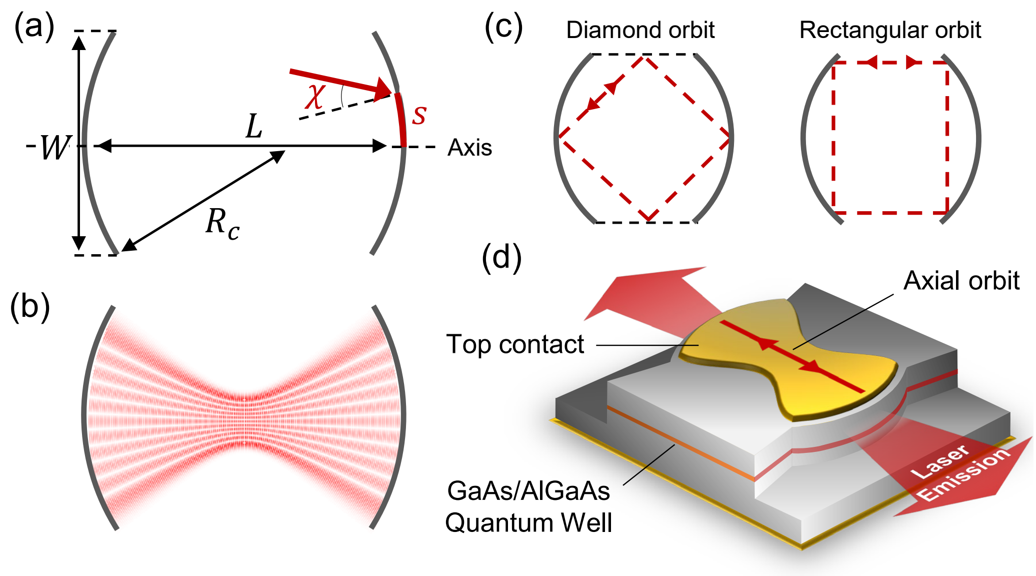

Figure 3.1: **Schematic of on-chip stable cavity laser.** (a) 2D symmetric stable cavity defined by two concave circular mirrors with radius of curvature R_c and distance L. The cavity width W is the distance between two extremities of a curved mirror. Rays impinging on the cavity boundary are described by coordinates (s, χ), where s is the coordinate along the curved boundary, and χ is the angle of incidence with respect to the surface normal. (b) The spatial intensity profile of a high-order transverse mode in a stable cavity. (c) Non-axial orbits that lead to non-directional emission. (d) Three-dimensional sketch of the on-chip stable cavity with directional emission. The lasing modes are based on the axial orbit and thus have directional emission. The shape of the top metal contact matches the spatial profile of high-order transverse modes to ensure their spatial overlap with gain.

of the cavity is determined by the parameter $g = 1 - L/R_c$, which is known as cavity stability parameter. If R_c is larger than $L/2$, or g is within the range $(-1, 1)$, the cavity is called stable in the sense that rays starting near the cavity axis stay close to it and will remain inside the cavity [114]. In the paraxial limit, the resonances in the stable cavity are described by Hermite-Gaussian modes, which have different transverse profiles depending on the transverse mode number m. Figure 3.1(b) shows the spatial intensity profile of a high-order transverse mode with $m = 10$.

Reducing the speckle contrast $C = 1/\sqrt{M}$ to below the level of human perception $\simeq 0.03$ [115, 116] requires $M \sim 1000$ transverse modes to lase simultaneously and independently. Previous designs of stable cavity semiconductor lasers with curved facets [47, 48, 117] exhibited less than 10 transverse lasing modes. The challenge is to increase the number of transverse lasing modes by two orders of magnitude. To accommodate higher order transverse modes, we increase the cavity width W. For directional emission, all lasing modes must be based on the axial orbit, which is formed by a ray traveling back and forth along the cavity axis between the two mirrors. However, modes based on non-axial orbits like those in Fig. 3.1(c) can appear in wide cavities, yielding non-directional emission. We eliminate the reflecting surfaces at the lateral sides [black dashed lines in Fig. 3.1(c)], to suppress the non-axial modes based on the periodic orbits with bounces from the sidewalls, such as the diamond orbit [48, 117]. In addition, we set $W = L/\sqrt{2}$ to avoid the rectangle orbits in the stable cavity. A schematic of our design is shown in Fig. 3.1(d).

3.3 Fine tuning of the cavity geometry

3.3.1 Calculating passive resonances

To maximize the number of transverse modes with similarly high Q factors, we optimize the cavity shape by fine tuning R_c while keeping L and W fixed. We calculate the cavity resonances with the COMSOL eigenfrequency solver module. The cavity resonances are the solutions of the scalar Helmholtz equation

$$[\nabla^2 + k^2 n^2(x, y)] H_z(x, y) = 0 \tag{3.1}$$

with outgoing wave boundary conditions where k is the free-space wave number, n is the refractive index, and H_z is the z-component of the magnetic field. The cavity length is $L = 20.0$ μm and the transverse width $W = L/\sqrt{2} = 14.1$ μm, which is the maximum width for that the rectangle orbit is avoided [see Fig. 3.1(c)]. The refractive index of the

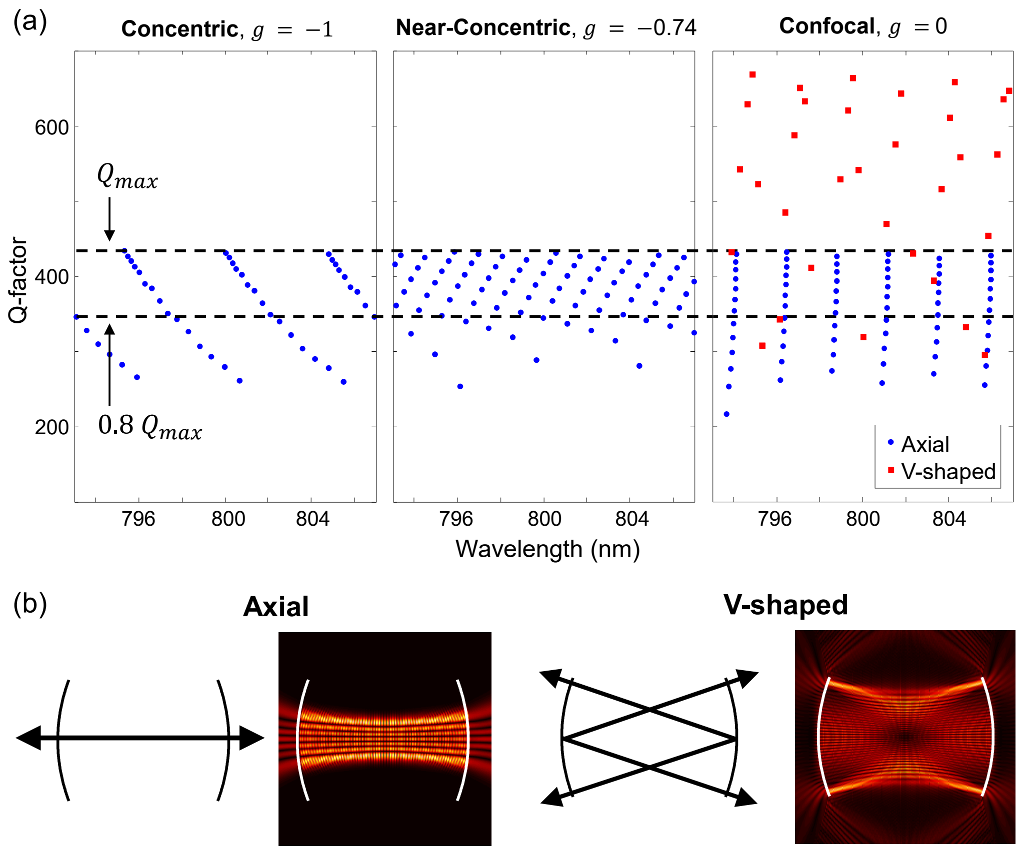

Figure 3.2: **High-Q modes in passive cavities of different geometries.** (a) Calculated quality factors and wavelengths of resonances in concentric ($g = -1$), near-concentric ($g = -0.74$), and confocal ($g = 0$) cavities. The upper dashed lines indicate the maximum Q factor Q_{max}. The lower dashed line is $0.8\,Q_{max}$, the lower limit of high-Q modes in our consideration. Blue dots are modes based on the axial orbit and red squares are modes on a non-axial orbit. (b) Examples of modes based on the axial mode (left) and the non-axial, V-shaped orbit (right).

cavity $n = 3.37$ corresponds to the effective refractive index of the vertically guided mode in the GaAs wafer used in the experiment. Transverse-electric (TE) polarization (electric field parallel to the cavity plane) is considered since GaAs quantum wells have higher gain for this polarization and the lasing modes are TE polarized.

Figure 3.2 shows the quality factors and wavelengths of cavity resonances in concentric ($g = -1$), near-concentric ($g = -0.74$), and confocal ($g = 0$) cavities. We calculate the Q-factor, $Q \equiv k_r/2k_i$, where $k = k_r - ik_i$ is the complex eigenvalue obtained from Eq.

3.1. The fundamental transverse Hermite-Gaussian modes ($m = 0$) have the highest Q-factors $Q_{max} \simeq 433$, which is equal to the Q-factor of a Fabry-Perot cavity with length L,

$$Q_{max} = \frac{2\pi\nu n L}{c \ln(1/R)} \tag{3.2}$$

where ν is the vacuum frequency, $R = [(1-n)/(1+n)]^2$ is the reflectivity of the cavity facet for normal incidence. We consider the high-Q modes of $Q \geq 0.8\, Q_{max}$, which are in between the two horizontal dashed lines in Fig. 3.2).

The numerically calculated mode wavelengths agree well with the analytic expression for the frequencies of Hermite-Gaussian modes [114],

$$\nu_{m,q} = \frac{c}{2nL}\left[q + \frac{1}{\pi}\left(m + \frac{1}{2}\right)\arccos(g)\right], \tag{3.3}$$

where $\nu = c/\lambda$ is the frequency, c is the speed of light, n is the refractive index, L is the cavity length, g is the cavity stability parameter, and (q, m) are the longitudinal and transverse mode numbers, respectively. The deviations between numerical and analytic mode wavelengths gradually grow as m increases and reach 0.04% for the highest-order high-Q transverse mode ($m = 23$) in the near-concentric cavity. The deviations are larger for the concentric cavity ($g = -1$), since it is at the border of the stability region where Eq. 3.3 no longer holds.

In addition to the usual Hermite-Gaussian modes based on the axial orbit, modes based on V-shaped orbits [see Fig. 3.2(b)] exist in confocal ($g = 0$) and near-confocal (g close to 0) geometries. These modes are indicated as red squares in Fig. 3.2(a), and in most cases exhibit higher Q-factors than the axial modes since the V-shaped orbit experiences total internal reflection at one mirror facet. Here we only consider the axial modes, excluding the non-axial orbits which are undesirable due to their non-directional output.

3.3.2 Maximizing high-Q modes

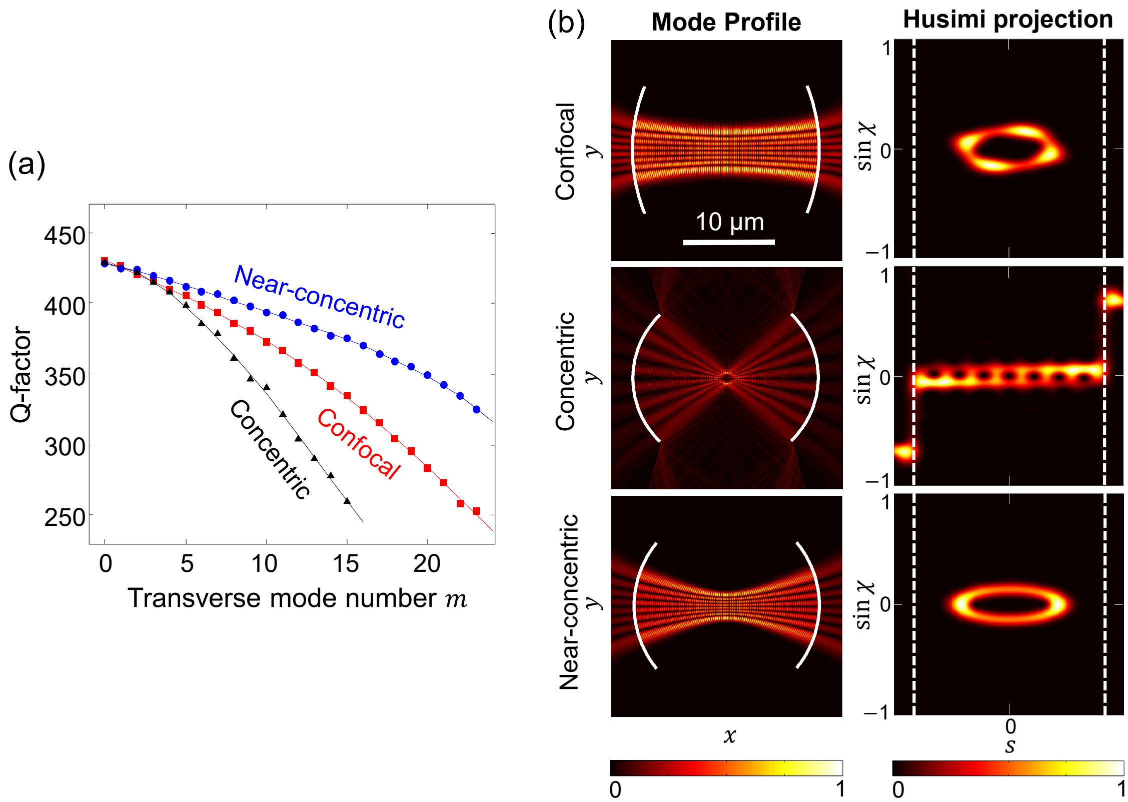

Figure 3.3: **Fine tuning of the cavity geometry to maximize the number of transverse modes.** (a), Dependence of quality factor Q on transverse mode number m for the optimized near-concentric ($g = -0.74$), confocal ($g = 0$), and concentric ($g = -1$) cavities. (b), Calculated spatial distributions of field amplitude (left) and corresponding Husimi projections (right) for high-order transverse modes ($m = 7$) in confocal, concentric, and near-concentric ($g = -0.74$) cavities. White solid lines in the left column represent the curved cavity facets, and while dashed lines in right column mark the endpoints of the facets.

Degenerate cavities with conventional mirrors can support transverse modes with nearly-degenerate Q-factors thanks to their self-imaging property [9, 118]. As an example of a degenerate cavity we consider the confocal geometry ($g = 0$). For the on-chip design with dielectric interfaces as mirrors, however, the Q-factor decreases significantly as the transverse mode number m increases as shown in Fig. 3.3(a). Figure 3.3(b) shows a typical mode laterally confined to the cavity axis, resulting in negligible diffraction loss.

We calculate its Husimi projection [64] from the overlap of its spatial field distribution with a minimal-uncertainty wave packet impinging onto the cavity boundary. It visualizes the angle of incidence χ of wave components at different positions s of the cavity boundary [see Fig. 3.1(a)]. In Fig. 3.3(b), the high-intensity spots in the Husimi map indicates the dominant wave components have nonzero angle of incidence onto the cavity mirrors. As m increases, wave components with increasingly higher incident angles appear. Thus high-order transverse modes in the confocal cavity experience higher loss since the reflectivity at a dielectric-air interface decreases with increasing χ for TE-polarized light, making the confocal cavity unsuitable for multimode lasing.

To solve this problem we consider the concentric cavity ($g = -1$), which does not have frequency degeneracy of its resonances. Since the concentric mirrors are part of a circle, any ray passing through the cavity center hits the boundaries perpendicularly. Indeed the Husimi projection in Fig. 3.3(b) is strongly localized at $\chi = 0$ and thus the angle-dependent reflectance is an insignificant loss mechanism. However, as the mode profile exhibits a large divergence, light leaks out via diffraction from the endpoints of the facets. These losses are evident in the Husimi projection from the high-intensity spots just outside the cavity facet. Since the higher order transverse modes experience stronger diffraction loss, the Q-factor decreases even more quickly with m than for the confocal case as seen in Fig. 3.3(a).

We gradually vary g from -1 to 0 in search for the optimal geometry that supports the largest number of high-Q transverse modes. Fig. 3.3(c) shows the number of transverse modes, that are based on the axial orbit and have Q-factors exceeding 0.8 times the maximal Q-factor, as a function of g. The optimal geometry $g = -0.74$ is near concentric. A slight deviation from the concentric shape makes the mode profiles laterally localized to the cavity axis [see Fig. 3.3(b)]. Moreover, the Husimi projection shows high-intensity spots centered at $\chi = 0$, which indicates most wave components have almost normal incidence on the cavity facet. Therefore, the near-concentric geometry minimizes both losses from angle-dependent reflectance and diffraction, resulting in the slowest decrease of Q with m.

Scaling of the number of modes with the cavity size

When comparing different cavity geometries, we simulated small cavities with length $L = 20$ μm and width $W = 14$ μm to keep the computation time reasonably short. However, the cavities used in experiments are much larger with $L = 400$–800 μm and $W = 283$–566 μm, in order to increase the total number of transverse modes and lower the pump current density to reduce heating. To verify that the optimal value of the stability parameter g found in simulations holds for larger cavities, we perform simulations with a $L = 40$ μm-long cavity.

Figure 3.4 shows the high-Q modes in two near-concentric cavities ($g = -0.74$) with $L = 20$ μm and $L = 40$ μm. The ratio $L/W = \sqrt{2}$ is the same for both cavities. The wavelengths and quality factors of the modes with relatively high Q are shown in Fig. 3.4(a). The maximum Q-factor Q_{max} of the $L = 40$ μm and $L = 20$ μm cavities are 867 and 433, respectively, as expected from Eq. 3.2. The shaded regions in Fig. 3.4(a) indicate the high-Q regions of $0.8\,Q_{max} \leq Q \leq Q_{max}$. The high-$Q$ resonances of the $L = 40$ μm-long cavity are more closely spaced than those of the $L = 20$ μm-long cavity since the total number of resonances is proportional to the area of the cavity.

Figure 3.4(b) shows the dependence of the Q-factors on the transverse mode number m for the near-concentric cavities ($g = -0.74$) for $L = 20$ μm and $L = 40$ μm. The Q-factors decrease approximately linearly with m, where the slope of the decrease for the $L = 40$ μm-long cavity is about one half of that for the $L = 20$ μm-long cavity. This indicates that the number of different transverse modes with high-Q is about twice as large for the $L = 40$ μm-long cavity as for the $L = 20$ μm-long cavity. This linear scaling is

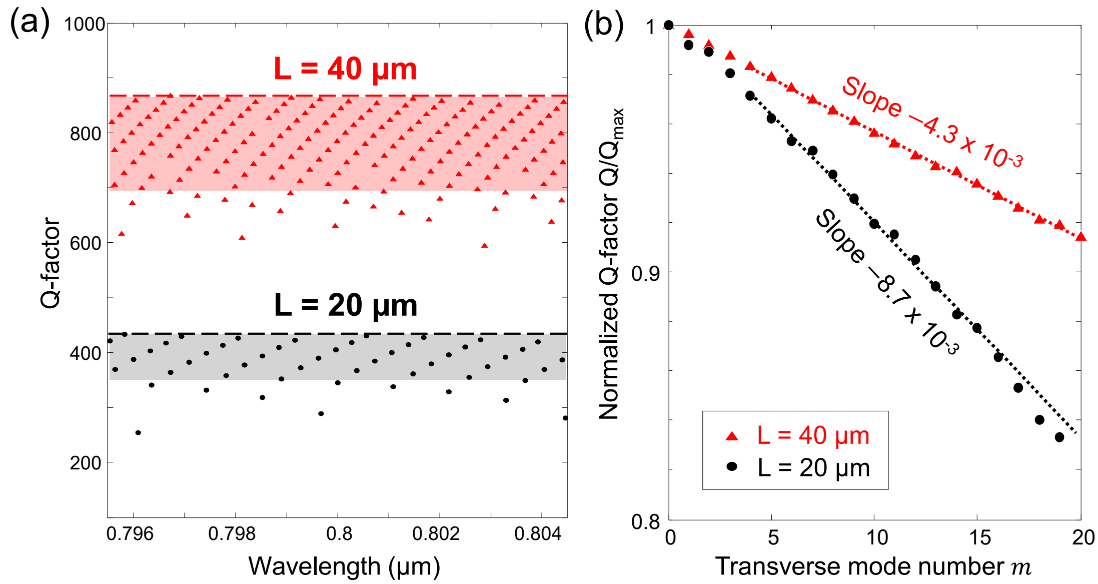

Figure 3.4: **Scaling of the number of transverse modes with cavity size.** (a) Calculated Q factors and wavelengths of modes with relatively high Q in near-concentric cavities ($g = -0.74$) with lengths $L = 40$ μm (red triangle) and $L = 20$ μm (black dots). The dashed lines represent the maximum Q-factors Q_{max} in the two cavities. The shaded areas indicate the high-Q regions of $0.8\, Q_{max} < Q < Q_{max}$. (b) Dependence of Q-factors on transverse mode number m for $L = 40$ μm (red triangle) and $L = 20$ μm (black dots). Q is normalized by Q_{max} of each cavity. The dotted lines are linear fits and their slopes are shown.

verified for another cavity geometry, $g = -0.54$, where the slopes are 1.2×10^{-2} and 6.1×10^{-3} for $L = 20$ μm and $L = 40$ μm-long cavities, respectively. Due to this linear scaling, the optimal value of g, at which the number of high-Q transverse modes is maximal, is independent of the cavity size.

3.3.3 Lasing of many transverse modes

The above optimization is based on the cavity resonances in the absence of gain. Gain competition can limit the number of lasing modes additionally. In order to quantify the effect of gain competition, we use the SALT (steady-state *ab-initio* laser theory) to investigate the effect of mode competition in an active cavity [87, 88]. We assume a spatially uniform distribution of pump and a nearly flat gain spectrum. Both axial and non-axial

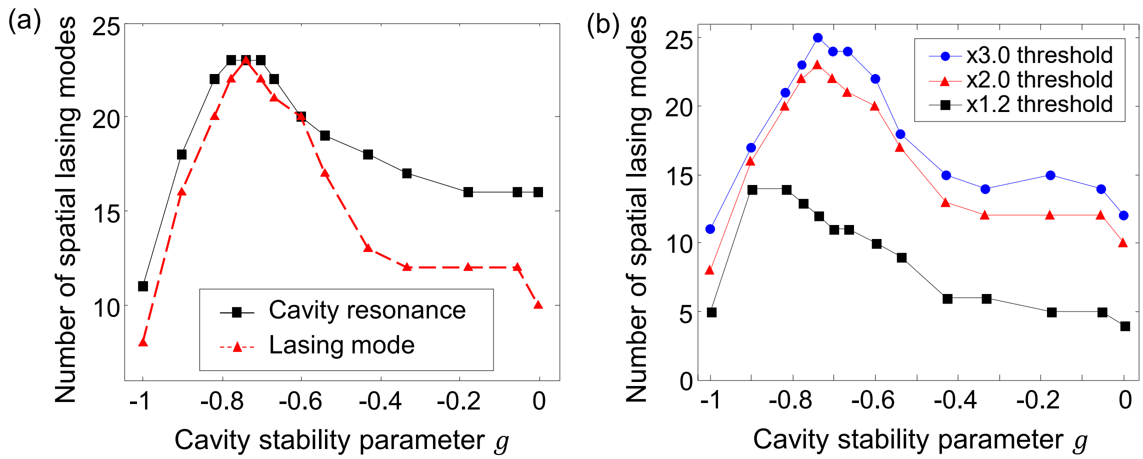

Figure 3.5: **Number of transverse lasing modes.** (a) Calculated number of high-Q resonances (black squares) and the number of lasing modes (red triangles) that are based on axial orbit and exhibit distinct transverse profiles as a function of cavity stability parameter g. (b) The number of transverse lasing modes at three different pumping levels.

modes are included in the simulations, but we count only the number of axial lasing modes that contribute to a directional output beam.

The red curve in Fig. 3.5(a) represents the number of different transverse axial lasing modes at a pump level of two times above the lasing threshold. In the confocal cavity, the number of lasing modes based on axial orbit is notably smaller than the number of high-Q passive modes due to the existence of non-axial modes with higher Q that lase first and saturate the gain for the axial modes (see Supplementary). For the optimized near-concentric cavity, most of the passive transverse modes with high Q can lase, indicating gain competition is insignificant.

Figure 3.5(b) shows the number of distinct transverse lasing modes at different pump levels, where only axial modes are counted. The pump level is defined with respect to the first lasing threshold of the axial modes. The maximum number of axial lasing modes is reached in the near-concentric regime of g close to -1. The optimal g value depends slightly on the pump level, but it remains at $g = -0.74$ when the pump exceeds twice of the lasing threshold.

3.4 Device fabrication

Based on the optimized cavity design, the laser devices are fabricated with photolithography followed by reactive ion etching from a commercial GaAs/AlGaAs quantum well epiwafer. To ensure spatial overlap of high-Q transverse modes with the quantum well gain, the top metal contact for current injection is shaped to match the spatial profile of highest-order transverse lasing modes. The scanning electron microscope (SEM) images in Fig. 3.6 show that the etched facets, which serve as curved end mirrors, are smooth and vertical.

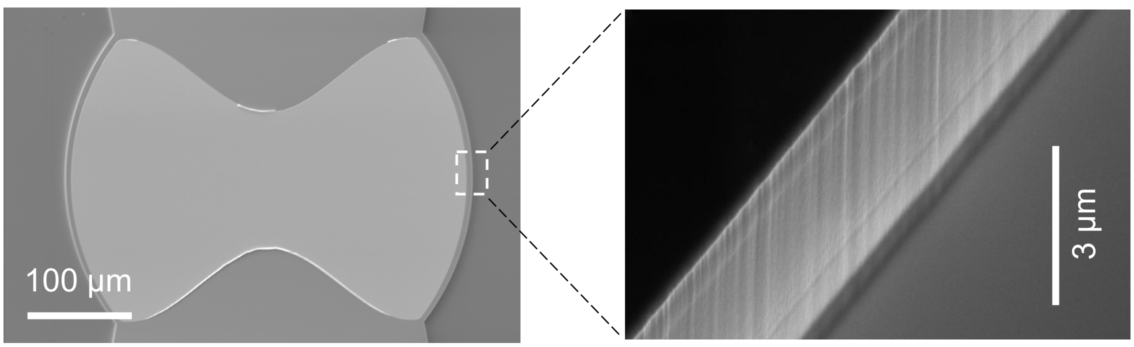

Figure 3.6: **Fabricated on-chip stable-cavity laser.** SEM images of a fabricated near-concentric ($g = -0.74$) cavity of length $L = 400$ μm and $W = 283$ μm. The etched facet is vertical and smooth.

Fabrication process

We use a commercial diode laser wafer (Q-Photonics QEWLD-808). The gain medium is a 12 nm-thick GaAs quantum well, embedded in the middle of an undoped 400 nm-thick $Al_{0.37}Ga_{0.63}As$ guiding layer, which itself is between p-doped and n-doped $Al_{0.55}Ga_{0.45}As$ cladding layers (each is 1.5 μm thick).

The laser cavities are fabricated by the following procedure. First the back contact made of Ni/Ge/Au/Ni/Au layers (thicknesses are $5/25/100/5/200$ nm, respectively) is deposited and thermally annealed at $390\,^\circ\mathrm{C}$ for 30 s. Then a 300 nm-thick SiO_2layer is deposited on the front side. The cavity shapes are defined by photolithography and transferred to the SiO_2 layer by reactive ion etching (RIE) with a CF_4 (30 sccm) and CHF_3 (30 sccm) mixture. After the removal of the photoresist, the remaining SiO_2 is used as mask for an inductively coupled plasma (ICP) dry etching with an Ar (5 sccm), Cl_2 (4 sccm), and BCl_3 (4.5 sccm) plasma mixture to create the cavities. The etch depth is about 4 μm to etch all the way through the guiding layer and partially into the bottom cladding layer. After the ICP dry etching, the SiO_2 mask is removed by RIE and a buffered oxide etch (BOE).

The top metal contacts are defined by negative photolithography, followed by Ti/Au (thicknesses $20/200$ nm) deposition. The boundaries of the top contacts are 5 μm away from the cavity edges to prevent the top contacts from hanging down and blocking the emission from the facets. The last process is the lift-off and the sample is cleaned by O_2 plasma afterwards.

3.5 Lasing characteristics

3.5.1 Laser testing

The fabricated samples are mounted on a copper plate and a tungsten needle (Quater Research, H-20242) is placed on the top contact for electric current injection. The lasers are pumped electrically by a diode driver (DEI Scientific, PCX-7401) which generates a series of rectangular current pulses. We use a pulse length of 2 μs and a low repetition rate of 10 Hz in order to reduce heating.

For measurements of optical spectrum, the laser emission is collected by a $20\times$ microscope objective (NA = 0.40). It is then coupled into a fiber bundle with a fiber collimator (NA = 0.50) behind the objective lens. Its spectrum is measured by an imaging monochromator (Acton SP300i) equipped with an intensified CCD camera (Andor iStar DH312T-18U-73).

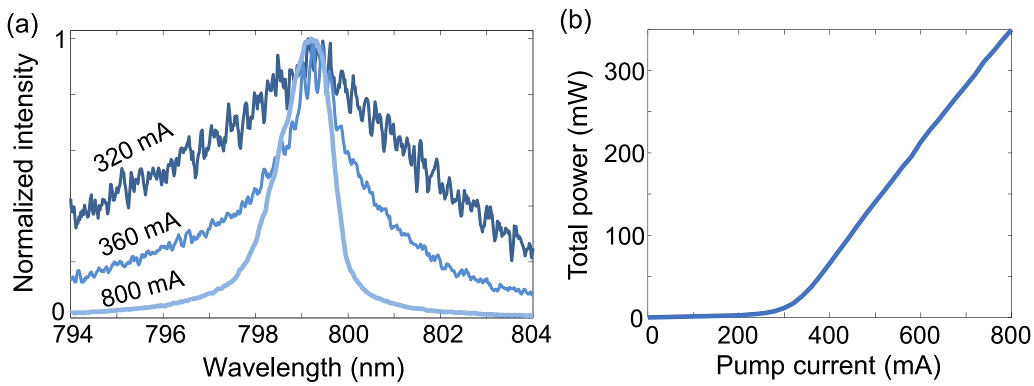

Figure 3.7: **Testing of a stable-cavity laser.** (a) Normalized emission spectra at different pump currents for a near-concentric cavity ($g = -0.74$) with $L = 400$ μm: below the lasing threshold (320 mA), just above the threshold (360 mA), and about two times above the threshold (800 mA). (b) Total emission power, from both end facets, versus the injection current.

Figure 3.7(a) shows the emission spectra from an optimized near-concentric cavity ($g = -0.74$) at different pump currents. A typical spectrum consists of many closely-spaced narrow peaks, indicating simultaneous lasing of many modes. More lasing peaks appear at higher pump currents, and they merge to a smooth, broad spectrum.

We measured the power of laser emission from one side of the cavity. For a near-concentric cavity ($L = 400$ μm) at pump current of 800 mA, the emission power collected by the objective lens (NA = 0.4) is $\sim$70 mW. The collection efficiency of the objective lens is 20 %, due to the divergence of laser emission, the finite NA and transmission of the lens, and the collection from one facet of the cavity. Thus, the total emission power reaches 350 mW at pump current of 800 mA, and the differential quantum efficiency is 0.8 W/A.

The curve of emission power versus pump current for a $L = 400$ μm-long cavity in Fig. 3.7(b) shows a lasing threshold of 360 mA, above which the emission power increases much more rapidly with the pump current. The threshold current density is inversely proportional to the cavity length L (not shown), as expected since the Q-factors increase with L linearly [114]. There is no significant difference between the lasing thresholds for cavities with the same L but different g.

3.5.2 Directional emission

To test the laser directionality, we measure the far-field emission patterns with the setup in Fig. 3.8(a). The objective lens is removed and the laser emission is measured after free-space propagation. A CCD camera (Allied Vision, Manta G-235B) is placed at a distance $D = 6$ cm from the cavity. This distance is on the order of the far-field distance $W^2/\lambda = 9.8$ cm, where $W = 280$ μm is the width of the cavity and $\lambda = 0.8$ μm is the emission wavelength in air. A large angular range is covered by moving the CCD camera on a rail while rotating the camera to face the cavity at every position. Since the distance R from the cavity to the camera varies with the position, the measured intensity is rescaled by $1/R^2$ accordingly. The recorded images are stitched together in the horizontal direction and vertically integrated to obtain the far-field patterns.

We measure the far-field emission patterns at a pump current two times above the lasing threshold. Figure 3.8(b) shows the far-field patterns for three cavity shapes. The far-field emission was measured at a distance $D = 6$ cm from the cavity facet. For a near-concentric cavity ($g = -0.74$), a directional output beam with a divergence angle (half width at half maximum) of 35° is observed. The concentric cavity ($g = -1$) shows a flat-top far-field pattern with sharp edges. This pattern is attributed to the broad angular divergence of modes in the concentric cavity. In contrast, the far-field pattern of the confocal cavity features sharp peaks on top of a broad background. The sharp peaks originate from lasing modes based on a V-shaped, non-axial orbit (see inset and Fig. 3.2(b)).

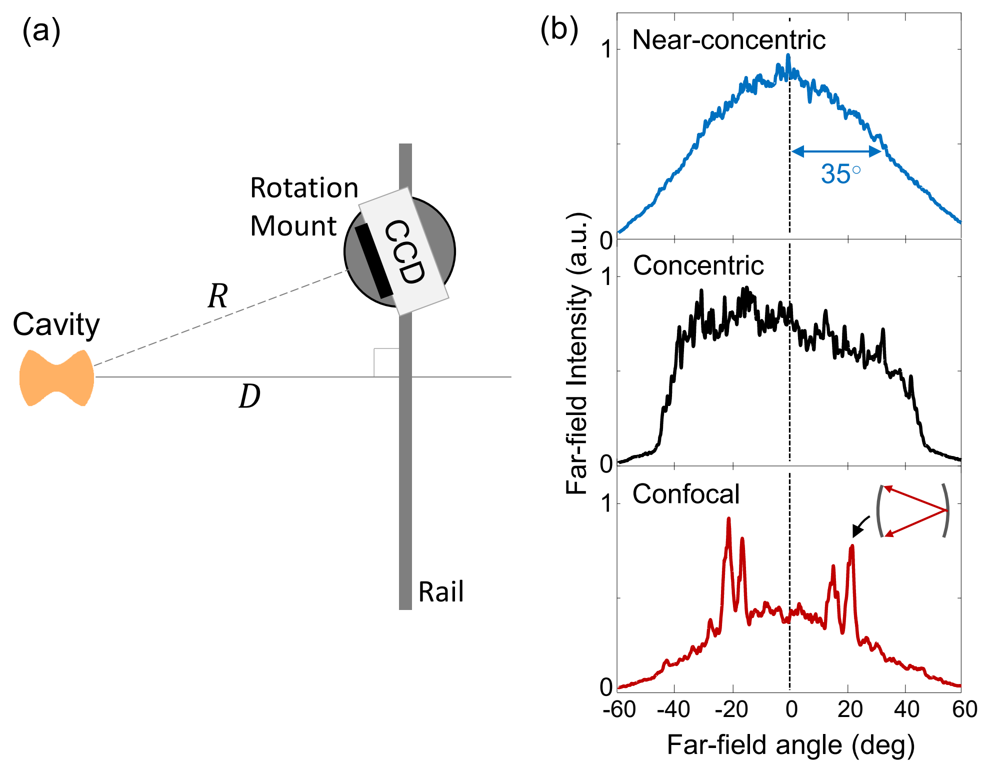

Figure 3.8: **Measurement of laser emission at the far-field** (a) Optical setup to measure the far-field emission patterns. The laser emission is directly measured with a CCD camera on a rotating mount on a rail. (b) Far-field intensity patterns of laser emission from three cavities with $g = -0.74, -1,$ and 0. The V-shaped orbit, which contributes to the sharp peaks in the far-field pattern of the confocal cavity, is drawn in the inset.

3.5.3 Low spatial coherence

We characterize the spatial coherence of the laser emission from the cavities of different shapes. The emission is coherent in the direction normal to the wafer since the sample has only one index-guided mode in the vertical direction. To measure the coherence of emission in the horizontal direction (parallel to the wafer), we create speckle patterns with a line diffuser (RPC Photonics, EDL-20) that scatters light only in the horizontal direction. The microscopic structure of the line diffuser consists of fine random elongated grains of about 10 μm width on top of a quasi-periodic structure of 100 μm scale.

The optical setup consists of an objective lens that collects the laser emission and a line diffuser that is placed in the pupil plane of the objective (6 mm diameter). A single 2 μs-long pump pulse is used for the laser emission. The laser emission fills the entire aperture of the objective and thus covers hundreds of random elongated grains of the line diffuser. A plano-convex lens in $f - f$ configuration between the diffuser and the CCD camera (Allied Vision, Mako G-125B) allows to measure the far-field speckle patterns.

Figure 3.9(a) is the measured speckle pattern from a near-concentric cavity laser. For comparison, the speckle pattern from a source with high spatial coherence, a frequency-doubled Nd:YAG laser (Continuum, Minilite), is also measured with the same optical configuration in Fig. 3.9(b). The typical speckle size on the CCD camera is 2.5 pixel calculated from the intensity autocorrelation function, so that the speckle contrast reduction due to undersampling is negligible [96]. For each speckle contrast measurement, speckle patterns are repeatedly measured for different lateral positions of the line diffuser, and the speckle contrasts for these different disorder realizations are averaged.

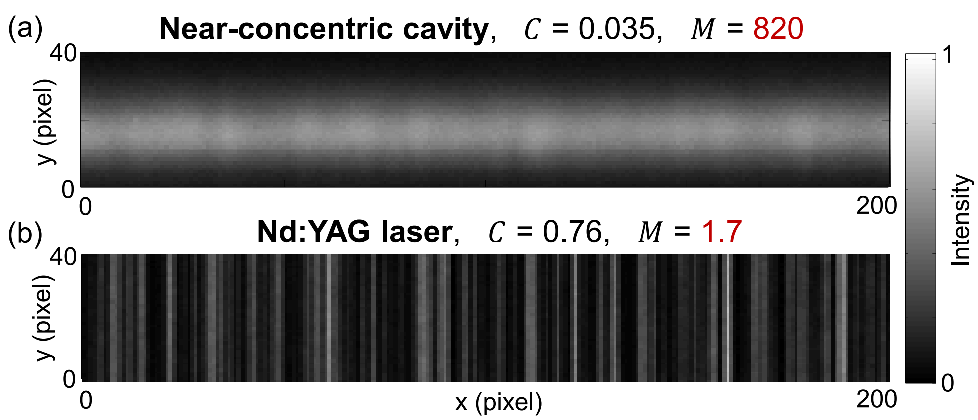

Figure 3.9: **Speckle patterns from a line diffuser.** (a) Laser emission from a near-concentric cavity ($g = -0.74, L = 400$ μm) passes through a line diffuser, and the far-field speckle pattern has an intensity contrast $C = 0.035$. The effective number of distinct transverse lasing modes is $M = 1/C^2 = 820$. (b) A spatially coherent Nd:YAG laser beam ($\lambda = 532$ nm) passing through the same diffuser creates a speckle pattern with contrast $C = 0.76$.

In order to quantify the spatial coherence, we calculate the speckle contrast defined as $C = \sigma_I/\langle I\rangle$, where σ_I and $\langle I\rangle$ are the standard deviation and mean of the speckle intensity, respectively. $M = 1/C^2$ gives the effective number of distinct transverse lasing modes [96]. Figure 3.10 gives the values of M for cavities with different g and L, measured at two times of the lasing threshold. The number of transverse lasing modes is the largest for the near-concentric cavity ($g = -0.74$). With the ratio W/L fixed, the number of transverse modes increases with L since a wider cavity supports more transverse modes. For the $L = 800$ μm near-concentric cavity ($g = -0.74$), about $1,000$ different transverse modes lase, and their combined emission reduces the speckle contrast to about 0.03.

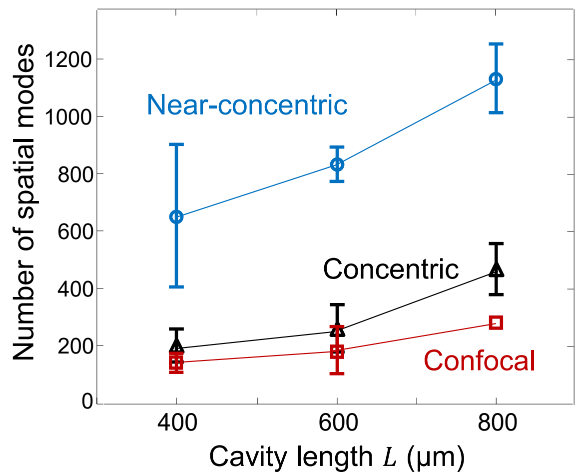

Figure 3.10: **Measured number of spatial lasing modes.** The number of transverse lasing modes in near-concentric ($g = -0.74$), concentric ($g = -1$), and confocal ($g = 0$) cavities with different length L. The error bars indicate the variation between different cavities of the same g and L.

3.6 Ultrafast decoherence

3.6.1 Time-resolved speckle

To examine the applicability of the optimized laser for ultrafast speckle-free imaging, we determine how fast decoherence of the emission occurs. We use a streak camera to measure the time-resolved speckle patterns with a temporal resolution of about 60 ps in a setup sketched in Fig. 3.11(a). Figure 3.11(b) shows the spatio-temporal evolution of the measured far-field speckle pattern of a near-concentric cavity laser ($g = -0.74$). The magnification in Fig. 3.11(c) reveals rapid spatial and temporal variations of the intensity pattern. To quantify the coherence time of the emission, we calculate the contrast of speckle patterns as a function of the integration time. As shown in Fig. 3.11(d), for a short integration time of $t_{\mathrm{int}} = 0.2$ ns, the speckle has a notable contrast of ~ 0.2. As the integration time increases, the speckle contrast drops quickly. Figure 3.11(e) summarizes the reduction of the speckle contrast for t_{int} from 100 ps to 500 ns. The $L = 800$ μm-long cavity laser features lower speckle contrast than the $L = 400$ μm-long cavity laser for all integration times. After a rapid drop, the contrast starts to saturate, exhibiting a kink at a few nanoseconds (indicated by the solid arrow). A second kink (indicated by a dotted arrow) follows at several tens of nanoseconds after which the speckle contrast further declines.

3.6.2 Frequency spacing of cavity resonances

The time scale of the speckle contrast reduction is related to the frequency differences of lasing modes when their linewidths are smaller than their frequency spacings. When the integration time t_{int} is shorter than the inverse frequency spacing of two modes, their temporal beating results in a visible interference pattern that oscillates in time. For an integration time longer than their beating period, the time-varying interference pattern is averaged out, hence the intensity contrast of the speckle pattern created by these two modes is reduced. With increasing integration time, more and more lasing modes become incoherent, as their frequency spacings exceed $1/t_{\mathrm{int}}$, and the speckle contrast continues dropping. Once t_{int} is long enough to average out the beating of even the closest pairs of lasing modes, the speckle contrast cannot reduce further. The first kink in Fig. 3.11 indicates that the speckle contrast saturates at the integration time of a few nanoseconds. This time scale is related to the average frequency spacing between neighboring modes.

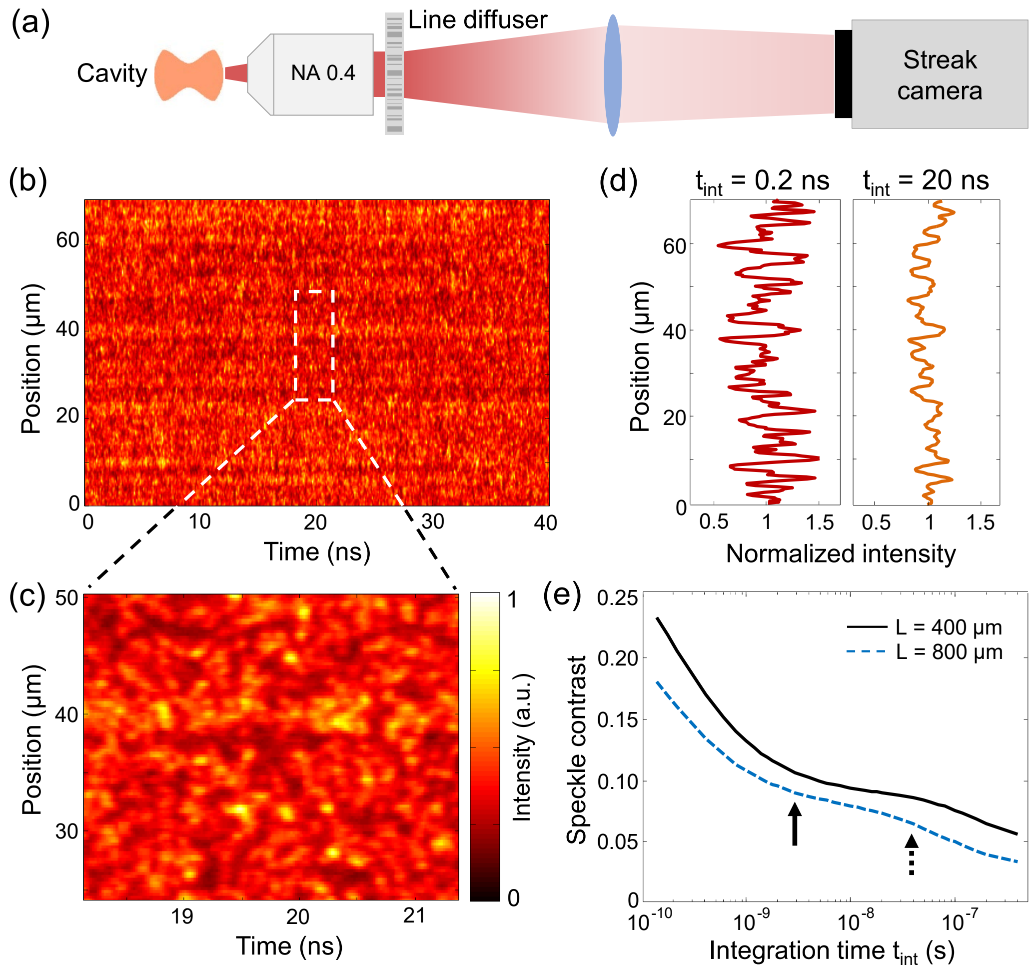

Figure 3.11: **Decoherence time for a near-concentric cavity laser.** (a) Schematic of the setup that measures speckle patterns with a CCD or streak camera. (b) The spatio-temporal profile of the far-field speckle pattern from a laser with $g = -0.74$ and $L = 400\ \mu$m. (c) Magnification of the speckle pattern revealing fast temporal evolution of the speckle grains. (d) Time-integrated speckle patterns for integration times 0.2 ns and 20 ns, exhibiting an intensity contrast of $C = 0.21$ and 0.098, respectively. (e) Dependence of speckle contrast on the integration time t_{int}, featuring two kinks at the integration times of a few nanoseconds (solid arrow) and several tens of nanoseconds (dotted arrow).

The average frequency spacing between adjacent modes is estimated as several hundred MHz in our cavities. Here we used the simulation results for a small cavity and apply linear scaling with the cavity size as explained in the previous section. For the near-concentric cavity ($g = -0.74$) with $L = 20\ \mu$m, the number of high-Q transverse modes is 23 as given in Fig. 3.5(a). The free-spectral-range (FSR) is given by the longitudinal mode spacing, $c/(2nL) = 2.225$ THz. Within one FSR, there is a series of transverse modes with $m = 0$–22. Thus the average frequency spacing between adjacent transverse modes is about 96.7 GHz for a $L = 20$ μm cavity. In the experiments, the laser cavities with $L = 400$ μm have both L and W increased by a factor of 20 compared to the simulated ones. Consequently, the FSR is reduced by a factor of 20, and the number of transverse modes within one FSR increases by 20. Therefore, the average mode spacing is reduced by a factor of 400, which yields 242 MHz. The beating of two modes is averaged out when the integration time is longer than the inverse mode spacing, which is about 4 ns. This estimation gives the correct order of magnitude for the integration time at which the speckle contrast stops dropping in Fig. 3.11(e).

The typical linewidth of semiconductor lasers (10–100 MHz) is smaller than the frequency spacing. Thus the integration time needed for contrast reduction is determined by the mode spacing and estimated to be a few nanoseconds, which matches the experimental observations.

3.6.3 Thermally-induced mode instability

In Fig. 3.12, the speckle contrast displays a second kink at several tens of nanoseconds after which the contrast further decreases. This behavior is caused by thermal effects that cause the lasing modes to change in time. We conduct time-resolved measurements of the lasing spectrum to observe the spectro-temporal dynamics. The gating function of the intensified CCD camera is used to acquire the lasing spectra with $10 - 50$ ns time resolution. The spectra from multiple measurements with consecutive time intervals during the pump pulse are combined to obtain the spectrochronogram of a whole pulse. Figure 3.12(a) is the measured spectrochronogram of a near-concentric cavity ($g = -0.74$) laser with $L = 400$ μm. Since thermal equilibrium is not reached, the emission spectrum red-shifts during the pulse due to sample heating. Figure 3.12(b) is the spectrochronogram

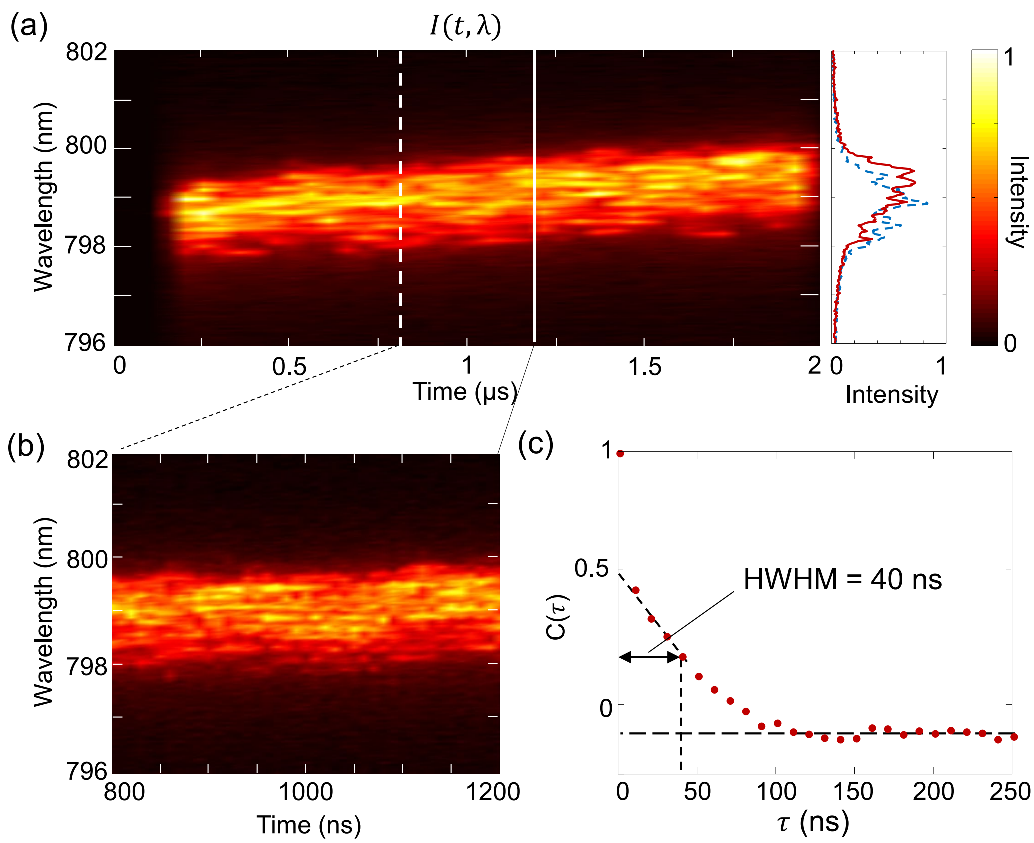

Figure 3.12: **Time-resolved spectra of laser emission.** (a) Measured spectrochronogram $I(t, \lambda)$ of laser emission from a near-concentric cavity ($g = -0.74, L = 400$ μm) at the pump current of two times the lasing threshold. The temporal resolution is 50 ns. The spectra at 0.8 μs and 1.2 μs are plotted on the right as dashed and solid lines, respectively. (b) Spectrochronogram during a 400 ns long interval measured with 10 ns resolution, showing that lasing peaks appear and disappear in time. (c) The autocorrelation function $C(\tau)$ of the time-resolved spectra in **b**. The half width at half maximum (HWHM) of $C(\tau)$ is about 40 ns.

in a 400 ns-long interval with a finer temporal resolution of 10 ns.

The measured spectrochronogram reveals changes of the lasing spectrum during the pulse. Lasing peaks appear or disappear over the course of the pump pulse as different lasing modes turn on or off. In order to quantify the time scale of these changes, we calculate the temporal correlation function of the spectral changes defined as [4]

$$C(\tau) = \sum_{\lambda} \langle \delta I(t, \lambda) \delta I(t + \tau, \lambda) \rangle_t, \tag{3.4}$$

where $\delta I(t, \lambda) \equiv [I(t, \lambda) - \langle I(t, \lambda) \rangle_t] / \sigma_I(\lambda)$ is the normalized change of the emission intensity and $\sigma_I(\lambda)$ is the standard deviation. The half width at half maximum (HWHM) of the temporal correlation function $C(\tau)$ gives the time scale of the spectral dynamics. In Fig. 3.12(c), the sharp drop of $C(\tau)$ at $\tau \sim 0$ is caused by the measurement noise. The HWHM of $C(\tau)$ is about 40 ns, extrapolated from the more gradual decrease of $C(\tau)$ after the initial drop. This is approximately the integration time in Fig. 3.11(e) where the second kink occurs, thus the further reduction of the speckle contrast is caused by the switching of lasing modes. The new lasing modes generate distinct speckle patterns that are superposed to the ones created by the old lasing modes, reducing the intensity contrast of the time-integrated speckle patterns.

3.7 Discussion and conclusion

In summary, we demonstrate directional emission, low spatial coherence and ultrashort decoherence time in a compact electrically-pumped semiconductor laser. By optimizing the shape of an on-chip near-concentric cavity, we maximize the number of transverse lasing modes and their emission greatly suppress speckle formation. The frequency detuning of lasing modes accelerate the decoherence of their emission, and low speckle contrast is obtained even with an integration time of a few nanoseconds. Such short decoherence time enables ultrafast speckle-free full-field imaging. Finally, we compare this work to the previous demonstration of spatially-incoherent non-modal emission from a broad-area vertical-cavity surface-emitting laser [119]. By carefully adjusting the pump conditions, the cavity is constantly modified by thermal effects, which disrupts the formation of lasing modes, leading to spatially incoherent emission [120, 121]. Our approach does not rely on thermal effects, and the decoherence time is two orders of magnitude shorter. Furthermore, our method does not utilize any transient process, thus it is applicable to steady-state lasing. With better thermal management, our laser may operate under constant pumping, emitting a continuous wave of low spatial coherence.

Chapter 4

Sensitive control of semiconductor lasers by cavity shape

4.1 Introduction

[1]In Chapter 3, we maximized the number of transverse lasing modes in a stable-cavity broad-area laser by tailoring the cavity geometry. By replacing the flat mirrors with concave mirrors with large curvature, high-order transverse modes become well confined in near-concentric cavities [1, 47]. While maintaining the low spatial coherence of laser output, the stable-cavity laser features greatly improved emission directionality compared to wave-chaotic cavities. However, such stable cavities still confine ray trajectories with a large range of propagation directions, leading to strongly divergent far-field emission [1]. The measured divergence angle of laser emission at the far-field reached 70°, which still would be incompatible with conventional collection optics. For the efficient collection of the laser emission, it is desirable to attain higher output directionality by staying closer to the Fabry-Perot geometry. To this end, in Chapter 4, we explore the vicinity of the

[1]The chapter material is primarily taken from reference [2]: Reproduced from Kyungduk Kim, Stefan Bittner, Yuhao Jin, Yongquan Zeng, Stefano Guazzotti, Ortwin Hess, Qi Jie Wang, Hui Cao, "Sensitive control of broad-area semiconductor lasers by cavity shape", *APL Photonics*, vol. 7, 056106 (2022), with the permission of AIP Publishing.

Fabry-Perot planar cavity geometry.

Fabry-Perot cavities with two planar facets have been widely adopted for semiconductor edge-emitting lasers. The planar facets are easily formed by cleaving the device during fabrication. This is in contrast to most solid state and gas laser cavities that have two concave mirrors arranged in such a way that the axial orbit is stable [114, 122, 123]. However, these planar broad-area high-power semiconductor lasers are highly susceptible to filamentation and irregular pulsation due to strong nonlinear interactions of the optical field and the gain medium [19–21, 23–26].

An interesting aspect of the planar Fabry-Perot cavity with profound impact on the lasing dynamics is that it is situated at the bifurcation between stable cavities with concave mirrors and unstable cavities with convex mirrors. One way of suppressing the semiconductor laser instabilities is to destabilize the cavity ray dynamics by tilting the planar facet [124, 125] or changing it to a convex shape [126–129]. Such cavities lase only in the fundamental mode, which stabilizes the temporal dynamics [130]. However, at high pump powers, additional transverse modes can lase nonetheless, and their nonlinear interactions with the gain medium brings back filaments and pulsations.

In this chapter, we investigate broad-area edge-emitting semiconductor laser performance as a function of the resonator geometry in the vicinity of the bifurcation at the planar cavity geometry. We experimentally demonstrate that a tiny modification of the Fabry-Perot cavity has a profound impact on the lasing dynamics and spatial coherence. As we slightly curve the two end facets to form a near-planar stable cavity with concave mirrors, the spatial structures of cavity resonances are strongly modified, which in turn alters their nonlinear interactions with the gain medium (GaAs quantum well). Consequently, the spatio-temporal stability of the lasing dynamics in near-planar cavities is greatly improved. Such a simple scheme of mitigating instabilities will facilitate the stabilization of high-power broad-area semiconductor lasers for applications in material processing [131] and laser pumping [132], as well as biomedical applications [133].

Moreover, the number of transverse lasing modes drastically increases compared to that in the planar Fabry-Perot cavity, resulting in a sharp drop of the spatial coherence of the emission. At the same time, the output beam has a far-field divergence angle notably smaller than that of stable cavities with strongly-curved facets [1]. This combination of sufficiently low spatial coherence and relatively good emission directionality makes our laser an ideal illumination source for speckle-free full-field imaging [14, 107].

4.2 Near-planar cavity

4.2.1 Ray dynamics

One interesting aspect of the ray-wave correspondence in optical resonators is the influence of bifurcation points, that is, geometries at which new periodic orbits are created or change their stability when the cavity shape is varied. Bifurcations of classical orbits have a significant effect on the properties of wave systems and require special treatment in semiclassical theories [134, 135]. For example, they lead to increased fluctuations of the density of states in microresonators [136, 137]. Here we investigate broad-area semiconductor lasers as function of the resonator geometry in the vicinity of a bifurcation.

We concentrate on the well-known case of a Fabry-Perot cavity with two planar facets, which is situated at the bifurcation between stable cavities with concave mirrors and unstable cavities with convex mirrors. In a stable cavity, rays in the vicinity of the axial orbit are trapped forever (assuming perfectly reflecting mirrors), while in an unstable cavity these rays will escape quickly. Even though the passive modes change continuously with the cavity geometry, a small perturbation of the Fabry-Perot cavity can thus cause a large change in the laser properties, which is useful for sensing applications [138, 139].

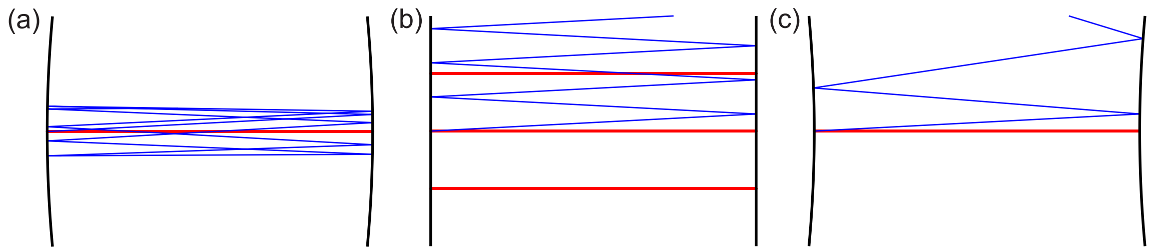

Figure 4.1: **Ray dynamics in an optical cavity with two mirrors.** Stability of ray dynamics in (a) a stable cavity ($g = 0.74$), (b) a Fabry-Perot cavity ($g = 1$), and (c) an unstable cavity ($g = 1.26$). The axial orbit is indicated in red, and a trajectory launched with an angular deviation of $3°$ is indicated in blue. The cavities have an aspect ratio of $W/L = 1/\sqrt{2}$, and the mirrors of the cavities in (a) and (c) have a radius of curvature or $R/L \simeq 3.85$.

Figure 4.1 shows examples of ray trajectories in a stable ($-1 < g < 1$), a Fabry-Perot ($g = 1$) and an unstable cavity $g > 1$. It should be noted that the terms stable and unstable actually refer to the axial periodic orbit (shown in red) and how it reacts to perturbations of its initial conditions, not to the cavity itself. In general, an optical cavity can exhibit several periodic orbits with different stability [1, 137], hence it is misleading to call a cavity itself stable or unstable. In the following we restrict ourselves to the axial orbit which is the only relevant one here.

A perturbation of the initial conditions can be a small change of the initial position and/or propagation direction of a trajectory. If a periodic orbit is stable, a slightly perturbed trajectory will stay close to it forever. This behavior is shown in Fig. 4.1(a) for a cavity with $g = 0.74$: the blue trajectory, which is launched with a direction deviating by $3°$ (but at the same position) always stays close to the axial orbit as it travels back and forth in the cavity. The same behavior is obtained when slightly changing the initial position. An important consequence of the stability of the axial orbit is that trajectories in its vicinity do not leave the cavity laterally and can hence support higher-order transverse modes with high Q factors.

If a periodic orbit is unstable, a slightly perturbed trajectory will travel away from it at an exponential rate. This case is exemplified in Fig. 4.1(c) for a cavity with $g = 1.26$: the blue trajectory propagates away from the axial orbit very rapidly without returning. Since the axial orbit is unstable, trajectories in its vicinity leave the cavity very quickly in the lateral direction, which greatly reduces the Q factors of higher-order transverse modes.

At the bifurcation point where the stability of the axial orbit changes from stable to unstable is the Fabry-Perot cavity ($g = 1$), for which the axial orbit is marginally stable. For marginally stable orbits, different perturbations of the initial conditions yield different results. When the initial direction of the axial orbit is changed, the perturbed trajectory propagates away linearly in time and leaves the cavity after a few round trips as shown by the blue trajectory in Fig. 4.1(b). This reduces the lifetime of higher-order transverse modes in the Fabry-Perot cavity. In contrast, perturbations of the initial position (but not direction) yield again periodic orbits as exemplified by the three red orbits in Fig. 4.1(b). So the axial orbit is part of a family of periodic orbits, consisting of all trajectories perpendicular to the planar end mirrors. In contrast, the axial orbit is called isolated when it is stable or unstable since it is the only periodic orbit in its vicinity in these cases.

Since the Fabry-Perot cavity is at a bifurcation point, small changes of the cavity geometry will strongly impact the behavior of trajectories around the axial orbit and lead to significant changes in lasing behavior because the stability of the axial orbit is related to the Q factors of higher-order transverse modes.

4.2.2 Cavity resonances

The dramatic change of the ray dynamics from planar to near-planar cavities has a strong influence on the spatial structure of the cavity resonances (i.e., solutions of the wave equation of the passive cavity). Due to the lack of lateral confinement in a Fabry-Perot cavity, the cavity resonances extend laterally across the entire end facets [Fig. 4.2(b)]. As the higher-order transverse modes exhibit larger transverse wavevector components $k_\perp$, their lateral leakage is stronger, and their quality (Q) factor is lower. In contrast, the lateral confinement of rays by concave mirrors reduces the transverse width of the cavity resonance, as seen in Fig. 4.2(c). The existence of confined trajectories in the vicinity of the cavity axis greatly enhances the Q factor of high-order transverse modes. Therefore, even a near-planar cavity can feature a relatively large number of transverse modes [Fig. 4.2(e)].

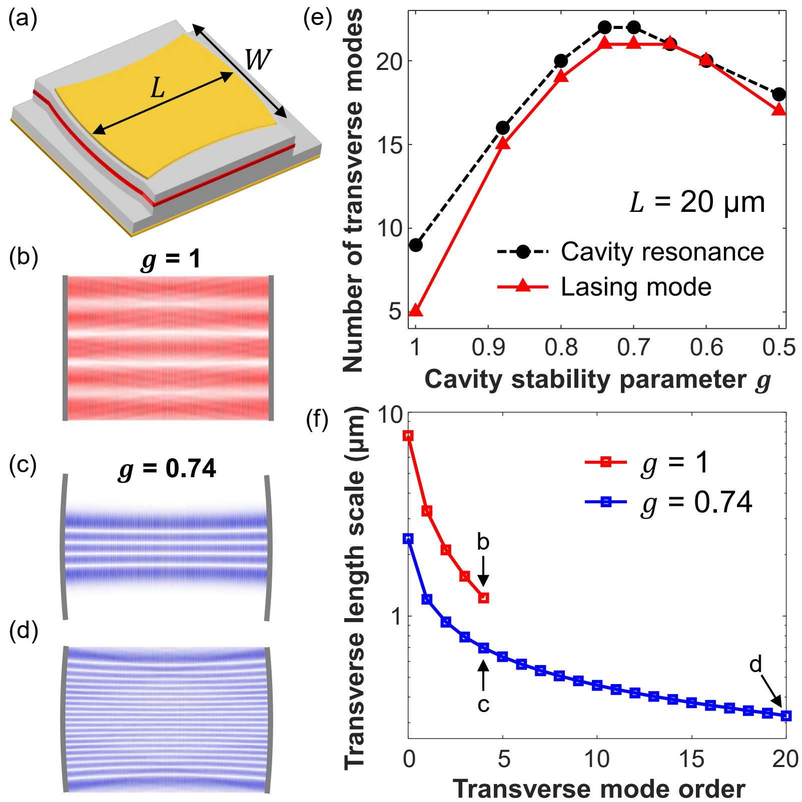

Figure 4.2: **Optical modes in a near-planar laser cavity.** (a) Schematic of a near-planar broad-area semiconductor laser with cavity length L and width W. (b) A passive mode of a planar cavity ($g = 1$) without mirror curvature, exhibiting a spatial profile extended over the entire facet. (c) A passive mode of the same transverse order in a near-planar cavity ($g = 0.74$), showing enhanced lateral confinement. (d) The profile of the highest-order transverse mode confined in the near-planar cavity ($g = 0.74$), featuring greatly decreased transverse wavelength. (e) The number of transverse modes in near-planar cavities. black dashed: passive resonances with a quality factor higher than $0.8\,Q_{\max}$. red solid: lasing modes at two times the lasing threshold in the presence of gain competition. (f) Reduction of the transverse characteristic length scale of the passive modes (on a logarithmic scale). Each curve stops at the highest-order transverse lasing mode calculated in (e). The modes in (b)-(d) are indicated with arrows.

The existence of high-order transverse modes and their lateral confinement in a stable cavity lead to a sharp drop in the characteristic length scale ξ of the optical intensity variation in the transverse direction. This has a profound impact on the nonlinear interactions between the cavity modes and the gain medium [3, 4]. ξ is given by the full-width at half-maximum of the transverse intensity correlation function. Since ξ varies in the longitudinal direction for $g \neq 1$, we average its value along the cavity axis. Higher-order transverse modes have smaller ξ. In a Fabry-Perot cavity with a GaAs quantum well (gain medium), only low-order transverse modes are confined, and intensity variations on the scale $\xi \gg \lambda$ result in local carrier-induced refractive index changes due to spatial hole burning. Optical lensing and self-focusing effects lead to the formation of spatial filaments, which are inherently unstable and cause irregular pulsations.

In a stable cavity, the ξ of high-order transverse modes can be sufficiently small so local refractive index variations cannot focus light and create a filament. Also the spatial modulation of the refractive index on such short scales supersedes and disrupts the large lenses induced by lower-order transverse modes, thus preventing filamentation. Therefore, an efficient way of reducing the spatio-temporal instability in a broad-area semiconductor quantum well laser is to minimize ξ via a stable cavity [3].

4.2.3 High-Q modes

To maintain a relatively narrow angular spread of the far-field emission, we optimize the stable cavity geometry in the vicinity of the planar cavity. In particular, we maximize the number of transverse lasing modes within the range $0.5 \leq g \leq 1$. Since the lasing modes need to have high Q factors, we calculate the high-Q transverse modes of passive cavities. Because the GaAs quantum well has preferential gain for transverse electric (TE) polarization, we calculate the modes with the electric field in the plane of incidence (p-polarization). The simulated cavities have the same aspect ratio $L/W = \sqrt{2}$ as the experimental ones, but are L = 20 μm long. The refractive index n = 3.37 in the cavity is equal to the effective index of the fundamental TE mode guided in the vertical direction of an GaAs/AlGaAs epiwafer. The wavelength range of numerical simulations is centered around 800 nm, which matches the gain spectrum of the GaAs quantum well.

The fundamental transverse mode has the highest quality factor $Q_{\max}$, which determines the lasing threshold. $Q_{\max}$ depends on the cavity length L and mirror reflectivity. It barely changes with g, thus curving the end facets has little effect on the lasing threshold. However, the Q factors of the high-order transverse modes are greatly improved in a stable cavity with concave mirrors, leading to a drastic increase in the number of lasing modes.

We show the number M_h of transverse modes with $Q > 0.8\,Q_{\max}$ in Fig. 4.2(e). As g decreases from 1, M_h increases rapidly and reaches its maximum at g = 0.7, then decreases. While the sharp rise results from the better lateral confinement of high-order transverse modes, the subsequent drop of M_h is caused by the reduced reflectivity for rays with non-perpendicular incidence. With increasing mirror curvature, the angles of incidence θ_i at the semiconductor-air interface increase, and for TE polarization the reflectivity decreases for θ_i going from 0 towards the Brewster angle [1]. Therefore, the number of high-Q transverse modes is maximal for a near-planar cavity.

4.2.4 Ray-wave correspondence

In the following, we discuss the correspondence between ray trajectory and passive mode in a near-planar cavity. We compare the same transverse mode of order $m = 7$ in cavities with three different stability parameters, in order to evaluate the effect of mirror curvature on the transverse mode profile and the Q factor. The real-space intensity distributions for $g = 0.94, 0.80$ and 0.50 are shown in Figs. 4.3(a, c, e), respectively. With decreasing g (increasing mirror curvature), the transverse mode profile becomes narrower, indicating modes with increasingly high order can be confined in the cavities. However, the Q factor

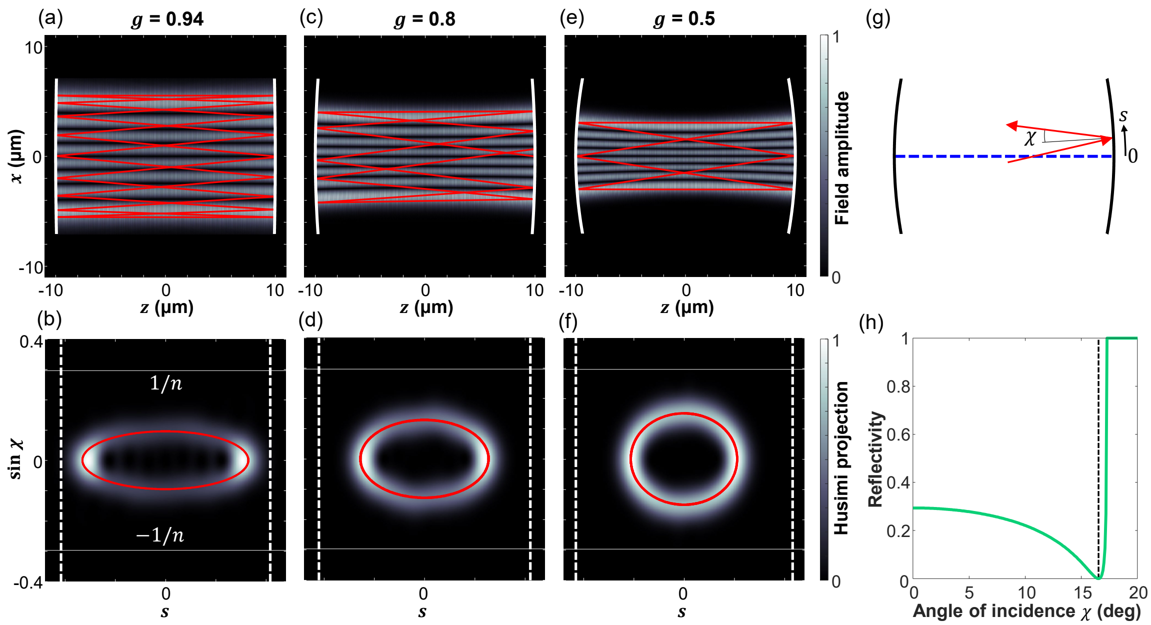

Figure 4.3: **Ray-wave correspondence in a near-planar cavity.** Comparison of transverse modes of order $m = 7$ in $L = 20$ μm long cavities with (a, b) $g = 0.94$, (c, d) $g = 0.8$, and (e, f) $g = 0.5$. (a, c, e) Field intensity profiles in real space with (a) $\lambda = 798.4$ nm and $Q = 420.8$, (c) $\lambda = 799.8$ nm and $Q = 410.8$, and (e) $\lambda = 800.0$ nm and $Q = 399.8$. Exemplary parts of the corresponding trajectories are superimposed as red lines. (b, d, f) Husimi distributions of the modes shown in panels (a, c, e), respectively. The corresponding trajectories in Birkhoff coordinates are superimposed as red points. The vertical white dashed lines indicate the endpoints of the right mirror and the horizontal gray lines indicate the critical angle. (g) Definition of the Birkhoff coordinates: the position s on the right mirror and the angle of incidence χ. The blue dashed line indicates the optical axis ($s = 0$). (h) Reflectivity for p-polarized light at a semiconductor-to-air interface with refractive index contrast 3.37. The vertical dashed lines marks the Brewster angle at $16.5°$.

decreases from $Q = 420.8$ for $g = 0.94$ to $Q = 399.8$ for $g = 0.5$ (cf. Table 4.1). The dependency of the mode width and the Q factor on g can be explained by analyzing the corresponding ray trajectories.

A useful tool for analyzing the ray-wave correspondence in optical microcavities are the so-called Husimi functions [64, 140], which can be considered as a phase-space representation of a mode. They are obtained by calculating the overlap of the wave function with a wave packet of minimal uncertainty with specific position and momentum. Here we use the Husimi function for dielectric resonators introduced in Ref. [64]. The Poincaré surface of section is given in Birkhoff coordinates $(s, \sin\chi)$ as shown in Fig. 4.3(g): s denotes the location of incidence of a ray on the right mirror (normalized by the total circumference of the resonator, s_{t}), where $s = 0$ is at the center of the mirror, and χ is the angle of incidence with respect to the surface normal.

The Husimi functions of the three modes considered here are shown in Figs. 4.3(b, d, f). They have a roughly elliptic structure, where the semi-axes in s direction decrease with increasing g since the modes become narrower. The semiaxes in $\sin\chi$ direction increase, which means that the modes contain wave components with higher angles of incidence. Table 4.1 gives the angles $\chi_{\max}$ at which the maxima in the $s = 0$ section of the Husimi distributions are found. The increase of $\chi_{\max}$ with decreasing g can explain the decline of the Q factors since the reflectivity at the semiconductor-air interface decreases towards the Brewster angle for p-polarization as shown in Fig. 4.3(h).

We calculate the corresponding trajectories by launching rays at the center of the mirror ($s = 0$) with the angles $\chi_{\max}$ given in Table 4.1. Their time evolution for 2000 reflections is computed. The real space and phase space representations of these trajectories are superimposed in red in Figs. 4.3(a-f). Each reflection at the right mirror is indicated as a point in phase space [Figs. 4.3(b, d, f)], though the points are so dense that they appear as a

g	λ (nm)	Q	$\chi_{\max}$ (deg)	$\tau(L/c)$	Q_{ray}
0.94	798.4	420.8	5.5	2.68	421.2
0.80	799.8	410.8	7.4	2.62	411.2
0.50	800.0	399.8	8.7	2.56	402.2

Table 4.1: Properties of the passive cavity modes and corresponding ray trajectories shown in Fig. 4.3 for different stability parameters g. λ and Q are the resonance wavelength and the quality factor, respectively, and $\chi_{\max}$ is the maximal angle of incidence in the Husimi function. τ is the fitted lifetime of the trajectory and Q_{ray} the corresponding quality factor for a $L = 20$ μm long cavity at $\lambda = 800$ nm.

continuous line. The agreement with the Husimi functions is excellent, demonstrating that these are indeed the trajectories on which the modes are based. In real space [Figs. 4.3(a, c, e)], only the first few reflections are shown for better visibility.

The trajectories cover a finite transverse region of the cavity, and the outmost segments of the trajectories coincide with the most intense regions of the wave functions. Furthermore, the maximal angles of incidence χ of the trajectories (at the center of the mirror) increase with decreasing g. The intensity of a trajectory decreases at each reflection according to the Fresnel reflection coefficients for p polarization [cf. Fig. 4.3(h)], leading to an exponential decay in time [5]. The fitted lifetimes τ as well as the corresponding quality factors Q_{ray} for a $L = 20$ μm long cavity are given in Table 4.1 and show excellent agreement with the Q factors of the modes. This demonstrates that refraction at the semiconductor-air interfaces is the dominant loss mechanism responsible for the decrease of the Q factors as the mirror curvature increases. The slightly smaller Q factors of the modes can be attributed to diffraction losses not considered in the ray tracing simulations.

Therefore, maximizing the number of transverse lasing modes requires balancing two effects. On one hand, increasing the mirror curvature reduces the width of the modes so transverse modes of higher order can fit into the cavity laterally. This leads to the strong increase of the number of lasing modes when transitioning from a Fabry-Perot cavity with $g = 1$ to a stable cavity with $g < 1$. On the other hand, the refractive losses for high-order modes of p-polarization grow with the mirror curvature, leading to an increase of the lasing threshold. Both effects are intuitively explained by the corresponding ray trajectories as shown above. It should furthermore be noted that the optimal stability parameter g depends both on the aspect ratio W/L of the cavity and the refractive index.

4.3 Laser testing

We test the near-planar cavity lasers fabricated with the process in Section 3.4. The optical measurement setup is described in Section 3.5.1. An exemplary LI curve of a laser diode with $g = 0.88$ is shown in Fig. 4.4(a). The typical lasing threshold current is about 500 mA. The threshold current densities, averaged for multiple cavities of g = 0.74, 0.88, and 1, are $(0.52 \pm 0.02)\ \mathrm{kA/cm^2}$, $(0.52 \pm 0.03)\ \mathrm{kA/cm^2}$, and $(0.49 \pm 0.03)\ \mathrm{kA/cm^2}$, respectively. Therefore, no significant difference in the lasing threshold current density is found for different cavity shapes. The optical spectrum of the lasing emission is centered at 799 nm [Fig. 4.4(b)]. The spectral width is about 1 nm, with individual lasing peaks so densely packed that they cannot be resolved by our spectrometer.

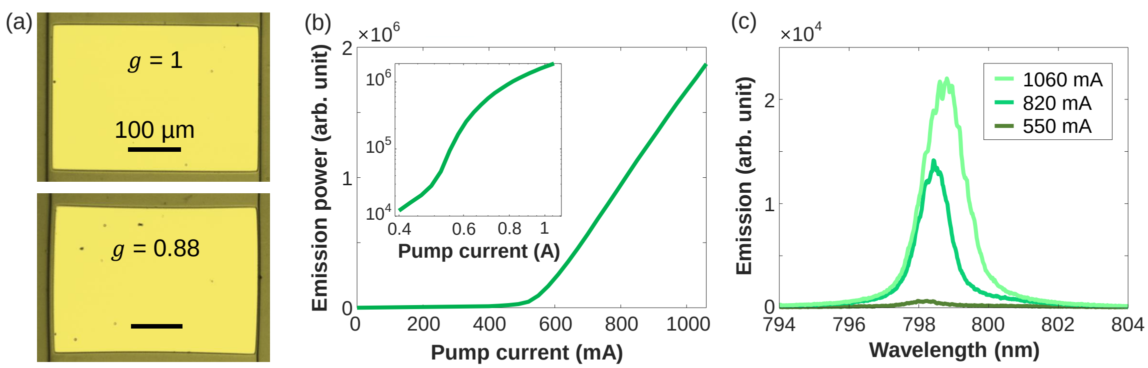

Figure 4.4: **Testing of near-planar cavity lasers.** (a) Optical microscope images of cavities (top-view) with $g = 1$ and $g = 0.88$, showing a tiny difference in the mirror curvature. (b) The LI curve of a near-planar ($g = 0.88$) cavity laser shows a clear threshold at the pump current of 500 mA. Inset: the LI curve in logarithmic scale featuring the S-shape that is typical for lasers. (c) Optical spectra of lasing emission of the cavity in (b) at pump currents just above, 1.5 times, and 2 times the lasing threshold. Increasing the injection current above the threshold broadens the lasing spectrum.

4.4 Highly multimode lasing

4.4.1 Number of transverse lasing modes

We measure the number of transverse lasing modes in cavities of different g. The setup described in Section 3.5.3 was used. The laser emission passes through a diffuser and creates a speckle pattern in the far field. The number of transverse lasing modes M_l is estimated as $1/C^2$, where C is the speckle intensity contrast [1, 96, 109]. Because the edge emission from the laser contains multiple transverse modes in the horizontal direction and a single guided mode in the vertical direction (perpendicular to the wafer), a line diffuser (RPC Photonics, EDL-20) is used and the far-field speckle intensity variation in the horizontal direction is recorded, as shown in Fig. 4.5(a).

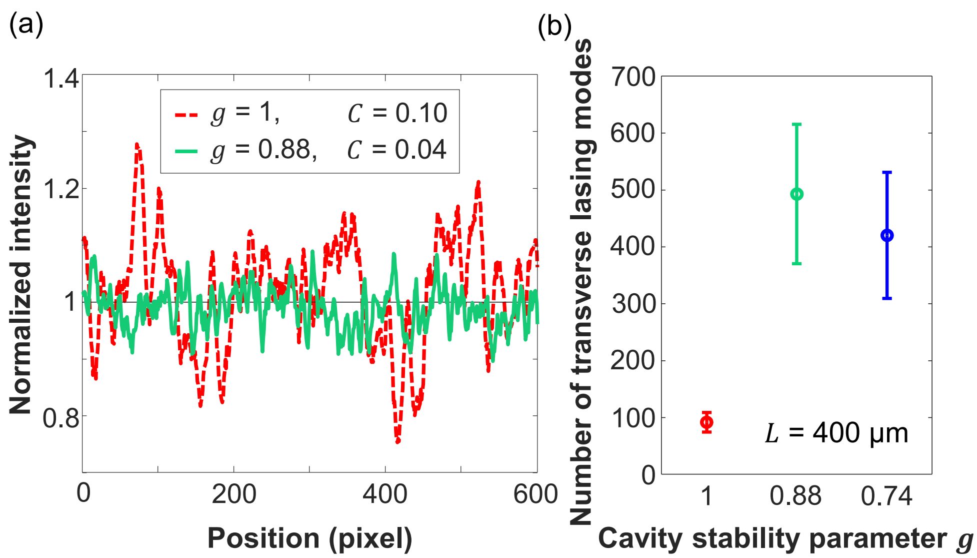

Figure 4.5: **Number of transverse lasing modes in near-planar cavities.** (a) Measured intensity fluctuations of far-field speckles created by a line diffuser illuminated with laser emission from planar (red dashed) and near-planar (green solid) cavities. The speckle contrast C is reduced from 0.1 at $g = 1$ to 0.04 at $g = 0.88$. (b) Number of transverse lasing modes M_l, estimated from C, at two times of the lasing threshold. All laser cavities have length L = 400 μm (20 times longer than the simulated cavities in Fig. 4.2). M_l increases sharply as g decreases from 1. The error bars denote variations among multiple fabricated devices of the same geometry g.

The speckle intensity contrast C decreases with decreasing g, indicating an increase in the number of transverse lasing modes M_l. For g = 1, the number of transverse lasing modes, averaged over multiple devices, is approximately 100. Once g is reduced slightly to 0.88, M_l is enhanced 5 times to about 500. Such rapid increase of M_l is consistent with the numerical simulation in Fig. 4.2(e). Further reducing $g = 0.74$ does not increase M_l any more, in contrast to the numerical results in Fig. 4.2(e). We attribute this difference to the spatially inhomogeneous current injection in our devices, which modifies the number of transverse lasing modes M_l (See Section 4.4.3). With spatially homogeneous pumping, we expect M_l to be higher, particularly for $g = 0.74$. We also note that the number of transverse lasing modes in the near-planar cavities is close to the previously reported value for a near-concentric ($g = -0.74$) cavity [1]. Therefore, even minimal curvature of the end facets is sufficient to obtain a large number of transverse lasing modes and reduce the spatial coherence.

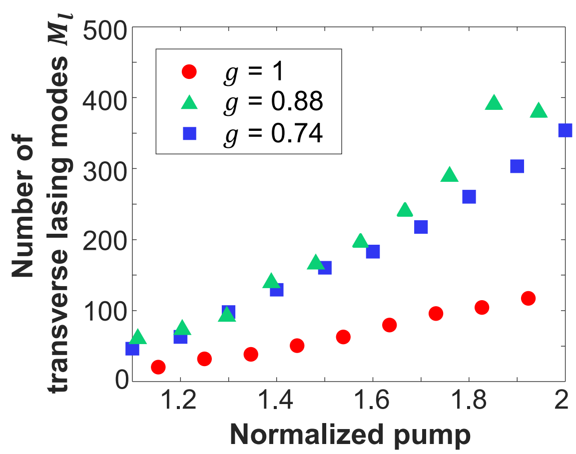

Figure 4.6: **Modal behavior of near-planar cavity lasers.** The number of transverse lasing modes M_l in the planar ($g = 1$) and near-planar ($g = 0.74, 0.88$) cavities increases with the pump level. For each cavity, the pump current is normalized by the lasing threshold.

We also characterize the number of transverse lasing modes with respect to different pump current. Figure 4.6 shows the measured number of transverse lasing modes M_l as we gradually increase the injection current up to two times of the lasing threshold. For all cavity shapes, M_l increases with the pump strength, as more high-order transverse modes manage to lase. The near-planar cavities (g =0.74, 0.88) have larger M_l than the planar cavity ($g = 1$) over the entire range of pump current measured.

Regarding the measurement of spatial coherence, we comment on the beam parameter product, the product of the beam waist size and the far field angular spread of partially coherent light. While the low spatial coherence corresponds to a large beam parameter product, a large beam parameter product does not necessarily mean low spatial coherence. For example, a spatially coherent beam passing through an optical diffuser will spread in the far-field, making the beam parameter product large, even though the fields at all spatial locations remain coherent according to the mutual coherence function. Therefore, the beam parameter product is larger or equal to a minimal value given by the degree of spatial coherence. That is why we use the speckle intensity contrast, instead of the beam parameter product, to characterize the degree of spatial coherence of our laser emission.

4.4.2 Divergence of far-field emission

As more transverse modes lase, the divergence angle of the total emission increases. We measure the far-field emission pattern $I(\theta)$ in the horizontal direction, as shown in Fig. 4.7. The measurement setup is described in Section 3.5.2.

The filaments in a planar cavity of $g = 1$ makes $I(\theta)$ asymmetric and irregular [Fig. 4.7(a)]. Since the measured far-field emission intensity fluctuates with the far-field angle, we smooth out the intensity profile by a moving average over $5°$. The divergence angle $\Delta\theta$ is estimated by the full-width at half-maximum of the smoothed distribution of $I(\theta)$, and it equals 12°. With curved end facets, $\Delta\theta$ increases to 29° for $g = 0.88$ [Fig. 4.7(b)], and further to 39° for $g = 0.74$ [Fig. 4.7(c)]. We note that the measured far-field emission patterns are narrower than the simulated ones due to spatial inhomogeneity of current injection (See Section 4.4.3). While the increase of lateral divergence angle in the near-planar cavities

[Fig. 4.7(d)] is expected, the emission directionality is significantly improved compared to the near-concentric cavity with $g = -0.74$ and $\Delta\theta = 70°$ in Section 3.5.2. Moreover, the lateral divergence of emission from the near-planar cavity is comparable to the vertical divergence of the edge emitting laser. Therefore, the output beam is approximately circular and thus compatible with standard collection optics.

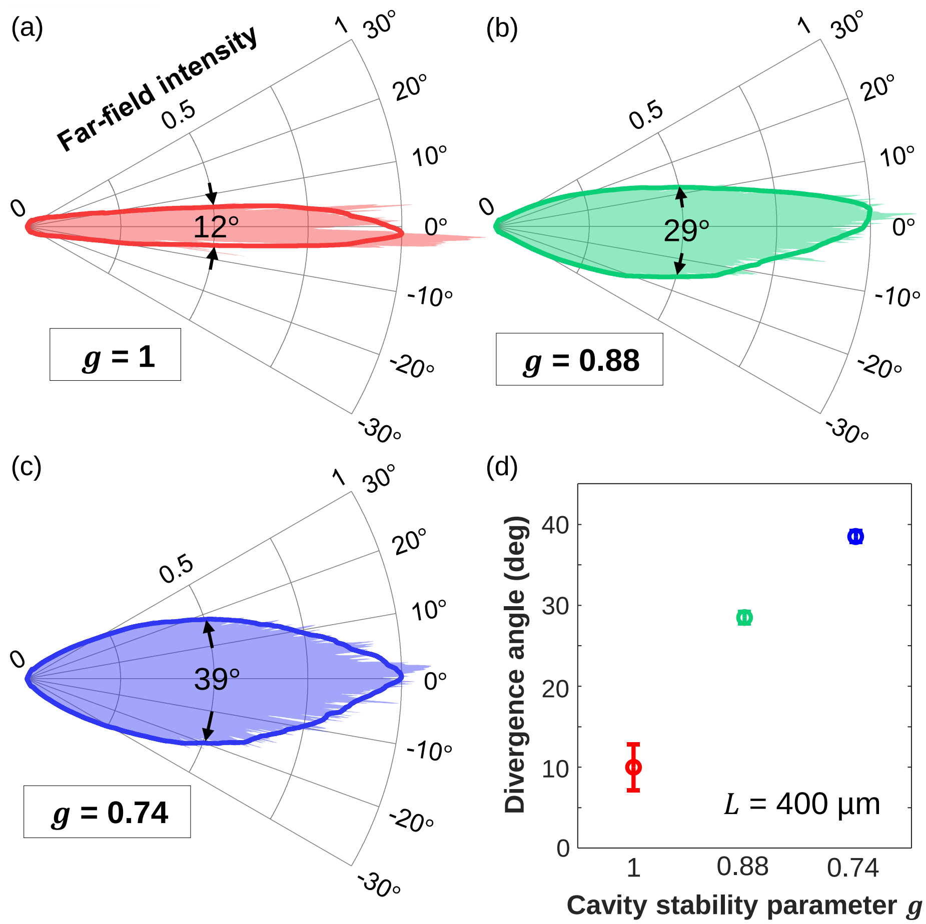

Figure 4.7: **Emission directionality of near-planar cavity lasers.** (a-c) Measured far-field emission patterns $I(\theta)$ from cavities of (a) g = 1, (b) 0.88, and (c) 0.74. The shaded area represents the measured intensity profile, and the solid line denotes the smoothed profile with the maximal value normalized to 1. The angular full-width at half maximum $\Delta\theta$ is indicated by arrows. (d) Divergence angles $\Delta\theta$ as function of g. All cavities have the same dimensions as those in Fig. 4.5. The error bars denote variations among different cavities with the same g.

Additionally, we characterize the divergence angle by the second-moment width, so-called D4σ width, defined by 4 times the standard deviation of the intensity distribution. For cavities of g = 1, 0.88, and 0.74, the D4σ full divergence angle of the far-field patterns are 37°, 56°, and 69°, respectively.

4.4.3 Spatially nonuniform pumping

In Fig. 4.5, a similar number of transverse lasing modes M_l were observed for $g = 0.88$ and $g = 0.74$. This experimental result deviates from the simulation which predicts a larger M_l for $g = 0.74$ in Fig. 4.2(e). The numerical simulation assumes spatially uniform pump. Experimentally, the current injection through the top contact may be nonuniform, which will modify M_l. To resolve the discrepancy of M_l, we investigate spatially nonuniform pumping in this section.

Spatial mapping of current injection

To map the spatial profile of current injection, we measure the emission intensity distribution on the cavity facet at a pumping level well below the lasing threshold. The spontaneous emission dominates over the stimulated emission, and its spatial profile directly reflects the current distribution. Figure 4.8(a) shows the near-field emission patterns for g = 1, 0.88 and 0.74. The emission spectra do not change with the pump current, confirming that stimulated emission is negligible. In all three cavities, the spontaneous emission is stronger in the center, reflecting larger current density there than close to the boundaries.

Number of transverse lasing modes

To analyze how the spatially nonuniform pumping affects lasing, we use the SPA-SALT (single-pole approximation steady-state *ab-initio* theory) [60, 87, 88] to calculate the number of lasing modes and the modal intensities. Simulating the experimental cavities of

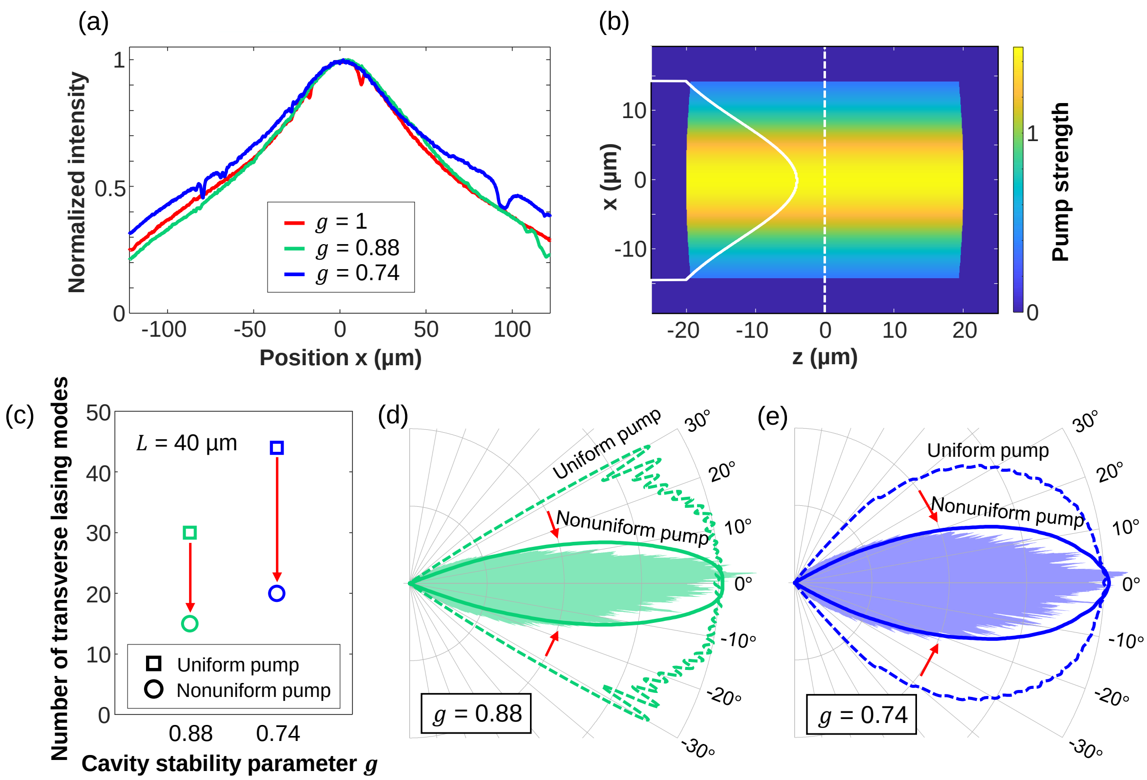

Figure 4.8: **Spatially nonuniform pumping.** (a) At the pumping level of 0.4 times of the lasing threshold, the spontaneous emission dominates. Its nonuniform intensity distribution at the cavity facet reflects the nonuniform current density profile. Each curve is averaged over 5 cavities of the same geometry g. The field of view covers 90% of the entire facet. (b) Simulated spatial profile of pump strength, which varies only in the transverse direction (x). The cross-section of the pump is shown as white line. The cavity length L is 40 μm and the width W is $L/\sqrt{2}$ = 28.3 μm. (c) The number of transverse lasing modes, calculated by SPA-SALT, for spatially uniform pumping (square) and nonuniform pumping (circle). The red arrows mark the drop in the number of transverse lasing modes due to spatially nonuniform pumping. (d, e) Narrowing of the far-field intensity profiles caused by spatially nonuniform pumping in near-planar cavities of (d) $g = 0.88$ and (e) $g = 0.74$. The shaded area indicates the experimentally measured far-field pattern in Fig. 4.7, and the solid line represents the smoothed profile.

length L = 400 μm and width W = 283 μm is computationally demanding. Therefore we reduce the cavity dimension to L = 40.0 μm and W = 28.3 μm, but keep the aspect ratio $L/W = \sqrt{2}$.

With spatially uniform pumping, the number of transverse lasing modes at a pumping level of two times the lasing threshold are 44 and 30 [squares in Fig. 4.8(c)] for $g = 0.74$ and $g = 0.88$, respectively. We note that these numbers are twice of those in Fig. 4.2(e) for cavities of half the size, L = 20 μm. Thus, the number of transverse lasing modes increases linearly with the cavity size.

Here we apply the spatially nonuniform pumping in the transverse direction. As shown in Fig. 4.8(a), the pump strength is maximal at the center and decays towards the lateral boundaries. The transverse pump profile in simulations [Fig. 4.8(b)] is approximated by a Gaussian function with its full width at half maximum of 19.8 μm, which is 0.7 times the cavity width W. Such a profile promotes lasing in the lower order transverse modes which are concentrated in the center and have larger overlap with the pump than the higher order transverse modes. As the lower order modes lase efficiently and saturate the optical gain, it is harder for higher-order modes to lase. Consequently, the number of transverse lasing modes M_l decreases [circles in Fig. 4.8(c)].

The reduction in the number of transverse lasing modes is larger for $g = 0.74$ than $g = 0.88$. This is attributed to the different strength of lateral confinement of lasing modes, which affects their competition for gain. The $g = 0.74$ cavity has stronger lateral confinement and supports a larger number of transverse modes than $g = 0.88$. The transverse nonuniform pumping further enhances the mode competition, as the low-order transverse modes become dominant and more effectively prevent the high-order transverse modes from lasing. This effect is more severe in $g = 0.74$, which has a larger number of high-order transverse modes and tighter lateral confinement than $g = 0.88$. It leads to a larger decrease of the number of transverse lasing modes for $g = 0.74$. As a result, the number of transverse lasing modes of $g = 0.74$ becomes more similar to that of $g = 0.88$.

Far-field divergence

The far-field emission patterns are also affected by the spatially nonuniform pumping. As low-order transverse modes start to dominate lasing, the divergence of far-field emission becomes narrower. We calculate the far-field intensity patterns for near-planar cavities with L = 40 μm. Figures 4.8(d) and (e) show narrowing of the far-field emission once the pump becomes spatially nonuniform. The divergence angle (full width at half maximum) drops from 63° to 29° for g = 0.88, and from 82° to 40° for g = 0.74.

4.5 Spatio-temporal dynamics

Next we investigate the lasing dynamics of near-planar cavities and compare to the planar cavity. The emission intensity on one facet of the cavity is imaged by a $\times$20 objective lens onto the entrance slit of a streak camera (Hamamatsu C5680 with a fast sweep unit M5676). A single streak image covers a time window of 10 ns with a temporal resolution of about 30 ps. Figure 4.9(a) shows exemplary spatio-temporal intensity fluctuations of the laser emission from a planar cavity of $g = 1$. Such fluctuations comprise three different processes: (i) spatial filaments and their pulsations; (ii) spatio-temporal interference of transverse and longitudinal lasing modes; (iii) photo-detection noise of the streak camera. To separate the three fluctuation processes, we resort to the fact that they feature distinct spatial and temporal scales.

4.5.1 Separation of different fluctuations

We use the method developed in Section 2.3.5, which is described here again for the completeness of this chapter. After normalizing the measured intensity $I(x,t)$ by the average

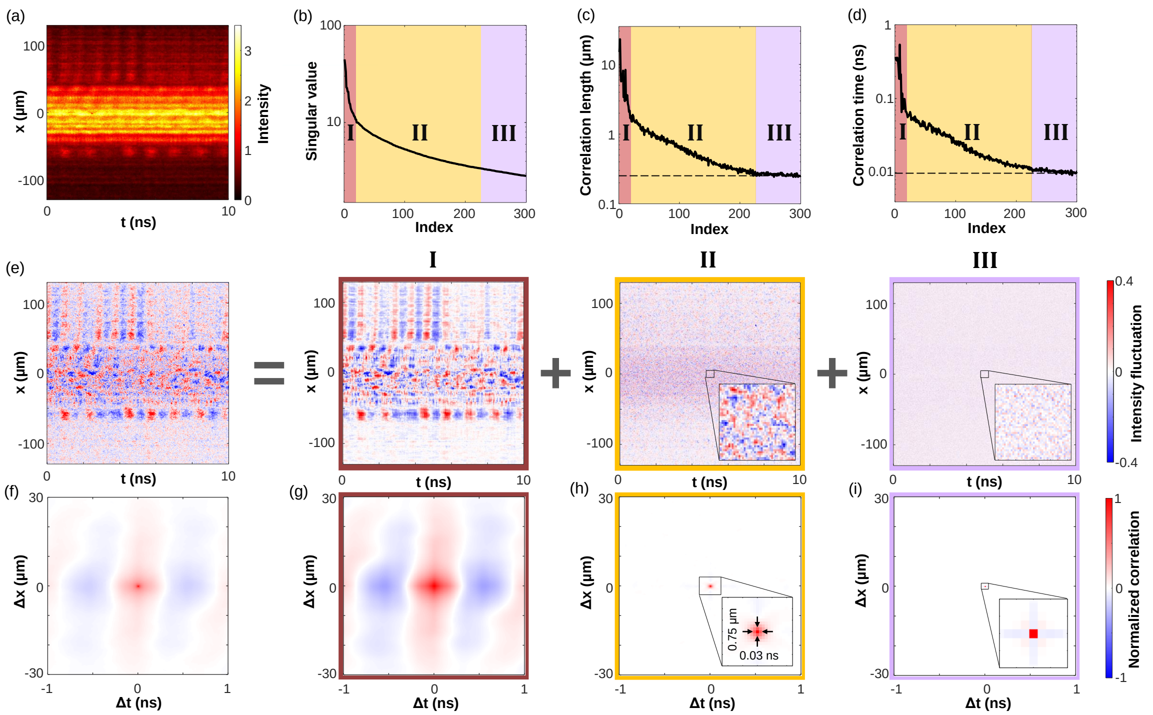

Figure 4.9: **Separating spatio-temporal intensity fluctuations of different origin by singular value decomposition (SVD).** (a) Streak image of emission intensity $I(x,t)$ on one facet of a Fabry-Perot cavity ($g = 1$). The pump current is two times the lasing threshold. (b) Singular values obtained by SVD of intensity fluctuations $\delta I(x,t) = I(x,t) - \langle I(x,t)\rangle_t$. (c) Correlation lengths and (d) correlation times of singular vectors. The horizontal dashed lines denote the size of a single pixel in space and time of the streak image. The singular vectors are categorized into three groups I, II, and III, which are marked by red, yellow and purple, respectively. (e) $\delta I(x,t)$ is the sum of intensity fluctuations caused by (I) filaments, (II) mode beating, and (III) detection noise. (f) The spatio-temporal correlation function of $\delta I(x,t)$ features both short- and long-range correlations. (g-i) Spatio-temporal correlation functions of intensity fluctuation for (g) group I (h) II, and (i) III, exhibiting distinct correlation scales in space and time. Insets: close-up around the origin. The numbers in (h) are the spatial and temporal correlation widths.

$\langle I(x,t)\rangle_{x,t}$, we conduct the singular value decomposition (SVD) of the intensity fluctuation $\delta I(x,t) = I(x,t) - \langle I(x,t)\rangle_t$:

$$\delta I(x,t) = \sum_{\alpha} s_\alpha u_\alpha(x) v_\alpha(t) \tag{4.1}$$

where s_α are singular values, $u_\alpha(x)$ and $v_\alpha(t)$ are the spatial and temporal singular vectors, respectively, and α denotes the index. The singular values s_α are arranged from high to low, and they represent the contributions of the α-th singular vector to the intensity fluctuation $\delta I(x,t)$. As shown in Fig. 4.9(b), s_α first drops sharply with increasing α, then decays more slowly for $\alpha > 20$. Hence, the first few singular vectors with large singular values dominate $\delta I(x,t)$.

To distinguish the singular vectors, we analyze their characteristic spatial and temporal scales. The correlation functions of $u_\alpha(x)$ and $v_\alpha(t)$ are defined as

$$\begin{aligned} C_\alpha(\Delta x) &= \langle u_\alpha(x) u_\alpha(x+\Delta x)\rangle_x \\ C_\alpha(\Delta t) &= \langle v_\alpha(t) v_\alpha(t+\Delta t)\rangle_t. \end{aligned} \tag{4.2}$$

The correlation length l_α is extracted from the full-width at half-maximum of $C_\alpha(\Delta x)$, and the correlation time τ_α from $C_\alpha(\Delta t)$. As shown in Figs. 4.9(c) and (d), both l_α and τ_α decrease rapidly with increasing α, till α reaches 20. Then they switch to a more gradual decay and eventually level off. When α exceeds 220, both spatial and temporal correlation scales are equal to the single pixel size of the streak image.

Since s_α, l_α and τ_α exhibit similar dependency on α, we separate the singular vectors into three groups, denoted as I, II, and III in Figs. 4.9(b)-(d). Then the spatio-temporal intensity fluctuation of each group is reconstructed by

$$\delta I_{\mathrm{R}}(x,t) = \sum_{\alpha\in\mathrm{R}} s_\alpha u_\alpha(x) v_\alpha(t) \tag{4.3}$$

where R is one of the three groups I, II, and III. The total intensity fluctuation is $\delta I(x,t) = \delta I_{\rm I}(x,t) + \delta I_{\rm II}(x,t) + \delta I_{\rm III}(x,t)$. In Fig. 4.9(e), $\delta I_{\rm I}(x,t)$, $\delta I_{\rm II}(x,t)$, and $\delta I_{\rm III}(x,t)$ display different spatial and temporal scales. To quantify the difference, we compute the spatio-temporal correlation function for each group,

$$C_{\rm R}(\Delta x, \Delta t) = \langle \delta I_{\rm R}(x,t) \delta I_{\rm R}(x+\Delta x, t+\Delta t)\rangle_{x,t}. \tag{4.4}$$

The spatial and temporal widths of $C_{\rm R}(\Delta x, \Delta t)$ give the correlation lengths and times for every group.

The first group $\delta I_{\rm I}(x,t)$ features strong intensity fluctuations on length scales from several to tens of micrometers, and a time scale of the order of 0.1 nanoseconds. Such scales are consistent with the typical size of spatial filaments and their oscillation frequencies. $C_{\rm I}(\Delta x, \Delta t)$ in Fig. 4.9(g) reveals long-range spatio-temporal correlations as a result of filament motion and pulsation.

The second group $\delta I_{\rm II}(x,t)$ features fluctuations on much shorter spatial and temporal scales. As seen in Fig. 4.9(e), $\delta I_{\rm II}(x,t)$ is stronger in the middle of the cavity (around x = 0), where the original emission intensity $I(x,t)$ in Fig. 4.9(a) is stronger. It implies that the group II also originates from the laser emission, more precisely, from the spatio-temporal interference of all lasing modes. $C_{\rm II}(\Delta x, \Delta t)$ in Fig. 4.9(h) exhibits only local correlations of the intensity fluctuations. Both the correlation length of 0.75 μm and correlation time of 0.03 ns are limited by the resolution of our photodetection.

For the third group, $\delta I_{\rm III}(x,t)$ is uniformly spread over the entire range of the streak image. It indicates the fluctuation is not due to the laser emission, but from the noise generated by the imaging apparatus. This is confirmed by $C_{\rm III}(\Delta x, \Delta t)$ in Fig. 4.9(i), which shows the spatio-temporal correlation scales equal to the pixel size of the image. Therefore, $\delta I_{\rm III}(x,t)$ represents the detection noise that fluctuates on the scale of a single pixel.

4.5.2 Spatiotemporal instabilities

The SVD can efficiently separate intensity fluctuations of different scales and origins. In the example of Fig. 4.9, the three groups contain singular vectors with consecutive indices α. In general, the singular vectors in each group have similar correlation scales, but not necessarily adjacent indices. Below we elaborate on the separation procedure based on distinct spatial and temporal scales of these fluctuations.

We first acquire an ensemble of spatio-temporal intensity distributions from the same laser cavity. Within a 2-μs-long pump current pulse, we measure 161 consecutive 10 ns-long streak camera images, which constitute a 1.61 μs-long total time window. The transient regime at the beginning of the current pulse is excluded. We denote the intensity fluctuations $\delta I^{(i)}(x,t)$ with the superscript $i = 1, ..., 161$ to indicate a series of streak camera images acquired at 161 measurement start times $t^{(i)}$. The difference between consecutive start times $t^{(i+1)} - t^{(i)}$ is 10 ns, equal to the duration of the individual streak images. The SVD of $\delta I^{(i)}(x,t)$ yields the singular values $s_\alpha^{(i)}$ and the spatial and temporal singular vectors $u_\alpha^{(i)}(x)$ and $v_\alpha^{(i)}(t)$, where α is the SVD index.

The characteristic length scales of the spatial and temporal singular vectors are given by the full-width at half-maximum (FWHM) of the correlation function given in Eq. 4.2. Figure 4.10 is a scatter plot of the correlation length $l_\alpha^{(i)}$ vs. the correlation time $\tau_\alpha^{(i)}$ of every singular vector of index α in the time window $t^{(i)}$. The gray line denotes the averaged correlation time at a fixed correlation length. For all cavity geometries, these lines exhibit a sharp change in slope. In order to define this transition, linear fitting is applied to find its exact position, which gives the critical correlation time τ_c. Typical τ_c is between 70 ps and 80 ps, and there is no systematic dependence of τ_c on the cavity geometry g. Group I includes all singular vectors with correlation times exceeding τ_c [on

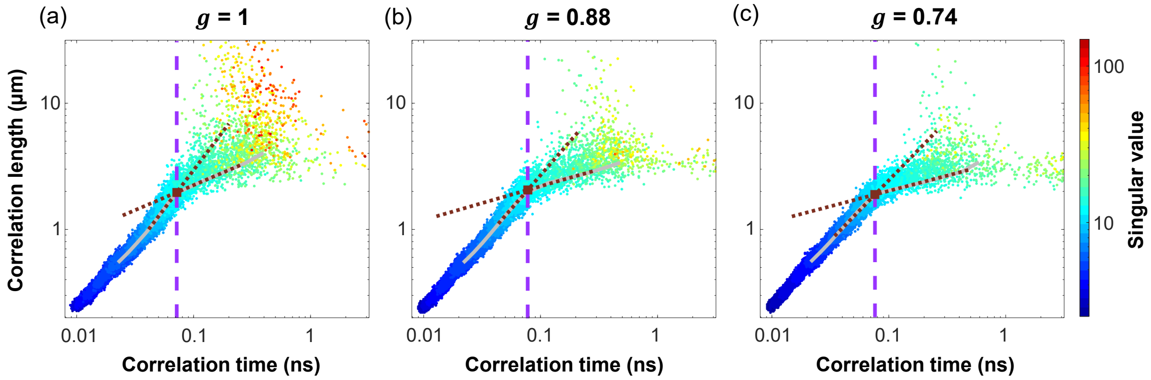

Figure 4.10: **Spatial and temporal correlation scales of singular vectors.** Scatter plot of correlation length versus correlation time for all singular vectors in 161 time windows for the three cavity geometries (a) $g = 1$, (b) $g = 0.88$, and (c) $g = 0.74$. The color of each data point reflects the magnitude of the singular value. The gray solid lines represent the average of all correlation times with the same correlation length. A linear fit (brown dotted lines) defines the correlation time (vertical dashed purple line) at which the slope of the gray line changes suddenly. It separates group I, singular vectors due to filaments, from groups II and III.

the right side of the dashed purple line in Fig. 4.10]. For the i-th time window, the group I of singular vectors is given by:

$$\mathrm{I}^{(i)} := \{\alpha | \tau_{\alpha}^{(i)} > \tau_c\}. \tag{4.5}$$

The spatio-temporal intensity fluctuation $\delta I_{\mathrm{I}}^{(i)}(x,t)$ caused by filaments is reconstructed by summing the singular vectors in group I,

$$\delta I_{\mathrm{I}}^{(i)}(x,t) = \sum_{\alpha \in \mathrm{I}^{(i)}} s_{\alpha}^{(i)} u_{\alpha}^{(i)}(x) v_{\alpha}^{(i)}(t). \tag{4.6}$$

4.5.3 Relative intensity fluctuation

Figure 4.10 shows the magnitude of singular values by color. The planar cavity $g = 1$ has a larger number of singular vectors with higher singular values. Here the singular value represents the fluctuation power carried by the corresponding spatio-temporal singular vector, as described below.

The SVD of the spatio-temporal intensity fluctuation $\delta I(x,t)$, of dimension $N_x \times N_t$, is given by [the superscript (i) is dropped for simplicity],

$$\delta I(x,t) = \sum_{\alpha} s_\alpha u_\alpha(x) v_\alpha(t), \tag{4.7}$$

where s_α is the singular value with index α, u_α is the coresponding spatial singular vector, and v_α the temporal singular vector. The singular vectors are ortho-normal:

$$\langle u_\alpha(x) u_\beta(x) \rangle_x = \delta_{\alpha\beta}/N_x \tag{4.8}$$

$$\langle v_\alpha(t) v_\beta(t) \rangle_t = \delta_{\alpha\beta}/N_t \tag{4.9}$$

where $\delta_{\alpha\beta}$ is the Kronecker delta. The fluctuation power of the spatio-temporal intensity is given by the variance of the intensity fluctuation $\langle \delta I(x,t)^2 \rangle_{x,t}$, where the average fluctuation $\langle \delta I(x,t) \rangle_{x,t} = 0$. Using the definition of SVD in Equation (4.7), the fluctuation power is

$$\begin{aligned} \langle \delta I(x,t)^2 \rangle_{x.t} &= \langle \{ \sum_{\alpha} s_\alpha u_\alpha(x) v_\alpha(t) \}^2 \rangle_{x,t} \\ &= \sum_{\alpha,\beta} \langle s_\alpha u_\alpha(x) v_\alpha(t) s_\beta u_\beta(x) v_\beta(t) \rangle_{x,t} \\ &= \sum_{\alpha,\beta} s_\alpha s_\beta \langle u_\alpha(x) u_\beta(x) \rangle_x \langle v_\alpha(t) v_\beta(t) \rangle_t. \end{aligned} \tag{4.10}$$

Using the orthonormality of the singular vectors [Equations (4.8) and (4.9)],

$$\begin{aligned} \langle \delta I(x,t)^2 \rangle_{x.t} &= \frac{1}{N_x N_t} \sum_{\alpha,\beta} s_\alpha s_\beta \delta_{\alpha\beta} \\ &= \frac{1}{N_x N_t} \sum_{\alpha} s_\alpha^2 \end{aligned} \tag{4.11}$$

where N_x and N_t are the total numbers of spatial and temporal sampling points in a streak image. This result shows that the singular value squared s_α^2 represents the contribution of the α-th singular vector to the spatio-temporal intensity fluctuation.

The fluctuating power $S^{(i)}$, carried by the filaments $\delta I_{\mathrm{I}}^{(i)}(x,t)$ in a time window i, can be written as

$$S^{(i)} = \langle \{\delta I_{\mathrm{I}}^{(i)}(x,t)\}^2 \rangle_{x,t} = \frac{1}{N_x N_t} \sum_{\alpha \in \mathrm{I}^{(i)}} [s_\alpha^{(i)}]^2, \tag{4.12}$$

This relation indicates that the intensity fluctuation caused by filaments can be described by summing over the square of singular values belonging to group I. The fluctuation amplitude p is hence defined as

$$p = \sqrt{\langle S^{(i)} \rangle_i}, \tag{4.13}$$

where $\langle \cdot \rangle_i$ is the average over different time windows.

Using this method, we investigate the spatio-temporal lasing dynamics in the near-planar cavities. Figures 4.11(b) and (c) are the scatter plots of spatial and temporal correlation scales for g = 0.88 and 0.74. Compared to $g = 1$ [Fig. 4.11(a)], the singular vectors with correlation lengths exceeding 10 μm are notably fewer, indicating slight curving of the end facets leads to a reduction of filamentation.

Figure 4.11(d) compares p for different cavity shapes. We average over 5 fabricated lasers for each g, and the error bars reflect the device-to-device variation. The mean fluctuation amplitude p for g = 0.74 is about half of that for $g = 1$. Therefore, the spatio-temporal dynamics becomes much more stable in the near-planar cavity lasers.

4.5.4 RF spectrum

We compute the radio-frequency (RF) spectrum of the intensity fluctuations caused by filaments. The spatially-resolved RF spectrum, shown in Figs. 5(e)-(g) of main text, is

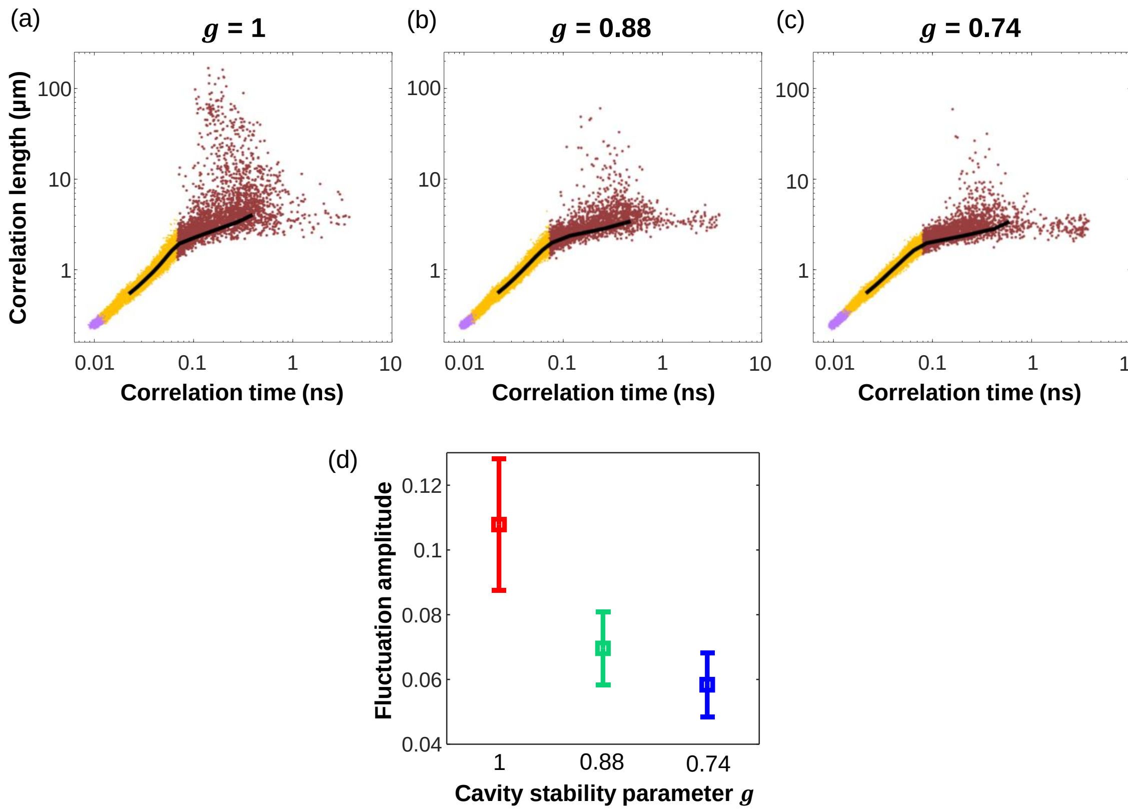

Figure 4.11: **Spatio-temporal dynamics of near-planar cavity lasers.** (a-c) Scatter plots of correlation lengths and times for all singular vectors of intensity fluctuations in laser cavities with (a) g = 1, (b) 0.88, and (c) 0.74. The black line denotes the average correlation time at a fixed correlation length, and its slope changes suddenly at the correlation time of 0.07 ns. The three groups of singular vectors with different origin are marked by (I) red, (II) yellow and (III) purple, respectively. (d) The amplitude of spatio-temporal intensity fluctuations caused by filaments (group I). The error bars denote variations among 5 fabricated cavities of the same g.

given by,

$$P(x, f) = \langle |\mathcal{F}\{\delta I_{\mathrm{I}}^{(i)}(x,t)\}|^2 \rangle_i \tag{4.14}$$

where $\mathcal{F}$ is the Fourier transform in time. We emphasize that the averaged intensity $\langle I^{(i)}(x,t)\rangle_{x,t}$ is normalized to 1 for all cavities in order to compare the RF power. In Fig. 4.12(a), $P(x, f)$ for g = 1 displays strong oscillations at a few GHz. Such oscillations become much weaker for g = 0.88 and 0.74 in Figs. 4.12(c) and (d).

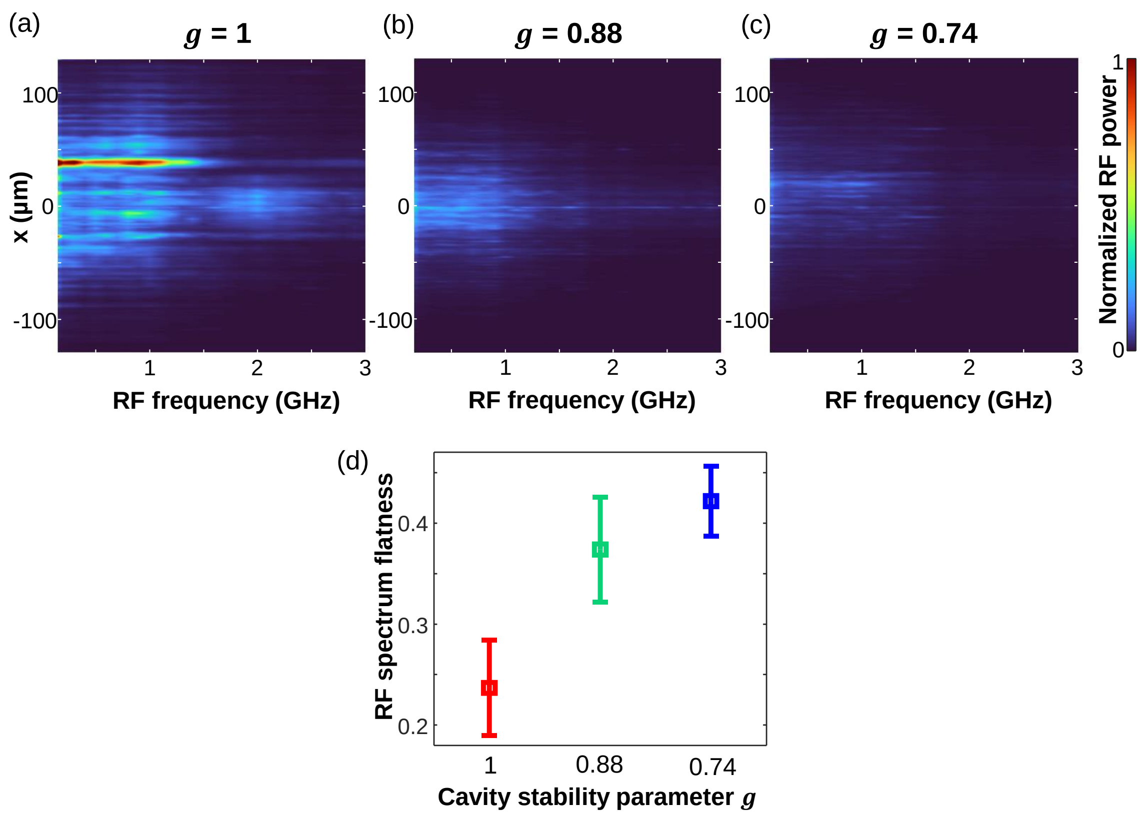

Figure 4.12: **RF spectrum of near-planar cavity lasers.** (a-c) Spatially resolved RF spectra for (a) g = 1, (b) 0.88, and (c) 0.74, showing a clear reduction of oscillatory power as g decreases. (d) Flatness of the spatially-averaged RF spectrum for group I. The increase in flatness indicates the suppression of RF peaks corresponding to intensity oscillations.

Suppression of intensity oscillations implies the RF spectrum has fewer features. To quantify the shape of the RF spectrum, we calculate the spectral flatness. We spatially integrate the RF spectrum $\langle P(x, f)\rangle_x$. The RF spectrum flatness F_s is defined by the geometric mean divided by the arithmetic mean in a frequency domain,

$$F_s = \frac{\exp\left\{\langle \ln[\langle P(x,f)\rangle_x]\rangle_f\right\}}{\langle P(x,f)\rangle_{x,f}}. \tag{4.15}$$

As the filament-induced intensity fluctuations are on the order of a few GHz, the flatness is computed within the frequency range up to 10 GHz. Figure 4.12(d) shows the flatness of RF spectra integrated spatially and averaged over 5 cavities for each g. Its value increases by a factor of 2 in the near-planar cavities, confirming the suppression of temporal intensity oscillations of the laser emission.

4.5.5 Spatio-temporal correlations

Lastly, we compare the spatio-temporal correlations of the laser emission intensity for different cavity shapes. The spatio-temporal correlation of laser intensity fluctuations caused by filaments (group I) is defined by,

$$\begin{aligned} C_{\mathrm{I}}(\Delta x, \Delta t) &= \langle C_{\mathrm{I}}^{(i)}(\Delta x, \Delta t)\rangle_i \\ &= \langle \delta I_{\mathrm{I}}^{(i)}(x,t)\delta I_{\mathrm{I}}^{(i)}(x+\Delta x, t+\Delta t)\rangle_{x,t,i}. \end{aligned} \tag{4.16}$$

It is peaked at the origin $\Delta x = 0$, $\Delta t = 0$. This peak represents the local correlations of intensity fluctuations, and its width gives the characteristic scale of the filaments. Beyond this peak are the nonlocal spatio-temporal correlations introduced by transverse movement and temporal pulsation of filaments [19].

Short-range correlations

Figure 4.13(a) shows the spatial correlation function $C_{\mathrm{I}}(\Delta x, 0)$ for different cavity geometries. Its FWHM gives the correlation length. The planar cavity ($g = 1$) has a correlation

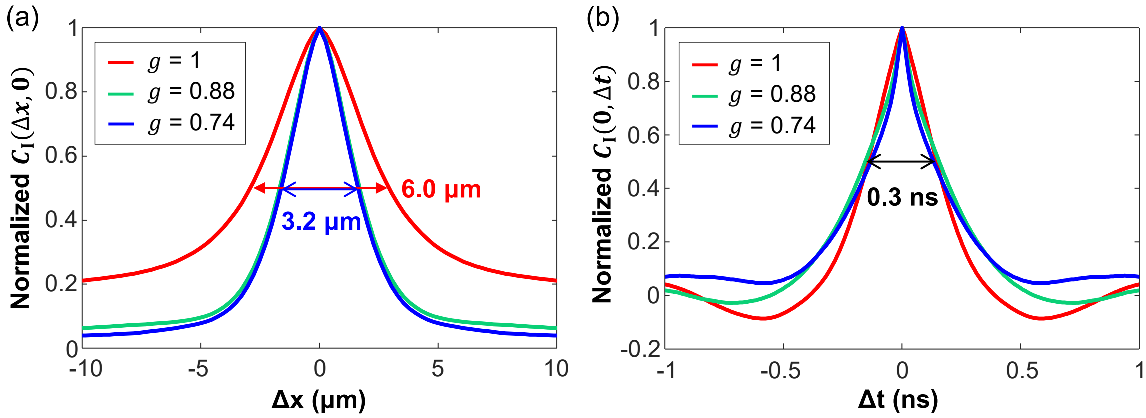

Figure 4.13: **Short-range correlations in near-planar cavity laser emission.** (a) Spatial correlation function $C_{\mathrm{I}}(\Delta x, 0)$ and (b) temporal correlation function $C_{\mathrm{I}}(0, \Delta t)$ of intensity fluctuations caused by filaments in different cavity geometries. The correlation functions are averaged over 5 different cavities for each value of g, to account for device-to-device variations. The FWHM of the correlation functions is indicated with arrows. The spatial correlation width decreases by a factor of 2 for the near-planar cavities ($g = 0.88$, 0.74), whereas the temporal correlation width remains nearly identical to that for the planar cavity ($g = 1$).

length of 6.0 μm, while in the near-planar cavities (g = 0.88 and 0.74) the correlation length is reduced by a factor of 2 to 3.2 μm. It reflects the decrease of filament size, as more high-order transverse modes lase in the near-planar cavity. Moreover, $C_{\mathrm{I}}(\Delta x, 0)$ for $g = 1$ exhibits a long tail at large Δx, reflecting the long-range correlations induced by filaments. In the near-planar cavities, the long tail of $C_{\mathrm{I}}(\Delta x, 0)$ is removed as a result of filament suppression.

Figure 4.13(b) shows the temporal correlation function $C_{\mathrm{I}}(0, \Delta t)$, averaged over 5 different cavities for each g. Its width gives the correlation time, which is approximately 0.3 ns, with little dependence on the cavity geometry. It is dictated by the inherent response time of carrier dynamics in the GaAs quantum well. For g = 1, the negative correlation at $|\Delta t|$ = 0.5 ns is more pronounced than for g = 0.74 or 0.88, reflecting stronger long-range temporal correlations in the planar cavity.

Long-range correlations

As the filaments move around in space and time, they induce nonlocal spatio-temporal correlations in the emission intensity [3, 19, 141]. To examine the nonlocal spatio-temporal correlations, we separate the regions of short-range and long-range correlations in Figs. 5(i-k) of the main text. Their boundary is set by an ellipse whose semi-axes are the spatial and temporal FWHM of the peak at origin. Then we average the modulus of $C_{\mathrm{I}}(\Delta x, \Delta t)$ outside the ellipse but within the range of $|\Delta x| < 30$ μm and $|\Delta t| < 1$ ns, where most correlations exist.

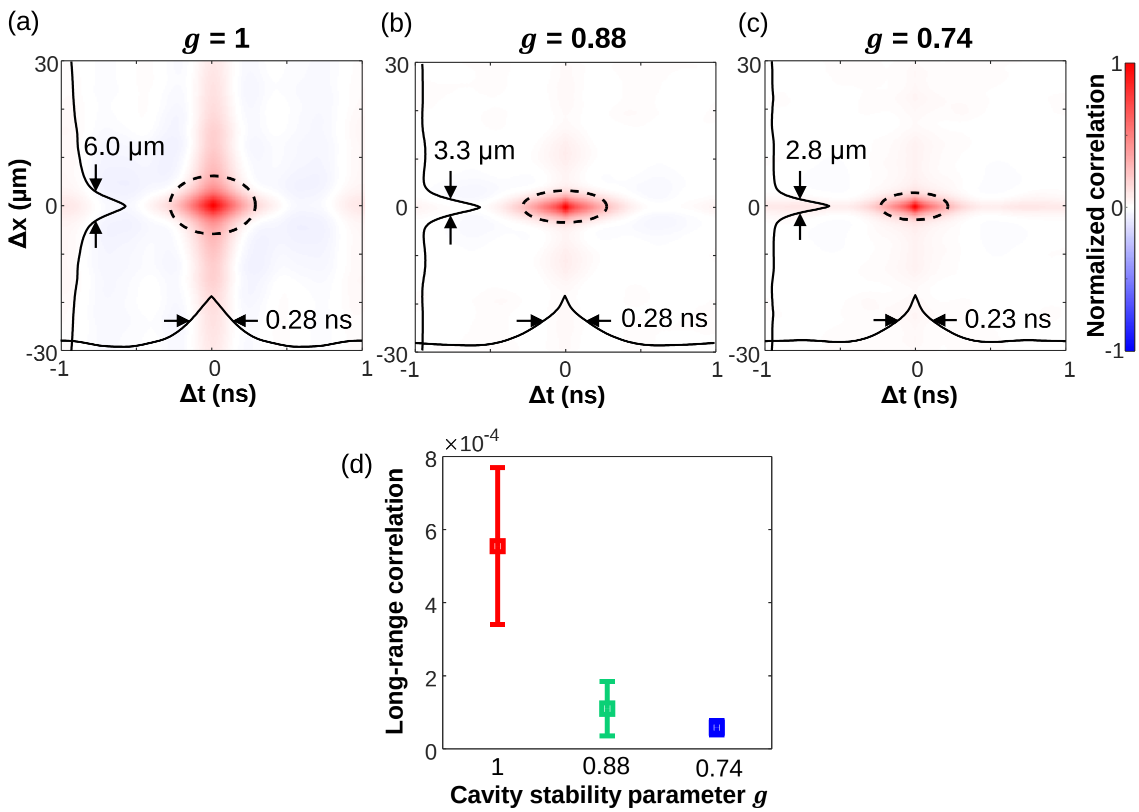

Figure 4.14: **Long-range correlations in near-planar cavity laser emission.** (a-c) Spatio-temporal correlation functions of the intensity fluctuations for group I, $C_I(\Delta x, \Delta t)$, in laser cavities of (a) $g = 1$, (b) 0.88, and (c) 0.74. The black solid lines are $C_I(\Delta x, 0)$ and $C_I(0, \Delta t)$. Their widths give the correlation length and time. The ellipse (black dashed line) divides the regions of local and nonlocal correlations, and its semi-axes are equal to correlation length and time. (d) Long-range spatio-temporal correlations in (a-c), given by the averaged magnitude of the correlation outside the ellipse.

Figures 4.14(a-c) show the spatio-temporal intensity correlation functions for group I, averaged over different time windows. Figure 4.14(d) shows the long-range spatio-temporal correlations are significantly reduced for g = 0.88 and 0.74 compared to g = 1. The suppression of non-local correlations indicates that the filaments are overall weaker in the near-planar cavity lasers, thus their spatio-temporal dynamics is more stable than that of the planar-cavity laser.

4.6 Discussion and conclusion

We demonstrate that the broad-area semiconductor laser characteristics can be dramatically changed by a small variation of the cavity shape. This is because the Fabry-Perot cavity with planar mirrors is located at a bifurcation point between stable and unstable ray dynamics. We curve the mirrors slightly and form a near-planar cavity with concave mirrors. As a result, the high-order transverse modes are well confined in the cavity, leading to a vast increase in the number of transverse lasing modes. The spatial coherence of laser emission is greatly reduced, which suppresses the speckle noise. Although the output beam has increased lateral divergence, its angular width is below 40°. Since the lateral divergence is comparable to the vertical divergence of an edge-emitting laser, the nearly circular beam can be easily collected with standard optics. Therefore, such a laser may be used as an illumination source for full-field speckle-free imaging. The advantage of our laser compared to e.g. an incandescent lamp which also produces no speckle noise is that the lamp emits into far too many spatial modes and thus has a low power per mode, whereas our laser emits into fewer modes and thus features a higher power per mode and better directionality. The greatly improved brightness facilitates high-speed imaging through absorbing or scattering media and real-time monitoring of moving objects or transient processes. Of course, the decrease of spatial coherence will increase the focal spot size and reduce the intensity for optical pumping, material processing, and other applications. However, in these applications, not only the brightness, but also the beam profile matters, e.g., the material processing usually requires a flat-top beam, which cannot be created by tight focusing of a spatially coherent beam. On the other hand, a laser with reduced spatial coherence may directly output a flat-top beam [14].

Curving the end facets also leads to a drastic modification of the spatio-temporal dynamics of broad-area semiconductor lasers. With many high-order transverse modes lasing, the characteristic length scales of intensity variations in the transverse direction are greatly reduced. Consequently, the self-focusing instability induced by spatial hole burning that leads to filamentation is prevented, and the spatio-temporal instability is mitigated. For a quantitative analysis of the lasing dynamics, we develop a method to separate the intensity fluctuations caused by different processes — filaments, mode beating, and detection noise. They have distinct spatio-temporal correlation scales, enabling us to separate filamentation from other processes. Compared to the planar cavity laser, the amplitude of spatio-temporal intensity fluctuations in the near-planar cavity is reduced by half. The RF spectrum (up to 10 GHz) becomes flattened as the temporal pulsation of emission intensity is weakened. Lastly, the reduction of filamentation in the near-planar cavity lasers decreases the long-range spatio-temporal correlations of intensity fluctuations. The stabilized laser output with negligible long-range spatio-temporal correlation will be useful for parallel random number generation [3].

To conclude, our method efficiently controls the nonlinear lasing dynamics by tailoring the resonator shape in the vicinity of a bifurcation point. The dramatic change in the spatial structures of cavity modes strongly affects their nonlinear interactions with the gain material. Our method is simple, robust, and works for a wide range of pump currents. It may be applied to high-power fiber and solid-state lasers, as well as other nonlinear dynamical systems. It can also be employed to control the time-reversed lasing and coherent perfect absorption [142–145].

Chapter 5

Massively parallel ultrafast random bit generation with a chip-scale laser

5.1 Introduction

[1]In Chapter 3 and 4, we designed, fabricated, and characterized the many-mode stable-cavity broad-area semiconductor lasers. In contrast to conventional lasers that aim to operate with a single spatial mode, our laser features hundreds of transverse modes lasing simultaneously. Moreover, the small characteristic length scale of high-order transverse modes effectively disrupts the self-focusing instability and thus suppresses the filaments. Our laser now will feature unique lasing dynamics orchestrated by spatiotemporal interference of many transverse lasing modes. In this chapter, we leverage the massive spatial degrees of freedom in lasing dynamics for a novel photonic application: random number generation.

The performance and reliability of our digital networked society are based on the ability to generate large quantities of randomness. An ever-increasing demand to improve the

[1]The chapter material is primarily taken from reference [3]: From Kyungduk Kim, Stefan Bittner, Yongquan Zeng, Stefano Guazzotti, Ortwin Hess, Qi Jie Wang, Hui Cao, "Massively parallel ultrafast random bit generation with a chip-scale laser", *Science*, vol. 371, 948-952 (2021). Reprinted with permission from AAAS.

security of digital information has shifted the generation of random numbers from sole reliance on pseudo-random algorithms to the use of physical entropy sources. Ultrafast physical random number generators are key devices for achieving ultimate performance and reliability in communication and computation systems [146, 147]. Semiconductor lasers that feature chaotic dynamics with tens-of-GHz bandwidth represent one prominent class of high-speed random number generators [148–163]. Initially, 1.7 Gb/s random bit generation (RBG) was achieved with combined binary digitization of two independent chaotic laser diodes [148]. Then from a single chaotic semiconductor laser, a 12.5 Gb/s RBG was demonstrated [149] with a subsequent boost to 300 Gb/s [150]. By coupling several lasers to further increase the bandwidth and using post-processing schemes to extract more bits in analog-to-digital conversion (ADC), the total RBG rate was pushed up to 2 Tb/s [158–160, 163]. However, the intrinsic time scales of lasing instabilities impose an ultimate limit on the entropy generation rate. A further increase in the RBG rate requires a different physical process with inherently faster dynamics.

Parallel RBG schemes can greatly enhance the generation rate and the scalability by producing many bit streams simultaneously. In the spatial domain, parallel generation of physical random numbers was realized by sampling two-dimensional laser speckle patterns created by a moving diffuser or a vibrating multimode fiber [164, 165]. As a result of inherently long mechanical timescales, the generation rates remain low (Mb/s). Chaotic broad-area semiconductor lasers have been investigated for high-speed parallel-RBG [26], but correlations of intensity fluctuations at different spatial locations impede independent parallel bit stream generation. Spectral demultiplexing of amplified spontaneous emission [166, 167] or heterodyning chaotic laser emission [154] are used for parallel RBG with rates up to hundreds of Gb/s per channel. So far, such spectral-domain parallel RBG has been demonstrated with fewer than 10 channels.

In this chapter, we demonstrate a method that enhances the random bit rate in a single channel and also provides hundreds of channels for simultaneous generation of independent bit streams. The spatio-temporal interference of many lasing modes is used to generate picosecond-scale emission intensity fluctuations in space, so as to massively produce ultrafast random bit streams in parallel. This is achieved by tailoring the geometry of a broad-area semiconductor laser to vastly increase the number of transverse lasing modes, thereby suppressing characteristic dynamical instabilities such as filamentation. Specifically, we have designed a chip-scale laser diode to enable a large number of spatial modes lasing simultaneously with incommensurate frequency spacings, so that their interference patterns are complex and aperiodic. Spontaneous emission adds stochastic noise to make the intensity fluctuations unpredictable and non-reproducible.

5.2 Suppressing spatio-temporal correlations

A conventional broad-area edge-emitting semiconductor laser has a stripe geometry with two flat facets [Fig. 5.1(a)]. Characteristically, lasing occurs only in the low-order transverse modes. Nonlinear interactions between the light field and the gain material entail irregular pulsation and filamentation [22] [Fig. 5.1(b)]. The spatio-temporal correlation function of the intensity fluctuations is given by,

$$C(\Delta x, \Delta t) = \frac{\langle \delta I(x_0 + \Delta x, t + \Delta t) \delta I(x_0, t) \rangle_t}{\sqrt{\langle \delta I^2(x_0 + \Delta x, t) \rangle_t \langle \delta I^2(x_0, t) \rangle_t}} \tag{5.1}$$

where $\delta I(x,t) = I(x,t) - \langle I(x,t) \rangle_t$ represents the temporal fluctuation of emission intensity at the transverse position x on the end facet, and x_0 denotes the center of the facet [19]. $C(\Delta x, \Delta t)$ reveals non-local correlations in space and time [Fig. 5.1(c)]. On one hand, long-range temporal correlation reflects memory which degrades the quality of random bits generated at one spatial location. On the other hand, long-range spatial correlation means that the random bit streams generated at different locations are not completely independent, thus impeding parallel RBG [26].

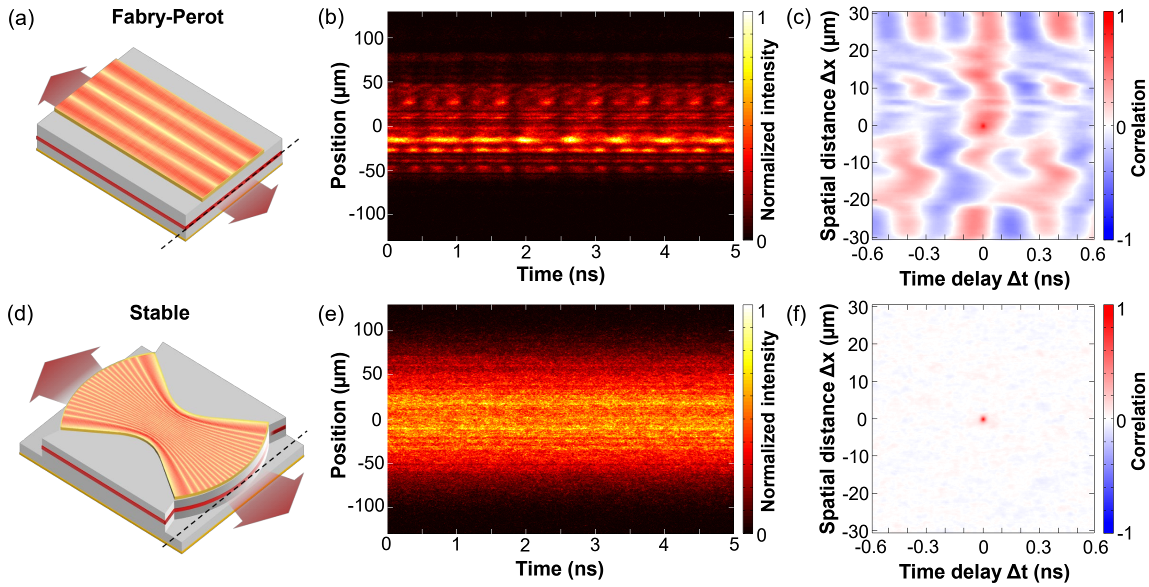

Figure 5.1: **Reducing spatio-temporal correlations of the lasing emission.** (a) A wide-stripe edge-emitting semiconductor laser with planar facets supports only low-order transverse modes with the typical spatial profile shown (not to scale). (b) Emission intensity $I(x,t)$ at one facet of a 100-μm-wide, 1000-μm-long GaAs quantum-well laser, measured by a streak camera, features filamentation and irregular pulsations. (c) The spatio-temporal correlation function $C(\Delta x, \Delta t)$ of the emission intensity in (b) reveals long-range spatio-temporal correlations. (d) Our specially-designed laser cavity with curved facets confines high-order transverse modes. The spatial intensity distribution of an exemplary high-order transverse mode is plotted. (e) The measured spatio-temporal trace of the lasing emission from our cavity of length 400 μm, width 282 μm and facet radius 230 μm is free of micrometer-sized filaments and GHz oscillations as seen in (b). (f) The spatio-temporal correlation function $C(\Delta x, \Delta t)$ of the emission intensity in (e) shows no long-range spatio-temporal correlations.

To achieve massively parallel ultrafast RBG, we enhance the number of transverse lasing modes by increasing the cavity width and curving the end facets [Fig. 5.1(d)], effectively suppressing modulational instabilities. High-order transverse modes are well confined inside such a cavity, and their optical gain is enhanced by tailoring the top metal contact shape. The number of transverse lasing modes is maximized by fine-tuning the cavity geometry, as described in Chapter 3 [1]. Lasing on small length scales of transverse wavelengths of high-order modes prevents lensing and self-focusing effects [4] that would normally cause filamentation and instabilities [Fig. 5.1(e)]. In turn, the absence of filaments and pulsations eliminates long-range spatio-temporal correlations in the lasing intensity [Fig. 5.1(f)]. It is this shortening of the correlation lengths in space and time that paves the ground for a substantial increase in the number of independent spatial channels for parallel RBG, as well as a great enhancement of the RBG rate of every individual spatial channel.

5.3 Spatio-temporal interference of many lasing modes

With lasing instabilities suppressed, the dynamic variations of the emission intensity are orchestrated by the interference of lasing modes with different frequencies. The characteristic time scale of such intensity fluctuations is inversely proportional to the spectral width of the total emission, and is $\sim$1 ps for the GaAs quantum-well laser. We show the spatio-temporal beat pattern of the intensity emitted at one laser facet in Fig. 5.2(a). The temporal correlation length is determined by the full width at half maximum (FWHM) of $C(\Delta x, \Delta t)$ in time [Fig. 5.2(b)]. Its value of 2.8 ps is limited by the temporal resolution of our detection.

For spatial-multiplexing of RBG, the number of independent parallel channels depends on the spatial correlation length of the lasing emission. Now with non-local correlations removed, the local correlation length estimated from the spatial FWHM of $C(\Delta x, \Delta t)$ is 1.5 μm [Fig. 5.2(b)], which is limited by the spatial resolution of our detection. Without the finite experimental resolution, our simulation gives a correlation length of 0.5 μm. This value is dictated by the transverse length of the highest-order transverse lasing mode. Thanks to this extremely short spatial correlation length, hundreds of independent spatial channels are available for parallel RBG.

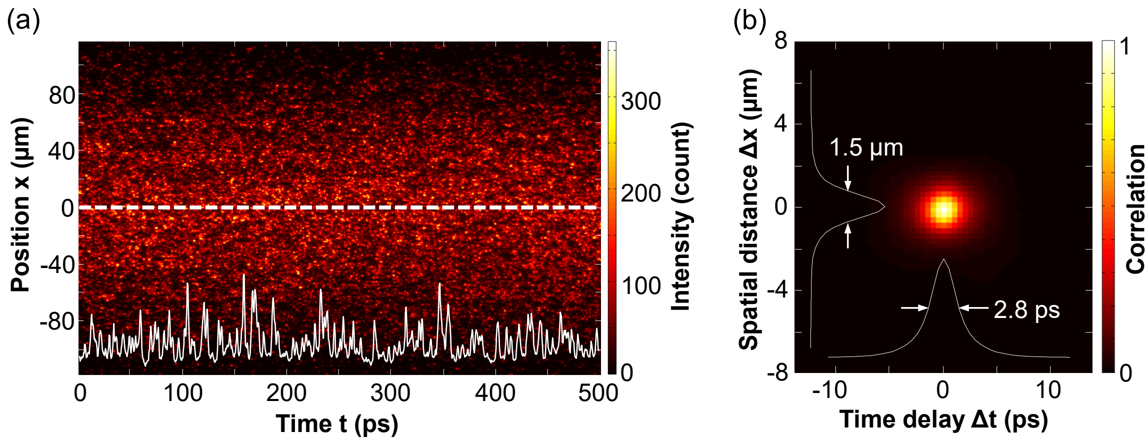

Figure 5.2: **Ultrafast beating of lasing modes.** (a) The lasing emission at one facet of our 600-μm-long cavity exhibits a spatio-temporal interference pattern. The white solid curve is the temporal intensity fluctuation at position x = 0 (white dashed line). (b) The correlation function $C(\Delta x, \Delta t)$ of the measured lasing emission intensity in (a) gives the spatial and temporal correlation widths of 1.5 μm and 2.8 ps.

Because the transverse mode frequency spacing in our cavity design is incommensurate to the longitudinal mode spacing, the spatio-temporal interference pattern cannot repeat itself. Moreover, the spontaneous emission, generated by quantum fluctuations, constantly feeds stochastic noise into the lasing modes, making their beat pattern unpredictable and irreproducible.

5.4 Numerical modeling

5.4.1 Lasing modes

We calculate the lasing modes of our stable-cavity laser. Figure 5.3(a) shows the quality (Q) factors and wavelengths of the passive modes. Since numerical modeling of a cavity as large as the fabricated lasers (L = 600∼800 μm) is too computationally expensive, we instead simulate a smaller cavity of the same geometry (L = 40 μm). In Fig. 5.3(b), the modes are arranged in terms of their transverse and longitudinal mode indices. Although its size is relatively small, the simulated cavity exhibits about 50 transverse modes. The number of transverse modes scales linearly with the cavity size [1].

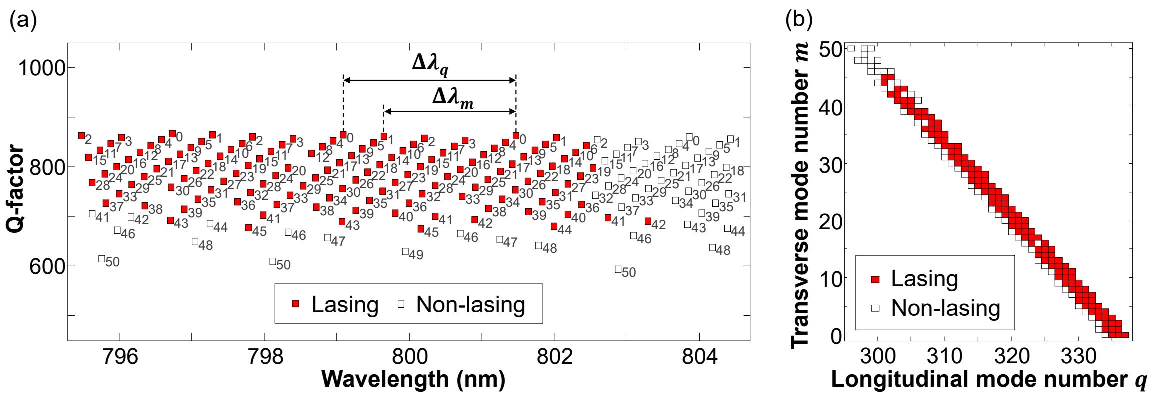

Figure 5.3: **Cavity resonances and lasing modes.** (a) Calculated Q factors and wavelengths of the resonant modes (black open squares) in a cavity with length $L = 40$ μm, width $W = 28.2$ μm, curvature radius of the end facets $R = 23$ μm, and effective refractive index n = 3.37. The transverse mode number m is written next to each mode. The longitudinal mode spacing (free spectral range) $\Delta\lambda_q$ and the transverse mode spacing $\Delta\lambda_m$ are indicated by arrows. The modes that lase for pumping at two times the lasing threshold are marked by red solid squares. (b) The cavity resonances (black open squares) and lasing modes (red solid squares) shown in (a) are arranged in terms of their longitudinal and transverse mode numbers. Almost all transverse modes lase even in the presence of gain competition.

Mode competition for optical gain tends to reduce the number of transverse lasing modes. We calculate the lasing modes using the single pole approximation steady-state *ab-initio* laser theory (SPA-SALT) [60, 87, 88], taking gain saturation fully into account. We assume a spatially uniform distribution of the pump and a flat gain spectrum within the wavelength range of 795−805 nm.

The modes that lase in the simulation are marked by red squares in Fig. 5.3(b). When the pump is two times the lasing threshold, the number of transverse lasing modes M is 46. Hence, most of the transverse modes in the cavity can lase in spite of gain competition.

5.4.2 Many-mode interference

Given that most of transverse modes manage to lase, we model the observed lasing dynamics by many-mode interference of passive resonances oscillating at their resonant frequencies. To simulate a large cavity of size equal to the fabricated one (L = 600 μm), we compute the mode frequencies $\nu_{m,q} = c/\lambda_{m,q}$ with the analytical expression for Hermite-Gaussian modes [114],

$$\nu_{m,q} = \frac{c}{2nL}\left[q + \frac{1}{\pi}\left(m + \frac{1}{2}\right)\arccos(g)\right] \tag{5.2}$$

where $g \equiv 1 - L/R$ is the cavity stability parameter, which is $g = -0.74$ for the lasers considered here. The effective refractive index n is set to 3.37.

The longitudinal mode spacing is $\Delta\nu_q = \nu_{m,q+1} - \nu_{m,q} = c/2nL$, and the transverse mode spacing is $\Delta\nu_m = \nu_{m+1,q} - \nu_{m,q} = (c/2nL)\arccos(g)/\pi$. Their ratio is $\Delta\nu_m/\Delta\nu_q = \arccos(g)/\pi$. It is an irrational number for g = -0.74, making the longitudinal mode spacing incommensurate with the transverse mode spacing.

The total emitted field is a sum of fields in numerous transverse and longitudinal modes with frequencies within the GaAs QW gain spectrum. The spatio-temporal intensity pattern at one facet can be written as

$$I(x,t) = \left|\sum_{m=0}^{M-1}\sum_{q} A_{m,q} e^{i\phi_{m,q}(t)} \psi_m(x) e^{i2\pi\nu_{m,q}t}\right|^2, \tag{5.3}$$

where $\psi_m(x)$ represents its transverse field profile on the end facet, and $A_{m,q}$ and $\phi_{m,q}$ denote its global amplitude and phase.

For the single-channel dynamics at one spatial location x_0, we neglect the modal amplitudes and assume their same contribution, i.e. $\psi_m(x_0)$ = 1. The emission intensity at single spatial channel is,

$$I(t) = \left| \sum_{m=0}^{M-1} \sum_q A_{m,q} e^{i[2\pi\nu_{m,q}t + \phi_{m,q}(t)]} \right|^2 \tag{5.4}$$

with $A_{m,q}$ approximated by $\sqrt{S(\lambda_{m,q})}$, where $S(\lambda_{m,q})$ is the fit of the measured emission spectrum in Fig. 5.4(a). The total number of transverse modes is M = 200 as in the experiments [1].

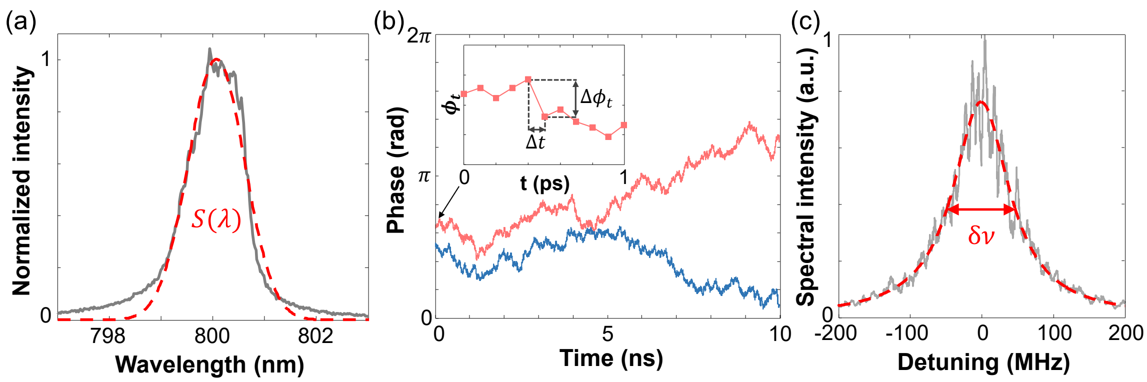

Figure 5.4: **Modeling of single-channel dynamics.** (a) Time-integrated spectrum of measured lasing emission at two times above the lasing threshold (gray solid line). The FWHM is 1.3 nm. The spectrum $S(\lambda)$ is fitted by a Gaussian function (red dashed line). (b) Simulated random phase drift in time for two lasing modes. The inset shows the phase change $\Delta\phi_t$ after a single time step Δt. (c) The simulated optical spectrum of a single lasing mode is fitted by a Lorentzian function with a FWHM of 96 MHz, which is close to the mode linewidth $\delta\nu = 100$ MHz.

To account for the spontaneous emission, we introduce a stochastic fluctuation to the phase $\phi_{m,q}(t)$ of each lasing mode [168], which follows,

$$\Delta\phi(t) = \phi(t + \Delta t) - \phi(t) = \sqrt{2\pi\delta\nu\Delta t}\, Z(t), \tag{5.5}$$

where $Z(t)$ is a normal-distributed random number with a standard deviation of 1, and Δt is the discrete time step. The mode linewidth is set to $\delta\nu$ = 100 MHz, which is typical for a GaAs/AlGaAs QW edge-emitting multi-mode laser [169, 170]. As shown in Fig. 5.4(b), the phase of each mode undergoes a random walk. The optical spectrum of a single lasing mode, calculated via the temporal Fourier transform of its field, exhibits a Lorentzian-shaped line with FWHM equal to $\delta\nu$ as shown in Fig. 5.4(c).

To take into account the temporal resolution of photodetection, we convolve the simulated time trace with a temporal point spread function (PSF). The PSF of the streak camera is approximated by a Lorentzian function with a FWHM of 1.2 ps. The convolution smoothens the time trace, and increases the temporal correlation width (FWHM) to 2.8 ps, in agreement with the experimental value [Fig. 5.2(b)].

5.5 Radio-frequency spectrum

We experimentally characterize the RF spectrum of the emission intensity by performing the Fourier transform of a time trace at the spatial location $x = 0$, measured by a streak camera, and taking the modulus. Thanks to the ultrafast dynamics of lasing intensity, the measured radio-frequency (RF) spectrum is extremely broad, as shown in Fig. 5.5. Its bandwidth, which contains 80% of the entire spectrum, is 315 GHz. For comparison, the numerically-simulated spectrum is even broader with a bandwidth of 632 GHz. After accounting for the temporal resolution of photodetection, the simulated RF spectrum matches the measured one (See Fig. 5.5). This agreement confirms that the ultra-broad spectrum results from the interference of many transverse and longitudinal modes.

To understand how the broad RF spectrum is formed, we vary the number of transverse modes M while keeping the number of longitudinal mode groups constant. This corresponds to changing the width of a laser cavity while keeping its length fixed. With only the fundamental transverse mode M = 1 [Fig. 5.6(a)], the RF spectrum features multiple peaks separated by the longitudinal mode spacing (free spectral range) $\Delta\nu_{\mathrm{FSR}} = \Delta\nu_q = c/2nL$. With increasing M, each peak becomes a group of peaks that originate from the beating

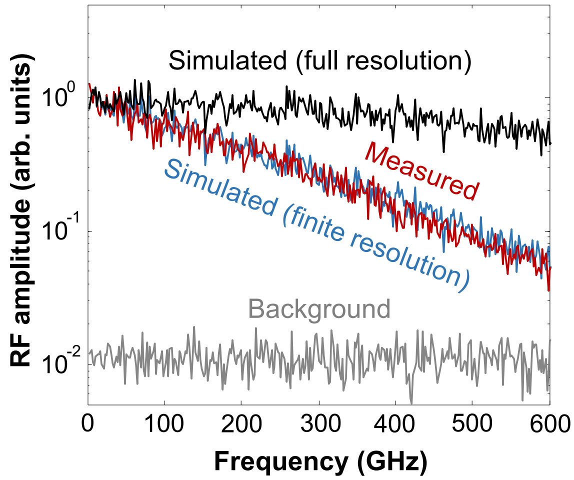

Figure 5.5: **Radio-frequency spectrum.** The RF spectrum (the modulus of Fourier transform) of the emission intensity at $x = 0$, at the middle of the cavity facet, (red) is much higher than the background (gray) with the laser turned off. The simulated spectrum (black) is broader, but becomes narrower when the temporal resolution of our detector is taken into account (blue), in agreement with the measured one (red).

of transverse modes. For the cavity with $g = -0.74$ considered here, the transverse mode spacing is incommensurate with the free spectral range because $\arccos(g)/\pi$ is an irrational number. As a result, the additional beating frequencies that appear when increasing the number of transverse modes eventually fill the entire frequency range. With $M = 200$ transverse modes in Fig. 5.6(c), the spectrum becomes continuous and featureless, in agreement with the experimental data in Fig. 5.5.

We comment on possible deviations of lasing frequencies in experiment from analytic resonant frequencies. Experimentally with electric current injection, the spatially inhomogeneous distribution of carriers can cause non-uniform changes of the refractive index, making the lasing mode frequencies deviate from the passive cavity mode frequencies. Nevertheless, the experimentally measured RF spectrum of the lasing emission in Fig. 5.5 remains flat and smooth, similar to the numerically simulated spectrum of the passive cavity. Due to the presence of hundreds of lasing modes with many different frequency spacings between them, there is an almost continuous distribution of time scales in their

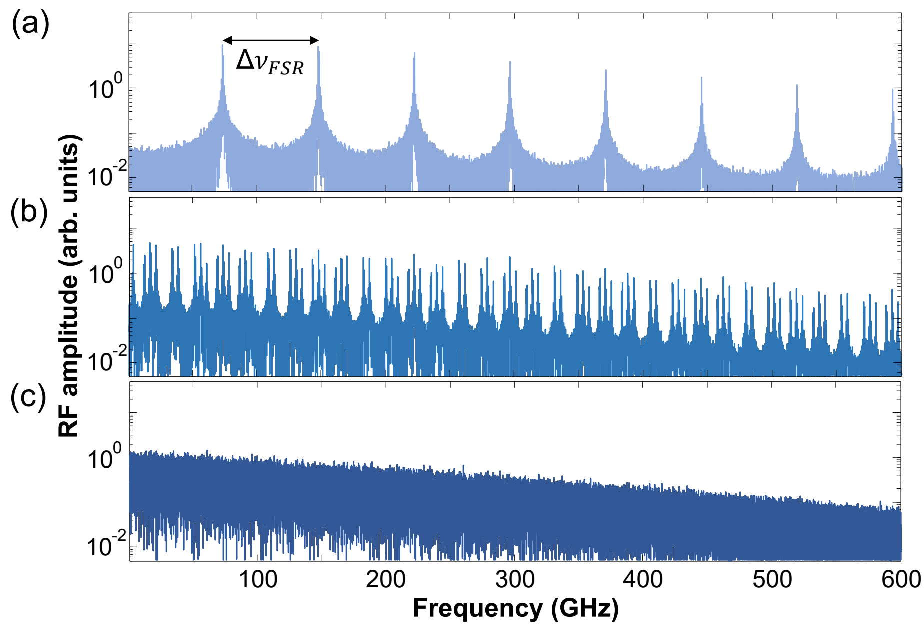

Figure 5.6: **Simulated RF spectrum.** Fourier transform of the simulated emission intensity with the number of transverse modes (a) $M = 1$, (b) $M = 6$, and (c) $M = 200$. The number of longitudinal mode groups is fixed at 8. The spectrum becomes more and more densely packed and flat with increasing M.

interference pattern, so even if some of the time scales were by chance commensurate, the effect would be lost in the sea of other incommensurate ones.

5.6 Random bit generation

5.6.1 Data acquisition

We used a device with a cavity length L = 800 μm and width W = 566 μm. The lasing threshold is 800 mA. We injected electric current at 1600 mA, which is two times above the threshold. To reduce sample heating, we use a diode driver (DEI Scientific, PCX-7401) to generate 150-ns-long current pulses at a repetition rate of 7 Hz.

The lasing emission on one end facet is imaged by a 20× microscope objective (NA = 0.4) and a lens (focal length 150 mm) onto the entrance slit of a streak camera (Hamamatsu

C5680). The fast sweep unit (M5676) of the streak camera records the spatio-temporal traces of the emission intensity. Due to the limited field of view of the imaging optics, only the emission from the central part of the laser facet is collected.

In experiment, a single streak camera image has a time window of 500 ps. Due to the finite length of the time windows measurable by the streak camera, we concatenate 10^6 streak camera images from consecutive pulses to obtain a 0.5-ms-long time trace for each spatial position.

Concatenating time traces

Since the temporal measurement range of our streak camera is limited, it is impossible to measure a long continuous time trace. Instead we make separate measurements and concatenate the time traces. Since this process could potentially increase the randomness, here we check numerically whether the entropy generation rate is changed by it.

Using Eq. 5.4 to simulate the many-mode interference, we obtain a 1.5-μs-long time trace of the emission intensity in a single spatial channel. We repeat this process with different random phases for each mode, and obtain 3000 time traces. Short segments of three such traces are shown in Fig. 5.7(a). Then we extract 500-ps-long segments in consecutive time windows from each trace, and concatenate these segments together for a trace of length 1.5 μs as shown in Fig. 5.7(b). We calculate the Cohen-Procaccia entropy rate (See Section 5.8.1) of the original trace and the concatenated trace. Fig. 5.7(c) shows complete agreement of the two curves, indicating that the process of concatenating windows from different time traces does not affect entropy generation. We also concatenate the same time windows of different traces, and the Cohen-Procaccia entropy rate is the same as well.

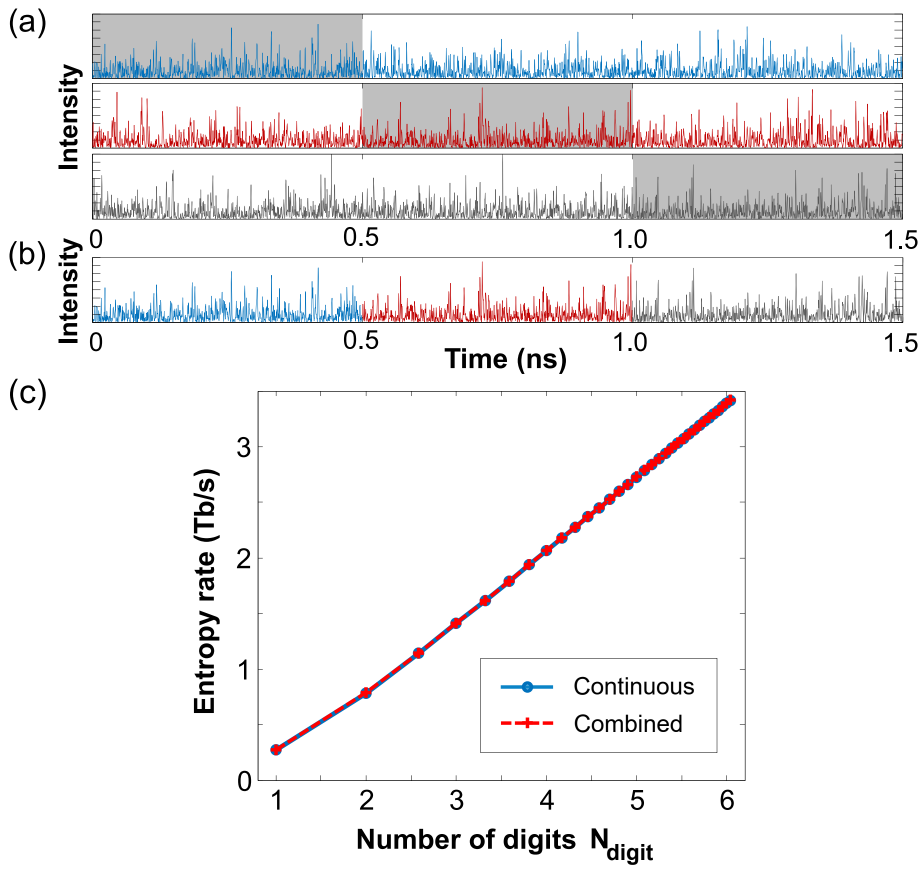

Figure 5.7: **Concatenating time traces.** (a) Three continuous time traces of the emission intensity in a single spatial channel are generated by simulating the many-mode interference in the laser. The shaded areas represent the temporal range measured by the streak camera. (b) A time trace is formed by concatenating the shaded parts of the three traces in (a). (c) The Cohen-Procaccia entropy rate estimate of a single 1.5-μs-long trace as in (a) is equal to that of the concatenated trace as in (b). The sampling period τ is 1.5 ps, and the embedding dimension d is 2.

5.6.2 Sampling of intensities

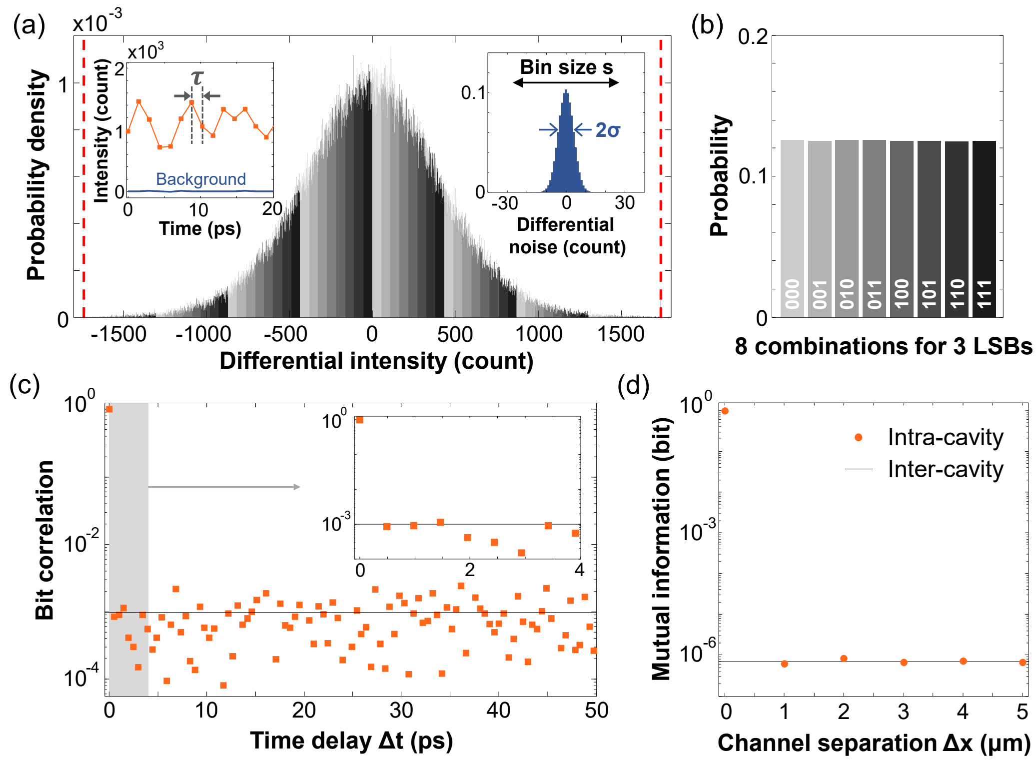

Figure 5.8: **Random bit generation.** (a) The PDF of the differential intensity, $\Delta I_n = I_{n+4} - I_n$, which is digitized to 6 bits by binning the range [-1740, 1740] counts (vertical red dashed lines) into 2^6 = 64 equally spaced intervals. Three LSBs are taken from each sample. The gray scale of the bars represents their eight combinations. Left inset: A segment of intensity time trace of a single spatial channel (red line), sampled at intervals τ = 1.46 ps (red dots). The blue curve is the background count. Right inset: The PDF of the differential background count with a standard deviation $\sigma = 3.9$ counts, much smaller than the bin size $s = 54$ for ΔI_n. (b) The probability for all eight combinations of three LSBs is almost equal. (c) A bit stream with length N = 2^{20} has a bit correlation (red squares) around the lower limit $1/\sqrt{N}$ (black line). Inset: Close-up of short delay times. (d) The mutual information between bit streams in two channels with varying separation (Intracavity) is equal to that between the streams from two independent lasers (Intercavity).

To generate random bits, we divide the laser end facet into 1-μm-wide spatial channels. In a 2D streak image of the spatio-temporal intensity of the laser emission, each spatial channel of width Δx = 1 μm contains 4 spatial pixels. Because of the restricted field of view of our collection optics, only 254 spatial channels are recorded simultaneously, which is about half of the number possible with complete collection of emission. We sample the emission intensity at every spatial channel at intervals of τ = 1.46 ps (sampling rate 683 GHz; Fig. 5.8(a), left inset), which corresponds to 3 temporal pixels of a streak image. We sum the intensities of $4 \times 3 = 12$ pixels in a streak image to obtain one intensity value I_n.

Figure 5.9(a) shows the probability density function (PDF) of the sampled intensity I_n in one spatial channel. The PDF exhibits an exponentially decaying tail, which is a characteristic of Rayleigh speckle patterns. The PDF is not a perfect exponential function due to the finite spatial and temporal resolution of the measurement. This asymmetric PDF can lead to biased bits, which degrade the quality of random bits generated.

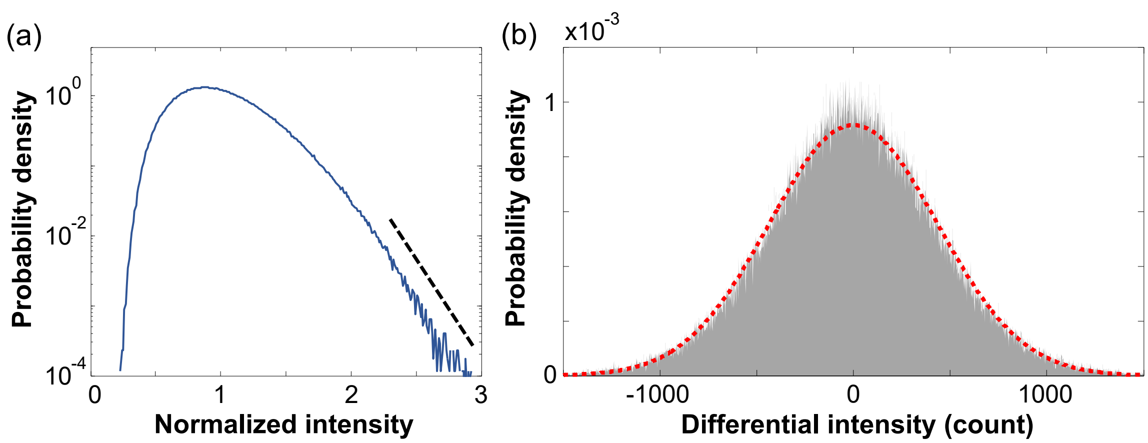

Figure 5.9: **Intensity PDF.** (a) The PDF of the measured intensity I_n of emission in a single spatial channel. The temporal resolution is 1.46 ps and the spatial resolution is 1 μm. The black dashed line indicates an exponential decay. (b) The PDF of the differential intensity $\Delta I_n = I_{n+4} - I_n$ is symmetric and well fitted by a Gaussian function (red dotted line).

To make the distribution symmetric, we perform a subtraction of sampled intensities. We adopt the procedure from [149] to obtain a sequence of differential intensities $\Delta I_n = I_{n+m} - I_n$ by subtracting the intensities separated by a sample distance of m. For a small m, the PDF of ΔI_n deviates notably from a Gaussian function, because of the temporal correlation of I_n. The non-Gaussian PDF will introduce bias among different combinations of the three LSBs taken for RBG. A large m produces a bit stream with long-range correlations, which also degrade the random bit quality. We choose m = 4 as an optimal sample distance. Figure 5.9(b) shows the PDF of the differential intensity from experimental data, which is well fit by a Gaussian function.

Effect of noise on binning

The streak camera background counts fluctuate on the spatial scale of a single pixel. The noise contribution to RBG is determined by its fluctuation, not its mean value which cancels out in the differential intensity. The standard deviation σ of the differential background count (with the laser turned off) is 1.1. When summing over 4×3 = 12 pixels, the standard deviation is increased $\sqrt{12} = 3.46$ times to σ = 3.9 [Right inset of Fig. 5.8(a)].

Since σ is much smaller than the bin size $s = 54$ of differential intensity ΔI_n in Fig. 5.8(a), the random bits are determined predominately by the laser emission. However, if the value of ΔI_n is close to the boundary of one bin, the noise could alter the bit extraction. This is estimated to happen for 3.3% of the bits in the spatial channel shown in Fig. 5.8(a). The percentage can be reduced by increasing the signal strength with better collection of the laser emission.

5.6.3 Digitization and post-processing

Random bit generation demands negligible correlation between successive bits. Here digitization and post-processing play a crucial role in removing the remaining correlation. The differential intensity ΔI_n is digitized to $N_{\text{digit}} = 6$ bits [Fig. 5.8(a)], and three least significant bits (LSBs) are used for RBG [149]. All eight combinations for three LSBs have almost equal probability [Fig. 5.8(b)]. We remove the residual bias by performing exclusive-OR (XOR) on two bit streams from distant spatial channels, which reduces the number of parallel bit streams to 127.

Figure 5.8(c) reveals that the correlation between bits in a single bit stream reaches the limit $1/\sqrt{N}$ given by the bit stream length N. In Fig. 5.8(d), we calculate the mutual information between a pair of bit streams, Y_i and Y_j, generated in parallel by,

$$h(\Delta x) = \left\langle \sum_{Y_i, Y_j} p(Y_i, Y_j) \log_2 \frac{p(Y_i, Y_j)}{p(Y_i) p(Y_j)} \right\rangle . \tag{5.6}$$

where $p(Y_i)$ is the probability density function (PDF) of a random bit stream Y_i, $p(Y_i, Y_j)$ is the joint PDF of two random bit streams Y_i and Y_j, and $\langle ... \rangle$ denotes an average over all pairs of channels i and j with a constant spatial distance Δx. Fig. 5.8(d) shows that the mutual information between any pair of bit streams is as small as the MI of uncorrelated bit streams from different lasers.

Reducing temporal and spatial correlations

We investigate the effect of digitization and post-processing on the temporal correlation functions in Fig. 5.10. For long time lags, keeping only the LSBs reduces the correlation below 10^{-3}, which is the lower limit given by the finite length of the bit stream (2^{20} samples). For short time lags (Fig. 5.10B), the correlation for the LSBs decays rapidly with the sample distance, greatly shortening the correlation time. The residual correlations are then completely removed by the XOR operation with another bit stream from a distant spatial channel. The correlation remains at the background level for any time delay, indicating the absence of correlations between successive bits.

We also examine the reduction of spatial correlations by digitization and post-processing. In Fig. 5.11 we compare the mutual information (MI) between two bit streams produced experimentally for three different cases: (i) thresholding $N_{\text{digit}} = 1$, the simplest bit-

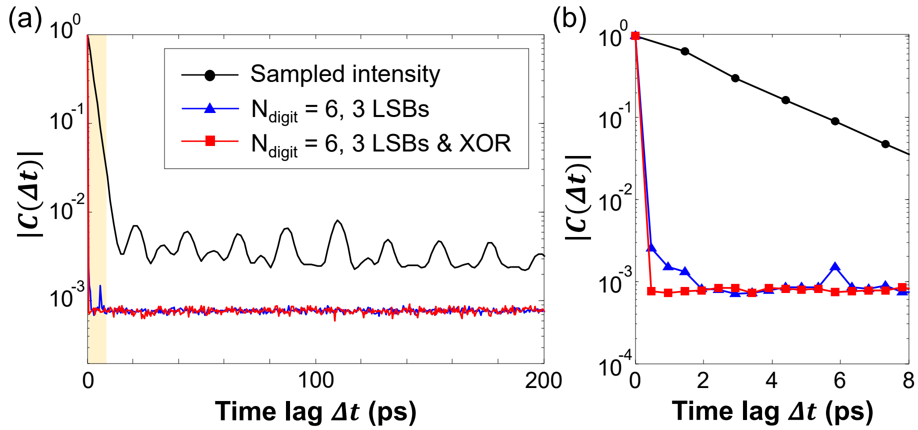

Figure 5.10: **Temporal correlation of bits in a single channel.** (a) The magnitude of the temporal correlation function $|C(\Delta t)|$ of the measured intensity trace sampled with τ = 1.46 ps (black circles), after keeping only the 3 LSBs (blue triangles), and after performing the XOR operation in addition (red squares). The correlation functions are averaged over spatial channels. The number of data points in time is 2^{20}. (b) The magnified view for short time lags shows the quick decay of correlations for the three LSBs. The small peak at 5.84 ps (= 4τ) is attributed to the subtraction of the sampled intensity $\Delta I_n = I_{n+4} - I_n$.

extraction scheme; (ii) keeping 3 LSBs from analog-to-bit conversion with N_{digit} = 6; and (iii) conducting XOR of (ii) with a bit stream from a spatially distant channel. In comparison to (i), the MI between neighboring channels (with 1 μm spacing) is reduced by five orders of magnitude in (ii). Moreover, the MI is further reduced at short-range in (iii). It stays at the residual level of 10^{-6} and becomes independent of the channel separation. Fig. 5.11(b) shows the residual MI is inversely proportional to the length of the bit stream N. For $N = 2^{20}$, the residual MI is less than 10^{-6} (circled in red). It is equal to the MI between any pair of channels in (iii), indicating all channels are statistically independent and their residual MI is a result of the finite bit stream length.

At the end, our scheme leads to a single-channel bit generation rate of 2 Tb/s. Our bit rate is twice the current single-channel record with off-line post-processing [158–160].

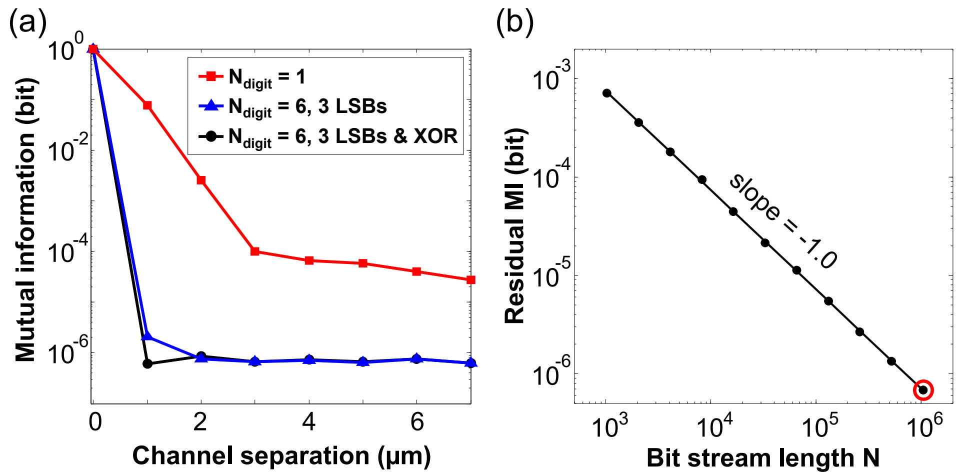

Figure 5.11: **Mutual information between two spatial channels.** (a) Mutual information (MI) of experimental bit streams produced by (i) thresholding (red squares), (ii) keeping 3 LSBs from N_{digit} = 6 bit conversion (blue triangles), (iii) calculating XOR of (ii) with a bit stream from a spatially distant channel (black circles). The MI is averaged over all channels. The MI decreases with the channel separation. (b) The residual mutual information of (iii) in (a) at channel separation $\Delta x \geq 1$ μm is inversely proportional to the bit stream length N, indicating it results from the finite stream length. The red circle indicates the length of the bit stream used in (a).

5.7 Random bit testing

We evaluated the quality of the generated random bits with two standard statistical test suites: NIST SP 800-22 and Diehard.

NIST SP 800-22

The NIST SP800-22 Random Bit Generator test suite consists of 15 different kinds of statistical tests, some of which include subtests [171]. Each test returns a single or multiple p-values. When the p-value exceeds a significance level of α = 0.01, the bit stream is considered random, as recommended by NIST. For k bit streams, we examine if they pass or fail each statistical test. The pass proportion should be within $(1-\alpha) \pm 3\sqrt{\alpha(1-\alpha)/k}$. For each spatial channel, we use k = 1000 bit sequences, each having 2^{20} bits, in total over

10^9 bits. As an example, Fig. 5.12 shows the test results for one bit stream. In panel (a), the pass proportions are all above the criterion indicated by the red line.

For a good random bit generator, the p-values from the k bit streams should be uniformly distributed. The composite P-value (p-value of the p-values) is a measure of uniformity of the p-values. The distribution of p-values is considered as uniform when the composite P-value is larger than a significance level of 10^{-4}. The example in Fig. 5.12(b) shows that the composite P-values of all subtests are above the significance level indicated by the red line.

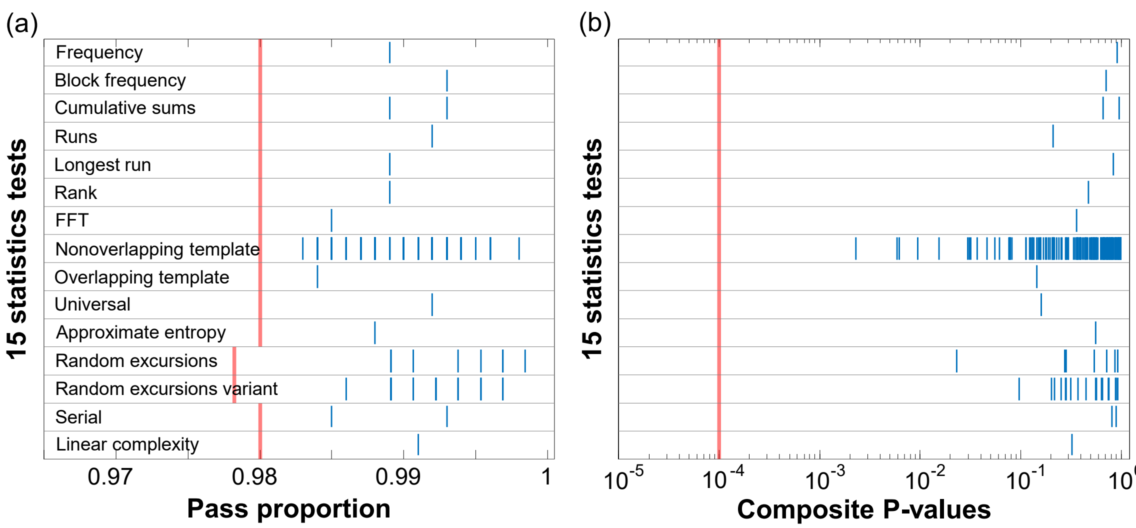

Figure 5.12: **NIST SP800-22 statistical test results for a single channel.** (a) Pass proportions and (b) composite P-values of 15 kinds of statistical tests for random bits generated experimentally in a single channel. Multiple (short, vertical) blue bars represent the subtests for each kind of statistical test. The red lines denote the pass criteria recommended by NIST.

Fig. 5.13(a) provides the test results for all of 127 parallel bit streams; 95 of them passed all NIST tests, yielding a pass rate of 75%. Considering the statistical nature of the NIST tests, the pass rate was previously evaluated for pseudo-random number generators and physical random number generators. In Ref. [172], the NIST test was applied to 100 different sample data sets (each set consisting of 1000 segments of 1 Mbit length), and a pass rate of 41%−56% was obtained for various representative pseudo-random bit generators. In Ref. [173], a pass rate of 59%−71% was reported for some well-known pseudo-random number generation algorithms including those recommended by NIST. In Ref. [161], a pass rate between 65% and 75% was obtained for a physical RBG based on a chaotic laser. By accounting for the correlations of the sub-tests included in the NIST test suite, the upper bound of the pass rate was estimated to be 80.99% [173]. Compared to the pass rates in these prior studies, our pass rate of 75% for all channels (Fig. 3E) is considered acceptable for reliable random bit generators.

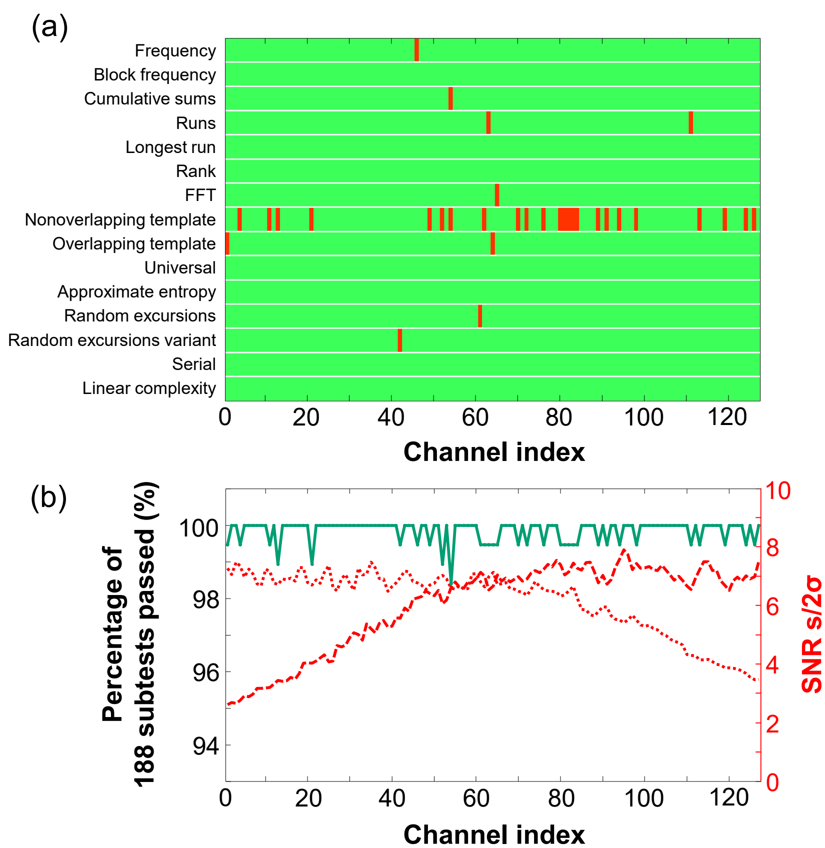

Figure 5.13: **Random bit evaluation.** (a) The NIST SP800-22 test results include 15 kinds of statistical tests, yielding a total of 188 subtests for 127 parallel bit streams. The green color denotes one stream passing one test; conversely, red denotes test failure. Ninety-five bit streams pass all subtests, yielding a pass rate of 75%, which is considered acceptable for a reliable RBG. (b) The percentage of all 188 subtests that every bit stream passes (green) is uncorrelated with the SNR $s/2\sigma$ of the corresponding pair of spatial channels (red dashed and dotted lines).

To investigate the effect of photodetection noise on the quality of random bits, we define the signal-to-noise-ratio (SNR) as the bin size s for digitization of ΔI_n divided by 2σ of the background fluctuation in a channel. Figure 5.13(b) shows that the percentage of all 188 subtests that every bit stream passes is uncorrelated with the SNR for the pair of spatial channels XOR'ed to create it, indicating that the level of detection noise does not affect the random bit quality.

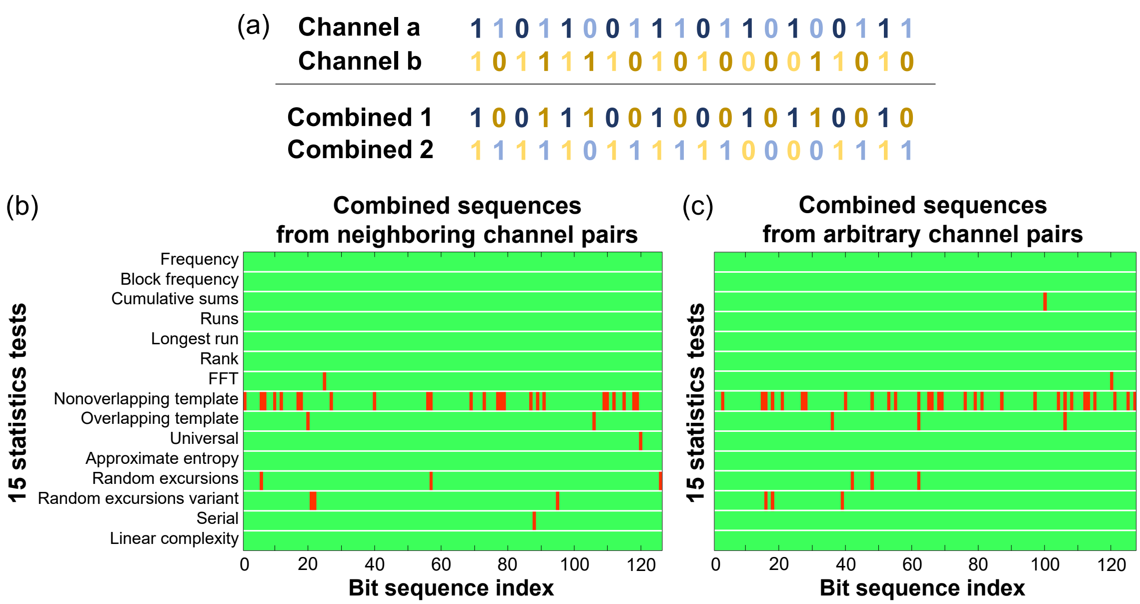

Figure 5.14: **NIST SP800-22 statistical test results for combined bit sequences.** (a) Schematic of combining two bit streams from channels a & b. The odd (even)-indexed bits from channel a is combined with the even (odd)-indexed bits from channel b. (b) The NIST test results for combined bit sequences created from neighboring spatial locations. The random bit streams from two adjacent channels are combined to produce two new bit sequences. In total 126 combined bit sequences are created from 126 original bit streams. 92 of them pass all NIST tests, yielding a pass rate of 73%. (c) The test result for combined bit sequences of randoms pairs of channels. 127 pairs are chosen randomly among the 127 channels, and a new bit sequence is constructed from each pair. 92 out of 127 pass all NIST tests, yielding a pass rate of 72%.

Finally, we verified the absence of short-range correlations in the parallel random bit streams. We combine odd bits from one stream and even bits from another to generate new sequences [See Fig. 5.14(a)]. The NIST tests of such combined bit sequences yield a pass rate of 72 to 73% [Fig. 5.14(b) and (c)], demonstrating that all the original parallel bit streams are truly independent.

Diehard test suite

We conducted the Diehard tests [174] to further assess the quality of parallel random bit streams. A random bit stream of bad quality returns p-values very close to 0 or 1. The entire test suite passes with a 95% confidence interval for p-values between 0.0001 and 0.9999 [175]. Figure 5.15(a) shows the Diehard test results for 100 Mbit from a single channel. The p-values from all the statistical tests are within the interval [0.0001, 0.9999], thus the entire test suite is passed.

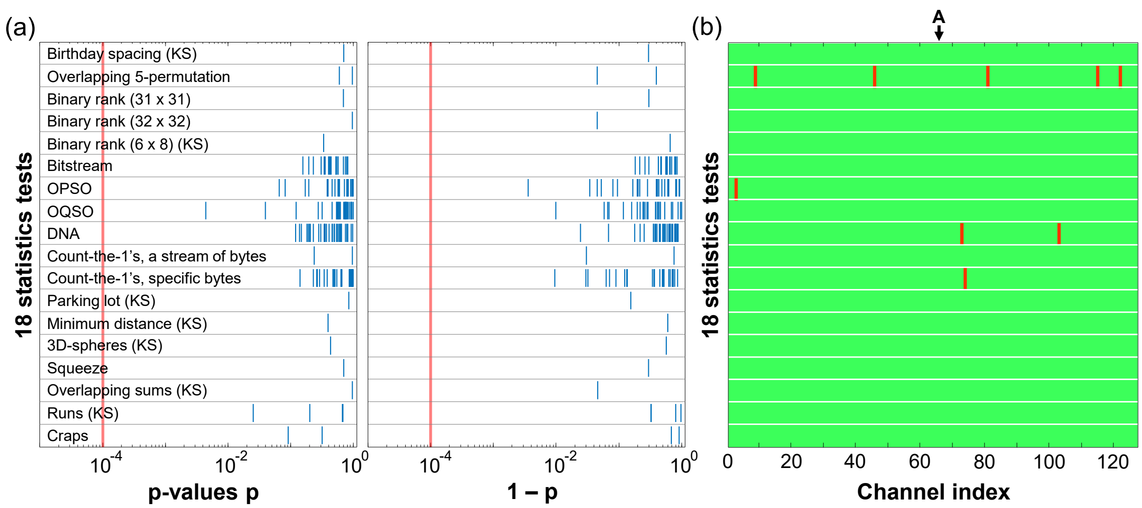

Figure 5.15: **Diehard statistical test results.** (**a**) p-values for 18 kinds of statistical tests are obtained with 100 Mbit from a single channel. Each blue (short, vertical) bar represents one p-value. (KS) denotes that the Kolmogorov-Smirnov test is performed to obtain the composite p-value. The red lines denote the minimum and maximum of the acceptable range of p-values: 0.0001 (left panel for p) and 0.9999 (right panel for $1-p$). (**b**) The test results for all channels. Red color indicates that the random bits fail the test. The black arrow denotes the channel (66th) used for (a). 118 out of 127 bit streams pass all the tests, yielding a pass rate of 93%.

Figure 5.15(b) shows the test results for all channels. Considering the statistical nature of the Diehard test, we evaluate the pass rate over all bit streams. Among the 127 bit streams, 118 bit streams completely pass the Diehard test, yielding a pass rate of 93%.

Finally we performed the Diehard tests on all parallel bit streams As shown in Table 5.1, the average pass rate over 10 separate tests with different data sets is 93%. As a reference, we repeat the tests with random bits generated by one of the widely used pseudo-RBG algorithms, Mersenne-Twister. With the same amount of random bits, the average pass rate over 10 tests is $92 \pm 2\%$. It is very close to the pass rate of all bit streams generated by our laser, thus certifying the randomness of our parallel RBG.

Test set	1	2	3	4	5	6	7	8	9	10	Average
Pass rate (%)	94	94	91	93	92	94	93	91	92	95	93 ± 1

Table 5.1: **Pass rate of the Diehard tests.** The percentage of parallel bit streams from 127 channels, each 100 Mbit long, that completely pass the Diehard tests. The same tests are performed over 10 independent sets of random bits generated by our laser. In total, $127 \times 10 \times 100$ Mbit are tested.

5.8 Information capacity

All these test results certify the randomness of our parallel random bits generated at a cumulative rate of 2 Tb/s $\times 127 = 254$ Tb/s. The very high RBG rate that we obtain indicates an enormous amount of entropy created by our laser. To establish its physical origin, we consider a simple model including only the interference of transverse and longitudinal lasing modes and spontaneous emission noise.

5.8.1 Entropy rate

Cohen-Procaccia entropy rate estimate

Using the Cohen-Procaccia algorithm [146, 176], we compute the entropy rate h_{CP} as a function of the bin size ϵ for intensity digitization and the temporal sampling period τ. For a time trace of emission intensity $I(t)$ at a single position of the laser facet, we construct d-dimensional data sets by introducing time delays: $I_1 = I(t)$, $I_2 = I(t + \tau)$, ...

, $I_d = I(t+(d-1)\tau)$. Then we randomly select N reference points in the d-dimensional space. For each reference point j, we compute $f_j(\epsilon)$, the fraction of other points within a d-dimensional box of width ϵ. The d-dimensional pattern entropy estimate is given by

$$H_d(\epsilon,\tau) = -\frac{1}{N}\sum_{j=1}^{N}\log_2[f_j(\epsilon)]. \tag{5.7}$$

The Cohen-Procaccia entropy rate estimate is then obtained by

$$h_{\mathrm{CP}}(\epsilon,\tau,d) = \tau^{-1}[H_d(\epsilon,\tau) - H_{d-1}(\epsilon,\tau)]. \tag{5.8}$$

Here $\epsilon = (I_{\max} - I_{\min})/2^{N_{\mathrm{digit}}}$, with $I_{\max}$ and $I_{\min}$ being the maximum and minimum intensities, respectively.

Single-channel entropy rate

We estimate the entropy rate h_{CP} for a bit stream generated from the simulated intensity fluctuations of a single spatial channel, simulated with Eq. 5.4. Figure 5.16 shows the convergence of h_{CP} for different embedding dimensions d. Both the interference of a large number of lasing modes and the spontaneous emission noise contribute to entropy generation. As a result of stochastic intensity fluctuations, h_{CP} increases linearly with the number of digits N_{digit}. We compare the entropy rate h_{CP} to the information theoretical limit h_0 given by,

$$h_0 = \min(\tau^{-1}, 2f_{BW})\{N_{\mathrm{digit}} - D_{\mathrm{KL}}[p(I)||u(I)]\} \tag{5.9}$$

where f_{BW} denotes the signal bandwidth, and $D_{\mathrm{KL}}[p(I)||u(I)] = \sum_I p(I)\log_2[p(I)/u(I)]$ is the Kullback-Leibler divergence [177] between the intensity PDF $p(I)$ and the uniform PDF $u(I)$ within the same range of digitization. The fact that h_{CP} reaches the information theoretical limit h_0 [146] indicates that the maximal possible bit rate for a single channel is achieved. This rate exceeds the experimentally obtained value because of the limited temporal resolution and dynamic range of the photodetector.

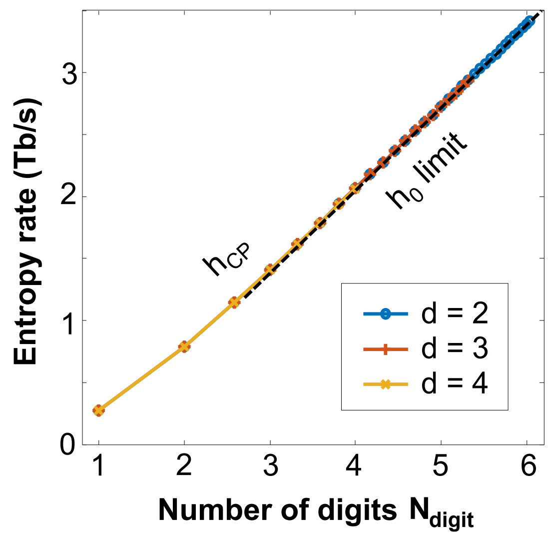

Figure 5.16: **Information capacity of simulated single-channel intensity dynamics.** The Cohen-Procaccia entropy rate estimate h_{CP} in a single spatial channel converges for different embedding dimensions d, and reaches the information theoretical limit h_0 (black dashed line), indicating that the maximum possible RBG rate is reached.

To understand how the number of transverse modes M and the spontaneous emission noise affect entropy generation, we vary M and turn on/off the phase noise when calculating the entropy rate. We calculate the original entropy created by multimode interference using a time trace of intensity without accounting for the finite temporal measurement resolution. The length of the simulated time traces is 1.5 μs. With only one transverse mode and without spontaneous emission noise, the intensity trace is periodic in time [Fig. 5.17(a)]. The periodic modulation results from the temporal beating of the longitudinal modes with equal frequency spacing. Fig. 5.17(d) shows the Cohen-Procaccia entropy rate h_{CP} versus the number of digits N_{digit} for embedding dimension d = 3. As N_{digit} increases, h_{CP} first rises then drops, as the intensity trace repeats itself in time and no additional entropy is created eventually. With M = 3 transverse modes, the intensity

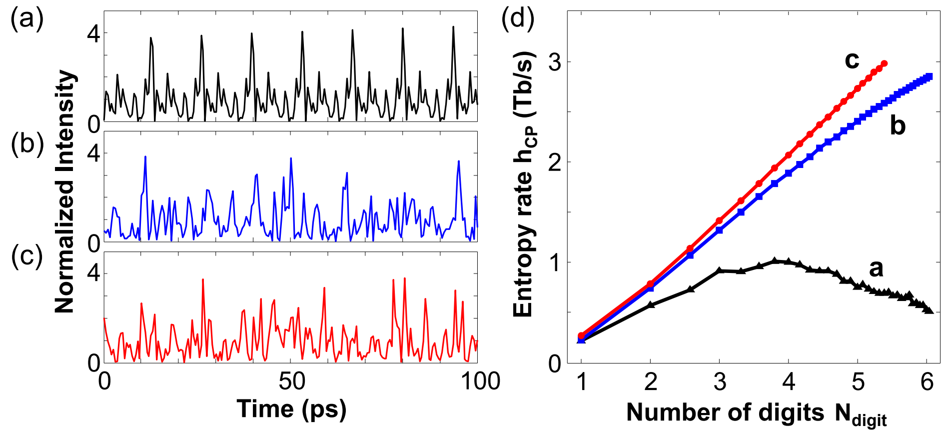

Figure 5.17: **Cohen-Procaccia entropy rate of simulated time traces.** (a) A portion of the simulated intensity time trace $I(t)$ with only the fundamental transverse modes (M = 1), and without spontaneous emission noise. (b) $I(t)$ with M = 3 and without spontaneous emission noise. (c) $I(t)$ with M = 3 and with spontaneous emission noise ($\delta\nu$ = 100 MHz). (d) Entropy rate h_{CP} for the time traces in (a)-(c) with embedding dimension d = 3. The sampling period τ is 1.5 ps.

trace in Fig. 5.17(b) exhibits more complex and aperiodic modulations. Since the transverse and longitudinal mode spacings are incommensurate, the temporal beating of modes produces an intensity trace that will never repeat itself. Consequently, h_{CP} keeps increasing with N_{digit}, first linearly then sublinearly in Fig. 5.17(d). Adding the spontaneous emission noise [Fig. 5.17(c)] contributes to entropy generation as can be seen in a further increase of h_{CP} in Fig. 5.17(d). Moreover, h_{CP} grows linearly with N_{digit} as a result of the stochastic noise.

5.8.2 Number of independent channels

Karhunen-Loeve decomposition

To determine how many independent spatial channels are available for parallel RBG, we investigated the effective spatial degrees of freedom (DoFs) of the emission pattern of our laser. We apply the Karhunen-Loeve decomposition of the intensity pattern $I(x, t)$ simulated with Eq. 5.3. We use a small cavity of length L = 40 μm, width W = 28.2 μm, radius of end facets R = 23 μm and effective refractive index n = 3.37. The mode frequencies $\nu_{m,q}$ and spatial field profiles $\psi_m(x)$ are obtained from the COMSOL calculation of cavity resonances. The amplitudes $A_{m,q}$ of individual lasing modes are calculated with SPA-SALT. Their phases $\phi_{m,q}$ are random numbers in the range of [0,2π).

From the intensity fluctuation $\delta I(x,t) = I(x,t) - \langle I(x,t)\rangle_t$, the spatial covariance matrix $C_{ab} = \langle \delta I(x_a,t)\delta I(x_b,t)\rangle_t$ is constructed and its eigenvalues λ_α are computed [20]. λ_α is sorted from high to low with the index α, and it reflects the amplitude of the corresponding eigenmode in $I(x,t)$. The value of λ_α has a sudden drop at $\alpha = 2M$, where M is the number of transverse lasing modes (Dashed line of Fig. 5.18). Hence, the spatial degrees of freedom is $2M$, where the factor 2 stems from the independent degrees of freedom in the amplitude and phase of the field of one mode.

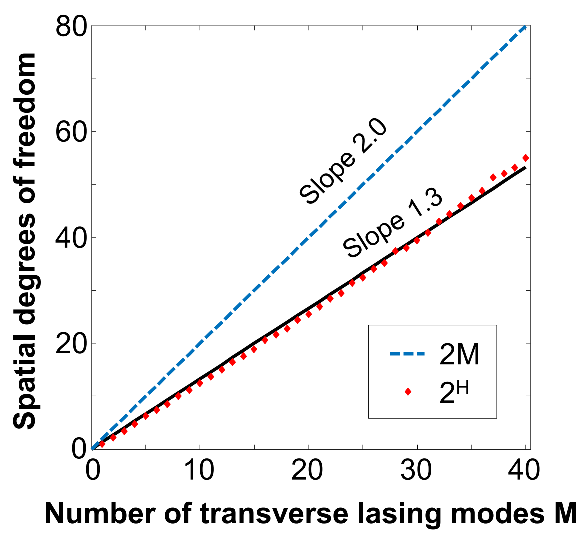

Figure 5.18: **Information capacity of simulated spatio-temporal intensity pattern.** The effective number of spatial degrees of freedom 2^H in the emission pattern grows linearly with the number of transverse lasing modes M. The black solid line is a linear fit. The blue dashed line is the naively expected number of spatial degrees of freedom $2M$, which exceeds 2^H.

Spatial complexity

As a consequence of gain competition and saturation, the mode amplitudes are not uniformly distributed, effectively reducing the spatial DoFs. We quantify the spatial complexity by the Shannon entropy of the eigenvalues [178]

$$H = -\sum_{\alpha} p_\alpha \log_2 p_\alpha, \tag{5.10}$$

where $p_\alpha = \lambda_\alpha / (\sum_\alpha \lambda_\alpha)$ is the normalized eigenvalue. The dotted line in Fig. 5.18 shows the spatial complexity as a function of the number of transverse modes M. The number of effective DoFs 2^H grows linearly with M, but with a slope smaller than 2. By maximizing M with our cavity design, the maximal number of spatial channels is available for parallel RBG. Keeping only three LSBs after digitizing the emission intensity further reduces the spatial correlation length, and the number of independent channels is thus further increased.

5.9 Discussion and conclusion

In this chapter, our proof-of-concept experiment demonstrates parallel RBG in 127 independent channels with a rate of 2 Tb/s per channel. Both the single-channel bit rate and the number of spatial channels are limited by the resolution and efficiency of our experimental apparatus. Improving the temporal resolution and the dynamic range of photodetection can double the single-channel bit rate to $\sim$4 Tb/s. If all the emission is collected with finer spatial resolution, our laser can produce $\sim$500 independent bit streams. Then the cumulative bit rate will reach 2 Pb/s.

It is possible to create a compact parallel-RBG system by integrating fast photodetectors with the laser in a single chip like the sketch in Fig. 5.19. Alternatively, commercially

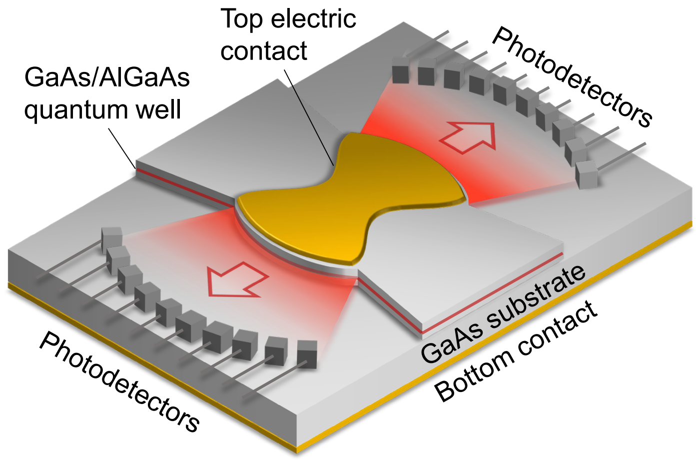

Figure 5.19: **Schematic of a compact parallel RBG system.** The many-mode electrically-pumped semiconductor laser with curved end facets creates ultrafast intensity fluctuation in space and time. Two arrays of fast photodetectors measure the laser emission.

available linear arrays of photodiodes may be butt-coupled to the laser chip on both ends. Although current photodiodes are not fast enough to fully resolve the temporal intensity dynamics, spatial multiplexing with hundreds of channels alone will drastically increase the RBG rate.

Compared to existing RBG schemes, our method, based on a single laser diode without optical feedback or optical injection, is extremely simple yet highly efficient. It does not necessitate any fine-tuning of operation parameters, and its performance is robust against fabrication defects. In our current experiments, the random bit streams are generated by a computer through off-line post-processing including XOR of bit streams from different locations. Real-time streaming of parallel random bits to a computer by conducting the post-processing (including XOR) "on the fly" remains a major technological challenge [161, 162].

Besides the application of RBG, the extraordinary spatio-temporal complexity of our laser facilitates rich, diverse dynamical behavior, which can be finely tailored via the cavity geometry. By varying the spatial structure of cavity modes and tuning their characteristic length scale, we could effectively manipulate their nonlinear interactions with the gain medium to create deterministic spatio-temporal structures on demand. Such an ability to control the number of active modes and their nonlinear interactions promotes our laser as a model system to study many-body phenomena and for harvesting spatio-temporal quantum fluctuations. Because our laser possesses a variety of temporal and spatial scales, it may also be useful for studying optical turbulence with high Reynolds numbers. Despite having a high-dimensional phase space with a complex landscape, our laser is compact and may be used for reservoir computing and for creating physical unclonable functions (PUFs).

Chapter 6

Many-mode surface-emitting lasers with asymmetric cavities

6.1 Introduction

In previous chapters, we studied the impact of cavity geometry on the lasing dynamics of edge-emitting quantum well semiconductor lasers. One drawback of the edge-emitting lasers with asymmetric laser cavities, particularly those with chaotic ray dynamics, is the lack of preferential direction of laser output. To reduce its divergence angle, in chapters 3 and 4, we considered a stable cavity configuration with two curved end facets. However, the emission from edge-emitting lasers still has a broad vertical divergence perpendicular to the wafer surface due to the small thickness of the guided layer. In this chapter, to further improve the emission directionality of many-mode lasers, we investigate a completely different laser structure: vertical-cavity surface-emitting lasers (VCSELs).

VCSELs have a laser cavity formed by a pair of distributed Bragg reflector (DBR) mirrors deposited on the top of a wafer. A cavity with an active layer resides between the DBRs. An optical mode is formed by reflection between two DBRs perpendicularly to the epitaxial layer surface. As a result, optical propagation is predominant in the vertical direction normal to the wafer surface, yielding an output beam of a relatively narrow divergence angle. Because of its compact size, low threshold current, and easy integration, VCSELs have been widely used in display, optical interconnects, and light-based detection and ranging (lidar) applications.

Large-area VCSELs are particularly interesting as they possess huge spatial degrees of freedom. The multiple lasing modes accommodate high emission power, facilitating sensing and imaging applications. In addition, the low spatial coherence of laser emission could be useful for speckle-free imaging [119, 120, 179]. From the physics point of view, many transverse modes enrich the spatiotemporal multimode lasing dynamics [180–184]. Furthermore, unlike edge-emitting lasers with dominant polarization, multiple polarization states exist in VCSELs. As a result, the large-area VCSELs manifest complex polarization dynamics [185, 186].

Here the cavity geometry adds another degree of freedom to control the lasing behaviors. Large-area VCSELs with various asymmetric cavity shapes have been investigated [187–198], revealing that the cavity ray dynamics dictate the spatial profiles of the output beam at the near-field and the far-field. Breaking the structural symmetry of the cavity shape can also boost the output power of large-area VCSELs by increasing the density of states [199]. However, the role of cavity shape for VCSELs in a highly multimode regime has not been extensively investigated yet. Enhancing the number of transverse lasing modes would pave the way to utilize the vast spatial degrees of freedom.

This chapter numerically investigates the impact of cavity shape on the number of lasing modes for large-area VCSELs. We developed a numerical framework to calculate the Q-factor and resonant frequencies of passive modes in VCSELs, applicable to any arbitrary cavity shape with material birefringence. We demonstrate that specific cavity shapes can support a larger number of lasing modes than conventional circular-shape cavities. Such large-area VCSELs with an enhanced number of lasing modes could facilitate speckle-free imaging with an improved emission directionality. Furthermore, our approach to simulating large-area VCSELs could be useful for studying their complex spatiotemporal polarization dynamics.

6.2 Simulation of VCSEL structures

Passive resonances in a laser cavity are the building blocks of studying lasing behavior. As seen in previous chapters, the spatial structure of passive modes can determine the quality factors and mode competitions, which dictate the lasing characteristics. To this end, it is desirable to calculate the passive modes in a large-area VCSEL. Unlike the edge-emitting lasers defined in a two-dimensional space, for VCSELs, there is an additional dimension perpendicular to the wafer surface. Hence, it is needed to simulate a three-dimensional (3D) structure. Methods have been developed to calculate the 3D photonic structures both in passive and active materials [199–201]. However, it is computationally demanding to simulate large-area VCSELs in 3D.

There are several approaches to reduce the computation domain of VCSELs, as illustrated in Fig. 6.1. Here we consider a VCSEL structure with a circular cross-section, consisting of a cavity of length L_{cav} between a pair of DBRs. The most common way to simplify the structure is using reduction by symmetry [See Fig. 6.1(a)]. As the structure has a cylindrical symmetry, the electric field can have a separable form,

$$\mathbf{E}(r,\varphi,z) = \tilde{\mathbf{E}}(r,z)\text{exp}(-im\varphi), \tag{6.1}$$

where m is the azimuthal mode number. Then, the governing wave equation for 3D passive resonances

$$\nabla \times (\mu_r^{-1} \nabla \times \mathbf{E}) - k^2 \epsilon_r \mathbf{E} = 0, \tag{6.2}$$

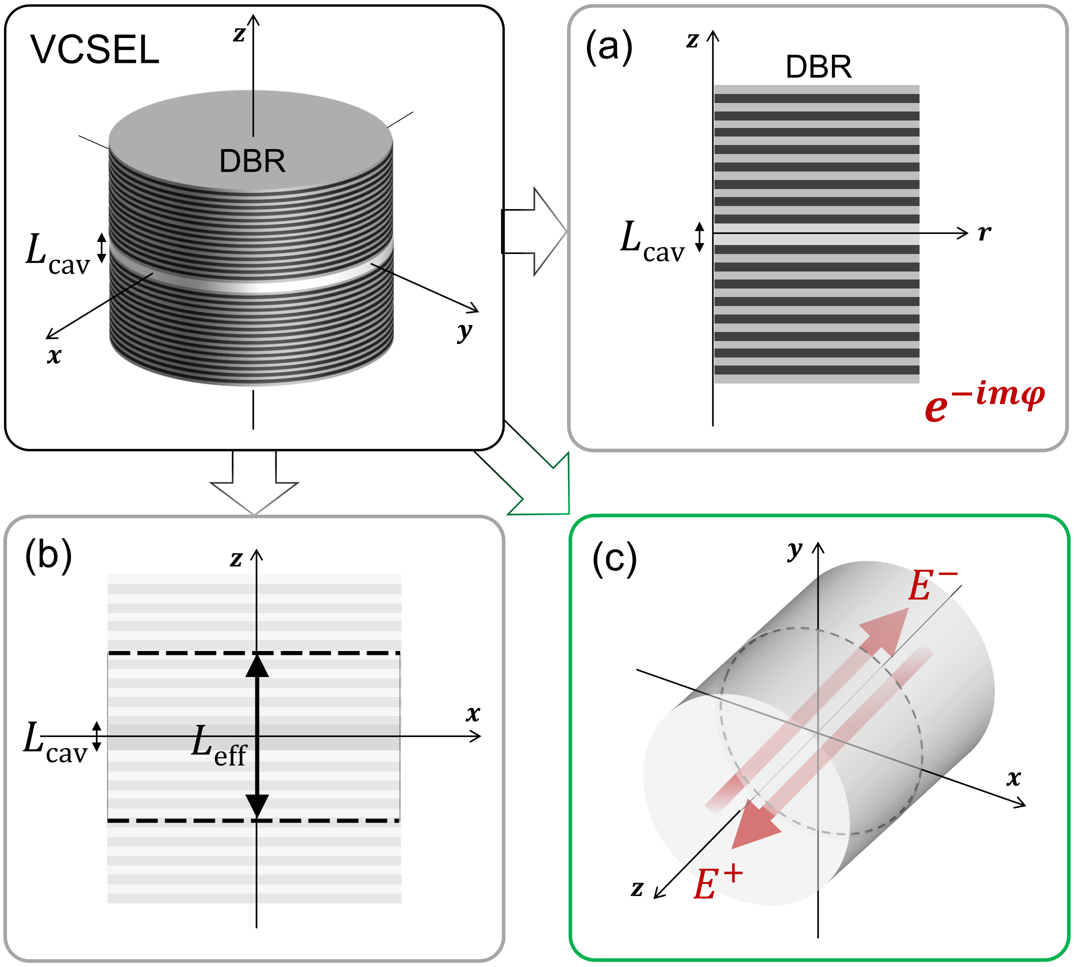

Figure 6.1: **Methods to calculating the passive modes in a three-dimensional VCSEL.** (Upper left) the original VCSEL structure consisting of a cavity with length L_{cav} sandwiched between two DBRs. (a) For a cylindrically symmetric structure, the computational domain can be reduced to a two-dimensional space with radial and axial coordinates. The solutions have azimuthal dependence $e^{-im\phi}$, where m is the azimuthal mode number. (b) The DBRs can be replaced by highly reflective mirrors (dashed lines) spaced by effective cavity length L_{eff}, which simplifies the simulation domain. (c) An optical mode of VCSEL can be approximated by a superposition of forward- and backward-propagating guided modes in a waveguide with the same cross-section.

can be rewritten as,

$$\left(\nabla - i\frac{m}{r}\hat{\varphi}\right) \times \left[\mu_r^{-1}\left(\nabla - i\frac{m}{r}\hat{\varphi}\right) \times \tilde{\mathbf{E}}\right] - k^2\epsilon_r\tilde{\mathbf{E}} = 0, \tag{6.3}$$

where ϵ_r and μ_r are the relative permittivity and permeability of the resonator, and k is the complex wavevector of a passive resonance. Now Eq. 6.3 solves for the electric field $\tilde{\mathbf{E}}(r, z)$ defined in a 2D domain with radial (r) and axial (z) coordinates. This symmetry reduction can significantly reduce the computation load. However, it is limited to structures with perfect cylindrical symmetry, which is not applicable for asymmetric cavities or birefringent material. As we are mainly interested in breaking the structural symmetry, a different method that does not rely on cylindrical symmetry is desirable.

Another method is to approximate the DBR as a single highly reflective mirror, as shown in Fig. 6.1(b). The hard mirror resonator with vanishing boundary conditions can replace the highly reflective DBRs [202–204]. As optical mode penetrates some distance into the DBRs as an evanescent wave [205], the effective cavity length L_{eff} between two highly reflective mirrors is larger than the actual cavity length L_{cav} between the DBRs. Without the stacks of thin dielectric layers, this simplified structure dramatically reduces the computation load. Moreover, as this method does not rely on symmetry in a transverse plane, it enables the simulation of any arbitrary cavity shape and anisotropic materials. However, given a single mirror, it is challenging to model the complex reflection behavior from the DBR: e.g., spectral response, phase shift, and the dependence on the angle of incidence. Hence, it is difficult to accurately estimate the Q-factors of passive resonances, especially for high-order transverse modes with a relatively large transverse wavevector.

Therefore, we resort to an approximation described in Fig. 6.1(c). We approximate a VCSEL mode as a superposition of forward and backward propagating waves between the DBRs. The propagating wave can be calculated by solving the guided modes of a waveguide with the same cross-section. It reduces the simulation dimension from 3D to 2D, greatly accelerating the computation. The reflection spectra of the DBRs, which are calculated separately, are then incorporated to estimate the quality factor of each mode. The following sections elaborate on the procedure and validate our approximation.

6.3 Approximation of VCSEL resonances

Simulation parameters

We first obtain the passive modes of the original 3D VCSEL structure. To this end, we simulate a circular-shape VCSEL with symmetry reduction [Fig. 6.1(a)]. We use COMSOL 2D axisymmetric model with the eigenfrequency analysis module.

The simulated VCSEL has a GaAs/AlAs epiwafer structure. The refractive index of GaAs and AlAs are n_H = 3.52 and n_L = 2.97, respectively. We design the DBR with the stop-band centered at λ_0 = 950.0 nm. To do so, the DBR has the repeated quarter-wave layers of GaAs and AlAs with thicknesses of $\lambda_0/4n_{H,L}$, which yield 67.47 nm and 79.97 nm, respectively. Both top and bottom DBRs have 19.5 pairs of GaAs/AlAs layers. A GaAs λ-cavity, with a thickness of L_{cav} = λ_0/n_H = 269.9 nm, resides between two DBRs. We assume that the entire layer structure is embedded vertically between two GaAs substrates. To this end, the impedance boundary conditions with a refractive index of n_H are imposed at the uppermost and lowermost layers.

In a radial coordinate, we assume a cavity with a radius of 5 μm. For conventional VCSELs, the lateral cavity boundary is typically defined by ion implantation or oxidization. To simply the structure and enhance the lateral confinement, we assume a pillar structure with the lateral boundary completely etched and exposed to air [See Fig. 6.1]. We impose the scattering boundary condition at the lateral end of the simulation domain.

Optical modes in a VCSEL

Using the reduction by symmetry method, we calculated 134 passive modes within the spectral range between 938.0 and 950.0 nm. Figure 6.2(a) shows an exemplary transverse profile of the calculated passive modes at the middle of the λ-cavity (z = 0). Due to the circular cavity shape with the high index contrast at the boundary, typical solutions are whispering-gallery modes. The Fourier transform in Fig. 6.2(b) reveals a circular distribution of spatial frequencies. For each passive mode, we can define a transverse wavevector k_t, which corresponds to the radius of the distribution in Fig. 6.2(b). For higher-order transverse modes, the magnitude of k_t becomes larger.

Figures 6.2(c) and (d) show the schematic of optical propagation in a VCSEL. Reflection occurs at the dielectric interface between the cavity and a DBR. The wavevector **k** determines the resonant frequency $\lambda = 2\pi n/|\mathbf{k}|$. The transverse component k_t is related to the transverse mode profile, as shown in Figs. 6.2(a) and (b). The axial component k_l is determined by the vertical cavity structure with DBRs, hence barely depends on the transverse mode profile. For a given wavevector **k**, we can define the angle of incidence θ on the cavity-DBR interface by $\theta = \tan^{-1}(k_t/k_l) \simeq k_t/k_l$ when this angle is sufficiently small. Higher-order transverse modes have a larger θ at the cavity-DBR interface.

Figures 6.2(c) and (d) also illustrate two possible polarization states. The s-polarization has the electric field perpendicular to the plane of incidence. Thus the electric field is dominant in the transverse plane (TE modes). On the other hand, the p-polarized light has the electric field parallel to the plane of incidence, and the magnetic field is dominant in the transverse plane (TM modes).

The polarization state is a dominant factor determining the mirror reflectivity. Figures 6.2(e) and (f) show the reflectivity as a function of the angle of incidence θ, calculated by the optical transfer matrix method [206]. For the s-polarization, the reflectivity in-

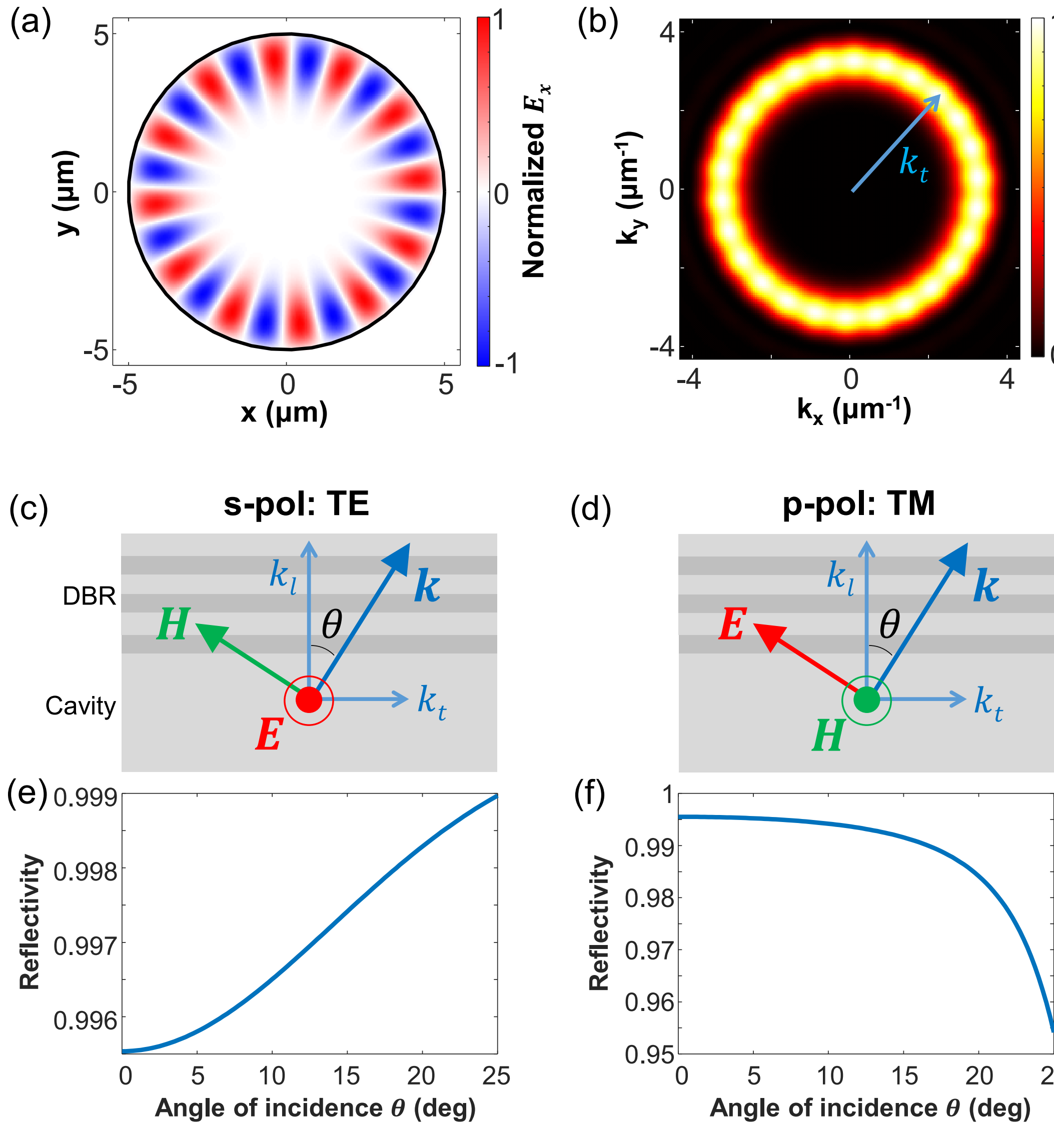

Figure 6.2: **A passive mode of a VCSEL with cylindrical symmetry.** (a) An exemplary electric-field distribution of a transverse mode profile at z = 0. The mode was obtained by simulating a VCSEL (radius of 5 μm) with reduction by cylindrical symmetry. The resonant wavelength is 940.0 nm, and the Q-factor is 5131. (b) The Fourier transform of the transverse mode profile in (a). The radius of the spatial frequency distribution defines the transverse wavevector k_t. (c,d) Possible polarization states of optical propagation. **E**, **H**, and **k** denote the electric field, magnetic field, and wavevector, respectively. k_t and k_l represent the wavevectors in a transverse and axial (vertical) direction. The s-polarization has **E** perpendicular to the plane of incidence, while the p-polarization has **E** parallel to it. (e,f) The reflectivity of the DBR calculated by optical transfer matrix method. With an increasing angle of incidence, the reflectivity increases for the s-polarized light, while it decreases for the p-polarized light.

creases with θ. In contrast, p-polarized light has decreasing reflectivity with θ. For a given angle of incidence θ smaller than Brewster's angle (not shown in Fig. 6.2), s-polarized light has a larger reflectivity than p-polarized light.

Propagating modes in a waveguide

As mentioned in Fig. 6.1(c), we approximate the VCSEL modes by a superposition of propagating and counter-propagating waves between two DBRs. We calculate the guided modes of an optical waveguide with the same cross-section as that in Fig. 6.2. We use a 2D COMSOL model with the mode analysis module. We set a circular region in the simulation with a radius of 5 μm. We choose the refractive index n_0 of 3.295, which is close to the averaged index of the DBRs $(n_H + n_L)/2$ = 3.245. The air surrounds the circular cross-section of the core, and we imposed perfectly matched layers at the outermost parts.

Figure 6.3 compares the optical modes in a VCSEL and an optical waveguide. An example of the transverse profile of the highest-order mode is shown in Fig. 6.3(a) and (b). The spatial profile of each mode for the VCSEL and the fiber has a good agreement with each other.

While the calculation of a VCSEL yields the resonant wavelengths (or frequencies), the mode analysis gives the effective indices n_{eff} of the guided modes. As shown in Fig. 6.3(c), the resonant wavelengths of a VCSEL and the effective indices of fiber have a linear relation. Here we convert n_{eff} of fiber to the corresponding wavelength,

$$\lambda = \lambda_0 n_{\text{eff}}/n_0, \tag{6.4}$$

where λ_0 = 950.0 nm as defined in the simulation of VCSELs. From Eq. 6.4, high-order guided modes will have shorter λ, which is consistent with VCSELs. The resonant wavelengths of VCSEL and the corresponding wavelengths of the guided modes in a fiber show

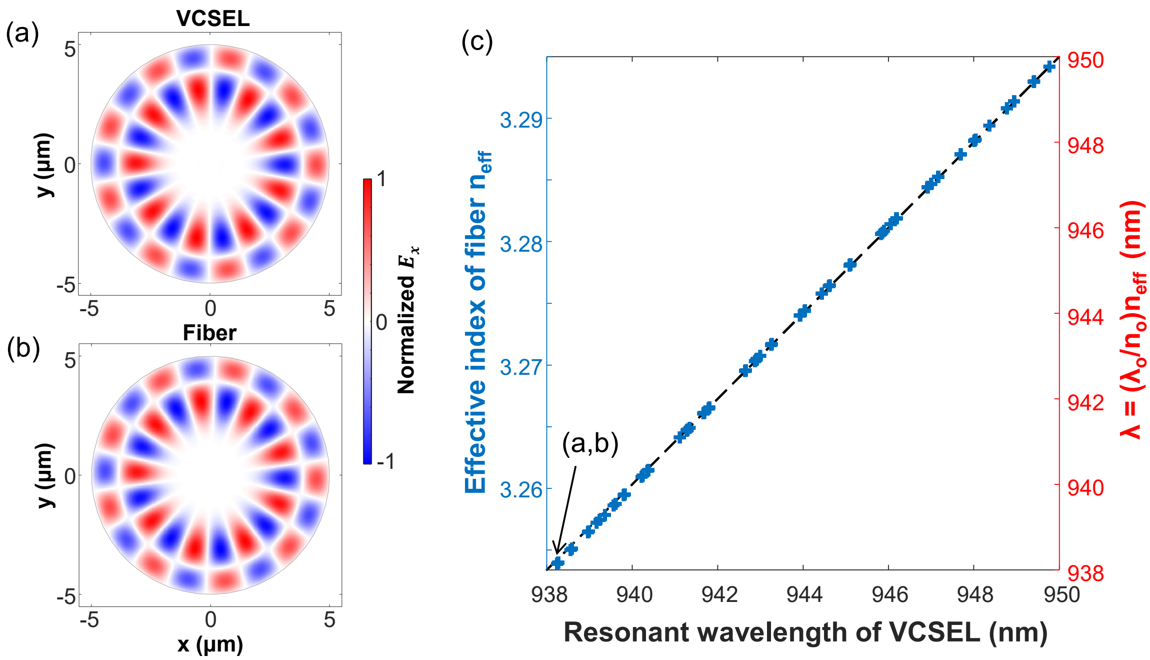

Figure 6.3: **Correspondence between optical modes in a VCSEL and an optical fiber.** The transverse electric-field profile of (a) a passive mode in a VCSEL and (b) a guided mode in an optical fiber show an excellent agreement. The resonant wavelength is 938.1 nm. (c) Scatter plot of 134 resonant wavelengths of a VCSEL and the effective indices of an optical fiber n_{eff}, showing a linear dependence. The arrow represents the mode in (a) and (b). The right vertical axis (red) represents n_{eff} converted into wavelength by the relation $\lambda = (\lambda_0/n_0)/n_{\text{eff}}$, where $n_0 = 3.295$ is the refractive index of the fiber core and $\lambda_0 = 950$ nm is the resonant wavelength of the DBR structure. The dashed black line is where the wavelengths of optical modes for the VCSEL and the fiber exactly match.

an excellent agreement. It validates our approximation with a waveguide to calculate the resonant frequencies of the VCSEL.

Estimation of Q-factors

Next, we estimate the Q-factors of the VCSEL modes. We start with the Q-factor of an optical mode in a Fabry-Perot geometry,

$$Q = 2\pi \frac{n_0 L}{\lambda_0 \ln(1/R)}, \tag{6.5}$$

where R is the reflectivity of the mirror, and L is the cavity length between two mirrors. The reflectivity R is a function of the angle of incidence and the polarization, which could be determined as follows.

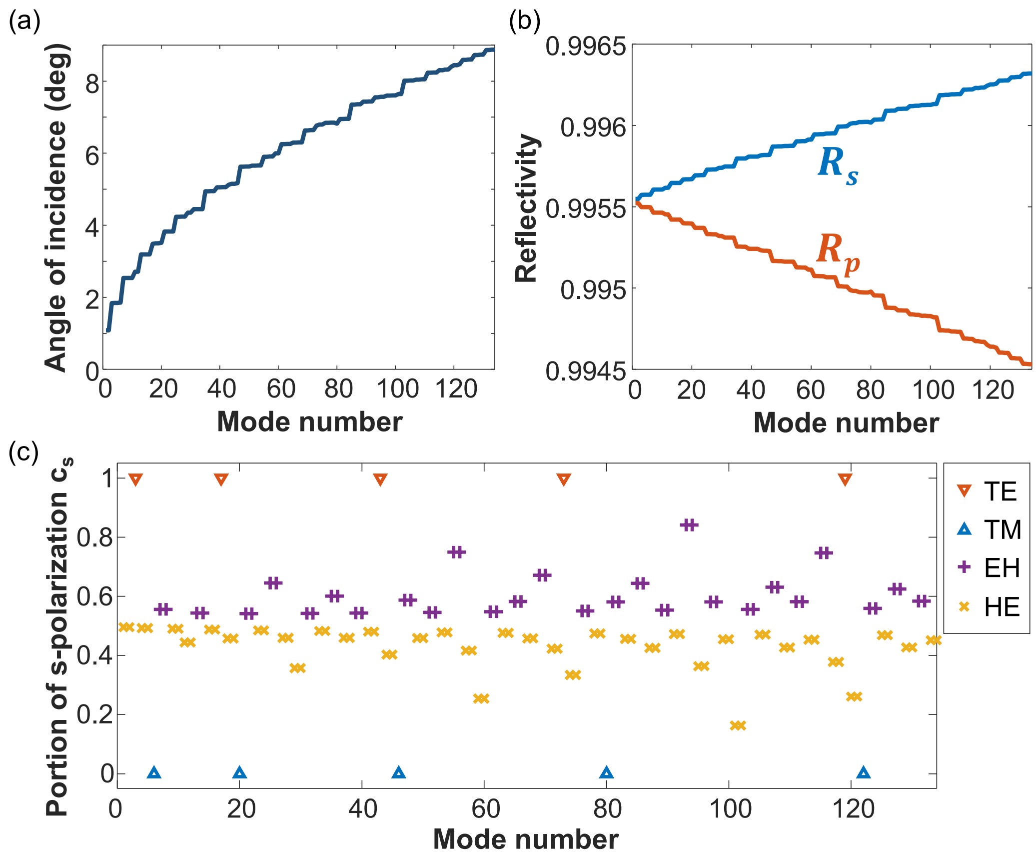

Figure 6.4: **Reflection behavior of optical modes at a DBR.** The guided modes in an optical fiber are used to simulate the reflection from the DBR. (a) The angle of incidence as a function of the mode number. High-order modes have a large angle of incidence. (b) The reflectivity of the DBR for s-polarization (R_s) and p-polarization (R_p) with the angle of incidence from (a). (c) The portion of the s-polarized wavevector component in the guided modes. The different polarizations in a circular waveguide (TE, TM, EH, HE) are denoted with distinct markers. The p-polarized component c_p is given by $1 - c_s$. TE polarization has c_s equal to 1, indicating pure s-polarization. A hybrid mode (EH) has c_s larger than 0.5, as TE-component is more dominant than TM-component.

For a guided mode with transverse profile $\mathbf{E}(x, y)$, we consider its Fourier transform $\mathbf{E}(\mathbf{k}_t)$ in a domain of transverse wavevector $\mathbf{k}_t = (k_x, k_y)$. The Fourier components are normalized by $\int |\mathbf{E}(\mathbf{k}_t)|^2 d\mathbf{k}_t = 1$. Then the averaged transverse wavevector is given by,

$$\langle|\mathbf{k}_t|\rangle = \int |\mathbf{k}_t||\mathbf{E}(\mathbf{k}_t)|^2 d\mathbf{k}_t. \tag{6.6}$$

The averaged angle of incidence $\langle\theta\rangle$ can be defined by,

$$\langle\theta\rangle = \frac{\langle|\mathbf{k}_t|\rangle}{k_l}, \tag{6.7}$$

where $k_l = 2\pi n_0/\lambda_0$ is the longitudinal wavevector component. Figure 6.4(a) shows $\langle\theta\rangle$ of the guided modes in a circular waveguide. The mode number is arranged from longer to shorter resonant wavelengths. As high-order modes have a larger transverse wavevector, the angle of incidence monotonically increases with the mode number.

Next, we calculate the reflectivity of the DBRs by the transfer matrix method [206]. For both s- and p-polarizations, the reflectance at the angle of incidence of $\langle\theta\rangle$ is computed. Here the incident wavelength is set to $\lambda_0\cos(\langle\theta\rangle)$ in order to maintain the wavelength in an axial direction as λ_0. Figure 6.4(b) shows the reflectivity for both polarizations. The reflectivity can be increased (s-polarized) or decreased (p-polarized) for higher-order modes.

Each guided mode can have either p-polarized or s-polarized wave component, or mixed states. To determine the portion of each polarization, we introduce the quantities:

$$c_s = \int |\hat{\mathbf{k}}_t \times \mathbf{E}(\mathbf{k}_t)|^2 d\mathbf{k}_t, \tag{6.8}$$

$$c_p = \int |\hat{\mathbf{k}}_t \cdot \mathbf{E}(\mathbf{k}_t)|^2 d\mathbf{k}_t, \tag{6.9}$$

where c_s and c_p represent the portion of s-polarized and p-polarized wave components, and $\hat{\mathbf{k}}_t$ is the unit transverse wavevector. The summation of c_s and c_p equals to 1. Figure 6.4(c) shows c_s for the guided modes. For a circular waveguide that was simulated here, the polarization of a guided mode can be classified into TE, TM, EH, and HE modes [207]. Different polarizations are denoted with distinct markers in Fig. 6.4(c). The quantity introduced in Eq. 6.8 exactly captures these polarization states: TE-modes with s-polarization [See Fig. 6.2(c)] has $c_s = 1$. Conversely, TM-modes with p-polarization [Fig. 6.2(d)] has $c_s = 0$. For hybrid modes, EH modes have dominant transverse electric-field, thus have c_s larger than 0.5. For HE modes with dominant transverse magnetic-field, c_s is smaller than 0.5.

For the cavity length L, we should use the effective cavity length L_{eff}, which takes into account the penetration distance into the DBR. We obtained L_{eff} using Eq. 6.5, where the Q-factor of the fundamental mode (HE11) and the reflectivity R at the normal incidence $\theta = 0$ are used. It yields the effective cavity length $L_{\text{eff}} = 1065$ nm. Alternatively, we estimated the effective cavity length by fitting an evanescent intensity decay in the DBR with an exponential function. The fitted penetration depth yields the effective cavity length (two times penetration depth plus the cavity length) of 1139 nm, which is different from L_{eff} by 7 percent. This deviation could be attributed to the non-uniform refractive index distribution in the DBR layers.

Lastly, we combine every quantity in Eq. 6.5. We can estimate the quality factor Q of a VCSEL mode using the guided mode solutions by,

$$Q^{-1} = c_p Q_p^{-1} + c_s Q_s^{-1}, \tag{6.10}$$

where

$$Q_{p,s} = 2\pi \frac{n_0 L_{\text{eff}}}{\lambda_0 \ln(1/R_{p,s})} \tag{6.11}$$

represent the Q-factors of pure p- or s-polarized light. Considering that there are two parallel intensity decay channels for p- and s-polarizations, the effective decay rate should be the weighted sum of the independent decay rates, or the inverse of the Q-factors, as shown in Eq. 6.10.

Validation of the approximation

A circular cavity with perfect cylindrical symmetry allows us to calculate the 3D resonances using reduction by symmetry. It could be a reference point to verify our approximation. Figure 6.5(a) compares the distributions of its Q-factors from both 3D calculation and our approximation in 2D. Our results using Eq. 6.10 show an excellent agreement with the 3D simulation results. It validates our approximation with the guided modes to calculate the Q-factors and the resonant wavelengths of passive modes in a VCSEL.

The Q-factors have a narrow distribution of around 5200, whose value is determined by the reflectivity of the DBRs and the effective cavity length. For the shorter wavelength, the Q-factor can be higher or lower than the averaged level due to the larger angle of incidence. We note that the Q-factor varies by only $\sim$20%, which is significantly smaller than circular edge-emitting microdisk lasers whose Q-factors differ by several orders of magnitude.

The mode with the highest Q-factor will dominate the laser emission. As shown in Fig. 6.5(b), the highest-Q mode is a high-order TE mode with pure s-polarization. To visualize the direction of the wavevector, we compute the Poynting vector S_t, given by $\mathbf{E}\times\mathbf{H}$ projected onto the transverse plane. For the TE mode in Fig. 6.5(b), the electric field is perpendicular to the transverse flux direction at every spatial location [See Fig. 6.5(d)]. Conversely, the lowest-Q mode is a high-order TM mode with pure p-polarization [Fig. 6.5(c)]. In the transverse plane, the electric field is parallel to the transverse flux direction at every location [Fig. 6.5(e)]. These passive resonance with the extreme Q-factors differ from the edge-emitting microdisk laser, whose highest-Q mode is the whispering gallery-type mode with a spatial profile localized at the cavity boundary.

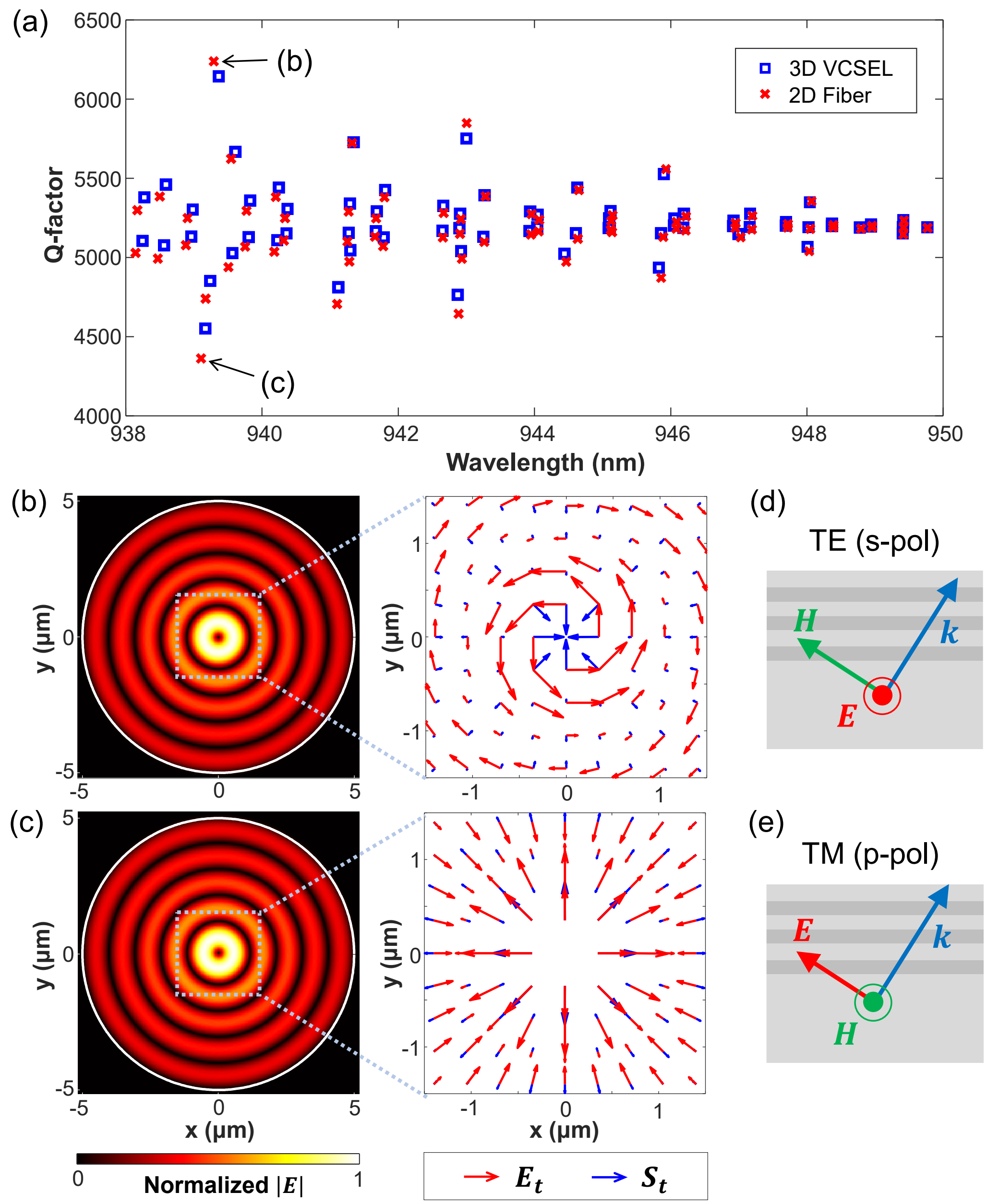

Figure 6.5: **Validation of approximating VCSEL modes by guided modes in a fiber.** (a) Blue squares: The mode distribution of a circular 3D VCSEL obtained using reduction by symmetry. It shows excellent agreement with the 2D fiber approximation (red crosses). (b) The transverse modal profile of the highest Q-factor (Q = 6238, $\lambda = 939.3$ nm). The red arrows represent the transverse electric field E_t, and the blue arrows represent the transverse Poynting vector S_t, defined by $\mathbf{E} \times \mathbf{H}$ projected onto a transverse plane. The highest-Q mode is a TE-mode with pure s-polarization, in which E_t and S_t are perpendicular at every location. (c) The lowest Q-factor mode (Q = 4361, $\lambda = 939.1$ nm) is a TM-mode with pure p-polarization, in which E_t and S_t are parallel to each other. (d,e) The schematic of TE and TM polarization, illustrating the modes in (b) and (c), respectively.

6.4 Calculating the passive modes

This approximation method greatly expands the variety of 3D cavity structures we can simulate: we can now calculate the passive modes with material birefringence and/or structural asymmetry, which are presented in this section.

6.4.1 Material birefringence

Typical AlGaAs wafers have anisotropic refractive indices depending on the crystal structure. The material birefringence is closely related to the polarization of the laser emission [208–211], and also can have a significant impact on dynamics of large-area VCSELs [184]. The difference in refractive index is on the order of 10^{-4} for AlGaAs materials [212, 213]. To this end, we introduce material birefringence by assuming the refractive index in the x- and z-direction $n_x = n_z = 3.2950$ and that in the y-direction $n_y = 3.2951$.

Figure 6.6(a) shows the passive mode distribution with material birefringence. Introducing the material birefringence does not significantly impact the distribution of quality factors. The modes with the highest and lowest quality factors are shown in Figs. 6.6(b) and (c). The spatial distributions of the wavefunctions correspond to the bouncing-ball orbits. The highest-Q mode [Fig. 6.6(b)] has the optical propagation in the x-axis, as shown in the direction of the transverse Poynting vectors. The electric field mostly aligns along the y-direction, perpendicular to the optical propagation. It resembles the s-polarized light, whose transverse electric field is normal to the transverse wavevector. In contrast, the electric field aligns parallel to the optical propagation in a transverse plane for the lowest-Q modes. This mode mainly contains p-polarized light, whose transverse electric field is parallel to the transverse wavevector.

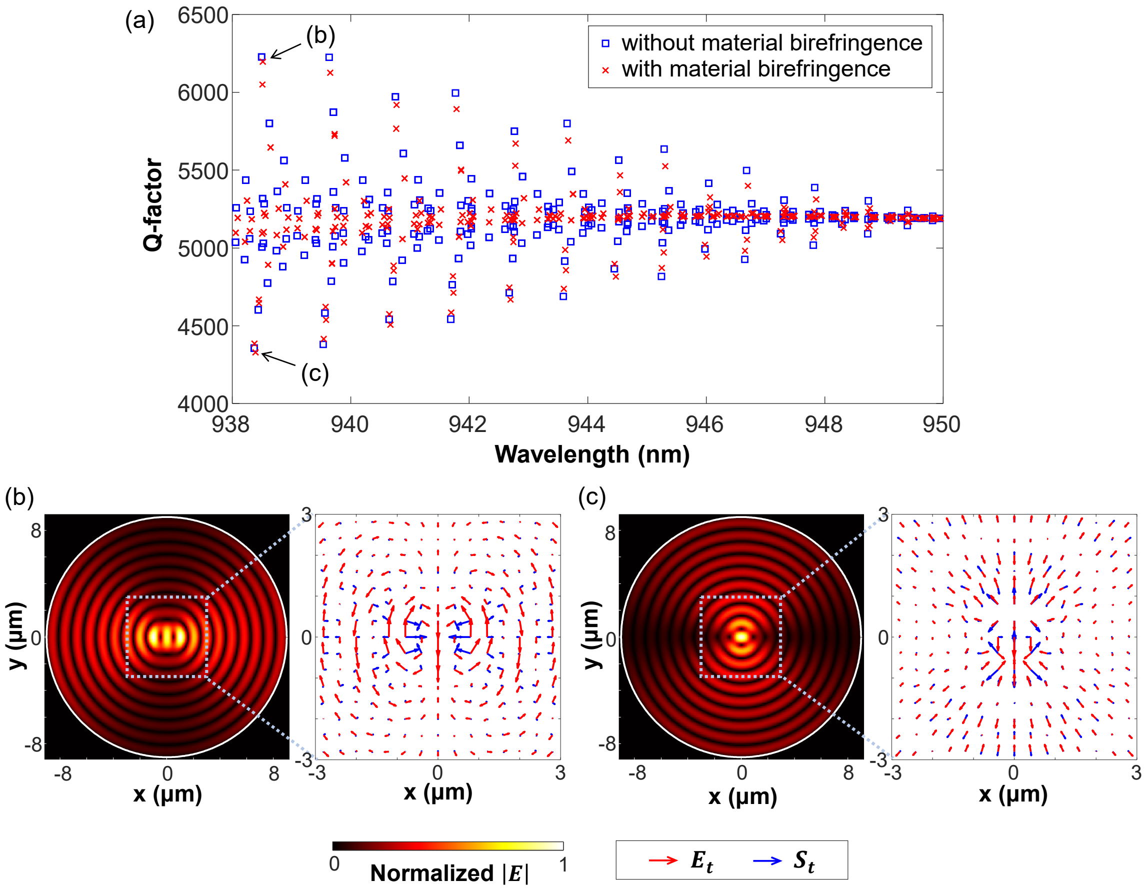

Figure 6.6: **Passive resonances of a VCSEL with material birefringence.** (a) The distribution of 456 passive modes in a 9 μm-radius VCSEL. Compared to the isotropic material (blue square), introducing the material birefringence of $n_y - n_x = 10^{-4}$ (red cross) does not have a significant impact on the mode distribution. (b) The mode profile of the highest-Q mode (Q = 6197, λ = 938.5 nm). On the right, the central region is zoomed-in and plotted with the transverse electric field and Poynting vector distributions (red arrows). The field amplitude and Poynting vector distribution reveal the optical propagation along the x-axis. The electric field is mostly parallel to the y-axis, perpendicular to the optical propagation. (c) The mode profile of the lowest-Q mode (Q = 4329, λ = 938.4 nm). The electric field is parallel to the optical propagation.

6.4.2 Structural asymmetry

Next, we break the symmetry in the cavity geometry. We consider a D-shaped cavity of R = 10 μm with an isotropic refractive index of 3.295. To ensure that the same number of modes are calculated, the cavity area is kept the same as the circular cavity in Section 6.4.1 (254 μm^2). Figure 6.7(a) shows the distribution of passive modes in a D-shaped VCSEL. For circular and D-shaped cavities, the average level of Q-factors is the same, around 5200. However, the distribution of Q-factors in a D-cavity is significantly narrower than in the circular cavity.

The highest and lowest-Q modes are shown in Figs. 6.7(b) and (c). Both of them have bouncing-ball orbits along the y-axis but have different polarizations. In a transverse plane, the highest-Q mode has an electric field nearly perpendicular to the optical propagation (s-pol). In contrast, the lowest-Q mode has an electric field almost parallel to it (p-pol). This result tells us that, as we have previously seen in Section 6.4.1, the bouncing ball orbits in a VCSEL are likely to have maximum or minimum Q-factors, as they possess almost pure s- or p-polarization.

Compared to Fig. 6.6(a), the modes with remarkably high or low Q-factors are significantly reduced in a D-shaped VCSEL. We attribute this to the chaotic ray dynamics in a D-shaped cavity. In a wave-chaotic cavity, an optical mode can barely maintain pure s- or p-polarization but has mixed polarization states. These hybrid polarization states could have moderate reflectivity, as the relatively high reflectivity of s-polarization and relatively low reflectivity of p-polarization are mixed. As a result, this cavity shape can narrow the distribution of Q-factors. Such a narrow distribution of Q-factor may enhance the number of lasing modes, as many modes can have similar lasing thresholds and lase together.

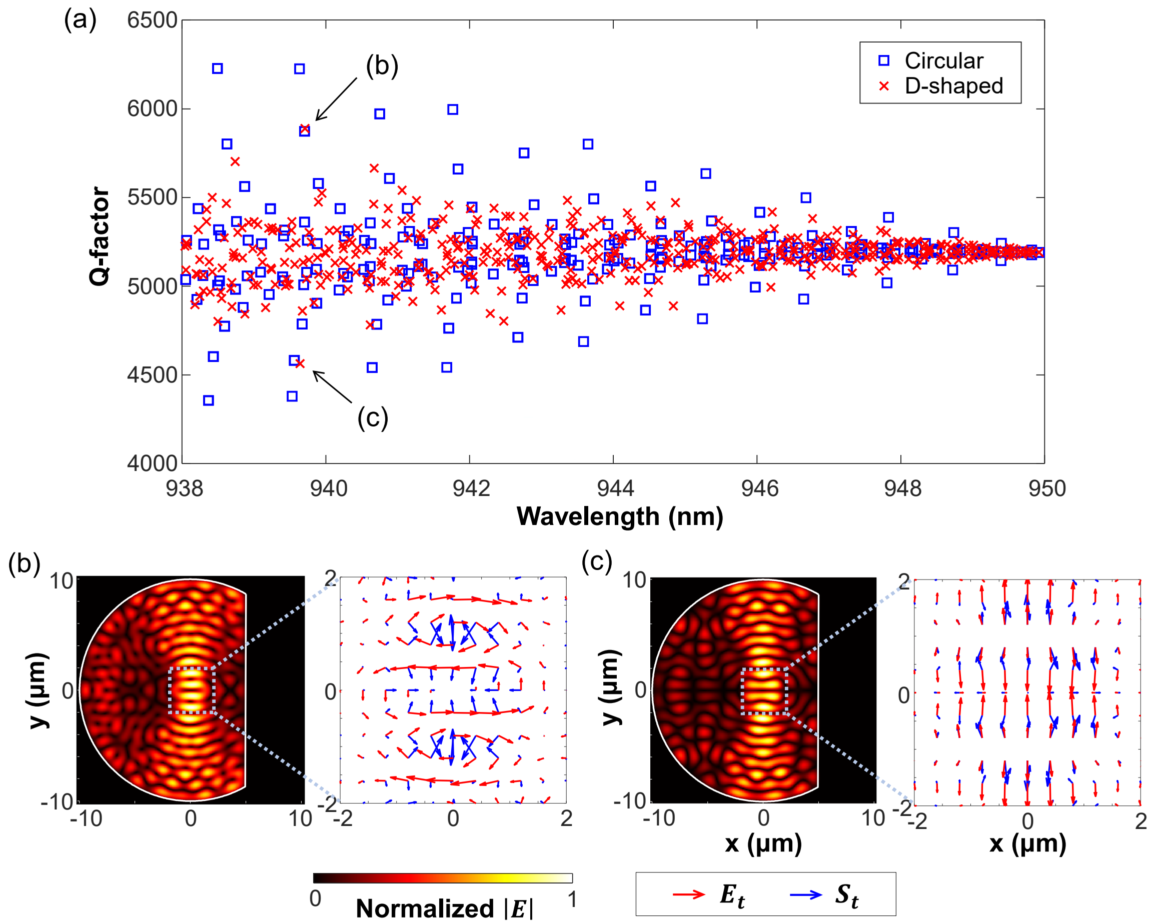

Figure 6.7: **Passive resonances in a VCSEL with asymmetric cavity shape.** (a) The distribution of 451 passive modes in a 10 μm-radius D-shaped VCSEL. No material birefringence is introduced. Compared to the circular cavity with the same area (blue square), the D-shaped cavity (red cross) has a considerably narrower distribution of Q-factors. (b) The mode profile of the highest-Q mode (Q = 5722, λ = 940.7 nm) of a D-shaped cavity corresponds to a bouncing-ball orbit. The electric fields (red arrows) align perpendicularly to the optical propagation direction (blue arrows). (c) The lowest-Q mode (Q = 4596, λ = 939.7 nm) also exhibits a bouncing-ball orbit. It has the electric field parallel to the optical propagation.

6.4.3 Birefringent asymmetric cavities

Lastly, we consider both the material birefringence and the asymmetric cavity shape. The interplay between material anisotropy and cavity geometry leads to diverse polarization states of light [214–216]. Our method would help study such behaviors; below, we show an example.

In Fig. 6.8, we consider a D-shaped cavity in a spatial coordinate (x, y), where x denotes the symmetric axis of the cavity [See the inset of Fig. 6.8(e)]. Here we assume birefringent axes (x', y') tilted by the angle α from the coordinate axes (x, y). The refractive index in x' and y' directions are 3.2950 and 3.2951, respectively.

Figure 6.8(a) compares the mode distributions with and without the material birefringence. Here α is 0 degree, in which the position coordinate and the birefringence axes match. No significant change in the distribution of Q-factors is observed. As the symmetry of the cavity is already broken by its geometry, adding additional asymmetry in the same directions by material anisotropy will have limited effects.

Here tilting the birefringent axes can play a role. As shown in Fig. 6.8(b), when α is 45 degrees, the distribution of the Q-factor can be further narrowed. Figures. 6.8(c) and (d) show the modes having the highest and lowest Q-factors when α is 45 degrees. The spatial distribution of the field amplitude is no longer symmetric with respect to the x-axis but tilted due to the material birefringence. By rotating the birefringent axes, which further breaks the symmetry of the cavity, s- and p-polarized lights can be mixed further. In turn, the most narrow distribution of Q-factors is attained when α is 45 degrees [Fig. 6.8(e)]. As shown here, manipulating material anisotropy would also impact the lasing characteristics of a VCSEL, and our method would be an efficient tool to simulate such effects.

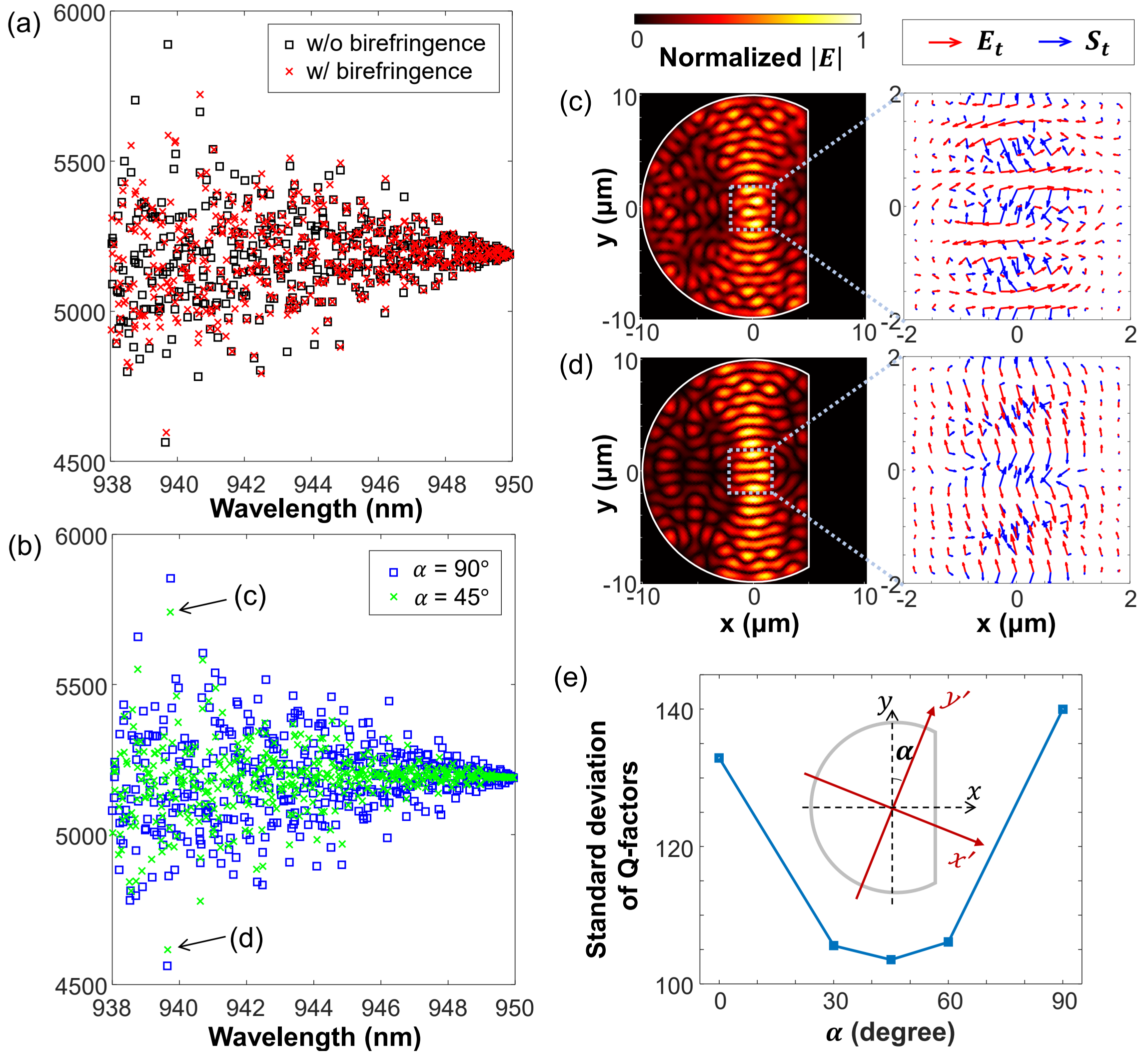

Figure 6.8: **Interplay of material birefringence and structural asymmetry.** (a) Introducing material birefringence in a D-shaped VCSEL. There is no significant difference in mode distributions between the isotropic (black square) and birefringent materials with $n_y - n_x = 10^{-4}$ (red cross). (b) Mode distributions with different orientations of the birefringent axes. The inset of (e) defines the spatial coordinates (x, y) and the material birefringent axes (x', y') with the tilt angle of α. With α = 45 degrees, the distribution of Q-factors is narrowed down compared to α = 90 degrees. (c,d) The spatial mode profiles with the highest Q (Q = 5741, λ = 939.7 nm) and the lowest Q (Q = 4617, λ = 939.7 nm) for α = 45 degrees. They are no longer symmetric with respect to y = 0 but slightly tilted due to the material birefringence. (e) The standard deviation of the Q-factors with different values of α. It is minimized when the structural and birefringent axes are mismatched by 45 degrees.

6.5 Number of lasing modes

We investigate how cavity shape can affect the number of lasing modes in a broad-area VCSEL. We employ SPA-SALT [87, 88] simulation, which takes into account the gain competition. Figure 6.9 shows eight different types of cavity geometry. The cavity size is designed so that all the geometries have the same area or density of states. Figure 6.9(a) is a conventional circular cavity with a radius of 9 μm. We include the cavities with chaotic ray dynamics [Figure 6.9(b-d)] and those with integrable ray dynamics [Figure 6.9(e-f)], which were investigated in Chapter 2. Additionally, we investigate a pentagon cavity [217, 218] in Fig. 6.9(g), and the Penrose unilluminable room [219–223] in Fig. 6.9(h).

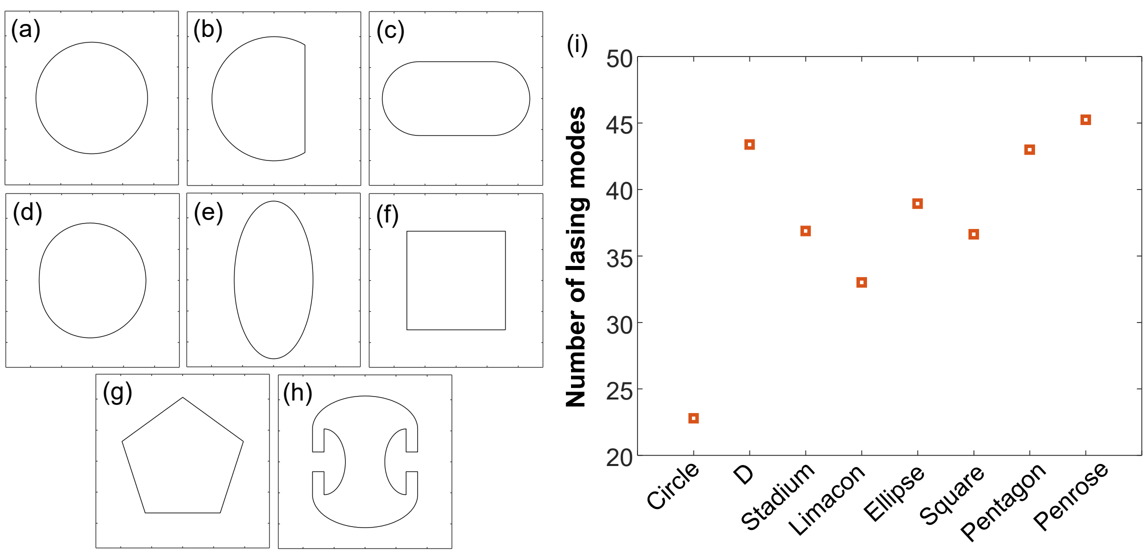

Figure 6.9: **Number of lasing modes in VCSELs with various cavity shapes.** Eight different geometries are simulated: (a) circle, (b) D-shaped, (c) stadium, (d) Limaçon, (e) ellipse, (f) square, (g) pentagon, and (h) the Penrose unilluminable room. The length of a grid is 5 μm for all panels. All the geometries have the same cavity area of 253 μm^2. (b) The number of lasing modes at ten times above the lasing threshold calculated by SPA-SALT. The D-shaped, the pentagon, and the Penrose unilluminable room cavities particularly feature a large number of transverse modes than other shapes.

For each cavity shape, we assume a birefringent material with the refractive index in the x- and z-direction $n_x = n_z = 3.2950$ and that in the y-direction $n_y = 3.2951$. We calculated approximately 450 passive resonances within the spectral range between 938 to 950 nm for each cavity. For the SPA-SALT calculation, we assume the gain bandwidth (FWHM) of 12 nm centered at 944 nm, nearly covering the entire spectral range. The number of lasing modes may vary with the peak wavelength of the gain spectrum. Hence, we calculated the number of lasing modes at different gain center wavelengths from 940 to 948 nm with 0.1 nm steps and averaged the results.

Figure 6.9(i) shows the number of lasing modes. We calculate the pump level of ten times above the lasing threshold, in which the number of lasing modes does not increase further with pump strength due to gain saturation. The circular cavity supports the lasing of 22 modes, the smallest among all cavity shapes. Breaking the structural symmetry can boost the number of lasing modes by a factor of two. Particularly, D-shaped and Pentagon cavity (44 lasing modes) and the Penrose unilluminable room (45 lasing modes) are promising for many-mode lasing. In order to understand the role of cavity geometry, the following section discusses the mechanisms to enhance the number of lasing modes.

6.6 Mechanisms for many-mode lasing

6.6.1 Narrow distribution of the quality factors

The narrow distribution of Q-factors can contribute to many-mode lasing. High-Q modes typically lase first due to the low lasing threshold. When the distribution of the Q-factor is narrow, the lasing thresholds could be similar to each other, and other modes can soon lase. Figure 6.10 shows the mode distributions in square and pentagon cavities. The pentagon shape considerably narrows down the distribution of Q-factors. We quantify the spread of the distribution by the standard deviation of the Q-factors [Fig. 6.10(e)]. The pentagon shape features the smallest standard deviation among all cavity shapes.

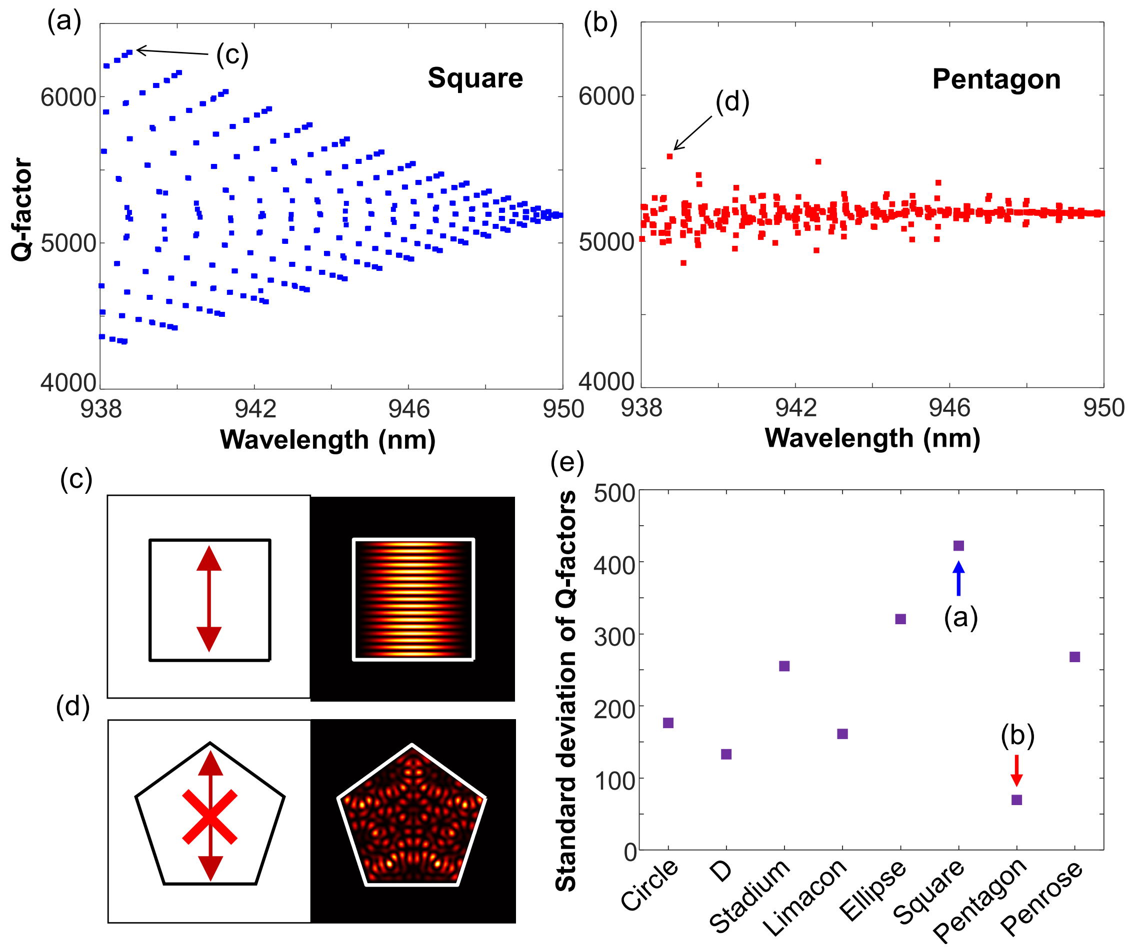

Figure 6.10: **Narrowing the distribution of Q-factors by modifying the cavity shape.** (a) The distribution of Q-factors in a square cavity. The side length of the cavity is 15.9 μm. (b) A pentagon cavity significantly reduces the spread of Q-factors. It has a side length of 12.1 μm, which yields the same area as the square cavity in (a). (c) The highest-Q mode in a square cavity (Q = 6350, $\lambda = 938.7$ nm). The schematic of the bouncing-ball orbit and the simulated intensity profile are shown. (d) The highest-Q mode in a pentagon cavity (Q = 5581, $\lambda = 938.7$ nm). The formation of the bouncing-ball orbit is prevented, which leads to a spatially extended modal profile. (e) The standard deviation of Q-factors for different cavity shapes. The square cavity has the broadest distribution of Q-factors (blue arrow). The pentagon shape features the narrowest distribution (red arrow), which may contribute to many-mode lasing.

Here the cavity ray dynamics play a significant role in determining the Q-factor. Figure 6.10(c) shows the highest-Q mode in a square cavity. This optical mode corresponds to a bouncing-ball orbit in a planar Fabry-Perot geometry. This type of mode can easily possess a pure s- (or p-) polarization, leading to a higher (or lower) Q-factor than the other modes. In contrast, the pentagon shape prevents the formation of such a trajectory due to the sharp corners [Fig. 6.10(d)]. As a result, optical modes have the spatial profile spread over the entire cavity. Due to its complex speckle-like wavefunction, consisting of many plane-wave components with diverse directions, the optical propagation does not have pure s- or p-polarization but has mixed polarization. It makes the reflectivity almost constant for every mode, which leads to a narrow distribution of Q-factors in Fig. 6.10(b). Therefore, the pentagon-shaped cavity would be advantageous for many-mode VCSELs.

6.6.2 Minimal modal overlap

We attained the largest number of lasing modes in the Penrose unilluminable room [219–223]. Its ray dynamics exhibit a unique property. Wherever a single-point light source is placed in a cavity, there will always be unilluminated regions that the light cannot reach. As a result, the optical confinement occurs at spatially distinct regions depending on the initial conditions. We simulate the passive resonances of this cavity in Fig. 6.11. We used the geometry described in Ref. [219] but smaller in length by a factor of 9.43. The four exemplary mode structures manifest spatially distinct profiles. For instance, it could be highly localized at the boundaries [Figs. 6.11(a)], spread over the cavity [Figs. 6.11(b)], or have bouncing-ball orbits [Figs. 6.11(c,d)] [219–222].

The spatial overlap between modes determine the gain competition, which has a profound impact on the behavior of multimode lasers. To this end, we quantify the overlap

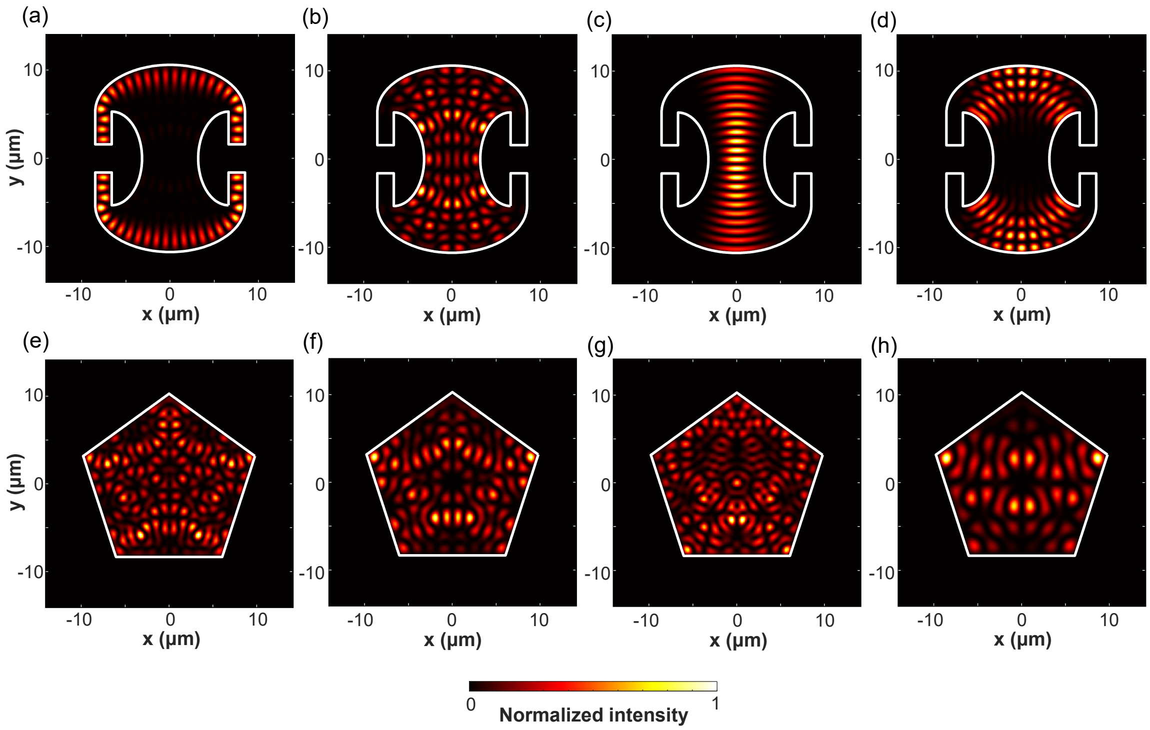

Figure 6.11: **Spatial structure of passive modes in asymmetric VCSELs.** The modes of the Penrose unilluminable room have distinct profiles at spatially separated locations inside the cavity. The resonant frequencies and Q-factors are (a) λ = 939.7 nm, Q = 5274, (b) λ = 939.6 nm, Q = 5055, (c) λ = 940.9 nm, Q = 6037, and (d) λ = 939.4 nm, Q = 5194. In contrast, spatial distributions of passive modes in a Pentagon cavity are spread throughout the entire cavity area. The exemplary modes have (e) λ = 938.7 nm, Q = 5581, (f) λ = 942.6 nm, Q = 5544, (g) λ = 939.5 nm, Q = 5454, and (h) λ = 945.7 nm, Q = 5401, respectively. Compared to Pentagon cavity, the spatially separated modes in the Penrose unilluminable room will reduce the mode competition and contribute to many-mode lasing.

between the spatial profiles:

$$\chi_{\mu\nu} = \frac{1}{A}\int |\mathbf{E}_\mu(\mathbf{r})|^2 |\mathbf{E}_\nu(\mathbf{r})|^2 d\mathbf{r}, \tag{6.12}$$

with the normalization $\int |\mathbf{E}_\mu(\mathbf{r})|^2 d\mathbf{r} = A$, where A is the area of a cavity. We note that Eq. 6.12 yields intensity overlap coefficients, unlike the complex-valued overlap coefficient in Ref. [87]. In our case, the passive modes have relatively high Q-factors due to strong lateral optical confinement; thus, the imaginary part of the field is relatively small.

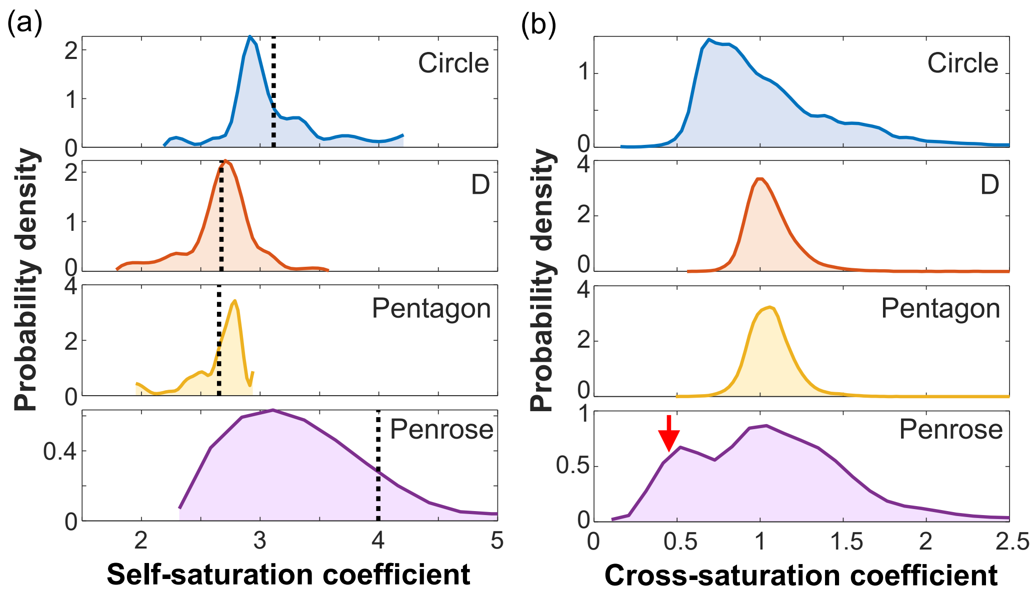

Figure 6.12: **Spatial overlap of VCSEL passive modes in various cavity shapes.** (a) Histogram of the self-saturation coefficients. The black dotted line denotes the mean value. The Penrose unilluminable room features remarkably higher self-saturation coefficients than other geometries. (b) Histogram of the cross-saturation coefficients. The Penrose unilluminable room features a significantly high probability of low cross-saturation coefficients (a red arrow), indicating reduced gain competition.

Hence we used the intensity overlap coefficients to calculate the number of lasing modes.

Figure 6.12(a) shows the self-saturation coefficients $\chi_{\mu\mu}$ of mode μ. It indicates the degree of spatial localization inside a cavity. In other words, its inverse is proportional to the modal area. The Penrose unilluminable room features diverse self-saturation coefficients, as illustrated in Fig. 6.11. Also, this cavity has the largest averaged value of the self-saturation coefficient among all cavity shapes. This result verifies the strong spatial localization of passive modes in the Penrose unilluminable room.

Such localized structures impact the overlap coefficient between distinct modes. Figure 6.12(b) shows the histogram of cross-saturation coefficients $\chi_{\mu\nu}$ between mode μ and mode ν. The circular cavity has whispering-gallery type modes, which lead to a long tail in the distribution of cross-saturation coefficients. The cavities with spatially extended modes—D-shaped and Pentagon—have a narrow distribution of cross-saturation coefficients. In contrast, the Penrose unilluminable room has a large probability of small overlap coefficients. In turn, this cavity shape can experience less mode competition. Even though its Q-factor has a broad distribution [Fig. 6.10(e)], this minimal mode competition becomes a dominant factor for highly multimode lasing. To sum up, the pentagon and the Penrose unilluminable room are promising cavity shapes for many-mode VCSELs, based on distinct physical mechanisms.

6.7 Spatio-temporal polarization dynamics

The multiple polarization states of VCSELs can lead to complex polarization dynamics. Even for VCSELs with a single transverse mode, the interplay of optical polarization states with the carrier spin dynamics results in diverse lasing behaviors such as polarization switching [211, 224–226] or chaos [57, 227]. In a broad-area VCSEL with larger spatial degrees of freedom, one can observe more complex nonlinear polarization and transverse mode dynamics [184].

Here we numerically demonstrate that even without the nonlinear light-matter interactions, multimode beating of different lasing modes can induce complex behaviors of polarization states in space and time. We simply consider the linear superposition of the passive resonances oscillating at their resonant frequencies,

$$\mathbf{E}(\mathbf{r}, t) = \sum_{\mu=1}^{M} A_\mu \mathbf{E}_\mu(\mathbf{r}) e^{i(\omega_\mu t + \phi_\mu)}, \tag{6.13}$$

where $\mathbf{E}_\mu(\mathbf{r})$ is the vector field profile of mode μ in a transverse coordinate $\mathbf{r}$, A_μ is its amplitude, and M is the number of modes that are oscillating simultaneously. We use the resonant frequency ω_μ calculated with the method developed in previous sections. The phase ϕ_μ is a random variable of uniform distribution within $[0, 2\pi]$, and here it is assumed constant in time for simplicity.

To understand the polarization dynamics from multimode beating, we first consider the simplest case with M = 2 in Fig. 6.13. We solve the passive modes of a circular-shaped VCSEL with a radius of R = 9 μm, and obtain two linearly-polarized fundamental (Gaussian) modes that are orthogonal to each other. In the presence of material anisotropy $n_y - n_x = 10^{-4}$, the vertically polarized mode (Mode 1) has slightly lower frequency than the horizontally polarized mode (Mode 2), with the frequency spacing $(\omega_2 - \omega_1)/2\pi$ = 9.6 GHz.

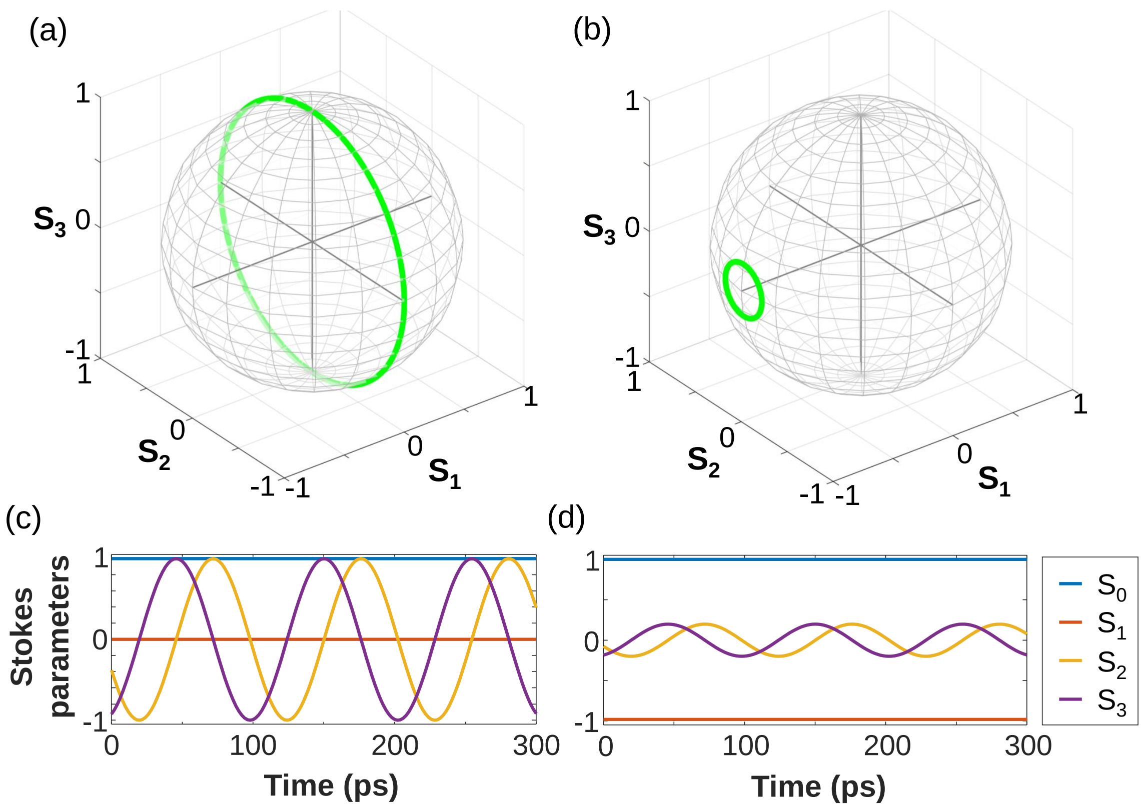

Figure 6.13: **Polarization dynamics with two orthogonal fundamental modes.** The polarization beating of vertically and horizontally polarized modes, with slightly different resonant wavelengths of 949.958 nm and 949.929 nm due to birefringent splitting, yields the motion on a Poincaré sphere. The trajectories are shown when (a) two modes have the same amplitude, and (b) the vertically polarized mode has a ten times larger amplitude than the horizontal one. (c,d) The temporal fluctuations of Stokes parameters for (a) and (b), respectively. Polarization dynamics features fast oscillation with the beat frequency of 9.6 GHz.

To analyze the polarization, we compute the spatiotemporally resolved Stokes parameters,

$$S_0(\mathbf{r},t) = \langle E_x(\mathbf{r},t)E_x^*(\mathbf{r},t) + E_y(\mathbf{r},t)E_y^*(\mathbf{r},t)\rangle_T \tag{6.14}$$

$$S_1(\mathbf{r},t) = \langle E_x(\mathbf{r},t)E_x^*(\mathbf{r},t) - E_y(\mathbf{r},t)E_y^*(\mathbf{r},t)\rangle_T \tag{6.15}$$

$$S_2(\mathbf{r},t) = \langle E_x(\mathbf{r},t)E_y^*(\mathbf{r},t) + E_y(\mathbf{r},t)E_x^*(\mathbf{r},t)\rangle_T \tag{6.16}$$

$$S_3(\mathbf{r},t) = \langle i\{E_x(\mathbf{r},t)E_y^*(\mathbf{r},t) - E_y(\mathbf{r},t)E_x^*(\mathbf{r},t)\}\rangle_T, \tag{6.17}$$

where E_x and E_y are the x and y components of the electric field, and T corresponds to the temporal resolution of the measurement. We note that in order to observe the dynamics in Eq. 6.13, one should resolve the largest frequency spacing, in other words, the temporal resolution T should be shorter than the coherence time of the laser emission. Otherwise, the Stokes parameters would yield unpolarized states of light.

Figure 6.13(a) is the case when the two modes have the same amplitude, or $A_{1,2}$ = 1. On a Poincaré sphere, the polarization state circles around the origin. As the orthogonal polarizations do not interfere, the intensity S_0 is maintained constant in time. Meanwhile, the polarization state repeatedly change between the ±45°-polarized light (S_2 = ±1) and the circularly polarized light (S_3 = ±1).

Figure 6.13(b) is when $A_1 = 10A_2$, or the vertically polarized component has ten times larger amplitude than the horizontal one. In this case, the trajectory is still circular but is localized around S_1 = -1, indicating the polarization is almost vertically polarized. Figures 6.13(c) and (d) show the temporal evolution of individual Stokes parameters. The oscillation frequency is equal to the mode spacing between the orthogonal modes, which is determined by the material birefringence.

Many-mode polarization dynamics

Adding more lasing modes and introducing asymmetry in cavity geometry can make the polarization dynamics more complex. To demonstrate this effect, we simulate a D-shaped cavity (R = 10 μm) with material birefringence $n_y - n_x = 10^{-4}$. Here M = 20 lowest-order transverse modes are obtained, and the interference pattern with the same amplitude $A_{\mu=1,\cdots,20} = 1$ is calculated. The frequency difference between the highest-order and the lowest-order (fundamental) transverse modes is 213 GHz.

Figure 6.14 shows the spatiotemporal evolution of polarization states for the many-mode D-shaped VCSEL. As shown in Fig. 6.14(a), the four Stokes parameters exhibit distinct spatial profiles at a fixed time. Moreover, in a Poincaré sphere of Fig. 6.14(b), the polarization states at different spatial locations exhibit distinct complex trajectories in time. Figs. 6.14(c) and (d) show the temporal evolution of individual Stokes parameters. The fluctuation time scale is about a few picoseconds, determined by the inverse of the largest mode spacing between the modes. These fluctuations are much faster than that from birefringence-induced mode spacing or the relaxation oscillations. This example demonstrates that many-mode asymmetric VCSELs can be used to accelerate the spatiotemporal polarization dynamics.

Degrees of freedom

Here a question is whether these four spatio-temporal Stokes parameters are independent of each other or have correlations among them. To this end, we employ the singular value decomposition (SVD) analysis on the Stokes-parameter matrices $S(\mathbf{r}, t)$, where position $\mathbf{r}$ is the row and time t is the column. It is analogous to the Karhunen-Loeve analysis in Section 5.8.2. The number of dominant singular values tells us how many degrees of freedom exist. Figure 6.15(a) shows the singular values of the matrices $S_{0,1,2,3}(\mathbf{r}, t)$, where

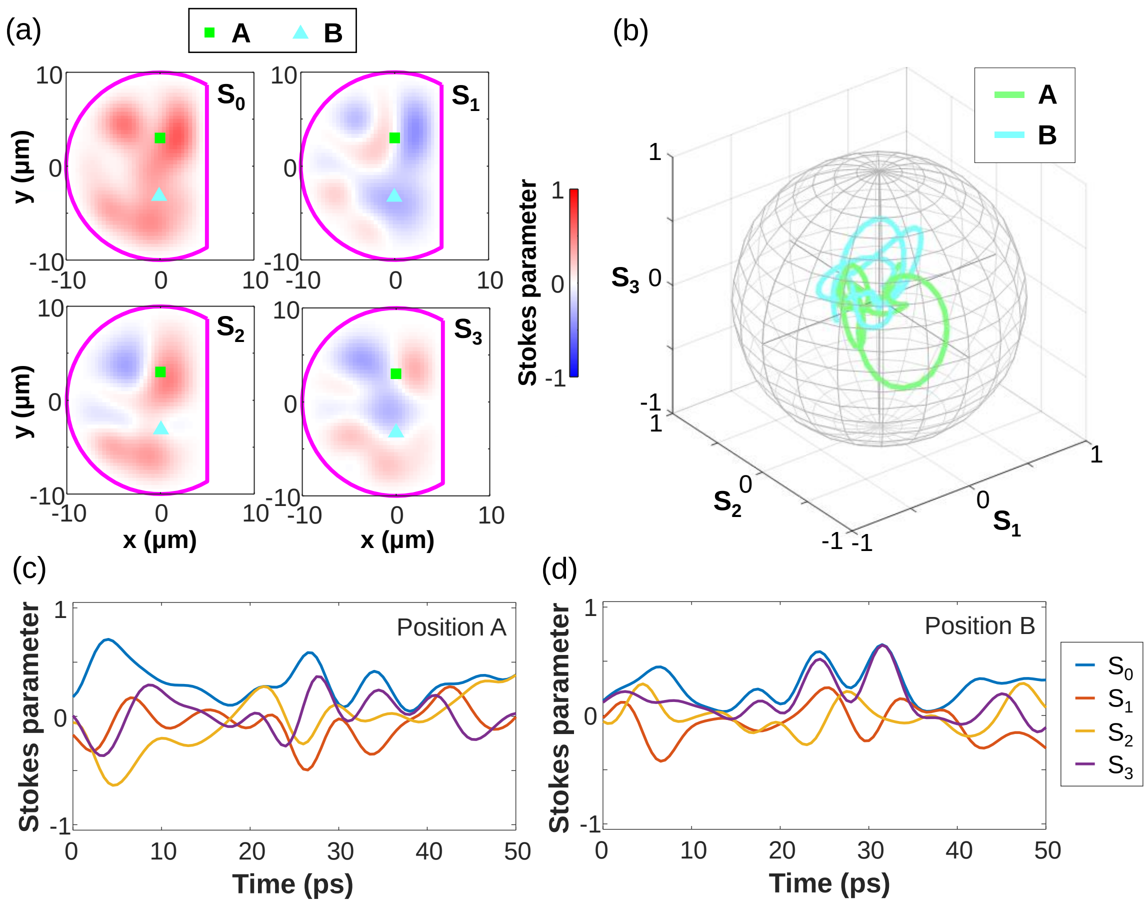

Figure 6.14: **Polarization dynamics in a many-mode VCSEL.** The spatiotemporal interference pattern of 20 different spatial modes with equal amplitude in a D-shaped cavity is simulated. (a) Snapshots of spatially-resolved Stokes parameters at a fixed time. (b) At a fixed spatial locations [A: (0,3) μm, B: (0,-3) μm], Stokes parameters change in time along complex and distinct trajectories in a Poincare sphere. (c,d) Temporal fluctuations of individual Stokes parameters for position A and B, respectively. The fluctuation time scale is on a few picoseconds, determined by the transverse mode spacing. Each of Stokes parameter S_0, S_1, S_2, and S_3 exhibit distinct trajectories in time.

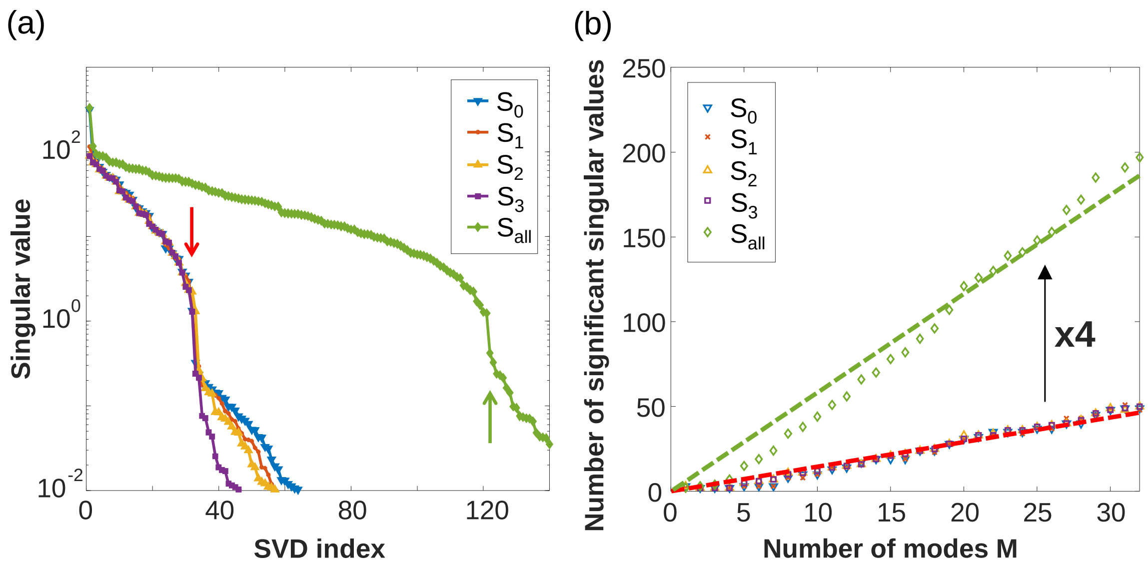

Figure 6.15: **Spatial degrees of freedom in the polarization dynamics.** (a) The distribution of singular values of the Stokes parameter matrices. The number of modes M is 20. The abrupt transition in singular value distributions indicates the number of significant singular values. From S_0 to S_3, the kink is at SVD index 32 (red arrow). For the concatenated Stokes parameter S_{all}, it is at 121 (green arrow). (b) The number of significant singular values as a function of M. The dashed lines indicate linear fit, with the slope of 1.45 for individual Stokes parameters and 5.82 for S_{all}. The spatial degrees of freedom of S_{all} is about four times larger than each Stokes parameter, which implies that S_0, S_1, S_2, and S_3 are independent of each other.

the position coordinate $\mathbf{r}$ being the row and the time coordinate t being the column. Here $S_{\text{all}}(\mathbf{r}, t)$ is obtained by concatenating the four Stokes parameter matrices in a row,

$$S_{\text{all}}(\mathbf{r}, t) = \begin{pmatrix} S_0(\mathbf{r}, t) \\ S_1(\mathbf{r}, t) \\ S_2(\mathbf{r}, t) \\ S_3(\mathbf{r}, t) \end{pmatrix}. \tag{6.18}$$

Any correlation between the Stokes parameters will reduce the degrees of freedom in S_{all}.

For the individual Stokes parameters, the singular value distribution has a sharp transition [red arrow in Fig. 6.15(a)] at the SVD index of 32. It indicates that each of the Stokes parameters has 32 dominant singular values, or the degrees of freedom, in the spatiotemporal dynamics. On the other hand, S_{all} has this transition at the SVD index of 121. This value is approximately four times larger than that of individual Stokes parameters.

Figure 6.15(b) shows the number of dominant singular values in $S_{0,1,2,3}$ and S_{all} for different number of modes. Adding more modes increases the degrees of freedom linearly. More importantly, the ratio between S_{all} and $S_{0,1,2,3}$ is almost constant at four. It indicates that there is no correlation among the four Stokes parameters. To see whether $S_{0,1,2,3}$ are the only independent variables, we also concatenated an additional parameter $S_4 = \langle E_x E_y^* + i E_y E_x^* \rangle_T$ in Eq. 6.18 and performed SVD. It did not further increase the number of dominant singular values, indicating S_4 are correlated with $S_{0,1,2,3}$.

To summarize, $S_{0,1,2,3}(\mathbf{r}, t)$ are independent of each other and provide many degrees of freedom of spatiotemporal polarization dynamics. In order to resolve such dynamics, the temporal resolution should be high enough to resolve the beating of any lasing modes; otherwise, one would observe just an unpolarized light. In real VCSELs, the interplay of gain material and optical field could be dominant, and hence our model may not fully capture the actual lasing dynamics. Nevertheless, nonlinear light-matter interactions would make these dynamics even more complex, opening the possibilities to utilize diverse and rich behaviors in many-mode VCSELs.

6.8 Discussion and conclusion

This chapter extended our method of controlling laser behaviors by cavity shape to surface-emitting lasers. We developed a numerical framework to calculate the passive resonances in a three-dimensional VCSEL structure. An optical mode in a VCSEL is approximated by a superposition of forward and backward propagating guided waves in an optical waveguide. Combining with the mirror reflectivity of the DBRs, we could efficiently calculate the quality factor of hundreds of transverse modes in a large-area VCSEL. Our approach significantly reduces the computation time from the full 3D simulation and allows the simulation of a broad cavity cross-section as large as tens of micrometers. More importantly, the simulated structure is not limited by the cylindrical symmetry; thus, we could simulate the cavity shape with structural asymmetry and intrinsic material birefringence.

Our numerical method, combined with SPA-SALT, enabled efficient calculation of the number of lasing modes in diverse cavity shapes. Specific cavity geometries— D-shaped, pentagon, and the Penrose unilluminable room— featured a larger number of lasing modes than conventional circular cavities. The D-shaped and pentagon cavities prevent the formation of bouncing-ball modes, which have pure p- or s-polarizations and thus typically have a high Q-factor in a VCSEL structure. Suppression of those modes leads to the narrow distribution of quality factors, and more modes manage to lase simultaneously. For the Penrose unilluminable room, the passive modes are spatially localized at different locations in the cavity. It could reduce the mode competition and consequently increase the number of lasing modes.

The asymmetric-cavity large-area VCSELs are the light sources with an improved directionality and rich lasing dynamics. Given many spatial lasing modes, it could be used as an illumination source for speckle-free imaging with an improved collection efficiency. Simultaneous oscillation of many modes with diverse polarizations will lead to complex spatiotemporal polarization dynamics. The fine-tuning of the cross-section of the cavity geometry may allow us to enhance the complexity of the polarization dynamics. This ultrafast polarization dynamics could be potentially used for random number generation [3]. Moreover, the complex dynamics of large-area VCSELs would facilitate reservoir computing [228, 229], whose performance relies on the complexity of the system.

Chapter 7

Conclusion

This dissertation presented a method to control broad-area semiconductor lasers and discussed the applications of many-mode lasers. In contrast to conventional lasers that aim to attain a single spatial mode and stable output in time, we focused on and explored complex lasers with many spatial degrees of freedom and a wide variety of lasing dynamics. Throughout the dissertation, we showed that cavity geometry is a powerful tuning parameter to control the characteristics of complex lasers.

We studied and utilized the ray-wave correspondence in various optical cavities. Modifying the cavity ray dynamics changes the spatial structure of passive resonances. Specifically, it affects their Q-factors and spatial overlap between modes. As a result, the number of lasing modes strongly depends on the cavity shape. Moreover, the cavity shape determines the spatial localization and the local characteristic length scale of the passive resonances. It affects nonlinear light-matter interaction in semiconductor gain material, which impacts spatiotemporal lasing dynamics. Our approach allows an advanced understanding of the relation between the cavity ray dynamics and the nonlinear lasing dynamics, which opens a possibility to engineer the lasing dynamics of highly multimode lasers by cavity shape.

In chapter 2, we investigated the lasing dynamics of asymmetric cavities with various ray dynamics. In the experiment, the cavity shape significantly impacts the spatial and temporal characteristic length scales of lasing dynamics. The fluctuating power of emission intensity could be varied by several orders of magnitude, proving that the cavity shape is a simple yet effective tool to suppress the lasing instabilities. Due to complex wave interference, the passive modes of wave-chaotic cavities generally have fine-grained structures and short local characteristic lengths. In turn, it leads to the most stable output beam. However, chaotic ray dynamics are unnecessary to suppress the instabilities; an integrable cavity with a short local characteristic length can also stabilize the lasers. We can further optimize the cavity boundary condition to minimize the characteristic length scale and improve the emission directionality.

In chapter 3, this dissertation resorts to a stable cavity configuration for an improved emission directionality. We could confine many high-order transverse modes by strongly curving two end facets of laser cavities. By fine-tuning the cavity geometry and considering the gain competition, we attain the maximal number of lasing modes at the near-concentric geometry. These laser geometries have a unique combination of hundreds of lasing modes, mW-level power per spatial mode, and decoherence time in a few nanoseconds. Compared to conventional speckle-free illumination sources like light-emitting diodes (LEDs) or incandescent light sources, the proposed laser would have superior performance thanks to its high signal-to-noise ratio. Moreover, compared to time-consuming methods of suppressing speckle artifacts, the ultrafast decoherence of this laser will enable speckle imaging of transient processes or fast-moving objects.

In chapter 4, we explored the vicinity of the planar cavity geometry to improve the emission directionality further. This chapter focused on the sensitivity of ray dynamics at the bifurcation point, which is well known for conventional solid-state laser cavities, but its consequences have been overlooked for semiconductor lasers with strong nonlinear light-matter interactions. A slight modification of mirrors could significantly improve the laser performance by boosting the number of lasing modes. More importantly, the small perturbation drastically reduces the spatio-temporal lasing instabilities. Compared to the near-concentric cavity in chapter 3, the number of spatial lasing modes in a near-planar cavity remains on the same level, while the divergence angle at the far-field is nearly halved. The lasing of many modes prevents the output beam from being focused tightly, and it would limit high-brightness applications. Nevertheless, such a laser with many spatial modes can readily create a specific beam shape, such as a flat-top beam, which is often needed for high-brightness applications but challenging to attain with a single-mode Gaussian beam. Moreover, we can apply the high sensitivity of nonlinear lasing behavior at a bifurcation point of cavity geometry to novel sensing applications.

In chapter 5, we utilized our many-mode stable-cavity laser for random bit generation. Tailoring the cavity shape suppressed the lasing instabilities and thus eliminated the long-range correlations in the emission intensity. It changed the governing physical process of lasing dynamics and drastically shortened the characteristic time scale: from the sub-nanoseconds of light-semiconductor interaction to the picosecond time scale of many-mode beating. Moreover, the vast spatial degrees of freedom from many transverse lasing modes enabled spatial multiplexing of emission intensity to generate independent random bit streams in parallel. The total bit rate was boosted by two orders of magnitude from the state-of-the-art. Improving the photodetection resolution and the field of view will further enhance the bit rate, eventually enabling the total bit generation rate of 1 Pb/s. We performed the proof-of-principle demonstration off-the-chip with post-processing. The next step will be integrating with an array of fast photodetectors, leading to real-time massively parallel ultrafast random bit generation.

In chapter 6, we extended the methodology of controlling dynamics by cavity shape to VCSELs. A numerical framework to calculate the passive resonances of a large-area VCSEL with any transverse cavity shape is developed, which is applicable for the cases with structural asymmetry and/or material birefringence. Specially designed cavity shapes enhanced the number of lasing modes. This many-mode lasing could be attained by narrowing the distribution of Q-factors or minimizing the spatial overlap between modes. With an improved directional output compared to edge-emitting lasers, these many-mode VCSELs could facilitate speckle-free imaging. Moreover, given massive spatial degrees of freedom, these VCSELs can exhibit rich and diverse lasing characteristics such as polarization dynamics and ultrafast transverse mode beating. The complex lasing dynamics of many-mode VCSELs will offer other opportunities to harness spatial degrees of freedom for novel photonic applications.

From a practical point of view, this framework of controlling the laser dynamics with cavity shape has advantages over established methods of laser stabilization. The proposed method is fundamentally compatible with the high-power operation in which high-order spatial modes are lasing. As high-order modes have short characteristic lengths, the self-focusing instabilities would further be disrupted with increasing pump levels in such many-mode lasers. Moreover, there is no need for the additional setup of external feedback or fine adjustment of operational parameters. This method of suppressing instabilities would be robust to fabrication errors. For instance, our approach is resilient to surface roughness on the cavity sidewall, as randomly scattered partial waves inside the gain material would further impede the self-focusing effect.

Though this dissertation focused on suppressing the instabilities, enhancing the instabilities by cavity shape is another interesting topic to explore. One would achieve stronger instability in a cavity shape that promotes the nonlinear light-matter interaction in active media. So far, conventional ways of creating optical chaos are to use external feedback, optical injection, or spatial/temporal modulation of injection current. Here tuning the cavity shape could be a more compact, robust, and efficient approach to modifying the RF spectrum of the laser emission. The on-chip broadband chaotic light source will be useful for many applications such as secure communications, optical computing, and sensing.

There still are many opportunities to control and utilize complex lasers. Other than the speckle-free light source or random bit generator, complex lasers could be used for reservoir computing or physical simulators that harness the huge spatial degree of freedom. Moreover, spatial modulation of the pump will add another degree of freedom to control the behavior of broad-area lasers, enabling the creation of complex states of light on demand. Many lasing modes will provide a massive number of tuning knobs that would create arbitrary laser output. Active spatiotemporal control of many-mode lasers will pave the way for innovative and versatile light sources, which can be widely adopted in applications ranging from imaging to optical computing. Furthermore, this general approach of controlling complex lasers by tuning resonator shapes is not restricted to semiconductor gain material. We could apply it to other nonlinear systems with instabilities, such as solid-state lasers. Moreover, for fiber lasers and amplifiers that are widely used in high-power systems, those with various cross-section shapes will facilitate diverse fiber-based applications such as optical communications.

Bibliography

[1] K. Kim, S. Bittner, Y. Zeng, S. F. Liew, Q. Wang, and H. Cao, "Electrically pumped semiconductor laser with low spatial coherence and directional emission," *Appl. Phys. Lett.* **115**(7), p. 071101, 2019. 1, 55, 80, 82, 83, 87, 92, 93, 118, 121, 123

[2] K. Kim, S. Bittner, Y. Jin, Y. Zeng, S. Guazzotti, O. Hess, Q. J. Wang, and H. Cao, "Sensitive control of broad-area semiconductor lasers by cavity shape," *APL Photonics* **7**(5), p. 056106, 2022. 1, 37, 39, 41, 80

[3] K. Kim, S. Bittner, Y. Zeng, S. Guazzotti, O. Hess, Q. J. Wang, and H. Cao, "Massively parallel ultrafast random bit generation with a chip-scale laser," *Science* **371**(6532), pp. 948–952, 2021. 1, 39, 86, 111, 113, 115, 181

[4] S. Bittner, S. Guazzotti, Y. Zeng, X. Hu, H. Yılmaz, K. Kim, S. S. Oh, Q. J. Wang, O. Hess, and H. Cao, "Suppressing spatiotemporal lasing instabilities with wave-chaotic microcavities," *Science* **361**(6408), pp. 1225–1231, 2018. viii, 3, 4, 7, 13, 17, 20, 22, 23, 28, 30, 31, 35, 42, 77, 86, 119

[5] S. Bittner, K. Kim, Y. Zeng, Q. J. Wang, and H. Cao, "Spatial structure of lasing modes in wave-chaotic semiconductor microcavities," *New J. Phys.* **22**(8), p. 083002, 2020. 1, 19, 20, 22, 29, 31, 43, 90

[6] H. Cao, J. Xu, Y. Ling, and A. Burin, "Lasing in disordered media," in *2002 Summaries of Papers Presented at the Quantum Electronics and Laser Science Conference*, p. 1, IEEE, 2002. 2

[7] D. S. Wiersma, "The physics and applications of random lasers," *Nat. Phys.* **4**(5), pp. 359–367, 2008.

[8] N. Bachelard, S. Gigan, X. Noblin, and P. Sebbah, "Adaptive pumping for spectral control of random lasers," *Nat. Phys.* **10**(6), pp. 426–431, 2014. 2

[9] J. Arnaud, "Degenerate optical cavities," *Appl. Opt.* **8**(1), pp. 189–196, 1969. 2, 62

[10] M. Nixon, B. Redding, A. A. Friesem, H. Cao, and N. Davidson, "Efficient method for controlling the spatial coherence of a laser," *Opt. Lett.* **38**(19), pp. 3858–3861, 2013. 56

[11] C. Tradonsky, S. Mahler, G. Cai, V. Pal, R. Chriki, A. A. Friesem, and N. Davidson, "High-resolution digital spatial control of a highly multimode laser," *Optica* **8**(6), pp. 880–884, 2021. 2

[12] L. G. Wright, D. N. Christodoulides, and F. W. Wise, "Spatiotemporal mode-locking in multimode fiber lasers," *Science* **358**(6359), pp. 94–97, 2017. 2

[13] X. Wei, J. C. Jing, Y. Shen, and L. V. Wang, "Harnessing a multi-dimensional fibre laser using genetic wavefront shaping," *Light: Sci. & Appl.* **9**(1), pp. 1–10, 2020. 2

[14] H. Cao, R. Chriki, S. Bittner, A. A. Friesem, and N. Davidson, "Complex lasers with controllable coherence," *Nat. Rev. Phys.* **1**(2), pp. 156–168, 2019. 2, 56, 82, 113

[15] Y. Eliezer, G. Qu, W. Yang, Y. Wang, H. Yılmaz, S. Xiao, Q. Song, and H. Cao, "Suppressing meta-holographic artifacts by laser coherence tuning," *Light: Sci. & Appl.* **10**(1), pp. 1–11, 2021. 2

[16] G. Van der Sande, D. Brunner, and M. C. Soriano, "Advances in photonic reservoir computing," *Nanophotonics* **6**(3), pp. 561–576, 2017. 2

[17] P. L. McMahon, A. Marandi, Y. Haribara, R. Hamerly, C. Langrock, S. Tamate, T. Inagaki, H. Takesue, S. Utsunomiya, K. Aihara, *et al.*, "A fully programmable 100-spin coherent ising machine with all-to-all connections," *Science* **354**(6312), pp. 614–617, 2016. 2

[18] J. Ohtsubo, *Semiconductor lasers: stability, instability and chaos*, vol. 111, Springer, 2012. 3, 4, 12, 26

[19] I. Fischer, O. Hess, W. Elsäßer, and E. Göbel, "Complex spatio-temporal dynamics in the near-field of a broad-area semiconductor laser," *Europhys. Lett.* **35**(8), p. 579, 1996. 3, 12, 81, 109, 111, 117

[20] O. Hess, "Spatio-temporal complexity in multi-stripe and broad-area semiconductor lasers," *Chaos, Solitons & Fractals* **4**(8-9), pp. 1597–1618, 1994. 36, 143

[21] O. Hess and T. Kuhn, "Maxwell-bloch equations for spatially inhomogeneous semiconductor lasers. ii. spatiotemporal dynamics," *Phys. Rev. A* **54**(4), p. 3360, 1996. 12, 81

[22] O. Hess and T. Kuhn, "Spatio-temporal dynamics of semiconductor lasers: Theory, modelling and analysis," *Prog. Quantum Electron.* **20**, pp. 85–179, 1996. 3, 117

[23] J. R. Marciante and G. P. Agrawal, "Spatio-temporal characteristics of filamentation in broad-area semiconductor lasers," *IEEE J. Quantum Electron.* **33**(7), pp. 1174–1179, 1997. 3, 12, 43, 81

[24] J. R. Marciante and G. P. Agrawal, "Spatio-temporal characteristics of filamentation in broad-area semiconductor lasers: experimental results," *IEEE Photonics Technol. Lett.* **10**(1), pp. 54–56, 1998. 12

[25] D. Scholz, H. Braun, U. T. Schwarz, S. Brüninghoff, D. Queren, A. Lell, and U. Strauss, "Measurement and simulation of filamentation in (Al, In) GaN laser diodes," *Opt. Express* **16**(10), pp. 6846–6859, 2008. 12

[26] M. Arahata and A. Uchida, "Inphase and antiphase dynamics of spatially-resolved light intensities emitted by a chaotic broad-area semiconductor laser," *IEEE J. Sel. Top. Quantum Electron* **21**(6), pp. 522–530, 2015. 3, 12, 81, 116, 118

[27] S. K. Mandre, I. Fischer, and W. Elsäßer, "Spatiotemporal emission dynamics of a broad-area semiconductor laser in an external cavity: stabilization and feedback-induced instabilities," *Opt. Commun.* **244**(1-6), pp. 355–365, 2005. 4

[28] S. Takimoto, T. Tachikawa, R. Shogenji, and J. Ohtsubo, "Control of spatio-temporal dynamics of broad-area semiconductor lasers by strong optical injection," *IEEE Photonics Technol. Lett.* **21**(15), pp. 1051–1053, 2009. 4

[29] R. K. Chang and A. J. Campillo, *Optical processes in microcavities*, vol. 3, World scientific, 1996. 5

[30] A. D. Stone, "Wave-chaotic optical resonators and lasers," *Phys. Scr.* **2001**(T90), p. 248, 2001.

[31] H. Schwefel, H. Tureci, A. D. Stone, and R. Chang, *Progress in asymmetric resonant cavities: Using shape as a design parameter in dielectric microcavity lasers*, World Scientific, 2004. 7, 11

[32] H. Türeci, H. G. Schwefel, P. Jacquod, and A. D. Stone, *Modes of wave-chaotic dielectric resonators*, vol. 47, Elsevier, 2005. 7, 15

[33] T. Harayama and S. Shinohara, "Two-dimensional microcavity lasers," *Laser Photonics Rev.* **5**(2), pp. 247–271, 2011. 11, 43

[34] H. Cao and J. Wiersig, "Dielectric microcavities: Model systems for wave chaos and non-hermitian physics," *Rev. Mod. Phys.* **87**(1), p. 61, 2015. 5, 7, 11, 15, 29, 43

[35] L. A. Bunimovich, "On the ergodic properties of nowhere dispersing billiards," *Communications in Mathematical Physics* **65**(3), pp. 295–312, 1979. 5, 19

[36] S. Ree and L. Reichl, "Classical and quantum chaos in a circular billiard with a straight cut," *Phys. Rev. E* **60**(2), p. 1607, 1999. 5, 19

[37] V. S. Ilchenko and A. B. Matsko, "Optical resonators with whispering-gallery modes-part ii: applications," *IEEE J. Sel. Top. Quantum Electron.* **12**(1), pp. 15–32, 2006. 6

[38] S. Sunada, T. Harayama, and K. S. Ikeda, "Multimode lasing in two-dimensional fully chaotic cavity lasers," *Phys. Rev. E* **71**(4), p. 046209, 2005. 7, 11

[39] T. Harayama, T. Fukushima, S. Sunada, and K. S. Ikeda, "Chaos and multi-attractors in fully chaotic 2D microcavity lasers," *Phys. Rev. Lett* **91**, p. 033902, 2003. 11

[40] M. Choi, T. Fukushima, and T. Harayama, "Alternate oscillations in quasistadium laser diodes," *Phys. Rev. A* **77**(6), p. 063814, 2008. 11

[41] S. Shinohara, T. Fukushima, S. Sunada, T. Harayama, K. Arai, and K. Yoshimura, "Anticorrelated bidirectional output of quasistadium-shaped semiconductor microlasers," *Opt. Rev.* **21**(2), pp. 113–116, 2014. 7, 11

[42] A. Levi, R. Slusher, S. McCall, J. Glass, S. Pearton, and R. Logan, "Directional light coupling from microdisk lasers," *Appl. Phys. Lett.* **62**(6), pp. 561–563, 1993. 7

[43] J. U. Nöckel, A. D. Stone, G. Chen, H. L. Grossman, and R. K. Chang, "Directional emission from asymmetric resonant cavities," *Opt. Lett.* **21**(19), pp. 1609–1611, 1996.

[44] G. Chern, H. Tureci, A. D. Stone, R. Chang, M. Kneissl, and N. Johnson, "Unidirectional lasing from InGaN multiple-quantum-well spiral-shaped micropillars," *Appl. Phys. Lett.* **83**(9), pp. 1710–1712, 2003.

[45] H. G. Schwefel, N. B. Rex, H. E. Tureci, R. K. Chang, A. D. Stone, T. Ben-Messaoud, and J. Zyss, "Dramatic shape sensitivity of directional emission patterns from similarly deformed cylindrical polymer lasers," *JOSA B* **21**(5), pp. 923–934, 2004.

[46] Y.-F. Xiao, C.-L. Zou, Y. Li, C.-H. Dong, Z.-F. Han, and Q. Gong, "Asymmetric resonant cavities and their applications in optics and photonics: a review," *Frontiers of Optoelectronics in China* **3**(2), pp. 109–124, 2010. 7

[47] S. A. Biellak, Y. Sun, S. S. Wong, and A. E. Siegman, "Lateral mode behavior of reactive-ion-etched stable-resonator semiconductor lasers," *J. Appl. Phys.* **78**(6), pp. 4294–4296, 1995. 8, 59, 80

[48] T. Fukushima, T. Harayama, P. Davis, P. O. Vaccaro, T. Nishimura, and T. Aida, "Ring and axis mode lasing in quasi-stadium laser diodes with concentric end mirrors," *Opt. Lett.* **27**(16), pp. 1430–1432, 2002. 59

[49] H. E. Tureci, H. Schwefel, A. D. Stone, and E. Narimanov, "Gaussian-optical approach to stable periodic orbit resonances of partially chaotic dielectric microcavities," *Opt. Express* **10**(16), pp. 752–776, 2002.

[50] S. Shinohara, T. Harayama, and T. Fukushima, "Fresnel filtering of gaussian beams in microcavities," *Opt. Lett.* **36**(6), pp. 1023–1025, 2011. 8

[51] N. Abraham, L. Lugiato, and L. Narducci, "Overview of instabilities in laser systems," *JOSA B* **2**(1), pp. 7–14, 1985. 12

[52] C. Weiss, "Chaotic laser dynamics," *Opt. Quantum Electron.* **20**(1), pp. 1–22, 1988. 12

[53] X.-Q. Qi and J.-M. Liu, "Photonic microwave applications of the dynamics of semiconductor lasers," *IEEE J. Sel. Top. Quantum Electron.* **17**(5), pp. 1198–1211, 2011. 12

[54] M. Sciamanna and K. A. Shore, "Physics and applications of laser diode chaos," *Nat. Photonics* **9**(3), pp. 151–162, 2015. 12

[55] M. C. Soriano, J. García-Ojalvo, C. R. Mirasso, and I. Fischer, "Complex photonics: Dynamics and applications of delay-coupled semiconductors lasers," *Rev. Mod. Phys.* **85**(1), p. 421, 2013. 12

[56] L. Furfaro, F. Pedaci, M. Giudici, X. Hachair, J. Tredicce, and S. Balle, "Mode-switching in semiconductor lasers," *IEEE J. Quantum Electron.* **40**(10), pp. 1365–1376, 2004. 12

[57] M. Virte, K. Panajotov, H. Thienpont, and M. Sciamanna, "Deterministic polarization chaos from a laser diode," *Nat. Photonics* **7**(1), pp. 60–65, 2013. 12, 174

[58] A. Klaedtke and O. Hess, "Ultrafast nonlinear dynamics of whispering-gallery mode micro-cavity lasers," *Opt. Express* **14**(7), pp. 2744–2752, 2006. 12

[59] A. Cerjan, S. Bittner, M. Constantin, M. Guy, Y. Zeng, Q. J. Wang, H. Cao, and A. D. Stone, "Multimode lasing in wave-chaotic semiconductor microlasers," *Phys. Rev. A* **100**(6), p. 063814, 2019. 14, 20, 21, 27, 43

[60] S. F. Liew, L. Ge, B. Redding, G. S. Solomon, and H. Cao, "Pump-controlled modal interactions in microdisk lasers," *Phys. Rev. A* **91**(4), p. 043828, 2015. 17, 23, 96, 121

[61] M. V. Berry, "Regular and irregular semiclassical wavefunctions," *J. Phys. A: Math. Gen.* **10**(12), p. 2083, 1977. 18, 49

[62] A. I. Shnirel'man, "Ergodic properties of eigenfunctions," *Uspekhi Matematicheskikh Nauk* **29**(6), pp. 181–182, 1974. 18

[63] K. Husimi, "Some formal properties of the density matrix," *Proc. Phys.-Math. Soc. Jpn.* **22**, p. 246, 1940. 19

[64] M. Hentschel, H. Schomerus, and R. Schubert, "Husimi functions at dielectric interfaces: Inside-outside duality for optical systems and beyond," *Europhys. Lett.* **62**(5), p. 636, 2003. 19, 63, 88, 89

[65] K. Clauß, M. J. Körber, A. Bäcker, and R. Ketzmerick, "Resonance eigenfunction hypothesis for chaotic systems," *Phys. Rev. Lett.* **121**(7), p. 074101, 2018. 19

[66] K. Clauß and R. Ketzmerick, "Local random vector model for semiclassical fractal structure of chaotic resonance states," *J. Phys. A: Math. Theor.* **55**(20), p. 204006, 2022.

[67] R. Ketzmerick, K. Clauß, F. Fritzsch, and A. Bäcker, "Chaotic resonance modes in dielectric cavities: Product of conditionally invariant measure and universal fluctuations," *arXiv preprint* **arXiv:2203.09752**, 2022. 19, 29, 43

[68] E. G. Altmann, J. S. Portela, and T. Tél, "Leaking chaotic systems," *Rev. Mod. Phys.* **85**(2), p. 869, 2013. 19, 29

[69] S. Sunada, S. Shinohara, T. Fukushima, and T. Harayama, "Signature of wave chaos in spectral characteristics of microcavity lasers," *Phys. Rev. Lett.* **116**(20), p. 203903, 2016. 20, 21, 43

[70] M. Robnik, "Classical dynamics of a family of billiards with analytic boundaries," *J. Phys. A: Math. Gen.* **16**(17), p. 3971, 1983. 20

[71] V. F. Lazutkin, "The existence of caustics for a billiard problem in a convex domain," *Mathematics of the USSR-Izvestiya* **7**(1), p. 185, 1973. 20

[72] J. Wiersig and M. Hentschel, "Combining directional light output and ultralow loss in deformed microdisks," *Phys. Rev. Lett.* **100**(3), p. 033901, 2008. 20, 29

[73] H. R. Dullin and A. Bäcker, "About ergodicity in the family of limaçon billiards," *Nonlinearity* **14**(6), p. 1673, 2001. 20

[74] J.-B. Shim, J. Wiersig, and H. Cao, "Whispering gallery modes formed by partial barriers in ultrasmall deformed microdisks," *Phys. Rev. E* **84**(3), p. 035202, 2011. 20

[75] Y.-Z. Gu, L.-K. Chen, Y.-J. Qian, Q. Gong, Q.-T. Cao, and Y.-F. Xiao, "Layered localization in a chaotic optical cavity," *Phys. Rev. E* **102**(6), p. 062208, 2020. 20

[76] M. V. Berry, "Regularity and chaos in classical mechanics, illustrated by three deformations of a circular 'billiard'," *Eur. J. Phys.* **2**(2), p. 91, 1981. 21

[77] J. B. Keller and S. Rubinow, "Asymptotic solution of eigenvalue problems," *Ann. Phys.* **9**(1), pp. 24–75, 1960. 21

[78] C.-H. Yi, J. Kullig, C.-M. Kim, and J. Wiersig, "Frequency splittings in deformed optical microdisk cavities," *Phys. Rev. A* **96**(2), p. 023848, 2017. 21

[79] A. Poon, F. Courvoisier, and R. K. Chang, "Multimode resonances in square-shaped optical microcavities," *Optics letters* **26**(9), pp. 632–634, 2001. 21

[80] S. Bittner, E. Bogomolny, B. Dietz, M. Miski-Oglu, and A. Richter, "Experimental observation of localized modes in a dielectric square resonator," *Phys. Rev. E* **88**(6), p. 062906, 2013. 21, 51

[81] S. Bittner, E. Bogomolny, B. Dietz, M. Miski-Oglu, and A. Richter, "Dielectric square resonator investigated with microwave experiments," *Phys. Rev. E* **90**(5), p. 052909, 2014. 51

[82] Y.-D. Yang and Y.-Z. Huang, "Mode characteristics and directional emission for square microcavity lasers," *J. Phys. D: Appl. Phys.* **49**(25), p. 253001, 2016. 21

[83] H. E. Türeci, A. D. Stone, and B. Collier, "Self-consistent multimode lasing theory for complex or random lasing media," *Phys. Rev. A* **74**(4), p. 043822, 2006. 23

[84] H. E. Türeci, A. D. Stone, and L. Ge, "Theory of the spatial structure of nonlinear lasing modes," *Phys. Rev. A* **76**(1), p. 013813, 2007.

[85] H. E. Tureci, L. Ge, S. Rotter, and A. D. Stone, "Strong interactions in multimode random lasers," *Science* **320**(5876), pp. 643–646, 2008.

[86] H. E. Türeci, A. D. Stone, L. Ge, S. Rotter, and R. J. Tandy, "Ab initio self-consistent laser theory and random lasers," *Nonlinearity* **22**(1), p. C1, 2008. 23

[87] L. Ge, Y. D. Chong, and A. D. Stone, "Steady-state ab initio laser theory: generalizations and analytic results," *Phys. Rev. A* **82**(6), p. 063824, 2010. 23, 65, 96, 121, 168, 172

[88] A. Cerjan, B. Redding, L. Ge, S. F. Liew, H. Cao, and A. D. Stone, "Controlling mode competition by tailoring the spatial pump distribution in a laser: a resonance-based approach," *Opt. Express* **24**(23), pp. 26006–26015, 2016. 23, 65, 96, 121, 168

[89] C.-G. Ma, J.-L. Xiao, Z.-X. Xiao, Y.-D. Yang, and Y.-Z. Huang, "Chaotic microlasers caused by internal mode interaction for random number generation," *Light: Sci. & Appl.* **11**(1), pp. 1–10, 2022. 26

[90] S. Bittner, C. Lafargue, I. Gozhyk, N. Djellali, L. Milliet, D. Hickox-Young, C. Ulysse, D. Bouche, R. Dubertrand, E. Bogomolny, *et al.*, "Origin of emission from square-shaped organic microlasers," *Europhys. Lett.* **113**(5), p. 54002, 2016. 29

[91] V. Bianco, P. Memmolo, M. Leo, S. Montresor, C. Distante, M. Paturzo, P. Picart, B. Javidi, and P. Ferraro, "Strategies for reducing speckle noise in digital holography," *Light: Sci. & Appl.* **7**(1), p. 48, 2018. 29, 56

[92] T. Burkhard, M. Ziegler, I. Fischer, and W. Elsasser, "Spatio-temporal dynamics of broad area semi-conductor lasers and its characterization," *Chaos Solitons Fractals* **10**(4), pp. 845–850, 1999. 36

[93] V. Bespalov and V. Talanov, "Filamentary structure of light beams in nonlinear liquids," *Soviet Journal of Experimental and Theoretical Physics Letters* **3**, p. 307, 1966. 43

[94] K. J. Vahala, "Optical microcavities," *Nature* **424**(6950), pp. 839–846, 2003. 43

[95] I. Daubechies, *Ten lectures on wavelets*, SIAM, 1992. 50

[96] J. W. Goodman, *Speckle phenomena in optics: theory and applications*, Roberts and Company Publishers, 2007. 56, 72, 73, 92

[97] J. C. Dainty, *Laser speckle and related phenomena*, vol. 9, Springer Science & Business Media, 2013. 56

[98] K. V. Chellappan, E. Erden, and H. Urey, "Laser-based displays: a review," *Appl. Opt.* **49**(25), pp. F79–F98, 2010. 56

[99] S. Lowenthal and D. Joyeux, "Speckle removal by a slowly moving diffuser associated with a motionless diffuser," *J. Opt. Soc. Am.* **61**(7), pp. 847–851, 1971. 56

[100] S. Kubota and J. W. Goodman, "Very efficient speckle contrast reduction realized by moving diffuser device," *Appl. Opt.* **49**(23), pp. 4385–4391, 2010. 56

[101] B. Redding, G. Allen, E. R. Dufresne, and H. Cao, "Low-loss high-speed speckle reduction using a colloidal dispersion," *Appl. Opt.* **52**(6), pp. 1168–1172, 2013. 56

[102] M. N. Akram, Z. Tong, G. Ouyang, X. Chen, and V. Kartashov, "Laser speckle reduction due to spatial and angular diversity introduced by fast scanning micromirror," *Appl. Opt.* **49**(17), pp. 3297–3304, 2010. 56

[103] R. Chriki, M. Nixon, V. Pal, C. Tradonsky, G. Barach, A. A. Friesem, and N. Davidson, "Manipulating the spatial coherence of a laser source," *Opt. Express* **23**(10), pp. 12989–12997, 2015. 56

[104] S. Knitter, C. Liu, B. Redding, M. K. Khokha, M. A. Choma, and H. Cao, "Coherence switching of a degenerate VECSEL for multimodality imaging," *Optica* **3**(4), pp. 403–406, 2016. 56

[105] C. Gouedard, D. Husson, C. Sauteret, F. Auzel, and A. Migus, "Generation of spatially incoherent short pulses in laser-pumped neodymium stoichiometric crystals and powders," *J. Opt. Soc. Am. B* **10**(12), pp. 2358–2363, 1993. 56

[106] B. Redding, M. A. Choma, and H. Cao, "Spatial coherence of random laser emission," *Opt. Lett.* **36**(17), pp. 3404–3406, 2011.

[107] B. Redding, M. A. Choma, and H. Cao, "Speckle-free laser imaging using random laser illumination," *Nat. Photonics* **6**(6), pp. 355–359, 2012. 82

[108] B. H. Hokr, M. S. Schmidt, J. N. Bixler, P. N. Dyer, G. D. Noojin, B. Redding, R. J. Thomas, B. A. Rockwell, H. Cao, V. V. Yakovlev, *et al.*, "A narrow-band speckle-free light source via random raman lasing," *J. Mod. Opt.* **63**(1), pp. 46–49, 2016. 56

[109] B. Redding, A. Cerjan, X. Huang, M. L. Lee, A. D. Stone, M. A. Choma, and H. Cao, "Low spatial coherence electrically pumped semiconductor laser for speckle-free full-field imaging," *Proc. Natl. Acad. Sci.* **112**(5), pp. 1304–1309, 2015. 56, 92

[110] A. Mermillod-Blondin, H. Mentzel, and A. Rosenfeld, "Time-resolved microscopy with random lasers," *Opt. Lett.* **38**(20), pp. 4112–4115, 2013. 57

[111] R. Chriki, S. Mahler, C. Tradonsky, V. Pal, A. A. Friesem, and N. Davidson, "Spatiotemporal supermodes: Rapid reduction of spatial coherence in highly multimode lasers," *Phys. Rev. A* **98**(2), p. 023812, 2018. 57

[112] R. J. Lang, A. G. Larsson, and J. G. Cody, "Lateral modes of broad area semiconductor lasers: theory and experiment," *IEEE J. Quantum Electron.* **27**(3), p. 312, 1991. 57

[113] S. Hartmann and W. Elsäßer, "A novel semiconductor-based, fully incoherent amplified spontaneous emission light source for ghost imaging," *Sci. Rep.* **7**, p. 41866, 2017. 57

[114] A. E. Siegman, *Lasers*, University Science Books, 1986. 58, 61, 70, 81, 122

[115] S. Roelandt, Y. Meuret, A. Jacobs, K. Willaert, P. Janssens, H. Thienpont, and G. Verschaffelt, "Human speckle perception threshold for still images from a laser projection system," *Opt. Express* **22**(20), pp. 23965–23979, 2014. 58

[116] G. A. Geri and L. A. Williams, "Perceptual assessment of laser-speckle contrast," *J. Soc. Inf. Display* **20**(1), pp. 22–27, 2012. 58

[117] T. Fukushima, S. Sunada, T. Harayama, K. Sakaguchi, and Y. Tokuda, "Lowest-order axial and ring mode lasing in confocal quasi-stadium laser diodes," *Appl. Opt.* **51**(14), pp. 2515–2520, 2012. 59

[118] S. Gigan, L. Lopez, N. Treps, A. Maître, and C. Fabre, "Image transmission through a stable paraxial cavity," *Phys. Rev. A* **72**(2), p. 023804, 2005. 62

[119] M. Peeters, G. Verschaffelt, H. Thienpont, S. K. Mandre, I. Fischer, and M. Grabherr, "Spatial decoherence of pulsed broad-area vertical-cavity surface-emitting lasers," *Opt. Express* **13**(23), pp. 9337–9345, 2005. 78, 148

[120] S. K. Mandre, W. Elsäßer, I. Fischer, M. Peeters, and G. Verschaffelt, "Evolution from modal to spatially incoherent emission of a broad-area vcsel," *Opt. Express* **16**(7), pp. 4452–4464, 2008. 78, 148

[121] G. Craggs, G. Verschaffelt, S. K. Mandre, H. Thienpont, and I. Fischer, "Thermally controlled onset of spatially incoherent emission in a broad-area vertical-cavity surface-emitting laser," *IEEE J. Sel. Top. Quantum Electron.* **15**(3), pp. 555–562, 2009. 78

[122] H. Kogelnik and T. Li, "Laser beams and resonators," *Appl. Opt.* **5**(10), pp. 1550–1567, 1966. 81

[123] N. Hodgson and H. Weber, *Laser Resonators and Beam Propagation: Fundamentals, Advanced Concepts, Applications*, vol. 108, Springer, 2005. 81

[124] J. Salzman, R. Lang, S. Margalit, and A. Yariv, "Tilted-mirror semiconductor lasers," *Appl. Phys. Lett.* **47**(1), pp. 9–11, 1985. 81

[125] R. Lang, J. Salzman, and A. Yariv, "Modal analysis of semiconductor lasers with nonplanar mirrors," *IEEE J. Quantum Electron.* **22**(3), pp. 463–470, 1986. 81

[126] J. Salzman, T. Venkatesan, R. Lang, M. Mittelstein, and A. Yariv, "Unstable resonator cavity semiconductor lasers," *Appl. Phys. Lett.* **46**(3), pp. 218–220, 1985. 81

[127] J. Salzman, R. Lang, A. Larson, and A. Yariv, "Confocal unstable-resonator semiconductor laser," *Opt. Lett.* **11**(8), pp. 507–509, 1986.

[128] M. L. Tilton, G. C. Dente, A. H. Paxton, J. Cser, R. K. Defreez, C. E. Moeller, and D. Depatie, "High power, nearly diffraction-limited output from a semiconductor laser with an unstable resonator," *IEEE J. Quantum Electron.* **27**(9), pp. 2098–2108, 1991.

[129] S. A. Biellak, C. G. Fanning, Y. Sun, S. S. Wong, and A. E. Siegman, "Reactive-ion-etched diffraction-limited unstable resonator semiconductor lasers," *IEEE J. Quantum Electron.* **33**(2), pp. 219–230, 1997. 81

[130] H. Adachihara, O. Hess, E. Abraham, P. Ru, and J. Moloney, "Spatiotemporal chaos in broad-area semiconductor lasers," *J. Opt. Soc. Am. B* **10**(4), pp. 658–665, 1993. 81

[131] L. Li, "The advances and characteristics of high-power diode laser materials processing," *Opt. Lasers Eng.* **34**(4-6), pp. 231–253, 2000. 81

[132] K. Shigihara, Y. Nagai, S. Karakida, A. Takami, Y. Kokubo, H. Matsubara, and S. Kakimoto, "High-power operation of broad-area laser diodes with GaAs and AlGaAs single quantum wells for Nd:YAG laser pumping," *IEEE J. Quantum Electron.* **27**(6), pp. 1537–1543, 1991. 82

[133] A. Müller, S. Marschall, O. B. Jensen, J. Fricke, H. Wenzel, B. Sumpf, and P. E. Andersen, "Diode laser based light sources for biomedical applications," *Laser Photonics Rev.* **7**(5), pp. 605–627, 2013. 82

[134] H. Primack and U. Smilansky, "Quantal consequences of perturbations which destroy structurally unstable orbits in chaotic billiards," *J. Phys. A* **27**(13), p. 4439, 1994. 82

[135] H. Schomerus and M. Sieber, "Bifurcations of periodic orbits and uniform approximations," *J. Phys. A* **30**(13), p. 4537, 1997. 82

[136] M. Sieber, "Semiclassical transition from an elliptical to an oval billiard," *J. Phys. A* **30**, pp. 4563–4596, jul 1997. 82

[137] A. Pascal, S. Bittner, B. Dietz, A. Trabattoni, U. C., M. Romanelli, M. Brunel, J. Zyss, and M. Lebental, "Waves and rays in plano-concave laser cavities: Ii. a semiclassical approach," *Eur. J. Phys.* **38**, p. 034011, 2017. 82, 83

[138] M. Humar, M. C. Gather, and S.-H. Yun, "Cellular dye lasers: lasing thresholds and sensing in a planar resonator," *Opt. Express* **23**(21), pp. 27865–27879, 2015. 82

[139] I. Riou, N. Mielec, G. Lefèvre, M. Prevedelli, A. Landragin, P. Bouyer, A. Bertoldi, R. Geiger, and B. Canuel, "A marginally stable optical resonator for enhanced atom interferometry," *J. Phys. B: At. Mol. Opt. Phys.* **50**(15), p. 155002, 2017. 82

[140] K. Husimi, "Some formal properties of the density matrix," *Proc. Phys.-Math. Soc. Jpn.* **22**(4), pp. 264–314, 1940. 88

[141] O. Hess and T. Kuhn, "Spatio-temporal dynamics of semiconductor lasers: Theory, modelling and analysis," *Prog. Quantum Electron.* **20**(2), pp. 85–179, 1996. 111

[142] Y. Chong, L. Ge, H. Cao, and A. D. Stone, "Coherent perfect absorbers: time-reversed lasers," *Phys. Rev. Lett.* **105**(5), p. 053901, 2010. 114

[143] A. Ghobadi, H. Hajian, B. Butun, and E. Ozbay, "Strong light–matter interaction in lithography-free planar metamaterial perfect absorbers," *ACS Photonics* **5**(11), pp. 4203–4221, 2018.

[144] G. Liu, J. Chen, P. Pan, and Z. Liu, "Hybrid metal-semiconductor metasurface based photo-electronic perfect absorber," *IEEE J. Sel. Top. Quantum Electron.* **25**(3), pp. 1–7, 2018.

[145] P. Tang, G. Liu, X. Liu, G. Fu, Z. Liu, and J. Wang, "Plasmonic wavy surface for ultrathin semiconductor black absorbers," *Opt. Express* **28**(19), pp. 27764–27773, 2020. 114

[146] J. D. Hart, Y. Terashima, A. Uchida, G. B. Baumgartner, T. E. Murphy, and R. Roy, "Recommendations and illustrations for the evaluation of photonic random number generators," *APL Photonics* **2**(9), p. 090901, 2017. 116, 139, 141

[147] M. Herrero-Collantes and J. C. Garcia-Escartin, "Quantum random number generators," *Rev. Mod. Phys.* **89**(1), p. 015004, 2017. 116

[148] A. Uchida, K. Amano, M. Inoue, K. Hirano, S. Naito, H. Someya, I. Oowada, T. Kurashige, M. Shiki, S. Yoshimori, K. Yoshimura, and P. Davis, "Fast physical random bit generation with chaotic semiconductor lasers," *Nat. Photonics* **2**(12), pp. 728–732, 2008. 116

[149] I. Reidler, Y. Aviad, M. Rosenbluh, and I. Kanter, "Ultrahigh-speed random number generation based on a chaotic semiconductor laser," *Phys. Rev. Lett.* **103**(2), p. 024102, 2009. 116, 130, 131

[150] I. Kanter, Y. Aviad, I. Reidler, E. Cohen, and M. Rosenbluh, "An optical ultrafast random bit generator," *Nat. Photonics* **4**(1), p. 58, 2010. 116

[151] A. Argyris, S. Deligiannidis, E. Pikasis, A. Bogris, and D. Syvridis, "Implementation of 140 Gb/s true random bit generator based on a chaotic photonic integrated circuit," *Opt. Express* **18**(18), pp. 18763–18768, 2010.

[152] K. Hirano, T. Yamazaki, S. Morikatsu, H. Okumura, H. Aida, A. Uchida, S. Yoshimori, K. Yoshimura, T. Harayama, and P. Davis, "Fast random bit generation with bandwidth-enhanced chaos in semiconductor lasers," *Opt. Express* **18**(6), pp. 5512–5524, 2010.

[153] J. Zhang, Y. Wang, M. Liu, L. Xue, P. Li, A. Wang, and M. Zhang, "A robust random number generator based on differential comparison of chaotic laser signals," *Opt. Express* **20**(7), pp. 7496–7506, 2012.

[154] X. Li and S. Chan, "Heterodyne random bit generation using an optically injected semiconductor laser in chaos," *IEEE J. Quantum Electron.* **49**(10), pp. 829–838, 2013. 116

[155] N. Oliver, M. C. Soriano, D. W. Sukow, and I. Fischer, "Fast random bit generation using a chaotic laser: approaching the information theoretic limit," *IEEE J. Quantum Electron.* **49**(11), pp. 910–918, 2013.

[156] X. Fang, B. Wetzel, J. M. Merolla, J. M. Dudley, L. Larger, C. Guyeux, and J. M. Bahi, "Noise and chaos contributions in fast random bit sequence generated from broadband optoelectronic entropy sources," *IEEE Trans. Circuits Syst. I Regul. Pap.* **61**(3), pp. 888–901, 2014.

[157] M. Virte, E. Mercier, H. Thienpont, K. Panajotov, and M. Sciamanna, "Physical random bit generation from chaotic solitary laser diode," *Opt. Express* **22**(14), pp. 17271–17280, 2014.

[158] R. Sakuraba, K. Iwakawa, K. Kanno, and A. Uchida, "Tb/s physical random bit generation with bandwidth-enhanced chaos in three-cascaded semiconductor lasers," *Opt. Express* **23**(2), pp. 1470–1490, 2015. 116, 133

[159] X. Tang, Z. M. Wu, J. G. Wu, T. Deng, J. J. Chen, L. Fan, Z. Q. Zhong, and G. Q. Xia, "Tbits/s physical random bit generation based on mutually coupled semiconductor laser chaotic entropy source," *Opt. Express* **23**(26), pp. 33130–33141, 2015.

[160] T. Butler, C. Durkan, D. Goulding, S. Slepneva, B. Kelleher, S. P. Hegarty, and G. Huyet, "Optical ultrafast random number generation at 1 Tb/s using a turbulent semiconductor ring cavity laser," *Opt. Lett.* **41**(2), pp. 388–391, 2016. 116, 133

[161] S. Shinohara, K. Arai, P. Davis, S. Sunada, and T. Harayama, "Chaotic laser based physical random bit streaming system with a computer application interface," *Opt. Express* **25**(6), pp. 6461–6474, 2017. 136, 145

[162] K. Ugajin, Y. Terashima, K. Iwakawa, A. Uchida, T. Harayama, K. Yoshimura, and M. Inubushi, "Real-time fast physical random number generator with a photonic integrated circuit," *Opt. Express* **25**(6), pp. 6511–6523, 2017. 145

[163] S. Xiang, B. Wang, Y. Wang, Y. Han, A. Wen, and Y. Hao, "2.24-Tb/s physical random bit generation with minimal post-processing based on chaotic semiconductor lasers network," *J. Lightwave Technol.* **37**(16), pp. 3987–3993, 2019. 116

[164] J. Marron, A. J. Martino, and G. M. Morris, "Generation of random arrays using clipped laser speckle," *Appl. Opt.* **25**(1), pp. 26–30, 1986. 116

[165] P. Lalanne, H. Richard, J. C. Rodier, P. Chavel, J. Taboury, K. Madani, P. Garda, and F. Devos, "2-D generation of random numbers by multimode fiber speckle for silicon arrays of processing elements," *Opt. Commun.* **76**(5-6), pp. 387–394, 1990. 116

[166] X. Li, A. B. Cohen, T. E. Murphy, and R. Roy, "Scalable parallel physical random number generator based on a superluminescent led," *Opt. Lett.* **36**(6), pp. 1020–1022, 2011. 116

[167] P. Li, K. Li, X. Guo, Y. Guo, Y. Liu, B. Xu, A. Bogris, K. A. Shore, and Y. Wang, "Parallel optical random bit generator," *Opt. Lett.* **44**(10), pp. 2446–2449, 2019. 116

[168] P. Gallion and G. Debarge, "Quantum phase noise and field correlation in single frequency semiconductor laser systems," *IEEE J. Quantum Electron.* **20**(4), pp. 343–349, 1984. 123

[169] C. Henry, "Phase noise in semiconductor lasers," *J. Lightwave Technol.* **4**(3), pp. 298–311, 1986. 123

[170] W. Elsäßer and E. Göbel, "Multimode effects in the spectral linewidth of semiconductor lasers," *IEEE J. Quantum Electron.* **21**(6), pp. 687–692, 1985. 123

[171] L. E. Bassham III, A. L. Rukhin, J. Soto, J. R. Nechvatal, M. E. Smid, E. B. Barker, S. D. Leigh, M. Levenson, M. Vangel, D. L. Banks, *et al.*, *SP 800-22 rev. 1a. a statistical test suite for random and pseudorandom number generators for cryptographic applications*, National Institute of Standards & Technology, 2010. 134

[172] A. Yamaguchi, T. Seo, and K. Yoshikawa, "On the pass rate of nist statistical test suite for randomness," *JSIAM Letters* **2**, pp. 123–126, 2010. 135

[173] D. Lihua, Z. Yong, J. Ligang, and H. Xucang, "Study on the pass rate of NIST SP800-22 statistical test suite," in *2014 Tenth International Conference on Computational Intelligence and Security*, pp. 402–404, IEEE, 2014. 136

[174] G. Marsaglia, "Diehard: a battery of tests of randomness," 1995. https://web.archive.org/web/20160125103112/http://stat.fsu.edu/pub/diehard/. 138

[175] K. H. Tsoi, K. H. Leung, and P. H. W. Leong, "High performance physical random number generator," *IET computers & digital techniques* **1**(4), pp. 349–352, 2007. 138

[176] A. Cohen and I. Procaccia, "Computing the kolmogorov entropy from time signals of dissipative and conservative dynamical systems," *Phys. Rev. A* **31**(3), pp. 1872–1882, 1985. 139

[177] T. M. Cover and J. A. Thomas, *Elements of information theory*, John Wiley & Sons, 2012. 140

[178] A. L. Franz, R. Roy, L. B. Shaw, and I. B. Schwartz, "Changing dynamical complexity with time delay in coupled fiber laser oscillators," *Phys. Rev. Lett.* **99**(5), p. 053905, 2007. 144

[179] F. Riechert, G. Verschaffelt, M. Peeters, G. Bastian, U. Lemmer, and I. Fischer, "Speckle characteristics of a broad-area VCSEL in the incoherent emission regime," *Opt. Commun.* **281**(17), pp. 4424–4431, 2008. 148

[180] O. Buccafusca, J. Chilla, J. Rocca, C. Wilmsen, S. Feld, and R. Leibenguth, "Ultrahigh frequency oscillations and multimode dynamics in vertical cavity surface emitting lasers," *Appl. Phys. Lett.* **67**(2), pp. 185–187, 1995. 148

[181] M. Giudici, J. Tredicce, G. Vaschenko, J. Rocca, and C. Menoni, "Spatio-temporal dynamics in vertical cavity surface emitting lasers excited by fast electrical pulses," *Opt. Commun.* **158**(1-6), pp. 313–321, 1998.

[182] J. Mulet and S. Balle, "Transverse mode dynamics in vertical-cavity surface-emitting lasers: Spatiotemporal versus modal expansion descriptions," *Phys. Rev. A* **66**(5), p. 053802, 2002.

[183] A. Barchanski, T. Gensty, C. Degen, I. Fischer, and W. Elsasser, “Picosecond emission dynamics of vertical-cavity surface-emitting lasers: spatial, spectral, and polarization-resolved characterization,” *IEEE J. Quantum Electron.* **39**(7), pp. 850–858, 2003.

[184] S. Bittner and M. Sciamanna, “Nonlinear polarization and transverse mode dynamics of a broad-area vcsel in continuous wave operation,” *arXiv:2203.14736* **arXiv preprint**, 2022. 148, 162, 174

[185] A. Molitor, T. Mohr, S. Hartmann, and W. Elsäßer, “Investigations on spectro-temporally resolved stokes polarization parameters of transverse multi-mode vertical-cavity surface-emitting lasers,” *IEEE J. Quantum Electron.* **52**(2), pp. 1–9, 2015. 148

[186] M. Plöschner, M. M. Morote, D. Dahl, M. Mounaix, G. Light, A. Rakic, and J. Carpenter, “Spatial, spectral, temporal and polarisation resolved state tomography of light,” *arXiv:2202.01932* **arXiv preprint**, 2022. 148

[187] Y.-F. Chen, K.-F. Huang, and Y.-P. Lan, “Localization of wave patterns on classical periodic orbits in a square billiard,” *Phys. Rev. E* **66**(4), p. 046215, 2002. 148

[188] K.-F. Huang, Y.-F. Chen, H. Lai, and Y.-P. Lan, “Observation of the wave function of a quantum billiard from the transverse patterns of vertical cavity surface emitting lasers,” *Phys. Rev. Lett.* **89**(22), p. 224102, 2002.

[189] Y.-F. Chen, K.-F. Huang, H. Lai, and Y.-P. Lan, “Observation of vector vortex lattices in polarization states of an isotropic microcavity laser,” *Phys. Rev. Lett.* **90**(5), p. 053904, 2003.

[190] Y.-F. Chen, K.-F. Huang, H. Lai, and Y.-P. Lan, “Rules of selection for spontaneous coherent states in mesoscopic systems: Using the microcavity laser as an analog study,” *Phys. Rev. E* **68**(2), p. 026210, 2003.

[191] T. Gensty, K. Becker, I. Fischer, W. Elsäßer, C. Degen, P. Debernardi, and G. P. Bava, “Wave chaos in real-world vertical-cavity surface-emitting lasers,” *Phys. Rev. Lett.* **94**(23), p. 233901, 2005.

[192] C. Chen, K.-W. Su, T.-H. Lu, C. Liu, Y.-F. Chen, and K.-F. Huang, “Generation of two-dimensional chaotic vector fields from a surface-emitting semiconductor laser: Analysis of vector singularities,” *Phys. Rev. E* **76**(2), p. 026219, 2007.

[193] C. Chen, C. Liu, K.-W. Su, T.-H. Lu, Y.-F. Chen, and K.-F. Huang, “Statistical properties of experimental coherent waves in microcavity lasers: Analogous study of quantum billiard wave functions,” *Phys. Rev. E* **75**(4), p. 046202, 2007.

[194] C. Chen, K.-W. Su, Y.-F. Chen, and K.-F. Huang, “Various high-order modes in vertical-cavity surface-emitting lasers with equilateral triangular lateral confinement,” *Opt. Lett.* **33**(5), pp. 509–511, 2008.

[195] R. C. Chen, Y. Yu, Y. Huang, C. Chen, Y.-F. Chen, and K.-F. Huang, “Exploring the origin of the directional emission from a microcavity with a large-aperture surface-emitting laser,” *Opt. Lett.* **34**(12), pp. 1810–1812, 2009.

[196] Y.-F. Chen, Y.-T. Yu, Y.-J. Huang, P.-Y. Chiang, K.-W. Su, and K.-F. Huang, “Extracting photon periodic orbits from spontaneous emission spectra in laterally confined vertically emitted cavities,” *Opt. Lett.* **35**(16), pp. 2723–2725, 2010.

[197] Y.-F. Chen, Y. Yu, P. Chiang, P. Tuan, Y. Huang, H. Liang, and K.-F. Huang, “Manifestation of quantum-billiard eigenvalue statistics from subthreshold emission of vertical-cavity surface-emitting lasers,” *Phys. Rev. E* **83**(1), p. 016208, 2011.

[198] Y. Yu, P. Tuan, P. Chiang, H. Liang, K.-F. Huang, and Y.-F. Chen, “Wave pattern and weak localization of chaotic versus scarred modes in stadium-shaped surface-emitting lasers,” *Phys. Rev. E* **84**(5), p. 056201, 2011. 148

[199] A. Brejnak, M. Gebski, A. Sokol, M. Marciniak, M. Wasiak, J. Muszalski, J. Lott, I. Fischer, and T. Czyszanowski, “Boosting the output power of large-aperture lasers by breaking their circular symmetry,” *Optica* **8**(9), pp. 1167–1175, 2021. 148, 149

[200] M. Dems, R. Kotynski, and K. Panajotov, “Planewave admittance method—a novel approach for determining the electromagnetic modes in photonic structures,” *Opt. Express* **13**(9), pp. 3196–3207, 2005.

[201] M. Dems, T. Czyszanowski, and K. Panajotov, “Numerical analysis of high Q-factor photonic-crystal VCSELs with plane-wave admittance method,” *Opt. Quantum Electron.* **39**(4), pp. 419–426, 2007. 149

[202] D. I. Babic and S. W. Corzine, “Analytic expressions for the reflection delay, penetration depth, and absorptance of quarter-wave dielectric mirrors,” *IEEE J. Quantum Electron.* **28**(2), pp. 514–524, 1992. 151

[203] D. I. Babic, Y. Chung, N. Dagli, and J. E. Bowers, “Modal reflection of quarter-wave mirrors in vertical-cavity lasers,” *IEEE J. Quantum Electron.* **29**(6), pp. 1950–1962, 1993.

[204] R. J. Ram, D. Babid, Y. York, and J. E. Bowers, “Spontaneous emission in microcavities with distributed mirrors,” *IEEE J. Quantum Electron.* **31**(2), pp. 399–410, 1995. 151

[205] S. M. Girvin and K. Yang, *Modern condensed matter physics*, Cambridge University Press, 2019. 151

[206] M. Born and E. Wolf, *Principles of optics: electromagnetic theory of propagation, interference and diffraction of light*, Elsevier, 2013. 153, 158

[207] K. Okamoto, *Fundamentals of optical waveguides*, Elsevier, 2021. 159

[208] K. D. Choquette, R. P. Schneider, K. L. Lear, and R. E. Leibenguth, "Gain-dependent polarization properties of vertical-cavity lasers," *IEEE J. Sel. Top. Quantum Electron.* **1**(2), pp. 661–666, 1995. 162

[209] M. San Miguel, Q. Feng, and J. V. Moloney, "Light-polarization dynamics in surface-emitting semiconductor lasers," *Phys. Rev. A* **52**(2), p. 1728, 1995.

[210] M. Van Exter, A. Al-Remawi, and J. Woerdman, "Polarization fluctuations demonstrate nonlinear anisotropy of a vertical-cavity semiconductor laser," *Phys. Rev. Lett.* **80**(22), p. 4875, 1998.

[211] T. Ackemann and M. Sondermann, "Characteristics of polarization switching from the low to the high frequency mode in vertical-cavity surface-emitting lasers," *Appl. Phys. Lett.* **78**(23), pp. 3574–3576, 2001. 162, 174

[212] S. F. Yu, *Analysis and design of vertical cavity surface emitting lasers*, vol. 7, John Wiley & Sons, 2003. 162

[213] A. Jansen van Doorn, M. Van Exter, and J. Woerdman, "Elasto-optic anisotropy and polarization orientation of vertical-cavity surface-emitting semiconductor lasers," *Appl. Phys. Lett.* **69**(8), pp. 1041–1043, 1996. 162

[214] K. D. Choquette and R. Leibenguth, "Control of vertical-cavity laser polarization with anisotropic transverse cavity geometries," *IEEE Photonics Technol. Lett.* **6**(1), pp. 40–42, 1994. 166

[215] P. Debernardi, G. P. Bava, C. Degen, I. Fischer, and W. Elsasser, "Influence of anisotropies on transverse modes in oxide-confined VCSELs," *IEEE J. Quantum Electron.* **38**(1), pp. 73–84, 2002.

[216] I. Babushkin, M. Schulz-Ruhtenberg, N. Loiko, K.-F. Huang, and T. Ackemann, "Coupling of polarization and spatial degrees of freedom of highly divergent emission in broad-area square vertical-cavity surface-emitting lasers," *Phys. Rev. Lett.* **100**(21), p. 213901, 2008. 166

[217] M. Lebental, N. Djellali, C. Arnaud, J.-S. Lauret, J. Zyss, R. Dubertrand, C. Schmit, and E. Bogomolny, "Inferring periodic orbits from spectra of simply shaped microlasers," *Phys. Rev. A* **76**(2), p. 023830, 2007. 168

[218] E. Bogomolny, N. Djellali, R. Dubertrand, I. Gozhyk, M. Lebental, C. Schmit, C. Ulysse, and J. Zyss, "Trace formula for dielectric cavities. ii. regular, pseudointegrable, and chaotic examples," *Phys. Rev. E* **83**(3), p. 036208, 2011. 168

[219] T. Fukushima, S. Shinohara, S. Sunada, T. Harayama, K. Sakaguchi, and Y. Tokuda, "Ray dynamical simulation of penrose unilluminable room cavity," in *Laser Science*, pp. JW3A–19, Optical Society of America, 2013. 168, 171

[220] T. Fukushima, S. Shinohara, S. Sunada, T. Harayama, K. Sakaguchi, and Y. Tokuda, "Lasing of TM modes in a two-dimensional GaAs microlaser," *Opt. Express* **22**(10), pp. 11912–11917, 2014.

[221] T. Fukushima, K. Sakaguchi, and Y. Tokuda, "Light propagation in a penrose unilluminable room," *Opt. Express* **23**(13), pp. 17431–17436, 2015.

[222] T. Fukushima, "Resonance modes extremely sensitive to the asymmetry of cavity shape," in *2020 22nd International Conference on Transparent Optical Networks (ICTON)*, pp. 1–4, IEEE, 2020. 171

[223] K. An, J. Kim, J. Kim, J. Seo, K.-W. Park, and S. Moon, "The illumination problem in open systems: Observation of a half-illuminated mode in a penrose cavity," *preprint* **v1**, 2022. 168, 171

[224] M. Willemsen, M. Khalid, M. Van Exter, and J. Woerdman, "Polarization switching of a vertical-cavity semiconductor laser as a Kramers hopping problem," *Phys. Rev. Lett.* **82**(24), p. 4815, 1999. 174

[225] M. Willemsen, M. Van Exter, and J. Woerdman, "Anatomy of a polarization switch of a vertical-cavity semiconductor laser," *Phys. Rev. Lett.* **84**(19), p. 4337, 2000.

[226] M. Sondermann, M. Weinkath, and T. Ackemann, "Polarization switching to the gain disfavored mode in vertical-cavity surface-emitting lasers," *IEEE J. Quantum Electron.* **40**(2), pp. 97–104, 2004. 174

[227] M. Virte, K. Panajotov, and M. Sciamanna, "Bifurcation to nonlinear polarization dynamics and chaos in vertical-cavity surface-emitting lasers," *Phys. Rev. A* **87**(1), p. 013834, 2013. 174

[228] X. Porte, A. Skalli, N. Haghighi, S. Reitzenstein, J. A. Lott, and D. Brunner, "A complete, parallel and autonomous photonic neural network in a semiconductor multimode laser," *J. Phys.: Photonics* **3**(2), p. 024017, 2021. 181

[229] J. Vatin, D. Rontani, and M. Sciamanna, "Experimental reservoir computing using VCSEL polarization dynamics," *Opt. Express* **27**(13), pp. 18579–18584, 2019. 181